Oxford Brookes University

Investigation into the Effect of Physical Size on Crack Initiation in Brittle Materials Subject to Mixed Mode Fracture (With Focus on Graphite Nuclear Reactor Cores)

George Peter Michael Kwasowski

February 2018

A thesis submitted for the partial fulfilment of the requirements of

Oxford Brookes University for the degree of MSc by Research

Abstract

This work explores experimentally and numerically the topic of size effect in simple and complex loading scenarios with a view to determining a suitable fracture prediction criterion for advanced gas-cooled reactor (AGR) graphite bricks. In this context size effect is taken to mean the non-constant nature of material properties when specimens are tested at different sizes. The literature shows that typically strength correlates negatively with increasing size. Conversely, the literature also shows that fracture toughness typically correlates positively with increasing size. The work presented here concentrates on concrete as an analogy of graphite. Specimens are tested at a range of sizes for splitting strength, flexural strength, compressive strength and fracture toughness. Scaling behaviour of mixed mode (I/II) fracture is also examined experimentally and through FEA. In total, data from over 750 specimens is presented. The project's experimental work is in agreement with the literature; showing a negative correlation between size and splitting strength while showing a positive correlation between size and fracture toughness. The testing and theoretical work is used to demonstrate the applicability of the FEA approach to the stress states found in late life AGR reactor graphite bricks; with the criterion shown to be size insensitive for Mode-II dominant stress states through the experimental testing and FEA modelling of three sizes of disc specimens with 90° re-entrant corners.

Acknowledgements

There have been too many people to thank along the way but there are several who stand out.

Gareth Neighbour. Without his input this adventure would have never begun.

Alan Steer and EDF Energy. For their interest in my early work.

Neil Fellows. My remaining supervisor who has been there through thick and thin.

John Durodola. For his belief in me.

Dedication

This work is dedicated to my parents. Both of whom died during this period of research.

Table of Contents

List of Figures

List of Equations

List of Tables

Nomenclature

ACI	American Concrete Institute
AGR	Advanced Gas-cooled Reactor
ASTM	American Society of Testing and Materials
BSI	British Standards Institute
EDF	Energy de France
FEA	Finite Element Analysis
FPY	Full Power Year
FPZ	Fracture Process Zone
IAEA	International Atomic Energy Agency
LEFM	Linear Elastic Fracture Mechanics
MTS	Maximum Tangential Stress
PMMA	Poly Methyl Methacrylate
SED	Strain Energy Density
SENB	Single Edge Notched Beam

List of Symbols

a	Crack length
α	Generalised FPZ Parameter
b	Breadth
d	Depth
E	Young's Modulus
E*	Young's Modulus Term
G	Strain Energy Release Rate
G_p	Plastic Strain Energy Release Rate
J_{IC}	Plane Strain J-Integral
K	Stress Intensity Factor
K_C	Fracture Toughness
K_{IC}	Plane Strain Fracture Toughness
m	Weibull Modulus
P	Load
P_c	Critical Load
r	Radius
U	Displacement
V	Volume
v	Poisson's Ratio
W	Strain Energy Density
W_C	Critical Strain Energy Density
Y	Dimensionless Geometry Parameter
γ	Surface Energy
ρ	Notch Radius
σ	Stress
σ_{flex}	Flexural Strength
σ_{split}	Splitting Strength
σ_t	Tensile Strength

1.0 Introduction

The UK fleet of advanced gas-cooled reactors (AGRs) is aging. In particular, the graphite bricks which make up the core of the AGRs are undergoing a complicated series of changes. It has been observed through X-ray imaging that bricks are going through a new period of cracking. These new cracks originate from keyways in the graphite bricks. There are concerns that this cracking will compromise the integrity of the AGR cores and in turn interfere with the ability to remove and insert fuel assemblies and control rods (Steer, 2007). The basic structure of the core is shown in Figure 1; the AGR core is made up of such layers. The keyways are clearly visible in the cylindrical bricks in Figure 1, each brick connected by radial keys and interstitial bricks. Fuel assemblies are inserted into the bores of the main bricks, control rods are inserted into the bores of the interstitial bricks.

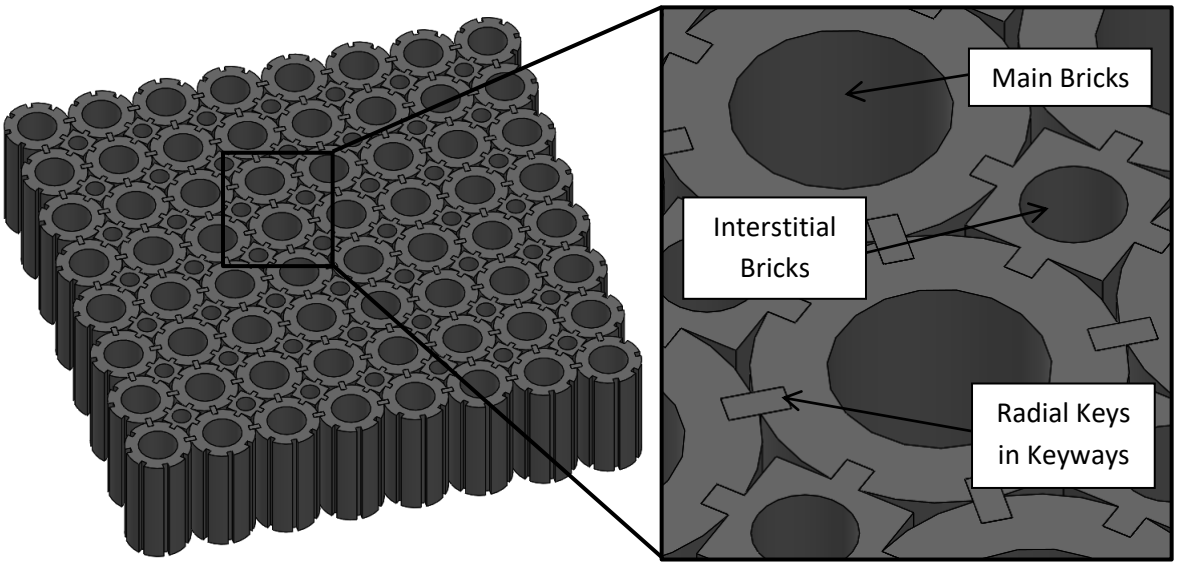

Figure 1. Simplified layer of bricks from AGR core with close up (based on Steer, 2007)

The cracking of the bricks is considered a life limiting ageing mechanism of the AGR cores. This project will work towards a better understanding of the current and future stress states in the keyways of graphite bricks and explore whether a versatile, scale insensitive FEA approach can be developed for late life AGR stress states by means of experimental testing and numerical modelling.

2.0 Aim

The aim of this research project is to explore experimentally and theoretically the suitability of a mixed mode failure criterion to the stress states in AGR graphite bricks. This will also involve the testing of an analogous material to graphite at a range of sizes to ensure the versatility of any approach.

To achieve this aim several intermediate objectives of study have been reached:

- Carry out a literature review, concentrating on;
    - Quasi-brittle materials and their behaviour.
    - Graphite and causes of stress in AGR bricks.
    - Testing of quasi-brittle materials.
    - Size effect in strength and fracture toughness.
    - Fracture and mixed-mode (I/II).
- Comment on literature, putting forward a generalised mixed-mode approach for determining failure loads in quasi-brittle components.
- Develop a versatile approach for characterising mixed-mode states.
- Apply new approach to late life stress states in AGR brick keyways.
- Generate experimental trends for size effect in simple geometries.
- Generate experimental trends for size effect across mixed-mode states.
- Compare the predicted mixed-mode failure loads with both the experimental data from mixed-mode specimens and the AGR stress state evolution over time to determine whether or not the mixed-mode approach in question has merit for application to AGRs.

3.0 Literature Review

This project will consider a range of topics to produce an output on the issue of the stress state in AGR bricks and the applicability of a given criterion to those stress states.

The topics under consideration include:

- The characterisation of brittle and quasi-brittle materials.
- The basic composition of nuclear graphite.
- The main life limiting causes of volumetric change in nuclear graphite components.
- Size effect with regards to strength and fracture toughness.
- The study of mode-I and mixed mode (I/II) fracture.
- Standards related to quasi-brittle material testing.

3.1 Review of Quasi-brittle Materials

This project is interested in exploring the applicability of a failure criterion to AGR bricks, with specific interest given to size effects. This will involve experimental work. Ideally this experimental work should have been carried out with IM1-24 graphite, the graphite that the AGR bricks are made out of. However, this is prohibitively expensive. This section will discuss damage mechanisms, plastic zones and an alternative material to graphite for experimental work.

3.1.1 Material Response and Damage Mechanisms

Figure 2 offers a comparison between the typical stress-strain responses of brittle, ductile and quasi-brittle materials in tension. A purely brittle material (e.g. glass) will give a trace similar to that in Figure 2(a), ductile materials (e.g. steel) will exhibit behaviour like Figure 2(b) while a quasi-brittle material (e.g. graphite or concrete) will give a trace similar to that of Figure 2(c). The physical cause for these differences can be explained through damage mechanisms.

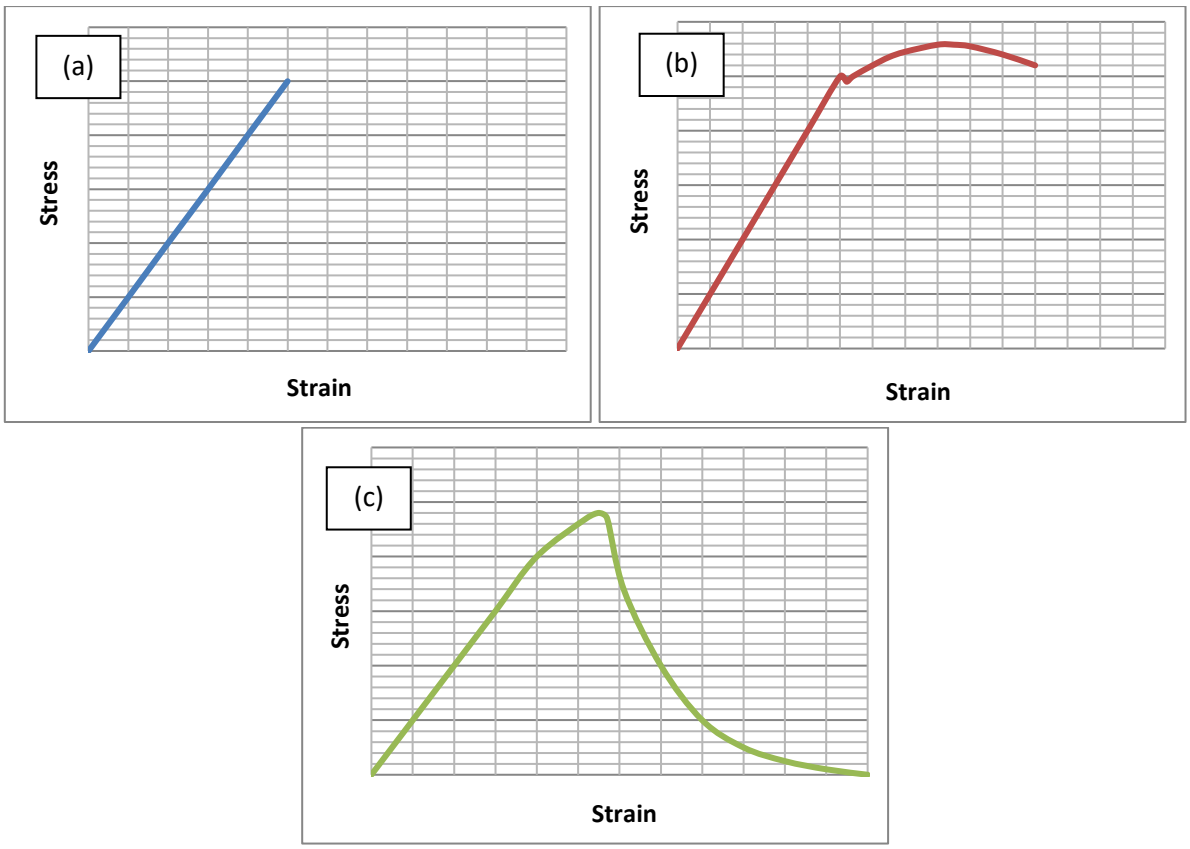

Figure 2 Brittle (a), Ductile (b) and Quasi-brittle (c) idealised stress-strain responses

Ductile materials do not feature in this project as it deals exclusively with brittle and quasi-brittle materials. However, it does require discussion. Ductile materials are highly ordered and have a crystallographic structure. Dislocations exist at the crystal level; it is the movement of these dislocations that allow for the atomic planes to slip. An idealised illustration of slip within a crystal is shown in Figure 3. It is this mechanism that allows metals, for example, to absorb energy and give the stress strain response described in Figure 2(b) rather than failing catastrophically without warning.

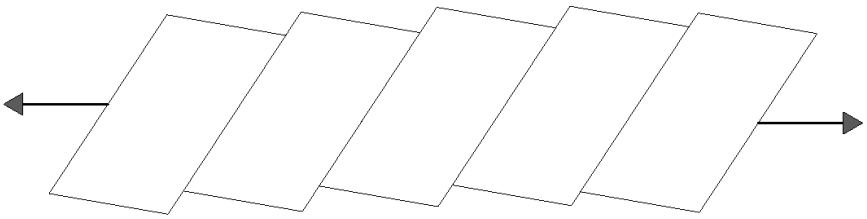

Figure 3. Simplified slip with parallel slip planes in an idealised crystal (based on Hull & Bacon, 2011)

In the cases of brittle and quasi-brittle materials there is no macroscopic plasticity, only a finite region of plasticity ahead of any advancing crack. In the case of a purely brittle material there is no substantial means of arresting a crack. However, in a quasi-brittle material energy is absorbed by a series of fracture mechanisms. Pre-peak non-linearity can be attributed to the growth of existing micro-defects and the nucleation of new defects at aggregate interfaces. Post-peak non-linearity can be attributed to the blunting of an advancing macro-crack by non-critically oriented defects, unbroken ligaments between defects and the bridging of the crack by friction between aggregate particles (Karihaloo & Huang, 1991). Figure 4 shows this quasi-brittle crack growth behaviour (arbitrarily pentagonal grains are distributed throughout the material but only illustrated in the fracture process zone, FPZ).

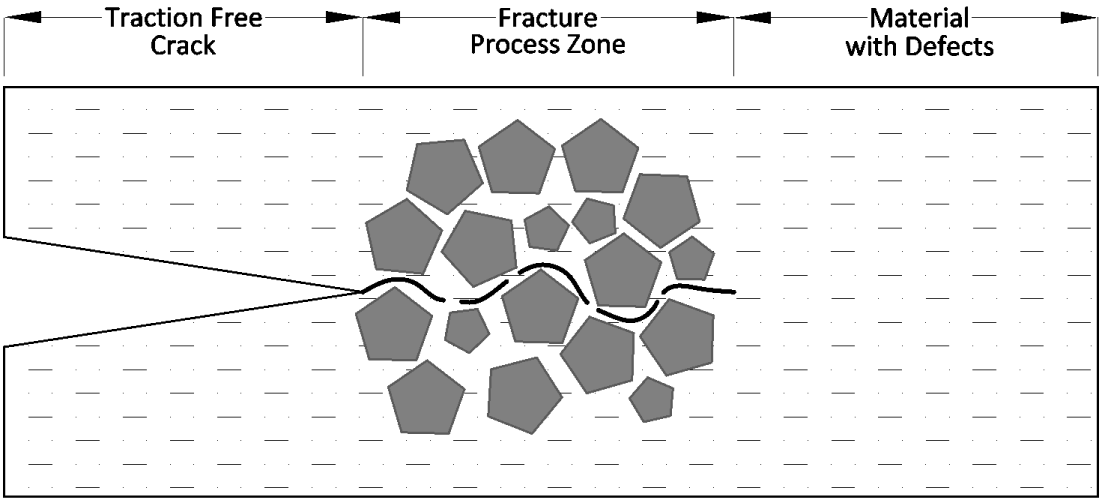

Figure 4. Crack progression in a quasi-brittle material (based on Karihaloo & Huang, 1991)

3.1.2 Plastic Zone, Fracture Process Zone and Damage Zones

There have been numerous formulations describing the aforementioned finite region of plasticity that precedes a crack. Early work in this area concentrated on the re-arrangement of the stress intensity factor, the radius of the plastic zone was a function of the yield stress and the Mode-I fracture toughness. A generalised expression for plastic zone radius is shown in Equation 1 (Kujawski & Ellyin, 1986). The stress ahead of a crack is visualised in Figure 5.

$$r_p = \alpha \left(\frac{K_{IC}}{\sigma_y} \right)^2 \quad (1)$$

Numerous modifications to this original expression have been made for differences in loading cases, materials, failure criteria and distinctions between plane stress and plane strain. Equation 1 has a parameter, α, which allows for easy comparison of these differences. For a perfectly linear-elastic material α is equal to $1/2\pi$ (≈0.159), this is directly from the stress intensity factor. Irwin (1958) put forward that for a ductile material it was twice that at $1/\pi$ (≈0.318) due to stress re-distribution. Empirical estimations were also made. For example, Dugdale (1960) presented an experimental case that it was as large as $8/\pi$ (≈0.393).

Figure 5 has been removed from this version of the thesis due to copyright restrictions

Figure 5. Stress distribution in plastic zone LEFM (Irwin, 1958)

More recent failure criteria have employed a similar approach to quantify the size of the fracture process zone seen in quasi-brittle materials. These make use of Equation 1 but typically consider the ultimate tensile strength rather than yield strength as they are describing a different process. They also contribute their own values for the aforementioned alpha parameter which try to take account of the physical processes in the FPZ such as bridging stress. One such example is found in the work of Bazant & Planas (1998), this is shown in Figure 6. Their work put forward a function for alpha; $n+1/\pi$, where n is the exponent of the function which describes the stress distribution in the FPZ. This is dependent on bridging stress. Bazant states that n can be between 7 and 14 for concretes, based on experimental work. This means that alpha can be between 2.5 and 5. This is an order of magnitude larger than the plastic process zones seen for ductile materials.

Figure 6 has been removed from this version of the thesis due to copyright restrictions

Figure 6. Stress distribution in fracture process zone according to Bazant & Planas (1998)

Research has also been done to consider multiple process or damage zones. Otsuka & Date (2000) carried out X-ray experiments with concrete in tension and proposed different process zones. They distinguished between the fracture process zone and an inner fracture core zone. The distinction here is that the core zone accounts for the growth of the macro-crack, which by their estimation accounts for approximately 70% of the energy dissipation. The outer process zone accounts for another 25% of energy dissipation through micro-cracking which doesn't contribute to the growth of the macro-crack. The last 5% being made up by a wider damage zone which serves to spread out the energy dissipation.

3.1.3 References to Graphite and Concrete Response

Historically there have been disagreements over the characterisation of materials such as concrete and graphite.

As far back as the work of Richart et al (1928), which considered a variety of compressive tests, the prevailing interpretation of concrete deformation was entirely based on slip. In contrast, thirty years later Berenbaum & Brodie (1959) carried out different tensile testing techniques of, amongst other materials, cement paste and considered it as a purely brittle material, with no reference at all to slip. As for graphite, work such as that by Davidson & Losty (1958) discusses deformation of graphite under torsional and flexural loading with reference only to slip and no other damage mechanism. Jenkins (1962) discusses the brittle nature of graphite but in the same piece of work concludes that graphite deforms by slip. Brocklehurst (1977), in his seminal work, makes direct reference to the possibility of plasticity in graphite but does express uncertainty; "*crack initiation may be preceded by plastic deformation*".

Now however, rock, concrete, graphite and ceramic materials are generally agreed to fall in the category of quasi-brittle (Bazant & Planas, 1998). The literature uses a range of terms (some interchangeable) to refer to the grouping of these materials. These include but are not limited to; heterogeneous, in-homogenous, disordered, granular, poly-granular, poly-crystalline and aggregate-composite.

It has become commonplace to see graphite researchers discuss and apply techniques from concrete analysis. Liu et al (2014) presented work on diametral compression of graphite (IM1-24) discs. In their work they recognise that the technique was first standardised in rock and concrete testing. Mostafavi & Marrow (2011) presented work in flexural testing of graphite with the theoretical framework on an FEA approach that was first developed for analysis of concrete. Srinivasan (2014) discusses the issue of size effect in nuclear graphite components. It is stated that the issue is not unique to graphite and that from a regulatory standpoint the adaptation of American Concrete Institute (ACI) standards is suitable for graphite components.

3.1.4 Summary

This has served to offer a basis for understanding what a quasi-brittle material is and how it differs from other material types. It has also demonstrated that in the literature concrete and graphite are considered quasi-brittle materials. This gives the project confidence that any output generated by studying concrete is relevant to the study of graphite.

3.2 Nuclear Graphite and AGR Stress States

This subchapter will discuss nuclear graphite and the generation of stress in AGR bricks which may lead to failure.

3.2.1 Nuclear Graphite

Graphite is an allotrope of carbon; the atoms are arranged into crystalline layers within the grains. It occurs naturally in rocks such as coal. Since the 1940s graphites have been produced with exacting requirements for use in nuclear reactors. These have very low boron content (so as not to "poison" the fission cycle by absorbing neutrons), improved radiation stability (expanded upon in the next chapter), low coefficient of thermal expansion, high strength and low anisotropy.

A simple flow diagram of the Acheson process for graphite manufacture is shown in Figure 7. Most variations in the final graphite are due to differences within this flowchart.

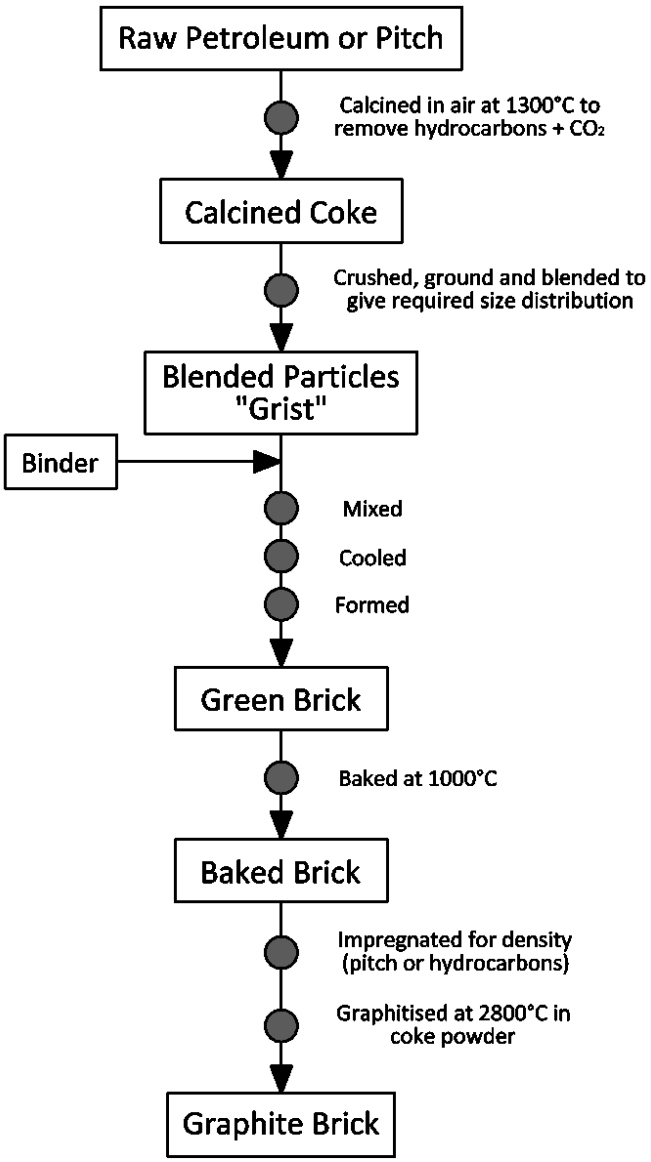

Figure 7. Simplified Acheson process for making graphite bricks (based on Kelly, 1978)

Variations within forming, raw materials and heating processes are detailed here. These variations are taken from Kelly (1978) and Liang (2012).

- Forming processes.
  - Vibration moulding. Vibrating a component in a mould while under pressure, resulting in improved porosity, density and homogeneity.
  - Isostatic pressing. The moulding of a component under high pressure within a fluid, such as an inert gas, common for powdered materials.
  - Extrusion. Forcing a powdered graphite mixture through a die at high pressure resulting in straight bars; produces anisotropic graphite.
- Raw materials.
  - Filler. This is the majority of the material; particles of carbon aggregate which can range from needle like to spherical. Has a significant influence on the brick's properties.
  - Binder and impregnants. Coal tar pitch or petroleum pitches, improves porosity and increases density.
  - Flour. Fine carbon particles, usually filler that has been crushed or ground.
- Heating processes.
  - Calcination. Heating of raw carbon source material in the presence of oxygen. Reduces volatile content of filler.
  - Baking. Anaerobic heating process. Typically around 1000°C.
  - Graphitisation. Anaerobic heating process via electric current or induction heating. Typically between 2500°C and 2800°C.

A small summary of graphites is given in Table 1.

Graphite	Usage	Grain Size, mean/max (μm)	Density (g/cm³)	Forming Process	Behaviour	Filler	References
PGA	Magnox, UK	1000/-	1.74	Extruded	Anisotropic	Needle coke	IAEA (2000)
IM1-24	AGR, UK	500/-	1.81	Moulded	Near Isotropic	Spherical coke	IAEA (2000), Marrow et al (2016)
H-451	GT-MHR, USA	500/-	1.79	Extruded	Near Isotropic	Mixed cokes	Burchell et al (2007)
IG-110	HTTR, Japan	25/-	1.78	Isostatic Pressing	Near Isotropic	Petroleum coke	Marrow et al (2016)
NBG-18	PBMR, SA	300/1600	1.85	Vibration Moulding	Near Isotropic	Pitch coke	Béghein et al (2012)
PCEA	VHTR, USA	150/800	1.84	Extruded	Near Isotropic	Mixed cokes	Contescu et al (2014)

Table 1. Several grades of nuclear graphite

For the purposes of this work IM1-24 is taken to mean all spherical gilsocarbon filler type reactor graphites in the AGR fleet. In reality, distinctions can be made between AGR graphites made by the three manufacturers; Anglo Great Lakes, British Acheson Electrodes Limited and Union Carbide (Minshall, et al., 1996). In fact, Eason et al (2007) discuss data from 88 different gilsocarbon graphites that are in service (distinguished between by identifying codes). However, these in depth distinctions are not made by all researchers.

3.2.2 Advanced Gas-cooled Reactor (AGR) Stress States

There are several life limiting physical phenomena at work in the AGR fleet and not all are related to the core itself. Some phenomena are given; mass loss due to radiolytic oxidation, neutron effects on the graphite core, neutron embrittlement of steel components.

This project is only considering the long term volumetric changes in the graphite bricks which make up the core of the AGR. This is because the cracking due to these volumetric changes pose a serious obstacle to EDF Energy's ability to extend the operating life of the AGR fleet (Heys, 2007).

The fundamental cause of the volumetric changes over the lifetime of the reactor is the collision of high energy (fast) neutrons with the carbon atoms that make up the graphite. The role of the graphite in the reactor is to moderate (slow down) the neutrons which the uranium fuel is giving off as part of the fission cycle (Glasstone & Sesonske, 2004). This moderation is done via so-called elastic collisions, or scattering. Here the light weight carbon atom absorbs a substantial portion of the kinetic energy of the neutron, slowing it down. This is in contrast to a heavier element, such as lead or tungsten, which will simply "reflect" the neutrons with little change in velocity.

The volumetric change behaviour exhibited by graphite is approximately parabolic. In early life the graphite is shrinking and in late life the graphite is expanding. The process is referred to as "turnaround" (Kelly, 1978). Figure 8 shows a typical plot of turnaround; in this case the graphite was IM1-24 and the neutron exposure was carried out at 650°C to give a good approximation to the conditions in the core of an AGR.

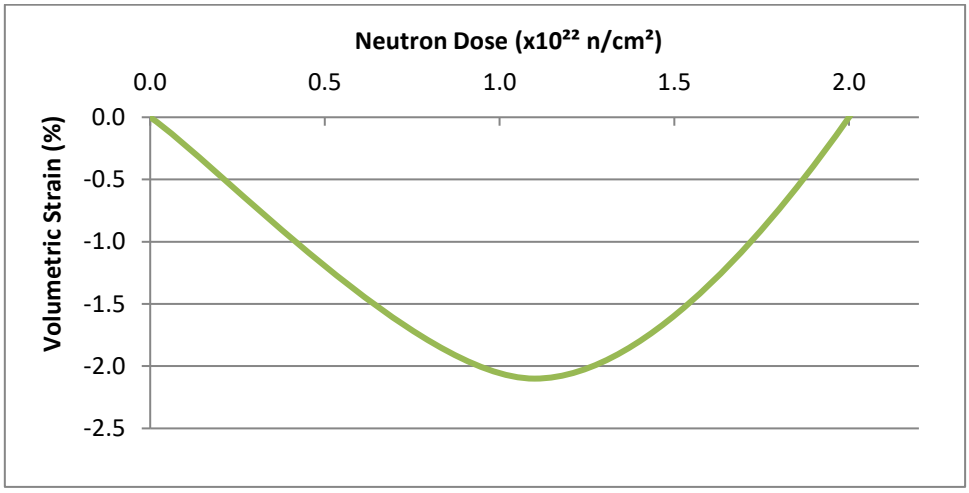

Figure 8. Turnaround in IM1-24 graphite (based on Kelly, 1978)

This process can be explained by means of the lattice structure of the graphite grains (Goeddel & Siltanen, 1967). When a fast neutron collides with a carbon atom it will be knocked out of its lattice site. The carbon atom can either re-join its plane at a vacant site or it can remain displaced and come to rest in an interstitial plane, between lattice planes. In early life the net effect of this is shrinkage along the lattice planes. Later in the life of the graphite grain the interstitial planes gain enough carbon atoms to form new lattice planes. This effect forces the existing lattice planes apart to accommodate the new plane. This causes expansion orthogonal to the direction of early life shrinkage. In late life the net effect is that the mechanism introducing new planes produces a

positive change in the volume of the grain which is larger than the aforementioned shrinkage mechanism (which will continue). When considering a component, made of near-isotropic graphite with grains in all possible orientations, the macroscopic neutron irradiation behaviour is like that seen in Figure 8. This behaviour has been demonstrated in IM1-24 by several studies, such as Kelly (1978) and Brocklehurst & Kelly (1993). Other graphites (such as IG-110 and NBG-18) have been developed with better irradiation performance but this work will not consider them in any detail.

Work was carried out by Tsang & Marsden (2006) to produce an FEA code from the experimental trends of Brocklehurst & Kelly (1993). This code was demonstrated in their later work (Tsang & Marsden, 2007) which explored the evolution of the strains at the bore and the keyway of the AGR brick through its lifetime. Of particular benefit was that the strain was communicated as a function of "full power years" (FPY) rather than in terms of neutrons. The strains for the keyway and bore are given against FPY in Figure 9.

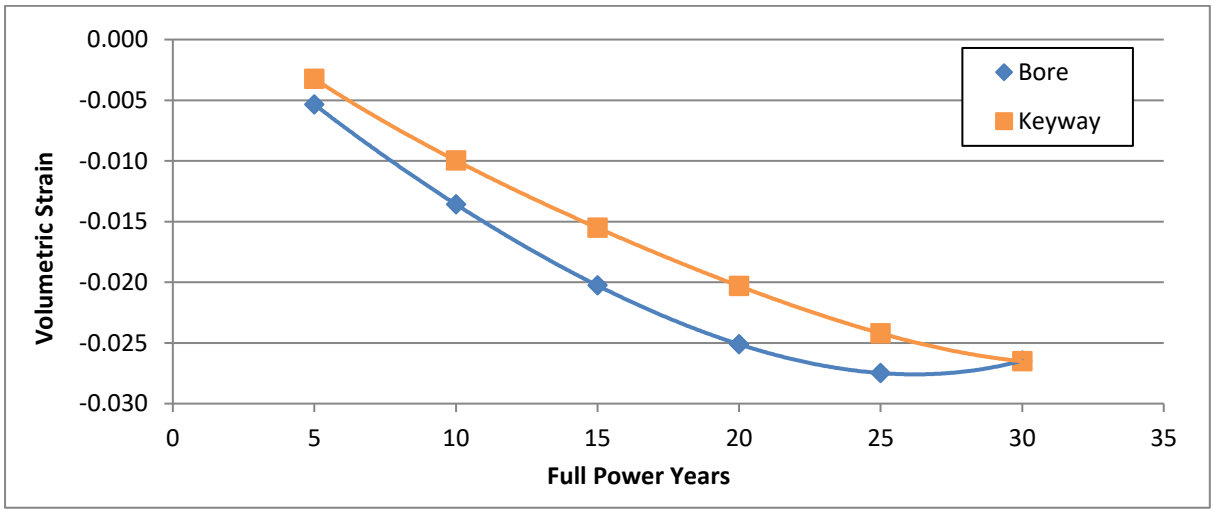

Figure 9. Strain as a function of "full power years" in AGR brick at the bore and the keyway (based on Tsang & Marsden, 2007)

At the macroscopic level, the understanding in the literature (Jones, 2007) is that in early life the internal circumference of the brick undergoes tensile strains while the outer circumference undergoes compressive strains. Post turnaround this reverses to a tensile outer circumference and a compressive inner circumference. This is illustrated in Figure 10.

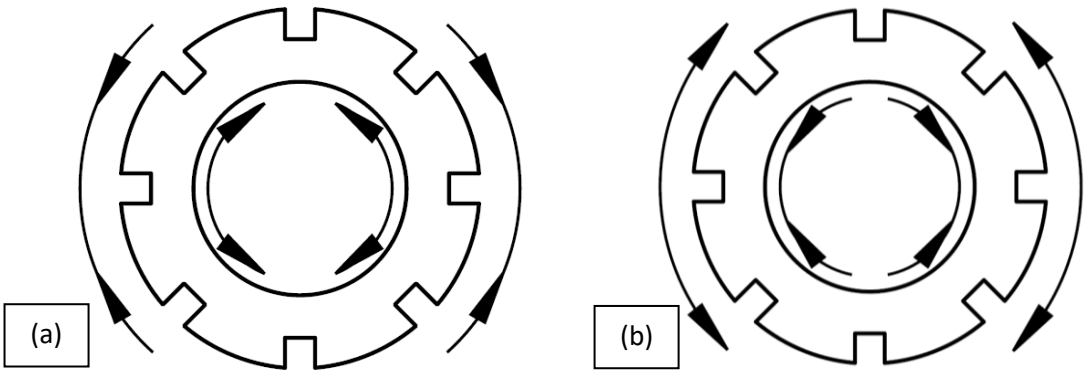

Figure 10. Pre turnaround, early life (a) and post turnaround, late life (b) tensile and compressive strains in AGR bricks

3.2.3 The Consideration of Size Effect in AGR Bricks

A topic which has seen some activity in recent years is the issue of size effect on material properties and its influence on the ability of engineers to accurately model the fracture behaviour of AGR bricks. Kipling et al (2010) explore the problem theoretically; considering the effect of specimen thickness on predicted biaxial strength by means of several existing analytical solutions. In their work they discuss the disparity in size between a typical test specimen and an AGR brick. They reference that a typical test specimen is 10,000 times smaller than a graphite brick. An AGR brick being approximately 80,000cm^3 while 8cm^3 is a realistic size of a three point bend graphite specimen. This is illustrated in Figure 11.

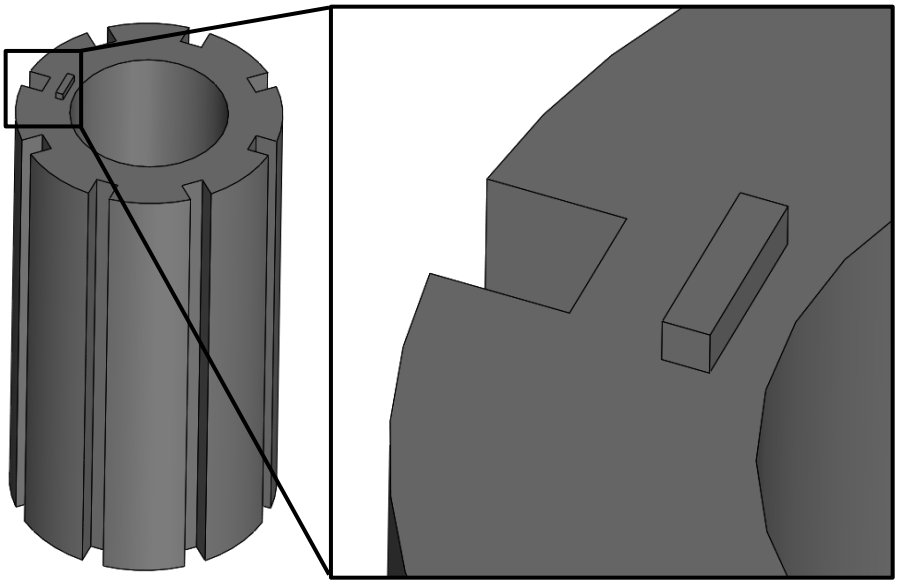

Figure 11. Illustration of disparity in size between a typical three point bend specimen and an AGR brick

A recent collection of papers (ASTM, 2014) was compiled on the issue of size effect in graphite components, some of which are referenced throughout this project. These works serve to highlight the necessity for failure criteria to be insensitive to specimen size. Size effect will play a significant role in this project with the view that any output should have the widest applicability and not be limited to small scale specimens.

It should be noted that this work will only be considering the radial keyways of the AGR bricks. In reality there are other features that are not shown in Figure 11. For example, there are shallow keyways on the top face of the bricks and corresponding lugs on the underneath of the bricks. Later AGR designs have small holes that run axially through the bricks to aid with coolant and inhibitor flow (very low concentration of methane helps discourage aforementioned radiolytic oxidation (Davies, 1996)). It is common for researchers to neglect these other features and solely concentrate on the keyways (Jones, 2007).

3.2.4 Summary

This subchapter has discussed the primary life limiting mechanism at work in AGR bricks; volumetric changes. It has also brought forward the concerns of researchers that size effect need to be considered when dealing with nuclear graphite.

3.3 Literature on Size Effect

This sub-chapter will look at the literature on size effect. It will primarily cover experimentally observed trends and hypothesis on the underlying physical phenomena that give rise to these trends. Major models for size effect will be discussed but will not form the majority of this chapter. Of particular interest within this work are the divergent trends seen in the typical behaviour of strength and fracture toughness. This chapter will also serve to introduce the project to different testing methods of brittle and quasi-brittle materials.

3.3.1 Basic Background

The basic concept of a structural size effect goes back hundreds of years. The first recorded instance of size effect being discussed is in the notes of Leonardo da Vinci, where he talks of long wires being weaker than short wires (translated and discussed in the work of Lund & Byrne, 2001). The experiment described in his notes details a system whereby a small basket would be filled with sand from a hopper until breaking the wire, repeating the experiment several times and then testing a wire of half the length, with the process repeating to yet shorter lengths of wire. Even in its simplicity this serves to illustrate the underlying principle of size effect with regards to strength, the larger a specimen is the higher the probability is that it contains a critical defect.

It took hundreds of years before there was any significant breakthrough in the study of size effect, with the development of linear elastic fracture mechanics (LEFM). Griffith showed experimentally that glass fibres exhibited a strong size effect; with 1mm² fibres giving a strength of 172MPa while 3.3E-3 mm² fibres had a strength of 3385MPa (Griffith, 1921). These findings were central to the development of LEFM. It should be noted that ductile materials express less size effect than brittle materials. This project isn't considering size effect in ductile materials.

The LEFM view of size effect has been expanded upon in the literature (Bazant & Planas, 1998). In a purely brittle material the size and tensile strength of similarly cracked specimens are related as shown in Equation 2 (Bazant & Planas, 1998). Parameters with a sub-script one denote original size and sub-script two denotes the second larger specimen, D being the characteristic dimension which is proportional to the defect.

$$\sigma_2 = \sigma_1 . \left(\frac{D_2}{D_1}\right)^{-\frac{1}{2}} \quad (2)$$

In the literature this relationship is shown to be valid for large specimens. Typically small specimens obey a constant strength criterion, intermediate sized specimens occupy a transitional range (more difficult to model) and large specimens tend towards the LEFM scaling law. There are usually orders of magnitude between the size of constant strength sized specimens and the LEFM-obeying specimens. This is described generically in Figure 12. This relationship can be seen in the work of Bazant & Planas (1998) for cementitious materials, concrete and mortar, across four loading cases; bending, eccentric compression, tension and shear. The transitional size effect behaviour is shown throughout the literature, with materials including ceramics, concrete and sea ice (Bazant, 2005).

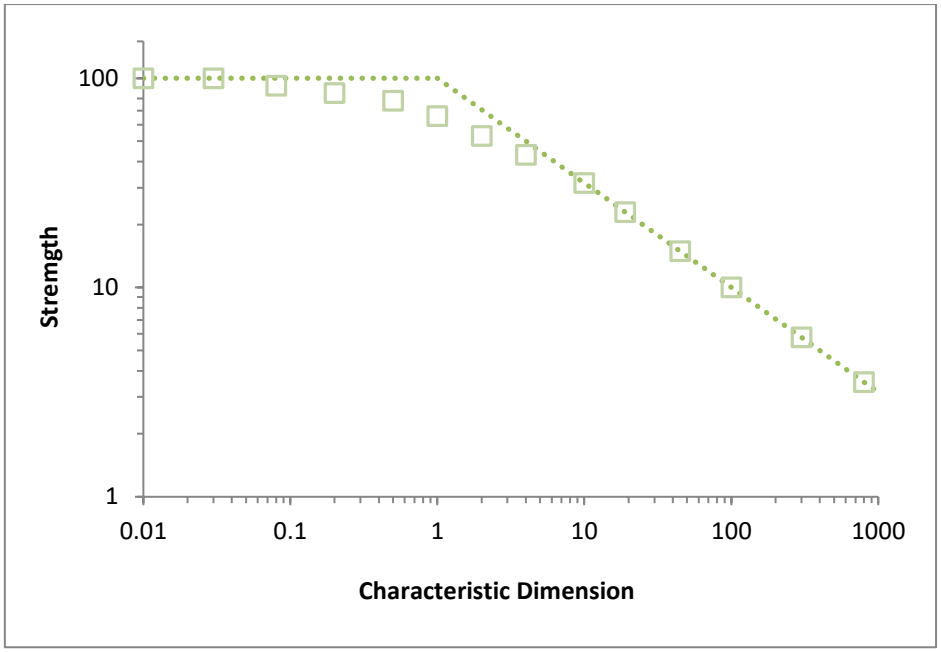

Figure 12. Size effect, idealised in dashed line with transition from constant strength criterion to LEFM (based on Bazant, 2005)

The LEFM scaling law has been shown in the literature to have good agreement with brittle and quasi-brittle materials at large sizes. An empirical fitting can be useful for transitional sizes. A typical approach is using single term Weibull modulus. The expression is shown in Equation 3 (Lewis & Oyler, 1976) and is similar to Equation 2. Here it is the specimen volume, V, that is considered and the modulus term, m, that describes the scaling effect.

$$\sigma_2 = \sigma_1 . \left(\frac{V_2}{V_1}\right)^{-\frac{1}{m}} \quad (3)$$

A low m value will fit data where there is a size effect while a high m value will fit data where there is not a size effect.

3.3.2 Size Effect Across Different Strength Parameters

As has been shown in the previous sub-chapter, it is typical for strength to negatively correlate with specimen size. This sub-chapter will look at experimental trends in the literature across different loading cases. All dimensions shown throughout are in millimetres.

3.3.3 Splitting and Tensile Strength

Direct tensile testing of brittle materials is not as common as induced tensile testing, typically referred to as splitting strength. This type of test results in failure due to an induced tensile stress which is orthogonal to the loading direction, it is treated as being analogous to tensile strength. Ordinarily test specimen geometries are cylinders or cubes, as shown in Figure 13 and Figure 14. The most common diameter to length ratio of cylindrical specimens is 2:1 but other ratios are explored in the literature. Cylindrical specimens can be loaded directly while cubic specimens require bars, referred to as bearing bars or strips, so as to concentrate the load.

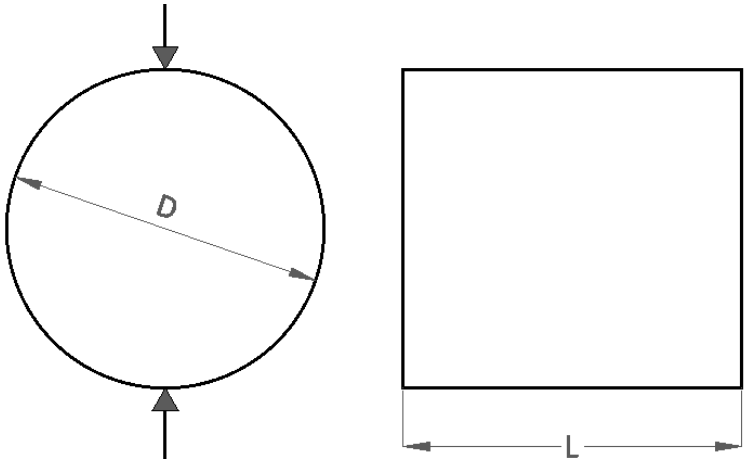

Figure 13. Splitting strength, typical cylindrical specimen in diametral compression

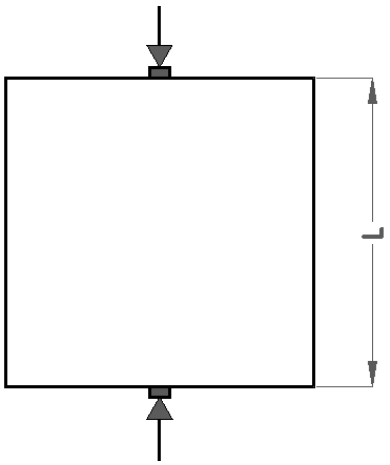

Figure 14. Splitting strength, cube specimen with loading bars

Experimental data for splitting strength of concrete from Kadlecek et al (2002) is given in Figure 15; the testing studied both cylinders and cubes. The data is communicated by means of fracture area (rather than characteristic dimension or specimen volume) and normalised strength. In both cases the data was normalised based on a 150mm dimension specimen (150mm length cube and 150mm diameter x 300mm cylinder).

In this study a simple power law was used to fit the experimental data. This relationship is in qualitative agreement with the aforementioned models for size effect; increases in size result in reduced strength.

Figure 15 has been removed
from this version of the thesis
due to copyright restrictions

Figure 15. Splitting of cylinders and cubes (Kadlecek, et al., 2002)

Splitting strength is often employed as it is more convenient than direct tensile testing of brittle materials; as such there is comparatively less data to draw on for direct tension, especially for concrete.

A direct tensile study of concrete was carried out by van Vliet & van Mier (2000). The specimen type under consideration was a classic dog bone geometry, as shown in Figure 16. A substantial range of sizes were tested, characteristic dimension (D) of 50, 100, 200, 400, 800 and 1600mm. All specimens, regardless of characteristic dimension, were 100mm thick. Their dataset is shown in Figure 17.

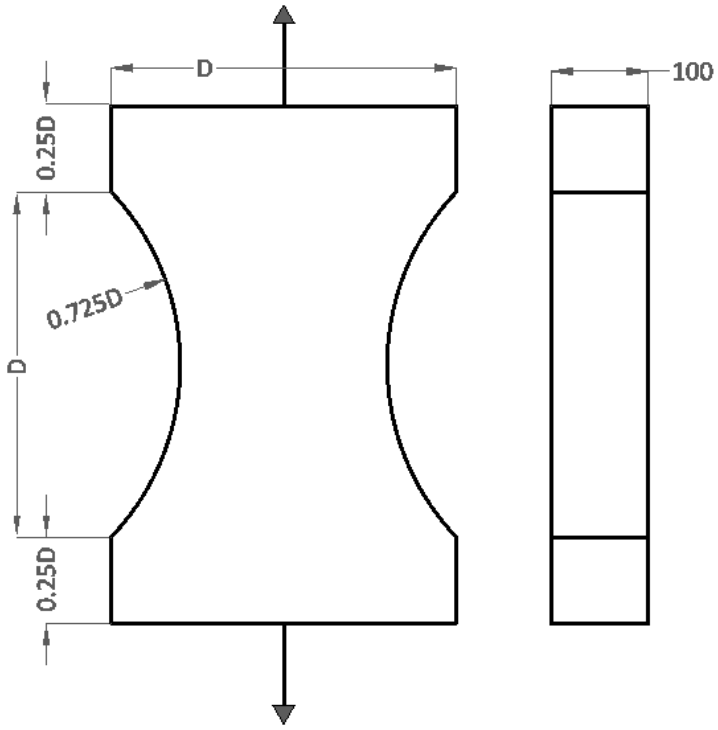

Figure 16. Dog bone geometry, ratios specific to the work of van Vliet & van Mier (2000)

Figure 17 has been removed
from this version of the thesis
due to copyright restrictions

Figure 17. Direct tensile testing of concrete (van Vliet & van Mier, 2000)

As with splitting, direct tension produced a typical negative correlation with increasing size. In this case, with the exception of the smallest specimen where a lot of scatter was reported, a Weibull modulus of 6 has been used to fit the experimental data. In terms of scaling, this does lend support to splitting strength being analogous to tensile strength.

Tensile size effect studies also exist for nuclear grades of graphite. However, in comparison to concrete, the range of size is usually limited. One example of a size effect study in the tensile strength of graphite is the work of Yoon et al (2011). In this study the material under consideration was NBG-18; a medium sized grain, vibration moulded, pitch-coke filler nuclear graphite. Sets of four different sized cylindrical specimens with proportional similarity were tested in tension. The geometry is shown in Figure 18. Specimens were attached to the test equipment with adhesive.

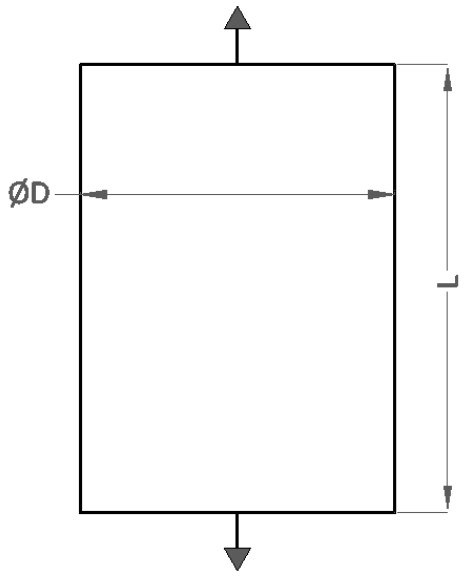

Figure 18. Plain cylindrical specimens in tension

The data, shown in Figure 19, was fitted in the literature with a Weibull modulus of 50. On first inspection this indicates that the NBG-18 doesn't exhibit as pronounced a size effect as concrete. It is worth re-iterating that the range of sizes is small, with the largest specimens only measuring approximately 12.5cm^3 (while the largest concrete tensile specimen discussed here was approximately 300000cm^3). As shown in Figure 12, size effect can become highly non-linear when considered across a large range of specimen sizes. It is possible larger sizes will show more of a size effect.

Figure 19 has been removed
from this version of the thesis
due to copyright restrictions

Figure 19. Size effect in tensile testing of NGB-18 graphite (Yoon, et al., 2011)

This sub-chapter has examined experimental trends in tensile and splitting size effect. In both concrete and graphite testing the typical view of increasing size tending to decreasing strength was upheld.

3.3.4 Compressive Strength

Brittle and quasi-brittle materials are regularly used in structures that undergo compressive loads, such as in bridges, buildings or nuclear reactor cores. There is ample literature covering size effect in relation to compression.

One such study by Yi et al (2006) is discussed. In this case concrete cylinders and cubes were tested in compression. The test geometries are illustrated in Figure 20. Cylinders were tested with a length to diameter ratio of 2:1, this is a typical ratio seen in the literature and standards (discussed later).

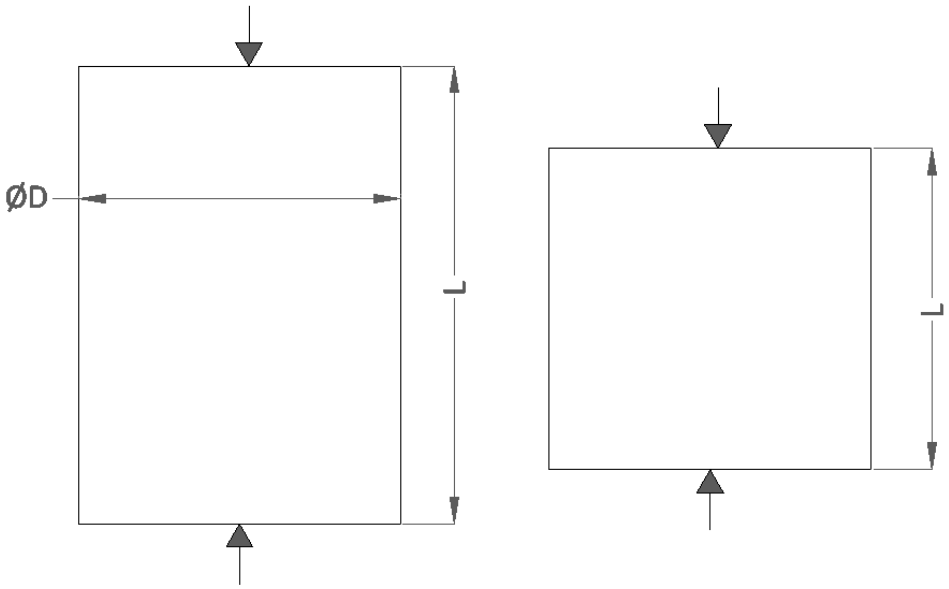

Figure 20. Compression of cylindrical specimens and cubic specimens

The experimental data is summarised in Figure 21. As before, increasing specimen size results in a reduction in strength. This suggests that the principle of increased probability of a critical defect with increasing scale is true in the case of compressive loading as well as the aforementioned tensile loading.

Figure 21 has been removed
from this version of the thesis
due to copyright restrictions

Figure 21. Compressive strength of (a) cylinders and (b) cubes (Yi, et al., 2006)

It should be noted that experimental studies exist that defy convention. One such example (Tokyay & Ozdemir, 1997) is shown in Figure 22 and Figure 23. In this study three concrete mixes with different water contents (nominally called weak medium and strong) were investigated across different sizes of cylinders and cubes. The cylindrical specimens showed very little size effect. However, the cubic specimens (especially the "strong" specimens) actually showed an increase in strength with size. A satisfactory explanation of this was not offered by the authors.

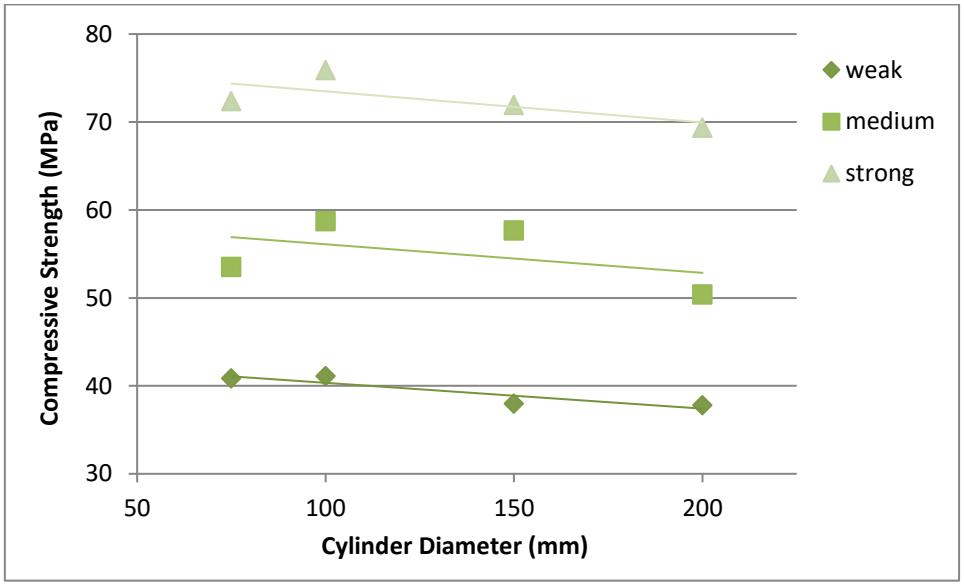

Figure 22. Size effect in compressive strength of cylinders, three different concrete mixes (based on Tokyay & Ozdemir, 1997)

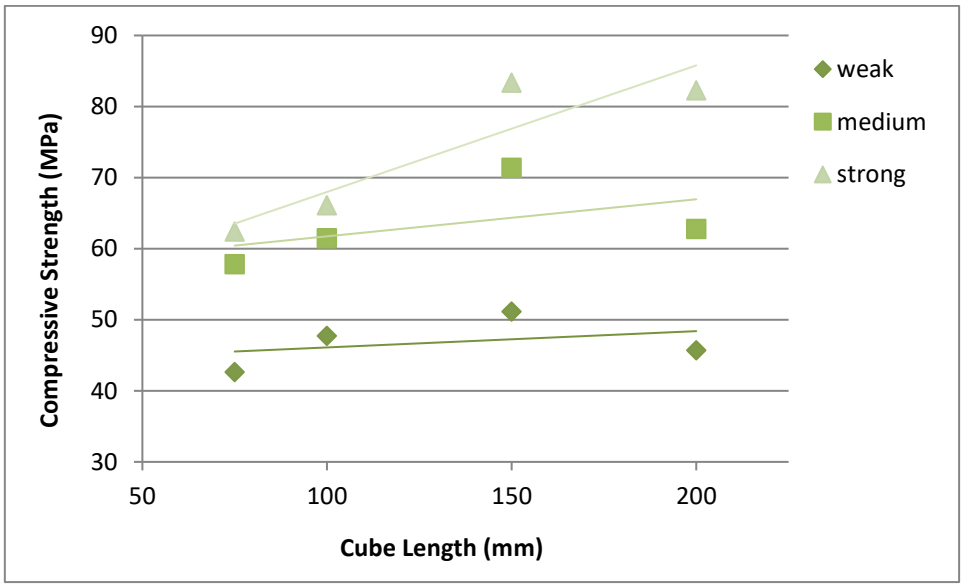

Figure 23. Size effect in compressive strength of cubes, three different concrete mixes (based on Tokyay & Ozdemir, 1997)

As has been shown, size effect in compression of concrete is not as reliable as size effect in tension of concrete. This is also seen to be the case with nuclear graphite. The work of Chi (2013) is summarised in Figure 24. Here cylindrical specimens were tested in compression. In this instance NGB-18 is tested in compression at several different sizes. The specimens were prepared from the graphite billet in two sets; one set aligned with the direction of moulding (a) and one set orthogonal to that (c). As with Figure 22, there is no distinct size effect. To echo earlier sentiments about graphite testing, the range of sizes goes from approximately ø3mm x 6mm up to ø20mm x 40mm. This is less than half the size of the smallest concrete specimens in Figure 21 and is less than a third of the size of the smallest concrete specimens Figure 22. It is feasible that this is still within the constant strength criterion range of sizes. Further testing would be required to determine whether or not the compressive strengths of these graphites are susceptible to size effects.

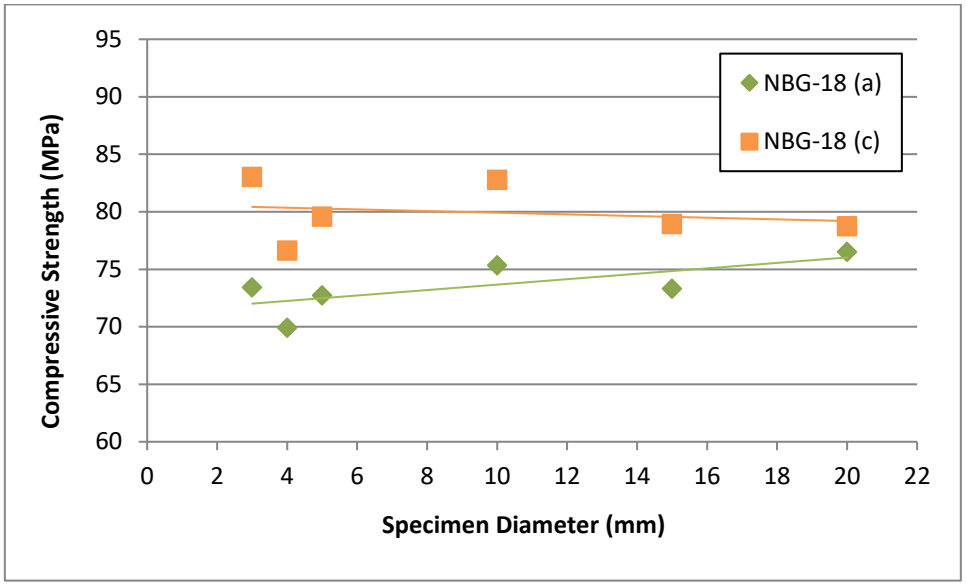

Figure 24. Size effect study into compression of NBG-18 graphite cylinders in orthogonal directions (based on Chi, 2013)

This sub-chapter has examined experimental trends for size effect in compression testing of brittle and quasi-brittle materials. The literature has not demonstrated consistent behaviour for size effect in compression. The literature has shown data sets with a negative correlation between size and strength, other data sets showing no appreciable size effect and also data sets with a positive correlation between size and strength.

3.3.5 Flexural Strength

Brittle materials are regularly used in beams. This sub-chapter considers the experimental trends seen in the literature relating to size effect in flexural strength of brittle materials.

One such study is shown in the work of Karikaloo et al (2003). Here concrete beams were tested in three-point bending with a span to depth ratio of 4:1. All specimens had a breadth of 100mm; this was not scaled with the depth. The loading case is shown in Figure 25.

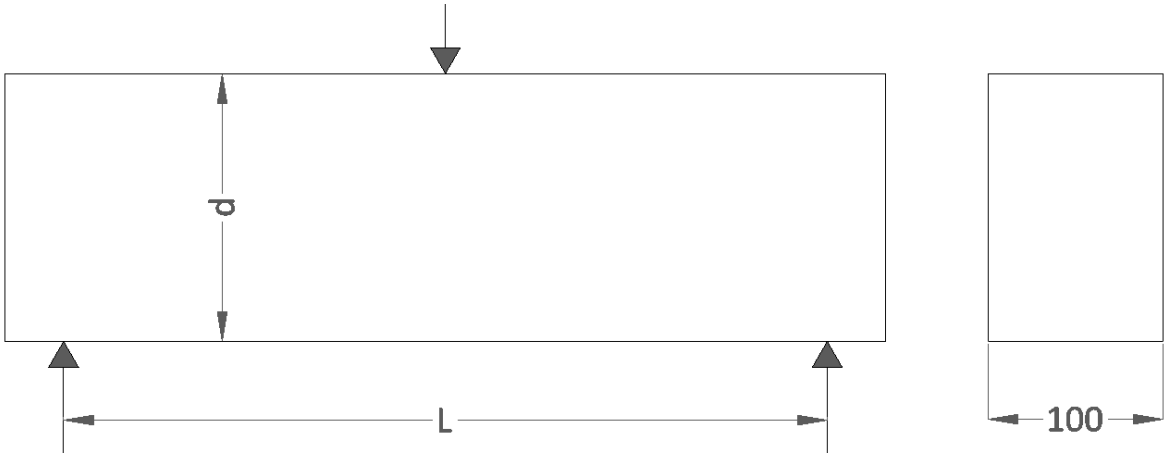

Figure 25. Geometry of three point flexural testing

The data is summarised in Figure 26. As with previous specimen types, increased size has resulted in a decrease in strength. The authors did not present a Weibull modulus value for this data set. The data suggests that stress gradients, such as in bending, are also susceptible to the same coalescence of defects that contribute to size effect (Bazant & Yavari, 2005).

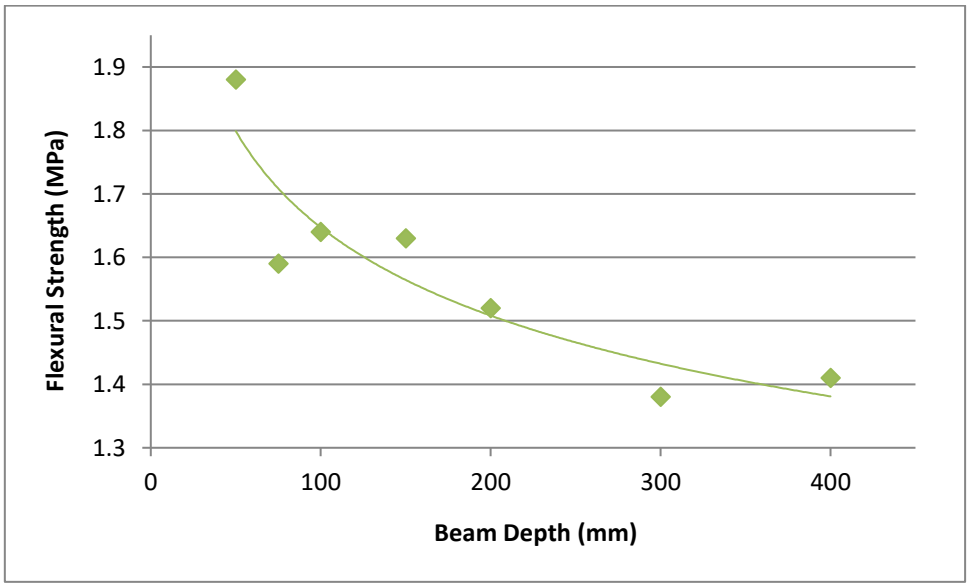

Figure 26. Flexural strength size effect in concrete (based on Karikaloo, et al., 2003)

Another study into size effect upon flexural strength in concrete (Jishan & Xixi, 1990) dealt with four-point bending of plain concrete beams. The geometry is shown in Figure 27. The beams had a depth to breadth ratio of 2:1, a support span to depth ratio of 3:1 and a support span to loading span ratio of 2:1.

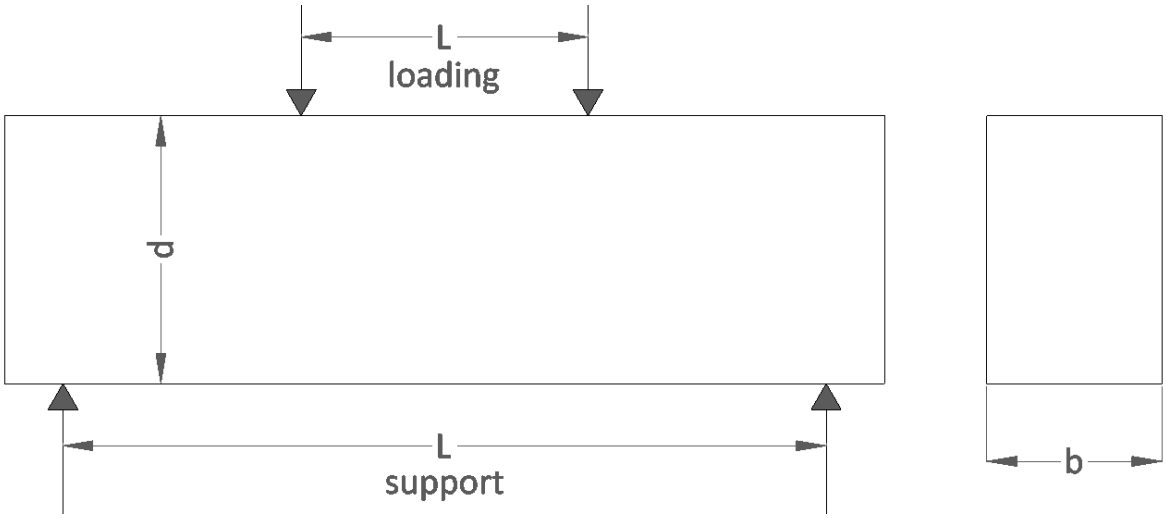

Figure 27. Geometry of four point flexural testing

The results are summarised in Figure 28. As seen up to this point, increasing size of specimens has lead to a decrease in strength. The researchers suggested that a Weibull modulus of 7 fits the experimental data well.

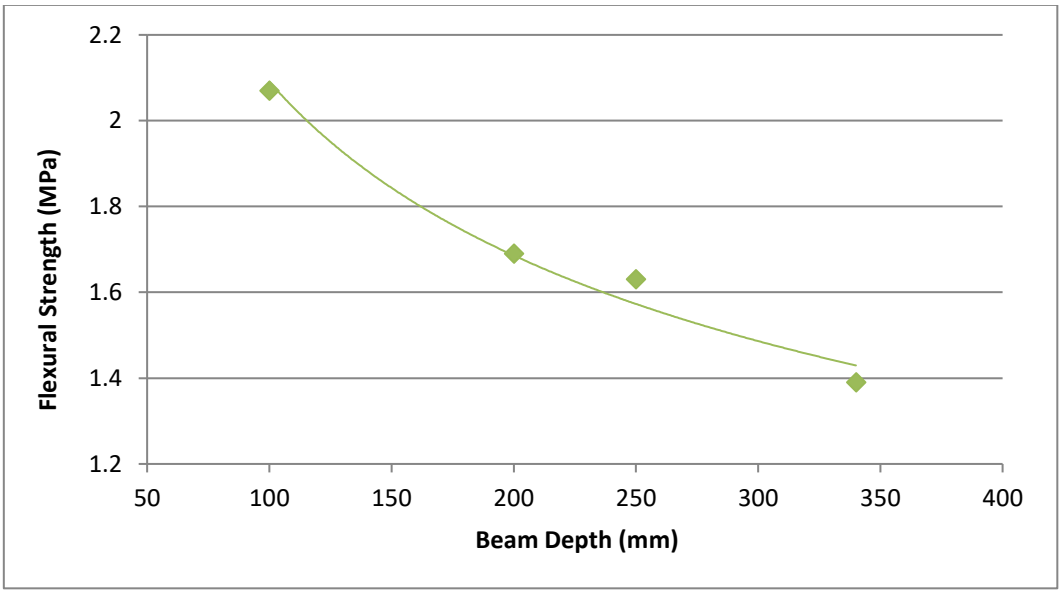

Figure 28. Four-point bending (based on Jishan & Xixi, 1990)

Size effect studies of flexural strength of graphite are also available in the literature. A study by Metcalfe et al (2014) is summarised in Figure 29. In this study different sized, square cross sections of IM1-24 graphite were tested in three point bending. The support span did not change; it was fixed at 15mm for all sizes. A size effect is shown, with the decrease in strength following the basic trend that has been shown up to this point. No Weibull value was presented for the data.

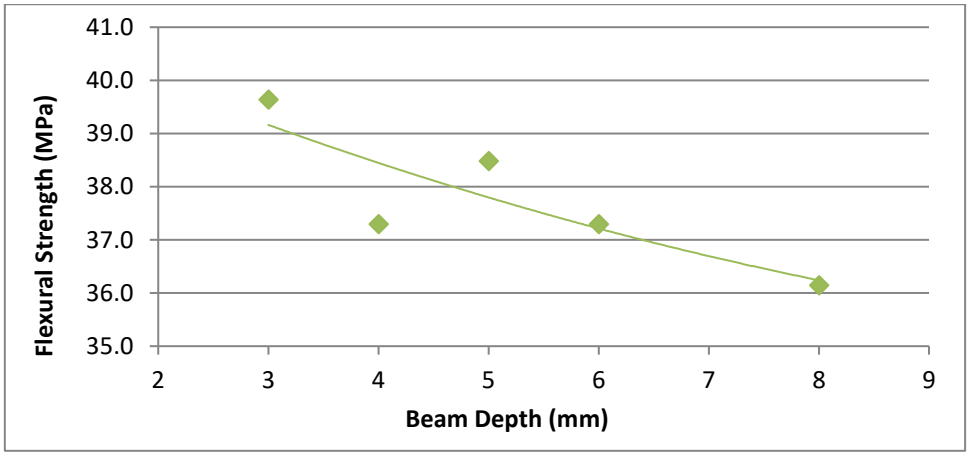

Figure 29. IM1-24 graphite tested in three point bend, different square sections (based on Metcalfe, et al., 2014)

A substantial study of IM1-24 from Brocklehurst (1977) is summarised in Figure 30. The loading case was four point bending with a range of geometry ratios but fixed support and loading spans of 38 and 19mm respectively. The dataset is particularly interesting as it covers, by the standards of graphite research, a very large range of specimen sizes. The specimens above approximately 1cm² decreased in strength following a Weibull modulus of 16.

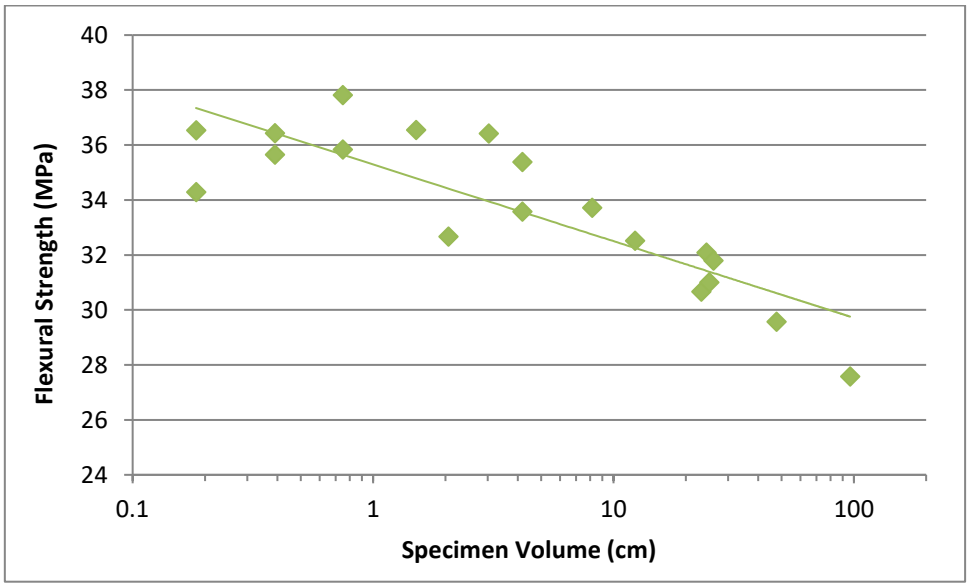

Figure 30. IM1-24 tested in four point bending, different volume specimens (based on Brocklehurst, 1977)

This sub-chapter has shown that in both concrete and graphite a size effect can be observed in flexural strength.

3.3.6 Fracture Toughness

Size effect studies in fracture toughness tend to show different behaviour to the size effect studies in strength that have been covered up to this point. This sub-chapter will explore the experimental trends in fracture toughness testing of brittle materials. The sub-chapter will also present any explanations from the literature that counter the prevailing concept of larger specimens being weaker than corresponding smaller specimens.

Figure 32 shows the results of Bazant et al (1991). Limestone was tested in single edge notched beams loaded by means of three point bending (SENB 3PT), as shown in Figure 31. Specimens were produced in four different depths; 13, 25, 51 and 102mm. All specimens had a breadth of 13mm. The span to depth ratio was 4:1 and the defect to depth ratio was 0.4:1. In this work the fracture toughness is seen to correlate positively with increasing size. This is in contrast to typical strength behaviour shown up to this point. It is proposed in the published work that this dataset will converge on a size independent (large scale) fracture toughness of approximately 0.97MPa√m. The fitting model is based on using linear regression to determine scaling parameters.

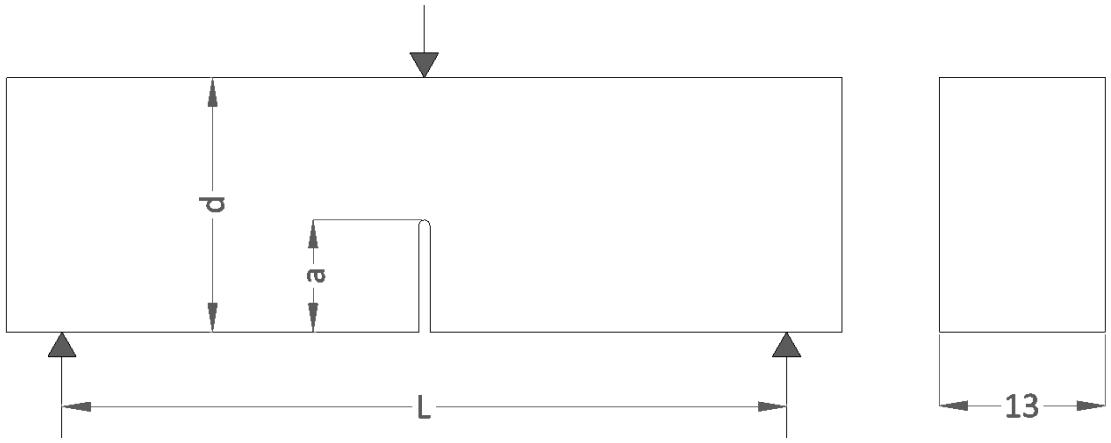

Figure 31. Three point single edge notched beam geometry

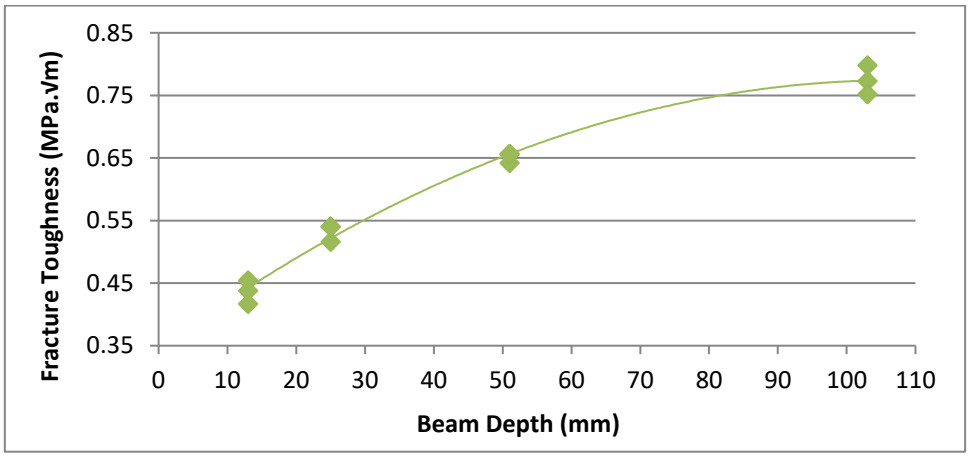

Figure 32. Fracture toughness size effect in limestone (based on Bazant, et al., 1991)

Bazant discusses that this size effect is related to the R-curve (crack resistance curve) but also states that R-curves are highly geometry specific. Further work into the same dataset by Ayatollahi & Akbardoost (2012) presented a fracture process zone radius based model for the size effect.

Figure 34 shows the work of Kataoka & Obara (2015). Sandstone was tested in edge notched semi-circular prismatic beams loaded in three point bending, shown in Figure 33. This is abbreviated to semi-circular bend; SCB. This was a particularly broad study. Geometrically similar specimens were tested at different radii; 12.5, 25, 37.5, 50, 100 and 150mm. Specimen breadth to radius ratio was 4:5 and the radius to notch ratio was 2:1. The support span to diameter ratio was 4:5. A positive correlation between size and fracture toughness is shown across the four smaller sizes. At the two largest sizes the fracture toughness has converged (≈0.88 MPa√m). The authors did not comment on the underlying mechanisms of this size effect. The work also included a second data set; a size effect study of 37.5mm radius SCB specimens with varying breadths (10, 20, 30 and 37.5mm). The data is not reproduced here. No appreciable size effect was observed in the second dataset. The second dataset is interesting as other research presents the idea that increasing the width of a specimen without increasing the depth will produce a decrease in measured fracture toughness. This is attributed to the difference between plane stress fracture toughness (thin specimens) and plane strain fracture toughness (thick specimens), this relationship is seen in the work of Poulose et al (1983). This is analogous to the relationship between strength and size.

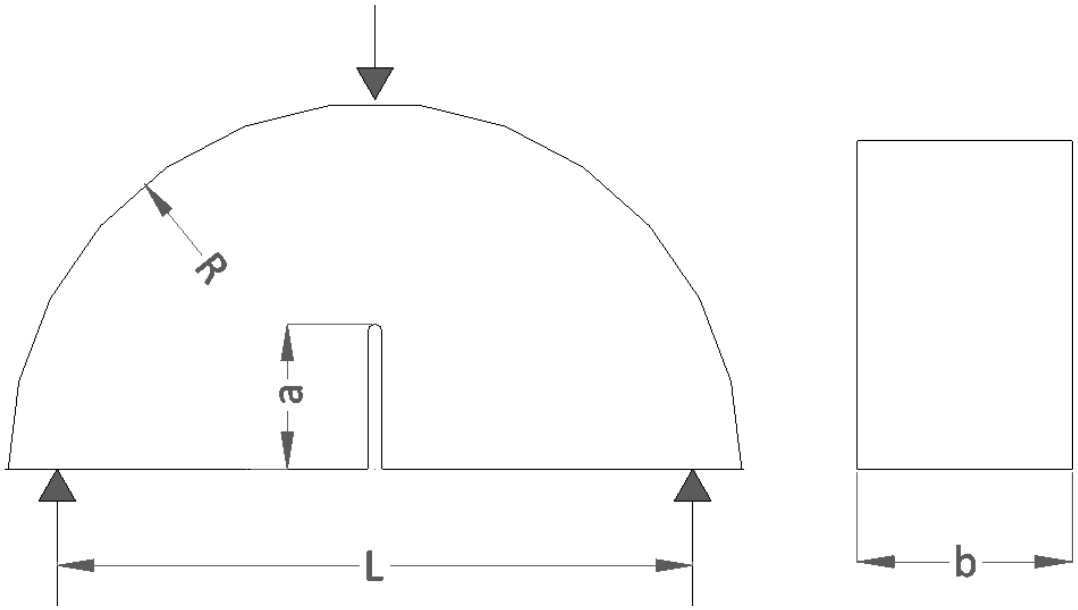

Figure 33. Notched semi-circular beam specimen geometry (based on Kataoka & Obara, 2015)

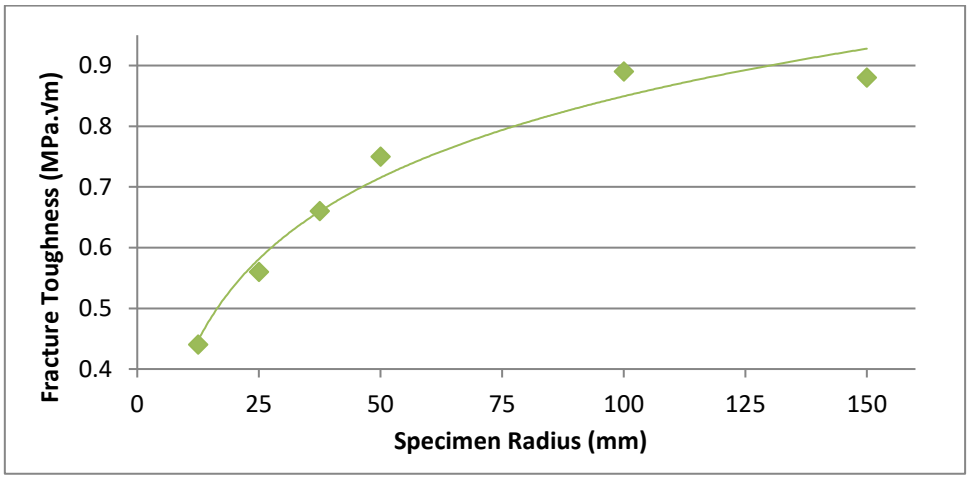

Figure 34. Fracture toughness size effect in sandstone (based on Kataoka & Obara, 2015)

Figure 35 and Figure 36 summarise the work of Wittmann et al (1990) which looked at the fracture properties of concrete at different sizes. The values given are in terms of fracture energy (critical strain energy release rate); which is proportional to fracture toughness. The specimen type was compact tension, where a comparatively thin square section of notched material is pulled in tension. The specimen height to notch ratio was 2.5:1 and the specimen width to notch ratio was 2.4:1. All specimens were 120mm thick. Six specimens were tested at each size. The specimen heights that were tested were 375, 750 and 1500mm. As can be seen, there is a size effect which has converged at approximately 160J of fracture energy. Above this point the fracture properties are size independent.

Figure 35 has been removed
from this version of the thesis
due to copyright restrictions

Figure 35. Compact tension specimen geometry (Wittmann, et al., 1990)

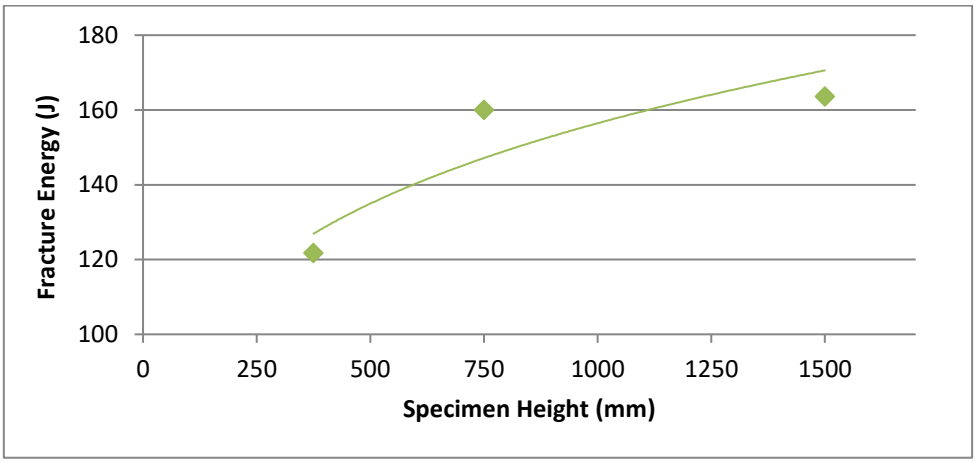

Figure 36. Fracture energy size effect in concrete (based on Wittmann, et al., 1990)

Wittmann et al (1990) does offer some discussion on the underlying mechanism for why this type of size effect is present. The mechanism under discussion is strain softening. The proposition is that there are two parameters which are changing simultaneously with scale which lead to this convergence of the fracture energy. These parameters are the stress to drive the crack and the crack opening displacements. The stress parameter decreases with size (as shown in earlier literature) while the crack opening displacements (and therefore global energy requirements) increase with size. A bi-linear approximation of exponential decay is used to model the fracture energy.

Figure 37 summarises a size effect study of the fracture toughness of IG110 graphite by Sakai & Nonoyama (2005). The testing was done with three point, single edge notched beams. This type of testing geometry has already been discussed and is shown in Figure 31. The beam depth to notch length ratio is 2:1. All specimens were 10mm in breadth. The support span to beam depth ratio was 4:1. A positive correlation between size and fracture toughness is shown, with a convergence at approximately 0.26MPa.√m.

The work also included specimens which were 5mm in breadth. They also showed a size effect but isn't included here as the range of sizes did not include 2.5 and 5mm deep beams. This dramatically reduced the observable size effect.

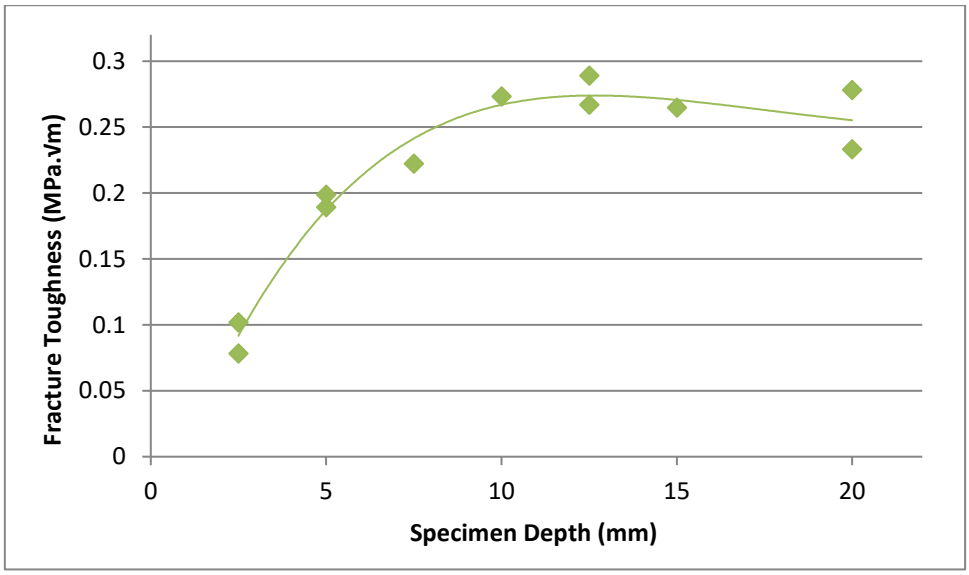

Figure 37. Size effect in fracture toughness of IG110 graphite (based on Sakai & Nonoyama, 2005)

The authors explain the observed size effect by means of a "finite non-negligible frontal process zone" which is ahead of the crack tip. The premise being that when the size of the fracture process zone is significant in comparison to the size of specimen the length of the notch needs to be augmented with the length of the process zone. This reduces the apparent fracture toughness.

Another data set which shows this type of scaling behaviour is presented by Akbardoost et al (2014). The work is similar to the aforementioned Kataoka & Obara (2015) but with the inclusion of mixed mode loading. Semi-circular beam specimens and cracked Brazilian disc specimens are tested with various modes, from Mode-I dominant to Mode-II dominant. Size effect is shown in both geometries and for both Mode-I and Mode-II fracture toughness values.

3.4 Mixed Mode (I/II) Fracture

This sub-chapter looks at the study of fracture and mixed Mode-I/Mode-II stress states up to recent developments.

The study of fracture and understanding of stress concentrations goes back nearly 100 years. It started in earnest with the fundamental theory of elasticity being used to consider the effects of stress concentrations, primarily in brittle materials (Griffith, 1921). Equation 4 shows the Griffith criterion, where σ_f is the stress at failure, a is the half crack length and γ is the surface energy. E* is a Young's modulus term which in plane stress is simply E but in plane strain it is $E/1\text{-}v^2$.

$$\sigma_f = \sqrt{\frac{2\gamma E^*}{\pi a}} \quad (4)$$

Later work expanded upon these principles to allow for ductile materials, where the energy requirements for fracture are higher (Irwin, 1948). The surface energy term from Griffith was replaced with a more general term, the strain energy release rate G, which encompassed both surface energy and the ability of the material to plastically dissipate energy, G_p. This is shown simply in Equation 5.

$$G = 2\gamma + G_p \quad (5)$$

Of pivotal importance to the study of fracture was the development of the stress intensity factor, K ($Pa.m^{½}$), shown in Equation 6. Stress intensity factors proposed a means to quantify the asymptotic stress state at the crack tip (Irwin, 1957).

$$K = \sigma_f\sqrt{\pi a} = \sqrt{EG} \quad (6)$$

Stress intensity factors were soon expanded upon to include shear and torsion (Irwin, 1958). These gave engineers the ability to describe and define increasingly complex stress states. The general expression for stress intensity is given in Equation 7; it relies on the distance ahead of the crack r and the angle from the plane of the crack θ. The angular expression is specific to the type of defect (edge crack, penny shaped crack etc.) and the specimen type (plate, beam, infinite domain, etc.).

$$\sigma(r,\theta) = \frac{K}{\sqrt{2\pi r}}\, f(\theta) \quad (7)$$

The critical stress intensity factor, the stress intensity factor at which a crack propagates, is normally referred to as the fracture toughness. Typically plane strain, Mode-I fracture toughness (K_{IC}) is taken as the standard parameter. Ordinarily specimens (such as SENB) are tested at increasing thickness, but without increasing other dimensions, until a lower value of fracture toughness is converged at. This is considered K_{IC}. Mode-II and Mode-III fracture toughness values do appear in the literature but are not yet considered mainstream. It is important to note that true K_{IC} values are not dealt with throughout this work due to the size effect nature of the research. Fracture toughness values should be considered K_C values, size and geometry specific, rather than K_{IC} values.

By the 1960s mixed mode fracture studies were being carried out, such as that shown in Figure 38. In this work acrylic plates with central cracks were exposed to a range of Mode I/II stress states. This represents an early use of maximum tangential stress (MTS) criterion to model the failure behaviour, with the model tracing an ellipse.

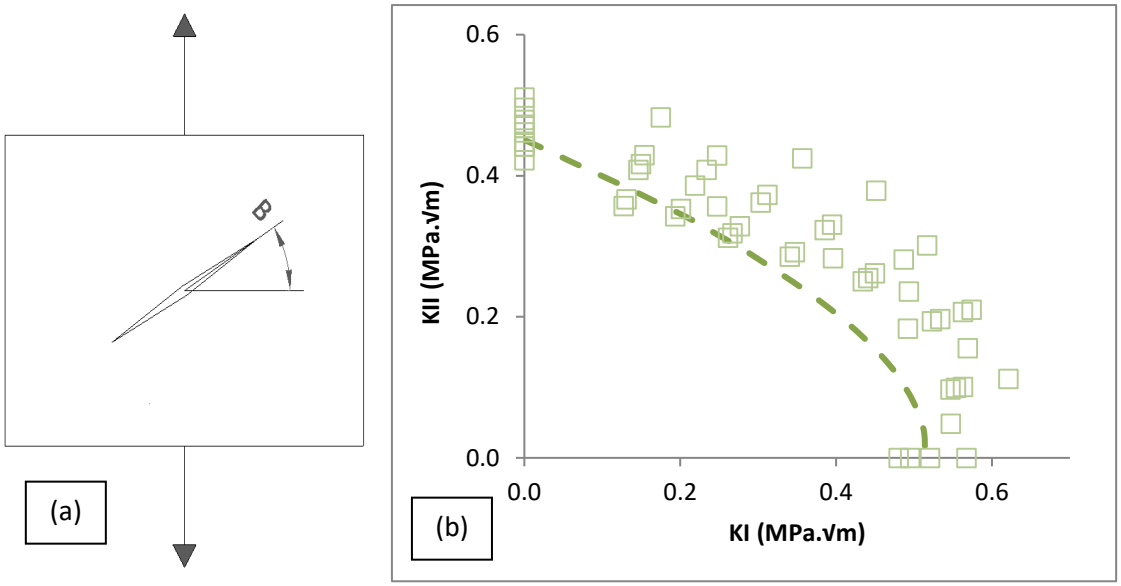

Figure 38. Summary of data (b) from cracked acrylic plates (a), mixed mode study (based on Erdogan & Sih, 1963)

The MTS criterion has been studied for decades. Numerous adjustments and interpretations of the MTS have been published over the years, with names such as generalised maximum tangential stress (Smith, et al., 2001), modified maximum tangential stress (Saghafi, et al., 2010) and maximum average tangential stress (Matvienko, 2012). This work will not be looking at these in depth. Broadly speaking they consider adjustments to either the application of the core mathematics of MTS (Williams, 1957). Often this involves the inclusion or exclusion of certain terms from the series expansion or the appending of a ratio to improve universality.

Simpler failure criteria than MTS have been posited by researchers. One such example is a pragmatic linear criterion which was shown to have good agreement with cracked steel specimens (Shah, 1974). The criterion is shown in Equation 8 and the data from the study is shown in Figure 39.

$$\frac{K_I}{K_{IC}} + \frac{K_{II}}{K_{IIC}} = 1 \qquad (8)$$

It is plain to see the appeal of a simple criterion such as this, especially when considering the amount of scatter seen in brittle fracture testing. There is an argument to be made that a linear criterion with a modest factor of safety is sufficient for most design applications. The majority of current work into MTS relies on a range of FEA approaches. The work of Aliabadi & Rooke (1991) features heavily in the area of numerical fracture mechanics.

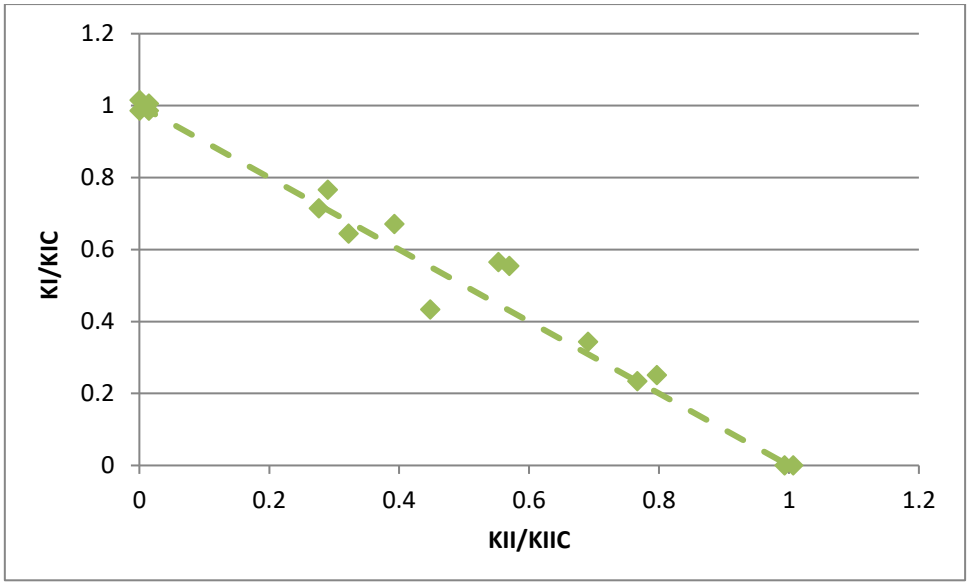

Figure 39. A pragmatic failure criterion showing good agreement with aluminium specimens (based on Shah, 1974)

An advance in the study of fracture came with the development of the J-integral by Rice (1968). Here the strain energy around the crack tip is determined by a closed contour integral. In isotropic, brittle materials the parameter J_{IC} is equal to G_{IC}, the units J/m². One benefit of the J-integral method is that it is insensitive to the path of the integral. One such path is shown in Figure 40.

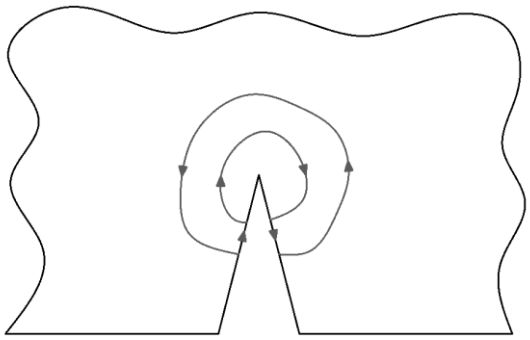
Figure 40. J-integral arbitrary contour path

The J-integral method has proved successful for ductile materials and is now used extensively in FEA packages. An example of the predictive ability of the approach is can be seen in the work of Livieri (2008), double edge notched PMMA specimens were tested in tension with varying notch radii. The J-integral method has been used in mixed mode problems as well. However, even in the 1990s there were publications (Rigby & Aliabadi, 1998) which suggested that previous authors had made mistakes in calculating Mode-II and Mode-III J-integrals.

A field that has undergone growth recently is control volume driven finite element methods. Fundamentally, fracture research has tried to bring the infinite stresses of elastic theory down to reality. Researchers have derived different control volumes within which to average physical quantities (stress, strain, nodal displacements) as a means to reach a finite description of the stress state at the tip of a crack. A generic crack tip and control volume is shown in Figure 41.

Failure is typically predicted when the average parameter under consideration within the control volume reaches a predefined failure value. Eg, $\sigma_{avg} = \sigma_f$.

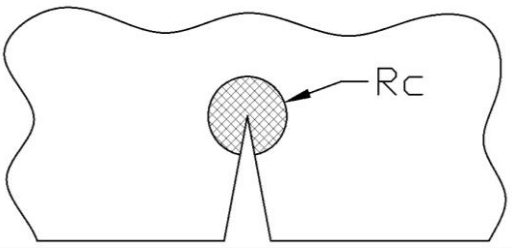

Figure 41. Generic control volume at tip of crack

Progress was made in control volume based approaches with Yosibash et al (2004). Here a solution for the control volume was presented that was a function of strength, fracture toughness and Poisson's ratio. The failure criterion applied within the control volume was that of strain energy density (SED) by means of finite element analysis. The advantage of this control volume over previous control volumes, such as that shown by Lazzarin & Zambardi (2001), is that it is insensitive to notch length, notch opening angle, notch orientation and loading case. One example of a study making use of the aforementioned control volume failure criterion (Yosibash, et al., 2004) can be seen in the work of Ayatollahi et al (2011). Here graphite disc specimens with three different central defect geometries (30, 60 and 90°) were tested in diametral compression. The discs were tested at several different loading angles; producing different mode I/II mixes (in a similar fashion to the cracked plate in Figure 38). Good agreement was found between the modelling and the experimental work, demonstrating good versatility for the approach.

3.4.1 Summary

This sub-chapter has summarised the main works in fracture and mixed mode study.

3.5 Standards for Brittle and Quasi-brittle material testing

Following on from the previous subchapters which have discussed size effect across a range of strength and fracture toughness tests, this subchapter considers standards which have been proposed to give uniformity of testing. The main resources in this area are BSI (British Standards Institute) and ASTM (American Society for Testing and Materials) standards.

3.5.1 Standards Related To Strength Parameters

A useful set of standards for strength testing of concrete can be found in the BS EN 12390 (2012) series. It is an 11 part series and covers (amongst other topics) compressive, flexural and splitting strength. The specimen types used throughout are cylinders, cubes and cuboids, these are discussed in part one of the series (BS EN 12390-1, 2012); cylinders have a length to diameter ratio of 2:1 and cuboids have a square cross section. General information on specimen preparation is given in part two (BS EN 12390-2, 2009a). Here practical aspects are covered, such as the importance of removing air pockets and keeping the specimens moist during curing. Basic practicalities such as these are of interest to the project.

BS EN 12390-3 (2009b) discusses compressive strength testing. The acceptable geometries are cylinders (loaded axially) and cubes. This standard details three means of "capping" the loaded faces of the specimens to ensure load distribution; molten sulphur, calcium aluminate cement or loose sand. No reference size is explicitly stated but part one of the series describes cubes lengths of 100, 150, 200, 250 and 300mm and cylinder diameters of 100, 113, 150, 200, 250 and 300mm.

BS EN 12390-5 (2009c) details the approach for flexural strength of cuboids. A three point and four point option is shown. As mentioned in part one of the series, the cuboids have a square cross section. The loading span to depth ratio is give as 3:1; this is low in comparison with other literature. No reference size is explicitly stated but cuboid depths of 100, 150, 200, 250 and 300mm are defined in part one of the series.

BS EN 12390-6 (2009d) shows the means for testing splitting strength. The allowable geometries are cylinders and cubes. It is interesting to note that in the introduction to this standard it is stated that cylinder size has not been found to have a large effect on reported strength while the reference size and method ("in cases of dispute") is given as 150mm diameter cylinders.

The British standards on these topics offer a complete picture of the typical testing seen up to this point in the literature. Other standards do exist in these areas, but few actually add to that covered by the BS EN 12390 series.

A standard that does add to this is ASTM C1231 (2000). Typically standards (as above) recommend capping compressive specimens as a means to ensure even load distribution, however, the aforementioned ASTM standard puts forward the option of using rubber pads rather than, for example, molten sulphur. This represents an interesting innovation in ease of testing that has not been discussed explicitly in the literature up to this point.

3.5.2 Fracture Toughness

ASTM E1290 (2002) offers several methods for calculating fracture toughness; compact tension, single edge notched beam (SENB 3PT) and arc-shaped bend specimen (similar to SENB but not seen thus far in the project). This standard is promising in that it defines the ratios to which each specimen must be made but does not prescribe specimen sizes; this is at the discretion of the researcher. Solutions for SENB specimens with square and 2:1 cross sections appear in this standard.

ASTM E1820 (2001) and ASTM E399 (2009) are similar to the aforementioned ASTM standard, with some overlap, but also considers different specimen ratios and offers solutions for other specimen types, such as disc shaped compact tension specimens and arc shaped tension specimens. It should be noted that E399 shares some solutions with ASTM E1290 (2002), previously mentioned.

BS EN ISO 23146 (2016) gives a single edge sharpened V-notched beam specimen approach to determining fracture toughness. This standard offers a three point and four point loading solution for the geometry type. The standard specifies a specimen geometry of 3 x 4 x 45mm. BS EN ISO 15732 (2005) is geometrically similar to the previous standard, however, this standard is for a single edge pre-cracked beam specimen (SEPB). Here a sharp notch is produced at the root of a blunt notch by fatigue loading. These two standards offer an insight into fracture toughness as they share the same mathematical solutions despite different methods of crack formation. In turn, these solutions came from the VAMAS round robin on fracture toughness (Kubler, 1999).

BS EN 14425-3 (2010) offers a chevron notched means for calculating fracture toughness. This has not been shown up to this point in the literature for quasi-brittle material testing. The notch geometry is shown in Figure 42. The standard gives a fracture toughness solution in four-point bending. This standard also recommends a specimen geometry of 3 x 4 x 45mm.

Figure 42. Basic illustration of Chevron type notch

It is interesting to note that BS EN 14425-3 (2010) was originally part of a larger collection; summarised in a technical specification development draft (DD CEN/TS 14425-1, 2003). The technical specification was meant to consider four test methods for ceramics; single edge fatigue notched beams, chevron notched beams, surface cracked beams (shallow defect) and single edge V-notched beams. Only the chevron notched beam standard came to fruition.

3.5.3 Summary

This subchapter has considered standards in the area of material testing. These will be of use as they offer more in-depth information than the literature alone. It is important to note that one aspect of experimentation is to stretch existing knowledge; in this case size effect is of significant interest. As such, standards will be treated as partially flexible frameworks rather than completely rigid rules.

3.6 Comments on Literature

The literature review has brought together a substantial amount of information on the topics of quasi-brittle material behaviour, size effect, causes of AGR stress and mixed mode fracture.

There are aspects of these topics which require more in-depth explanation before further work can be under taken. There are also topics which have been addressed to the satisfaction of the project.

One such topic which has been addressed sufficiently is that of the similarities between graphite and concrete. The project is confident that any output generated from work with concrete can be considered applicable to graphite. This is in agreement with Srinivasan (2014).

The project is not in a position to run its own FEA to determine from first principles the strains in AGR bricks. As a result the project will have to make use of the published strain data (Tsang & Marsden, 2007) to drive subsequent studies. The project is confident that their work is of a high standard based on their numerous works in this field.

All FEA simulations that will be carried out in this work will use Solidworks Simulation by Dassault Systèmes. This is an accessible software package which has the breadth to investigate both nodal displacements and strain energy density.

3.6.1 Topics for Further Discussion

The effect of size discussed in the literature brought to light a range of tests to characterise strength and fracture toughness for quasi-brittle materials. The project now only needs choose between them and suggest suitable standards to work do. Then a substantial testing regime can be put forward.

The literature review only gave a brief overview of the state of mixed mode. Of the criteria mentioned it is the control volume driven strain energy density FEA approach which is of the most interest to the project (Yosibash, et al., 2004). This is because it is a highly generalised approach, applicable to a range of defects and is governed only by material property inputs; it does not rely on any dimensionless parameters or shape factors. It is also easily applied within any FEA environment and does not rely on special element types. The rules of this criterion will be covered in the next chapter. As part of further discussion on mixed mode the issue of a suitable mixed mode test geometry will be addressed.

3.7 Discussion and Explanation

This chapter will bring forward information on the relevant topics so that work can be outlined in the methodology.

3.7.1 Material Property Test Selection

The literature review shed light on a range of different strength and fracture toughness tests. This subchapter will discuss them and their suitability for testing within the project with a view to achieving an experimental overview of size effect across a range of stress states.

There are attributes which are of benefit in all testing, such as ease of repeatability. As this project is also interested in size effect it is important for specimens and apparatus to scale easily. At the outset of test selection, the project has already determined that it will be working with concrete as a material. As such, the test specimens should lend themselves to ease of moulding. Within this point it is also of interest to have multiple types of test that can use the same moulds. As much as possible tests should be codified by existing standards.

The strength tests that have been shown in the standards and literature break down into several categories, including but not limited to; direct tensile, induced tensile (typically discs or cylinders), flexural (typically 3 or 4 point beams) and compressive (typically cylinders of cubes). There are of course distinctions, such as geometry variations, within these categories as well.

The fracture toughness tests break down into their own categories, effectively notched versions of the strength tests; single edge notched beams (typically 3 or 4 point), single edge notched tensile specimens and notched discs.

If there were a much larger number of distinctly different test specimens a matrix approach would be undertaken to decide upon a suitable series of tests. However, in actuality there are not many distinctly different tests that are well represented in the literature; especially when the basic requirements are applied.

Any tests involving direct tension of either plain or notched specimens won't be considered for testing. This is because the geometries present difficulty to moulding; direct tension strength test specimens require dog bone geometries and direct tension fracture toughness specimens typically require holes for loading.

This reduces the eligible tensile strength tests to induced tension. The most well represented induced tensile strength testing in the literature and standards is that of cylindrical splitting. This is appealing to the project as cylinders are easily moulded at a range of sizes and the testing only requires standard loading platens. Testing will use BS EN 12390-6 (2009d) as a framework but will explore specimen sizes outside of the typical range of specimen sizes.

All cylinders will have a length to diameter ratio of 2:1 in accordance with BS EN 12390-1 (2012).

With cylinders selected compressive strength from testing of cylinders is a natural choice as it is also well represented in the literature and standards. This means that the project can achieve a breadth of testing from one type of geometry. Testing will borrow from both BS EN 12390-3 (2009b) and ASTM C1231 (2000) to form a framework but will also explore specimen sizes outside of the typical range of specimen sizes.

Within the category of flexural strength testing there are only two distinct loading cases that are of practical interest to the project; three and four point bending of cuboids. While other means of flexural testing exist, such as “ring on ring” biaxial, they present challenges from the perspective of scaling (primarily related to complex testing equipment) that simpler tests do not. All tests that are being carried out will scale all parameters, including loading and support spans. This means that test equipment will also will also have to scale accordingly. In this regard, four point testing is not ideal from a practical perspective as it means that equipment will be needed that can accurately reproduce the necessary loading spans as well as the support spans. This is one extra variable that can be eliminated to ensure repeatable testing. In the interest of simplicity three point testing of plane cuboids with square cross sections and a depth to span ratio of 4:1 will be carried out. BS EN 12390-5 (2009c) will offer guidance on the flexural testing.

In turn, this confines fracture toughness testing to three point testing of a square section beam type specimen. The most explored specimen geometry within this category is single edge notched beams (SENB). Choosing SENB makes practical sense as the defect is simple to machine and sharpen. The span to depth ratio of specimens will be 4:1, as used for the plain flexural testing. ASTM E1290 (2002) will offer guidance on the testing. The project is confident in the use of SENB for fracture toughness testing. A large international round robin, which was discussed by Quinn (2002), showed that this approach showed good between-laboratory reproducibility.

The project will move forward with two distinct geometries and four basic tests. The geometries that will be produced are cylinders and cuboids. The cylinders will be employed in splitting and compressive strength tests while the cuboids will be used in three point flexural strength and single edge notched beam tests.

3.7.2 Strain Energy Density FEA

This subchapter lays out the rules of the control volume strain energy density FEA approach and discusses its application to different materials and specimen geometries. The control volume radius, placed at the crack tip, is shown in Equation 9 (Yosibash, et al., 2004). It was formulated by equating the critical strain energy density at a straight edge as being the same as the critical strain energy density at a crack tip.

$$R_c = \frac{(1+v)(5-8v)}{4\pi}\left(\frac{K_{IC}}{\sigma_f}\right)^2 \quad (9)$$

This was not the first time a control volume had been employed. However, it was the first time that a control volume was independent of loading case and geometry; instead it could be considered a material constant being that it is based on parameters which are assumed to be material constants. Failure is predicted to happen when the average strain energy density within the control volume reaches a critical value, W_c, shown in Equation 10.

$$W_c = \frac{\sigma^2}{2E} \quad (10)$$

The application of the control volume to different stress concentrations is shown in Figure 43. It also includes blunted defects, a contribution that was first shown in relation to testing of PMMA specimens (Lazzarin & Berto, 2005). [The r_0 term being equal to $\rho(\pi-2a)/(2\pi-2a)$].

Figure 43 has been removed
from this version of the thesis
due to copyright restrictions

Figure 43. Application of control volume at different stress concentrations (Ayatollahi, et al., 2011)

Rather than repetitively performing studies until an average of W_c is reached within the control volume the predicted critical load, Pc, can be determined through Equation 11 where the load the in FEA is P_{FEA} and the average strain energy density within the control volume is $W_{FEA\ avg}$.

$$P_c = P_{FEA}\sqrt{\frac{W_c}{W_{FEA\ avg.}}} \quad (11)$$

Researchers have applied this SED approach via FEA to a range of materials, geometries and loading cases to good effect. To name a few:

Lazzarin & Berto (2005) applied the criterion to an earlier data set of blunt-notched PMMA plates and beams, showing good agreement between experimental and theoretical failure values.

Gomez et al (2007) worked with notches and V-notches of varying notch radii in PMMA beams, exploring a range of mode I/II mixes.

Lazzarin et al (2008) used a modified SED criterion and showed good agreement with fatigue of welded joints. Although this project deals with brittle materials it is worth acknowledging the range of applicability of the SED FEA technique.

Ayatollahi et al (2011) successfully applied the criterion to graphite disc specimens with 30°, 60° and 90° re-entrant corners, exploring a range of mode I/II mixes.

Berto et al (2012a) applied the criterion to graphite plates with angled U-notches of varying radii, showing good agreement across a range of mode I/II mixes.

Berto et al (2012b) applied a modified criterion to torsion of V and U-notched graphite specimens in torsion. This was an interesting body of work which employed a Mode-III based formulation for the control volume term, rather than Mode-I. Good agreement was found with the experimental data.

Berto et al (2013) applied a modified criterion to blunt V-notched graphite plates under compression. Here the criterion was modified empirically to allow for compression.

SED FEA has been shown to have good agreement with experimental data across a breadth of materials (including several studies into graphite) and specimen types. This gives the project confidence that SED FEA is suitably generalised for application to the stress states found in AGR graphite bricks.

3.7.3 Square Defect Discs

Of particular interest to the project are the aforementioned 90° re-entrant corner (square) defect discs (regularly referred to in the literature as Brazilian discs). This is because they bear the most similarity to the geometries seen in the AGR graphite bricks, namely the keyways. This is illustrated in Figure 44. It is also encouraging that a significant proportion of the studies covering SED FEA have been applied to graphite specimens, three such studies were mentioned in the previous section.

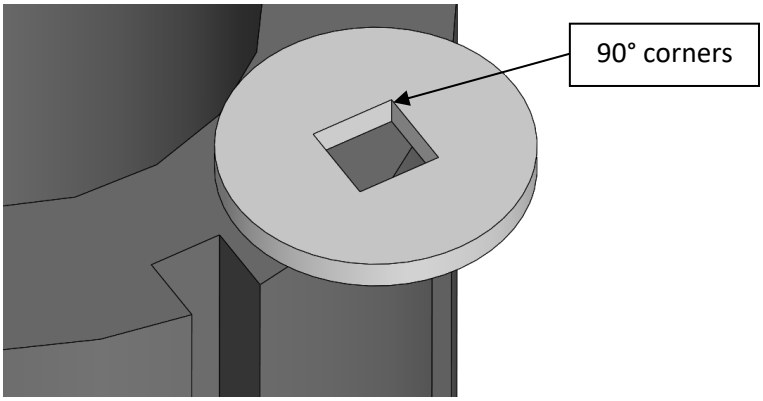

Figure 44. Square defect disc (150mm diameter) next to AGR keyway

The discs are tested by means of diametral compression (similar to the splitting test). The geometry is appealing from a practical point of view as one geometry can be used to explore a range of mode mixes simply by adjusting the loading angle. Figure 45 shows modal analysis by Torabi & Taherkhani (2011) in this area. Their work presented Mode-I and Mode-II notch shape factors for several variations of the disc specimen geometries (several different opening angles, defect to diameter ratios and corner radii). This project is currently only considering sharp 90° defects. The data shown here will be used later in the project (5.0 Mixed Mode (I/II) Nodal Displacement Characterisation) for comparison with a new nodal displacement mode ratio.

Figure 45 has been removed
from this version of the thesis
due to copyright restrictions

Figure 45. Mode data for sharp 90° corners in 0.4 ratio “defect to diameter” disc specimens (Torabi & Taherkhani, 2011)

3.7.4 Summary of Discussion

This discussion has outlined the test specimens and failure criterion that will form the basis of the work. This will now be formalised in the methodology.

4.0 Methodology

This methodology will detail the framework of how this project is going to explore the applicability of a failure criterion to the graphite bricks in an AGR.

Firstly the work will explore a new, generalised mixed mode ratio for describing the stress state at a re-entrant corner. The work will do this by considering the corners of a square defect disc from the perspective of a nodal displacement FEA approach. The output of this will be a new nodal displacement mixed mode ratio which will be compared to existing literature.

The project will then apply the life time strain data from the literature to the geometry of the AGR brick through FEA, specifically using a thermal analogy to reproduce the life time strain behaviour. The aforementioned generalised mixed mode ratio will be used to analyse the development of the stress state at the re-entrant corners in the keyway of the AGR brick by means of nodal displacements.

An experimental study to look at the effect of size on the splitting strength, compressive strength, flexural strength and fracture toughness of concrete will be undertaken. The diameters under consideration for splitting strength will be approximately 7, 14, 30, 42, 64 and 103mm. Splitting strength testing will be carried out in accordance with BS EN 12390-6 (2009d). In the case of compression the diameters under consideration will be 14, 30 and 64mm. Compression testing will be carried out in accordance with BS EN 12390-3 (2009b). For both three point flexural and SENB the specimen depths will be 8, 15 and 30mm. Flexural testing will be carried out in accordance with BS EN 12390-5 (2009c). SENB testing will be carried out in accordance with ASTM E1290 (2002) .

After this an experimental campaign into the size effect seen in mixed mode stress states will be undertaken. Concrete square defect discs with diameters of approximately 75, 150 and 300mm will be tested at loading angles 0, 15 and 30°.

A series of FEA studies, with material property inputs from the earlier work, will be undertaken to explore whether or not the criterion under consideration can make valid predictions for failure load across a range of sizes and mode mixes. These predictions and the insensitivity, or sensitivity, of the criterion to scale will demonstrate if the criterion has potential to be applied to AGR bricks.

5.0 Mixed Mode (I/II) Nodal Displacement Characterisation

This chapter will present a 3D FEA approach for characterising mixed mode (I/II) nodal displacements and compares it to published data for this specimen type. The FEA approach takes inspiration from a nodal technique for calculating stress intensity factors (Aliabadi & Rooke, 1991). The context of the work will be a square defect disc. This is because it is a versatile mixed mode (I/II) specimen which has been used extensively in the literature. This means that there is published data to draw on and compare with.

The FEA in this chapter was carried out in Solidworks Simulation. All FEA studies were 3D, linear elastic and used standard quality, parabolic tetrahedral elements. This element type has 11 nodes; four corner nodes and six mid-side nodes. A disc specimen with boundary conditions, loading and co-ordinate system is shown in Figure 46.

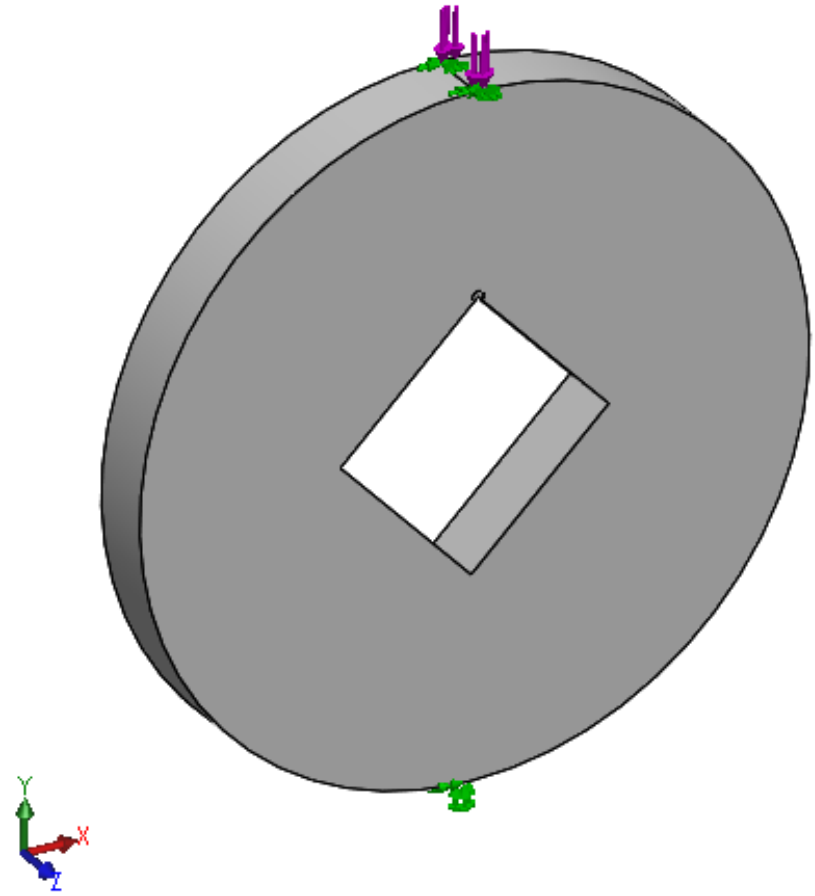

Figure 46. Overview of disc with co-ordinate system

So as to provide features for boundary conditions and loads all discs were blunted by 0.02mm on their upper and lower points of contact. This simulated localised crushing during loading. Studies were carried out to explore more complicated means of simulating loading; platens with friction conditions. However, there was no tangible difference in results so the less numerically intensive approach was implemented throughout. A blunted disc feature is shown in Figure 47.

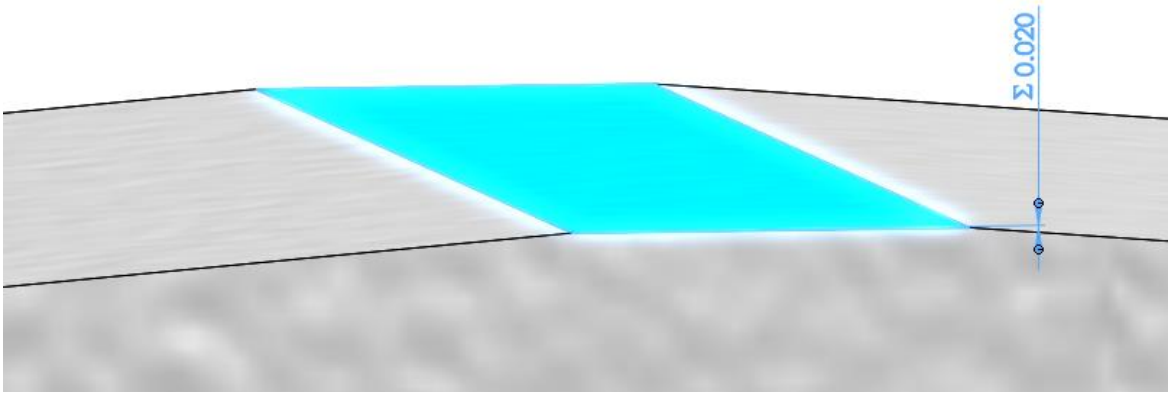

Figure 47. Blunted disc feature

The boundary and loading conditions are illustrated in Figure 48. The top of the disc is shown with with the loading direction normal to the surface and with the surface free to move only in direction y. All studies were carried out at a load of 100N. The bottom of the disc was fixed; not free to move in any direction. As described, studies were carried out which copied the physical test set up more closely but these gave no tangible difference in results and were computationally more intensive.

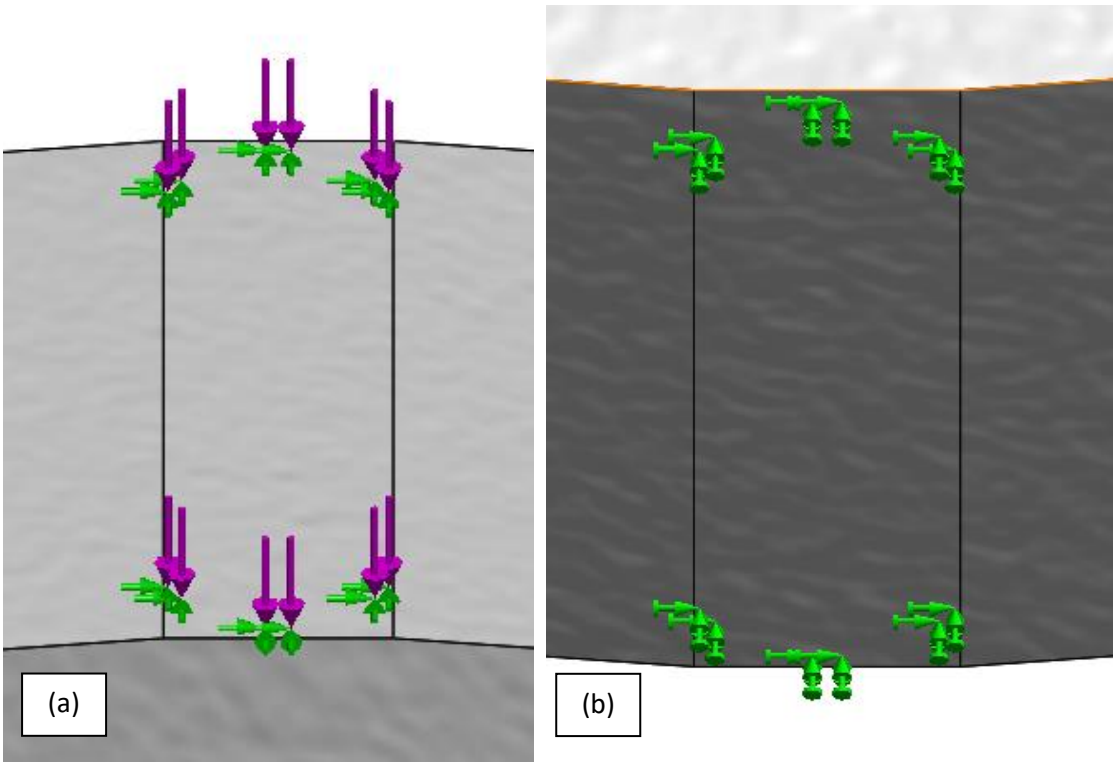

Figure 48. Top (a) and bottom (b) boundary conditions of a disc

All discs in this work followed the same dimensional ratios; 0.4:1 diagonal defect length to specimen diameter and 0.1:1 specimen thickness to diameter. Figure 49 shows a 100mm disc with mode I and mode II displacements with regards to the orientation of the defect. This is clarified in Figure 50 whereby the co-ordinate system is shown at the corner of the defect and has the Mode I and Mode II displacement directions.

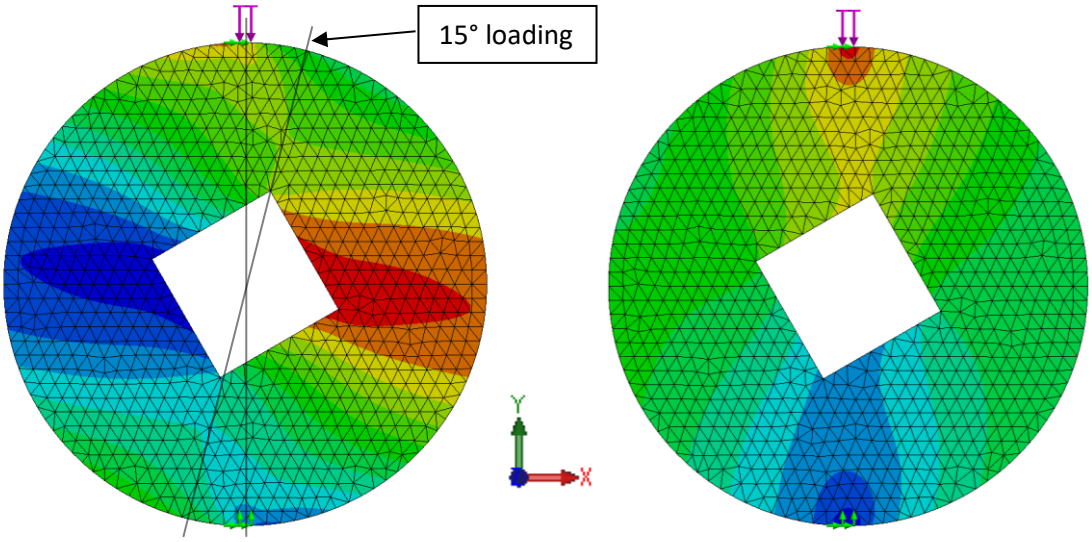

Figure 49. Square defect disc at 15° loading, nodal displacements

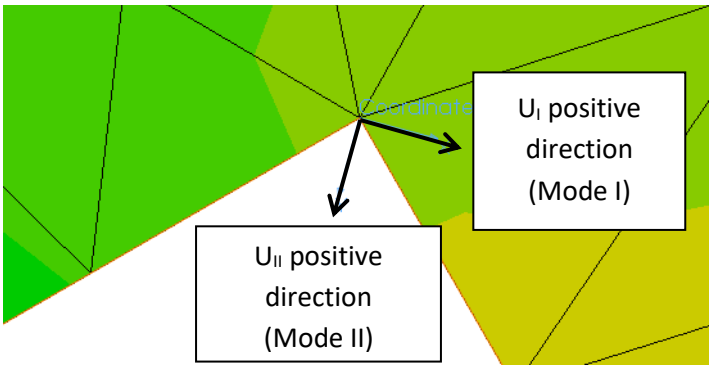

Figure 50. Local nodal co-ordinate system

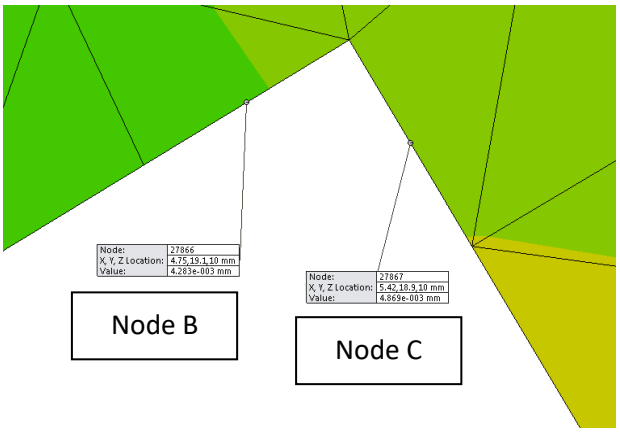

Figure 51. Nodal displacements at stress concentration

Figure 51 shows the probing of a pair of nodal displacements nearest to the crack tip. Mode I and Mode II nodal displacements at the stress concentration were recorded in this way at different mesh sizes and loading angles. The results of a mesh study at a 15° loading angle are shown in Table 2 and Figure 52. The ratio is calculated by dividing the difference in Mode I displacements by the difference in Mode II displacements.

Loading Angle (°)	Mode	Element Length (mm)	Displacement (mm) Node B	Displacement (mm) Node C	Nodal Displacement Ratio, ΔI/ΔII
15	I	1.0	4.348044E-03	4.929462E-03	**2.19**
	II	1.0	1.691746E-02	1.665189E-02	
15	I	2.0	4.167403E-03	5.072075E-03	**2.05**
	II	2.0	1.674464E-02	1.630327E-02	
15	I	3.0	4.019572E-03	5.119213E-03	**1.79**
	II	3.0	1.667680E-02	1.606323E-02	
15	I	4.0	3.938319E-03	5.248899E-03	**1.91**
	II	4.0	1.649499E-02	1.580969E-02	
15	I	5.0	3.728560E-03	5.157894E-03	**1.68**
	II	5.0	1.633753E-02	1.548684E-02	

Table 2. Mesh study for mixed mode ratio

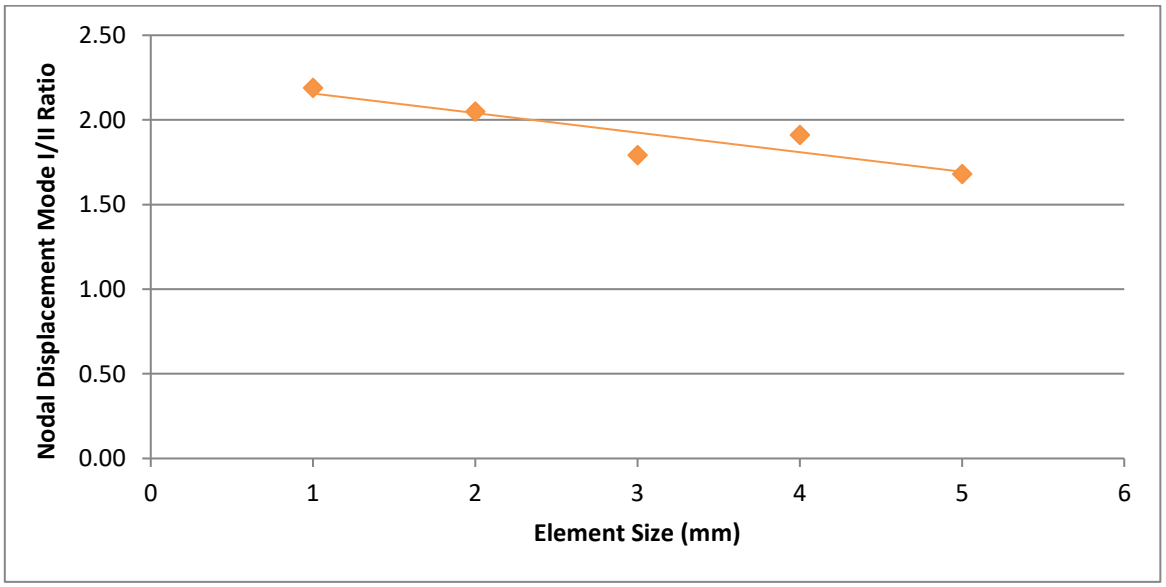

Figure 52. Mesh study for square defect disc at 15° loading angle

Variations on the underlying nodal techniques are presented by Aliabadi & Rooke (1991). For example, possible use of multiple node displacements (including nodes further away from the root) rather than a single nodal displacement approach which is shown here. It was determined that multiple point and extrapolation approaches did not present any improvement in mesh sensitivity. As such the project proceeded with the single nodal displacement ratio.

Figure 45 shows previous work to define the mixed mode (I/II) state at the corners of this type of specimen type; specifically the 0.4 notch length disc. The values in Figure 45 will be used to form a similar ratio, YI/YII, for comparison with the presented nodal displacement ratio.

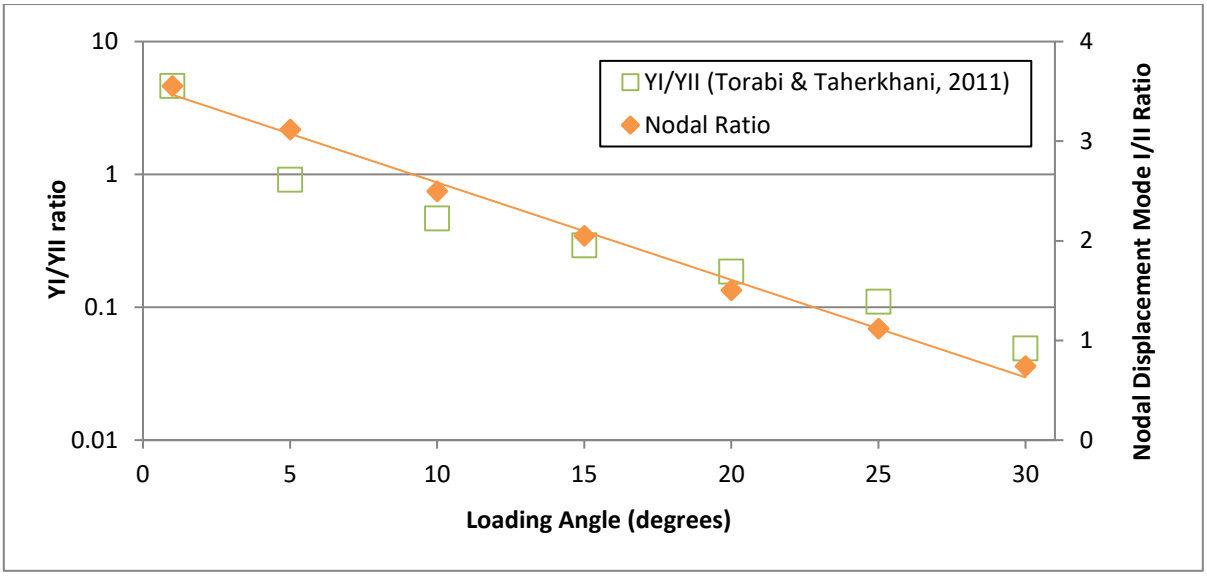

Figure 53. Comparison between published data, YI/YII (Torabi & Taherkhani, 2011), and new nodal displacement mode I/II ratio against loading angle for square defect disc

Figure 53 shows both the published YI/YII ratio (Torabi & Taherkhani, 2011) as well as the new direct nodal displacement mode I/II ratio as applied to the square defect disc from 1 to 30° with a 2mm mesh. The decision was taken not to plot the extremes of 0° and 35° loading angles as YI/YII goes to infinity and zero respectively. It should be stressed that in reality 0 and 35° are not going to be perfectly Mode I and perfectly Mode II. In the case of the square defect disc the stress states at the corners of the defect are induced opposed to direct. Simply put, you can confidently state a well-made tensile test specimen is pure in Mode I and a well-made shear test specimen is in pure Mode II. Outside of these cases it will be unusual to find pure cases of either Mode I or Mode II and, while an interesting test specimen, the square defect disc should not be considered representative of the full spectrum of Mode I and Mode II mixes.

A 2D FEA study was also carried out for comparison. This was successful in that it gave a very similar trend to the published YI/YII ratio but it was decided against in favour of the 3D nodal displacement mode ratio as it was thought that a ratio which spans several orders of magnitude, such as seen with the published YI/YII, was impractical. Avoiding this impracticality means that techniques for normalising the ratio, such as an inverse tan function (Akbardoost, et al., 2014), become unnecessary. The 2D nodal ratio was also more sensitive to meshing than the presented 3D nodal ratio.

It is also worth mentioning work in this field (Kotousov, et al., 2010) that explored the limitations of plane stress and plane strain interpretations of stress states when dealing with plates of finite thickness. Simply put, there is no generally recognised standard for when a plate is plane stress or plane strain, seeing as real objects aren't infinitely thin or infinitely thick. Using a 3D approach partially overcomes these limitations.

While there are differences between the YI/YII ratio and the 3D FEA nodal ratio (such as YI/YII needing to be graphed logarithmically) they do both indicate the transition from predominantly tensile (mode I) to predominantly shear (mode II). The project considers the nodal approach suitably generalised to apply to further stress states.

6.0 AGR Brick Stress State Characterisation

Based on the information outlined in the previous sub-chapter the project set out to describe the stress state observed at the corners of an AGR brick keyway by means of the direct nodal displacement mixed mode (I/II) ratio in a 3D FEA study. The material properties of the IM1-24 graphite are taken from an industry report (IAEA, 2000); density 1810kg/m^3, thermal co-efficient of expansion 4.3x10^{-6} K^{-1}, thermal conductivity 131 W/mK, Young's modulus 10.8GPa, Poisson's ratio 0.2. The geometry is taken from Tsang & Marsden (2007); 270mm internal diameter, 455mm outer diameter, keyways 33mm wide and 38mm deep.

Figure 54. A Heysham/Hartlepool AGR graphite brick

A 3D model of a graphite brick from a Heysham I/Hartlepool AGR is shown in Figure 54. It is in these bricks that fast neutrons are moderated down to thermal neutrons which are required to maintain fission at the low levels enriched uranium in the fuel. Typical studies into the aging of these bricks do not consider the whole brick as this would be computationally prohibitive. This study will follow suit and instead consider a segment of the brick 40mm deep. This is shown in Figure 55 meshed at 4mm. Deeper sections and finer mesh than this proved computationally impractical.

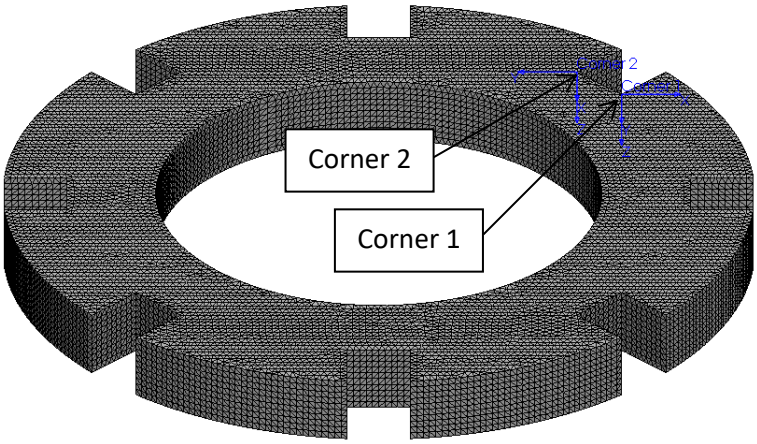

Figure 55. Segment of AGR brick

The premise of this study is to expand upon a model proposed in the literature (Tsang & Marsden, 2007), apply it to the AGR geometry and consider the mode I/II nodal displacements in the keyway corners. The two corners under consideration are shown in Figure 55, they are labelled with two local co-ordinate systems named Corner 1 and Corner 2. Efforts were made to instead consider a quarter portion of the AGR brick with symmetry conditions in place but this proved ineffective; nodal displacements between symmetrical corners were divergent.

As described, the input data is based on the work of Tsang & Marsden (2007). This work makes two extrapolations from their work:

1. The trends are taken forward by 10 FPY. This is based on Tsang and Marsden's work and the near parabolic strain turnaround behaviour seen in the literature (Kelly, 1978).
2. This work also presents strains at the outer circumference on the basis that the reduction in neutron flux from the keyway to the outer circumference will be similar to the reduction in flux from the bore to the keyway.

Table 3 and Figure 56 show the values the FEA was based on. This can be compared to the work of Tsang and Marsden which it is based on.

	Volumetric Strain		
Full Power Years	**Inner Bore**	**Keyway**	**Outer Circumference**
5	-0.00535	-0.00324	-0.00114
10	-0.01358	-0.00998	-0.00637
15	-0.02027	-0.01552	-0.01077
20	-0.02511	-0.02031	-0.01551
25	-0.02748	-0.02421	-0.02093
30	-0.02646	-0.02651	-0.02421
35	-0.02078	-0.02594	-0.02651
40	-0.00891	-0.02065	-0.02594

Table 3. Bore, Keyway and Outer strains based on Tsang & Marsden (2007)

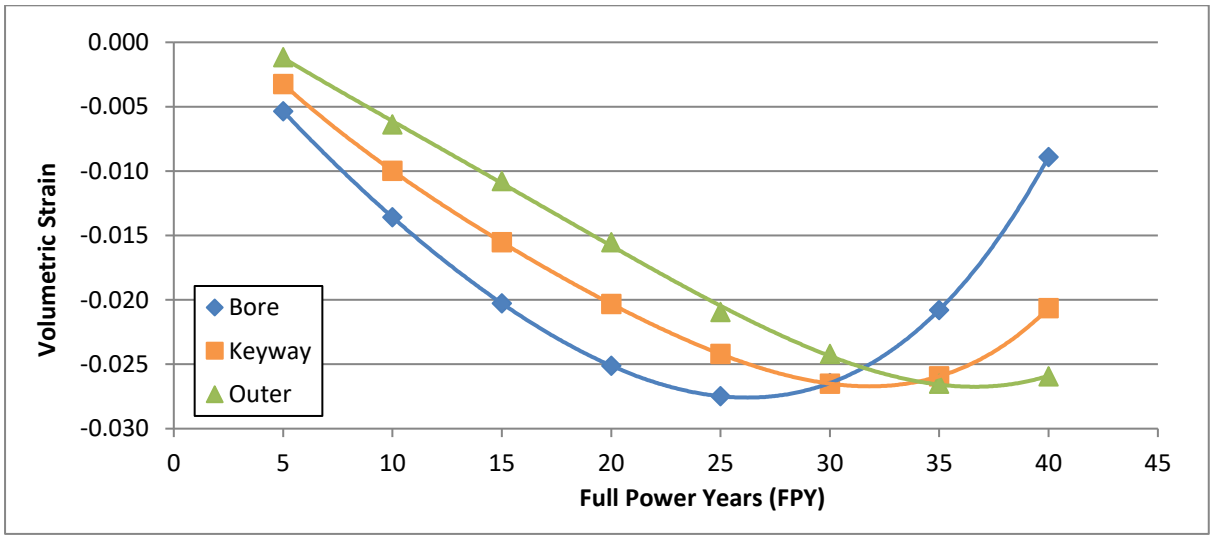

Figure 56. Strains against time for AGR graphite brick based on Tsang & Marsden (2007)

The FEA had two stages; firstly a thermal analogy to produce the volumetric change gradient described in Table 3 and then nodal analysis. Figure 57 shows the application of the thermal loads to the faces of the AGR brick section, it also shows the global and local co-ordinate systems. Thermal studies such as these do not require boundary conditions as there are no external forces to balance. Soft spring and inertial relief were enabled for these studies. Figure 58 shows the thermal gradient which reproduces the strains given in Table 3. This is an analogy of varying neutron flux through the AGR cross section.

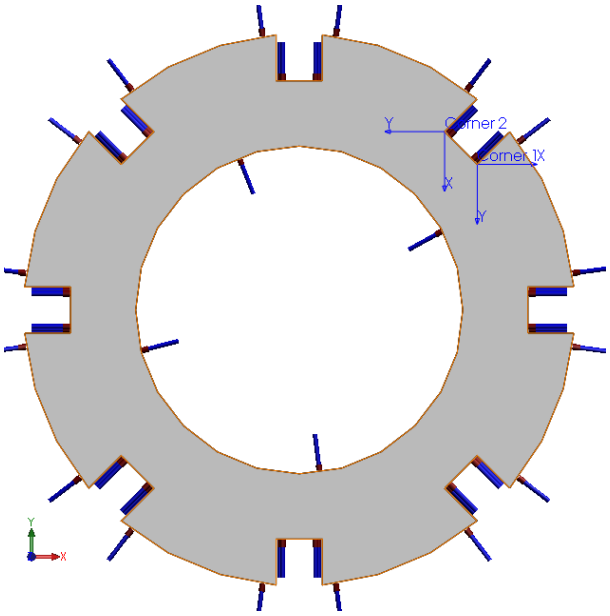

Figure 57. Thermal loading of AGR brick section, global and local co-ordinate systems

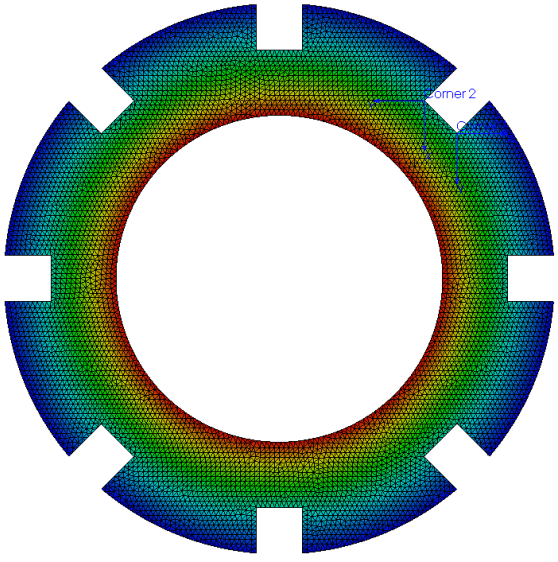

Figure 58. Volumetric change gradient through AGR brick cross section

Figure 59 demonstrates how, in the same way as the earlier mixed mode ratio work, the nodal displacements are probed at the mid-point of the first element. The co-ordinate system at Corner 2 can be seen Figure 59.

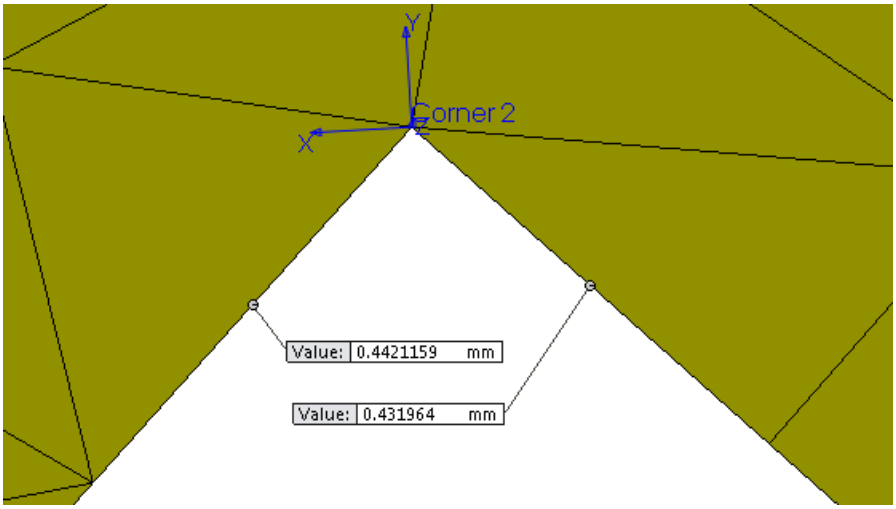

Figure 59. AGR keyway nodal displacements

As has been discussed, the prevailing macroscopic understanding of turnaround is that of a transition from a compressive outer circumference to a tensile outer circumference. This was visualised in Figure 10. This behaviour has been corroborated here by observing the macroscopic deformation of the keyways in Figure 60, Figure 61 and Figure 62. For the purpose of clarity the keyway deformation is shown at x20. In early life the outer circumference is in compression while in late life, after turnaround, the outer circumference is in tension.

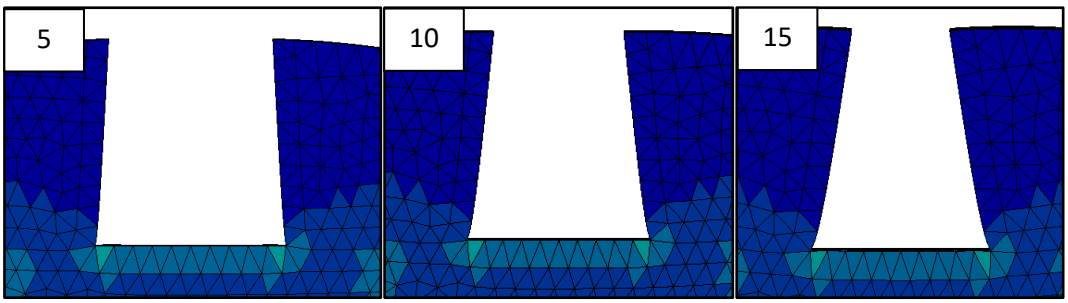

Figure 60. Keyway deformations, x20, at 5, 10 and 15 full power years

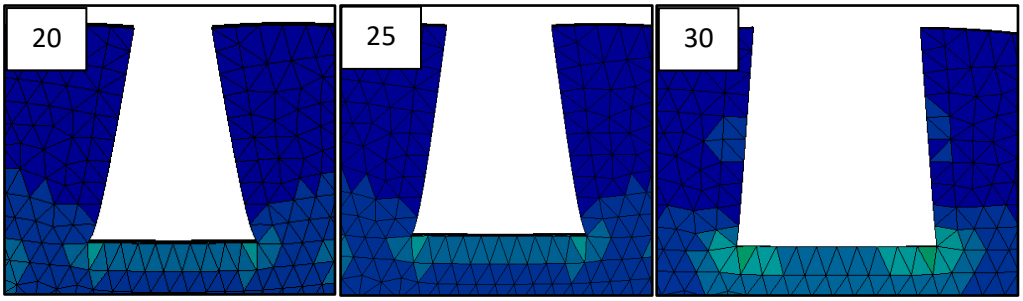

Figure 61. Keyway deformations, x20, at 20, 25 and 30 full power years

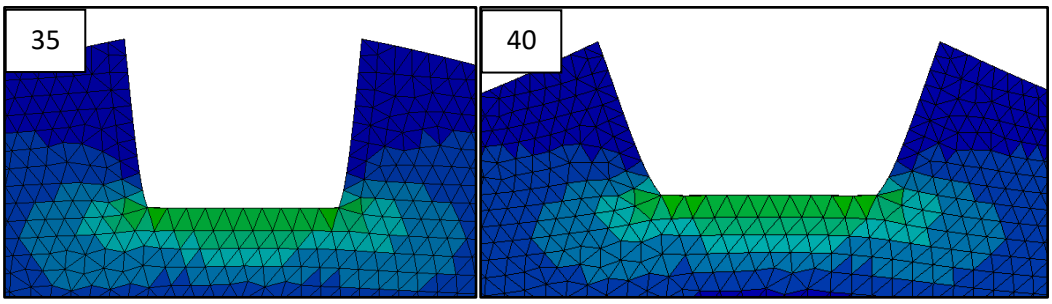

Figure 62. Keyway deformations, x20, at 35 and 40 full power years

Table 4 and Table 5 detail the mode I/II nodal displacements and mode ratios for both Corner 1 and Corner 2. The average difference between opposing corners was 4%.

			Displacement (mm)			
Full Power Years	Mode	Element Length (mm)	Node B	Node C	Nodal Disp. Mode I/II Ratio	
5	I	4.00	-0.5840809	-0.5608629	**I/II**	**-2.28**
	II	4.00	0.4324621	0.4426622		
10	I	4.00	-1.6092730	-1.5584460	**I/II**	**-2.91**
	II	4.00	1.2396520	1.2571390		
15	I	4.00	-2.4478350	-2.3749230	**I/II**	**-3.16**
	II	4.00	1.9017230	1.9247670		
20	I	4.00	-3.1110840	-3.0258290	**I/II**	**-3.66**
	II	4.00	2.4441420	2.4674430		
25	I	4.00	-3.5488020	-3.4647250	**I/II**	**-5.28**
	II	4.00	2.8363240	2.8522490		
30	I	4.00	-3.6200210	-3.5463900	**I/II**	**-17.51**
	II	4.00	2.9323880	2.9365940		
35	I	4.00	-3.1387410	-3.1816430	**I/II**	**-2.63**
	II	4.00	2.6515700	2.6352330		
40	I	4.00	-2.0013380	-2.0128180	**I/II**	**0.26**
	II	4.00	1.8007430	1.7559840		

Table 4. Corner 1 nodal analysis

			Displacement (mm)			
Full Power Years	Mode	Element Length (mm)	Node B	Node C	Nodal Disp. Mode I/II Ratio	
5	I	4.00	0.5613666	0.5851485	**I/II**	**-2.34**
	II	4.00	0.4421159	0.4319640		
10	I	4.00	1.5601070	1.6119130	**I/II**	**-2.98**
	II	4.00	1.2553680	1.2379520		
15	I	4.00	2.3775410	2.4517490	**I/II**	**-3.23**
	II	4.00	1.9219830	1.8990280		
20	I	4.00	3.0293110	3.1158880	**I/II**	**-3.73**
	II	4.00	2.4637540	2.4405320		
25	I	4.00	3.4689910	3.5539800	**I/II**	**-5.35**
	II	4.00	2.8477720	2.8318780		
30	I	4.00	3.5509660	3.6247290	**I/II**	**-18.12**
	II	4.00	2.9316580	2.9275880		
35	I	4.00	3.1849650	3.1432110	**I/II**	**-2.53**
	II	4.00	2.6303160	2.6468470		
40	I	4.00	2.0164190	2.0021130	**I/II**	**0.32**
	II	4.00	1.7519140	1.7968760		

Table 5. Corner 2 nodal analysis

The data is summarised in Figure 63 and Figure 64. It is shown that both the Mode-I and Mode-II nodal displacements turn around at approximately 20 FPY. The subsequent mode ratio turns around at approximately 30 FPY (the point at which the direction of shear is fully changing direction) and results in a shear dominant value, average between corners of 0.29, by 40 FPY. It should be noted that ratios such as these do have limitations when applied to nodal displacements that are changing direction. The mode ratio at approximately 30 FPY goes through a negative Mode-I singularity as the Mode-II displacements are reduced momentarily to zero. Further work is needed to improve this.

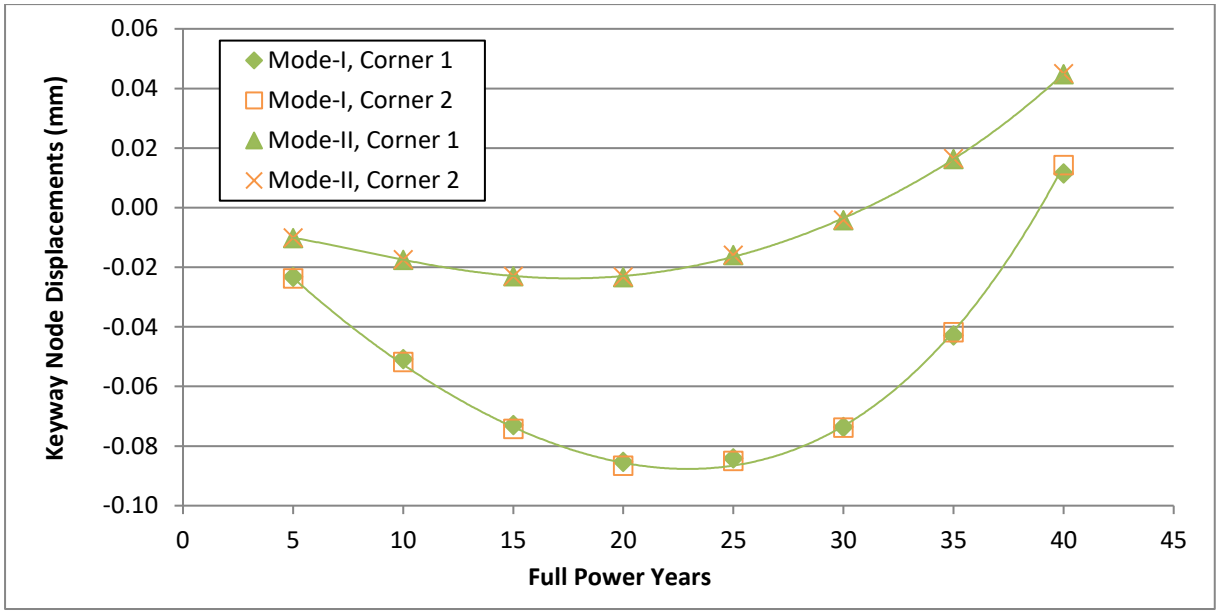

Figure 63. Keyway nodal displacements against full power years

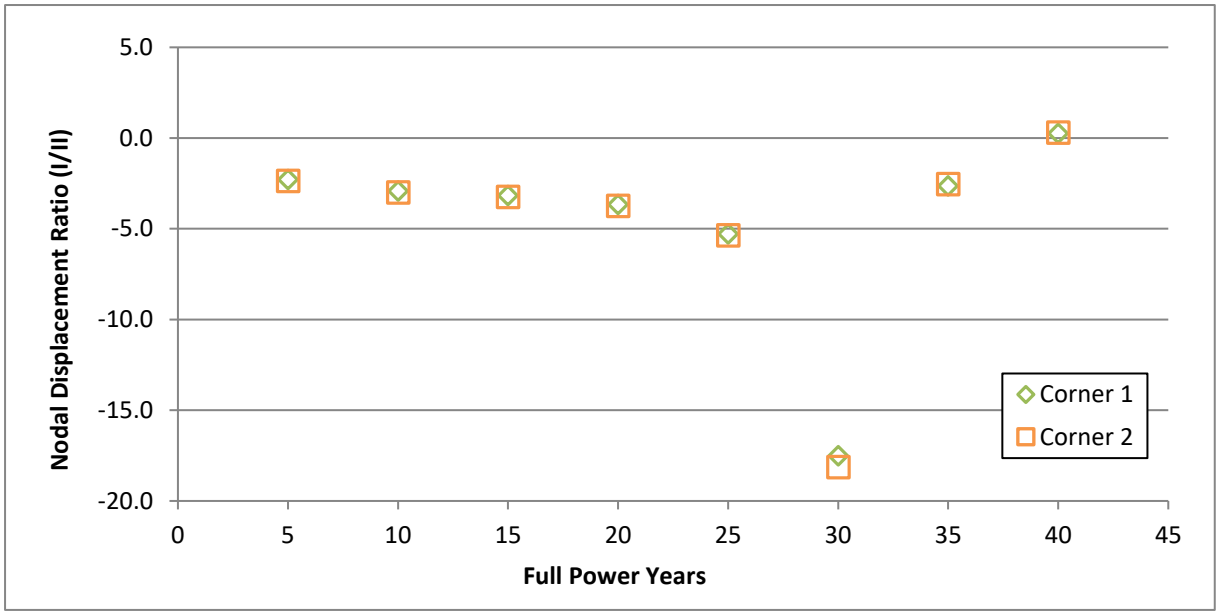

Figure 64. AGR keyway mode mix ratio against full power years

This sub-chapter has shown through a nodal study of AGR keyway stress states that late life AGR graphite bricks require a failure criterion which can operate in a mixed mode environment in light of the change to shear dominant by 40 FPY. These results offer a means for comparison between the later work (Chapter 8) and the stress states at reactor brick keyways.

7.0 Experimental Work

Experimental work was carried out to determine the effect of scale on four material properties of concrete; splitting strength, three point flexural strength, compressive strength and fracture toughness (SENB). Preliminary work was also carried out to identify and address any difficulties inherent to working with concrete.

7.1 Preliminary Work

Before the main body of experimental work could be carried out a period of preliminary work was embarked upon. The purpose of this work was to;

1. Build the skills required to successfully carry out testing.
2. Become familiar with the material, with a view to understanding specimen production.
3. Answer basic questions that could potentially undermine the body of experimental research if they were to go unanswered.

The project benefitted from the preliminary work which is described here.

7.1.1 Concrete Mixture Ratio and Additives

From the outset the project aimed to cast concrete into complex shapes after an exploratory stage of simple geometries. This required a concrete mixture that offered compatibility with complex moulds by virtue of low shrinkage. The project looked to the commercial world for a suitable concrete mixture. Decorative concrete tiles are made in highly detailed moulds; the project looked to learn from the manufacture of such products. One manufacturer of concrete tile moulding equipment recommends a mixture of one part cement to one part sand to 0.2 parts water to 0.01 parts Melflux 2651F plasticiser (Globmarble, 2014). Of particular importance is the addition of the polycarboxylic ether plasticiser and the low water content. High water content leads to high porosity and high shrinkage and is explored at great length in the literature (Powers, 1958). The plasticiser allows a lower water content by encouraging better distribution of the cement and water molecules in the concrete mixture (Ouchi, et al., 1997).

The project had access to a single complex “dog bone” mould to test the mixture for shrinkage. The aforementioned mixture was discovered to be too dry and therefore impractical to use with complex moulds. A mix with one part sand, one part cement, 0.4 parts water and 0.005 parts plasticiser was able to yield an uncracked dogbone specimen; this is shown in Figure 65. This was decided upon as a suitably low shrinkage mix.

Figure 65. Uncracked, complex concrete casting

Despite the project having access to the soft, silicone mould which made the specimen in Figure 65 the decision was made not to pursue the moulding technique further as it didn’t give the geometric certainty of hard moulds required for the work.

7.1.2 Mould Prototyping

A period of mould prototyping was undertaken. There were three geometry types that were explored; cylinders, cuboids and discs. Examining existing standards for concrete specimens (BS EN 12390-1, 2012) showed that it is typical for such specimens to be cast in either steel or polymer moulds. For ease of manufacture the project worked with polymer moulds. The standards are not prescriptive with regards to mould design. This meant that there was scope for experimenting with different aspects of mould design.

Cylindrical specimens are typically cast in tubular moulds. These can be either single piece or split. The project opted to work with single piece polymer tubes which would be cut from standard sizes. An important aspect of casting concrete cylinders is sealing the base. Several different ways of sealing the base of cylindrical moulds were experimented with. One approach that was experimented with was to produce steel discs and use them as plugs at the base of plastic tubes. This approach was found to be unsuitable as the interference fit required to properly seal the tubes produced concrete specimens that had an unacceptable draft angle. Another solution that was experimented with was sealing the tubular mould at the base with a concrete mixture and leaving it to dry before having the mould filled with further concrete mixture. This was explored as it was thought to be a scalable solution to mould sealing however it turned out to be unreliable. A more reliable and scalable means of sealing the moulds was found by using blue tack, rolled out into thin filaments and applied to the end of the tube. This is expanded upon in section 7.2.2 (Preparation).

The system of moulding in polymer tubes proved viable at a range of sizes; 103, 64, 42 and 30mm diameter tubes. A trial was performed with very small (7mm diameter) aluminium tubes, however this was unsuccessful. The outcome of the chemical reaction between the aluminium and cement produced a high level of porosity in the concrete. Figure 66 shows this.

Figure 66. Small concrete specimen cast in aluminium tube

Section 7.2.2 (Preparation) details a successful approach for producing small cylindrical specimens by means of drilling holes into thick plates of polymer, producing multiple cavity moulds.

The cuboid specimens were made in grey PVC multiple cavity moulds that are shown in section 7.4.2 Flexural Strength Preparation. An early version of this type of mould was experimented with that was made from medium density fibreboard (MDF), the results of that are shown in section 7.1.3 (Concrete Dehydration and Curing Procedure).

Time was also spent trying to produce entirely enclosed moulds for the disc specimens but this proved unfruitful. The open moulds used are shown in section 8.5 (Specimen Preparation).

7.1.3 Concrete Dehydration and Curing Procedure

Hydration refers to the chemical process by which water reacts with cement (Persson, 1996); it is an important aspect of the study of concrete. It has been discussed that plasticisers promote hydration, particularly for low water content mixtures, by more evenly distributing water molecules. It can take concrete days to fully hydrate. Achieving properly hydrated concrete can pose a challenge as adding excess water will compromise concrete through high porosity (Mir & Nehme, 2015) while too low a water content will yield under hydrated concrete. To ensure good quality concrete steps need to be taken to avoid dehydration after pouring concrete, regardless of the mixture selected or additives used. Figure 67 shows the outcome of an early prototype batch of cuboid specimens that were produced in early, prototype MDF moulds. The concrete was completely unviable, with the mix becoming dehydrated immediately after pouring.

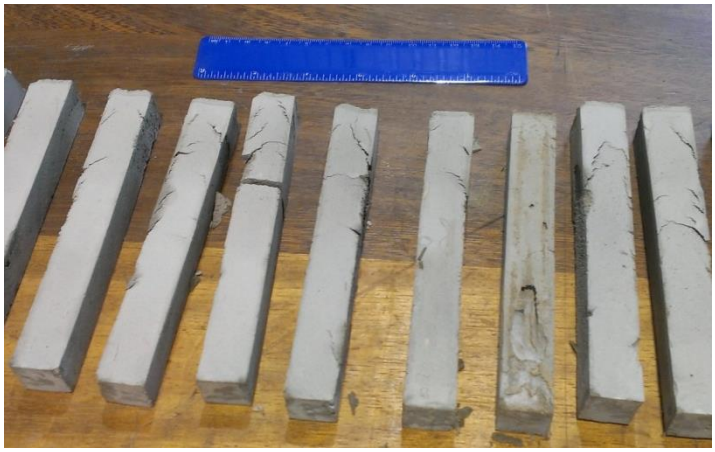

Figure 67. Severely dehydrated concrete specimens

The importance of avoiding dehydration was learnt through these early experiments. All subsequent moulds, regardless of geometry, were polymer due to their inherent low water absorption properties. The final polymer cuboid specimen moulds are shown in Figure 95 (section 7.4.2). Good moulds were found not to be the only pre-requisite for producing properly hydrated specimens. A procedure was necessary for each type of mould to ensure that the best possible hydration was achieved. Figure 68 shows a batch of cylindrical specimens underneath a protective membrane which has been secured in place with adhesive tape.

Figure 68. Cylinder specimens underneath a protective membrane

As well as the freshly poured concrete specimens, containers of water were placed underneath the membrane as well. This approach ensured that the concrete could begin to cure in a high humidity environment. This system proved effective. At the point of removing the membrane moisture could be observed to have condensed onto the internal surface of the membrane and specimens would still be moist to the touch. The cuboid specimens would undergo a similar process; after pouring the concrete the moulds were placed into a large box with approximately 30mm of water in, this was then covered with a membrane and sealed with adhesive tape.

After spending 24 hours in their respective high humidity atmospheres specimens were removed from their moulds and then, in accordance with good practice (BS EN 12390-2, 2009a) transferred to a container of water to complete their curing. The specimens would be kept in this way until immediately before testing. The reason for this being instructed by standards is twofold; it minimises the risk of producing dehydrated concrete and also means that all specimens are in the same condition at the point of testing.

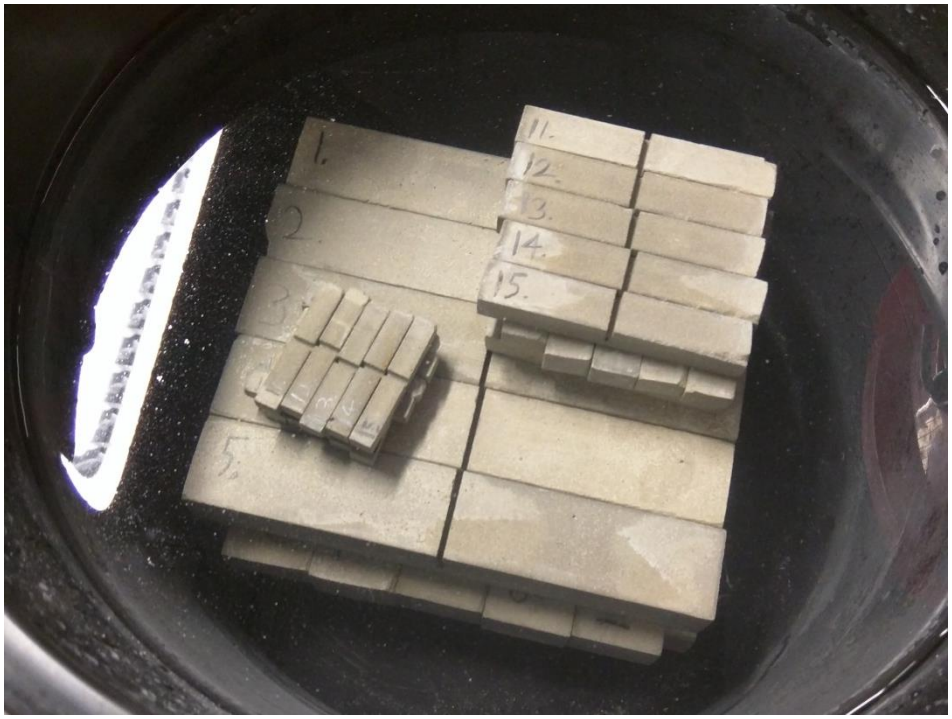

Figure 69. SENB specimens under water

Figure 69 shows a batch of SENB specimens curing in water. On average specimens in this project would stay in this condition for 10 days before testing. This is discussed in more detail in Section 7.1.5 (Age Strengthening).

7.1.4 Macroscopic Porosity

When casting components out of concrete it is important to ensure that a procedure is followed which does not result in large air pockets in the final product. Vibration is the typical means for dealing with air pockets in industry; this is shown in Figure 70.

Figure 70 has been removed
from this version of the thesis
due to copyright restrictions

Figure 70. Concrete vibrator and wooden form work (Purdy, 2009)

For batch production of smaller concrete components it is typical to use a vibrating table. The project did experiment with a small vibrating table of its own design but after mixed results decided upon a different technique to avoid excessive air pockets. Standards (British Standards Institution, 2009a) also offer a technique whereby the concrete is poured in stages. Here concrete is typically poured a quarter of a mould at a time and then "tamped" with a metal rod repeatedly (usually specified as 25 times per layer) before having further stages poured and tamped. This is shown in Figure 71.

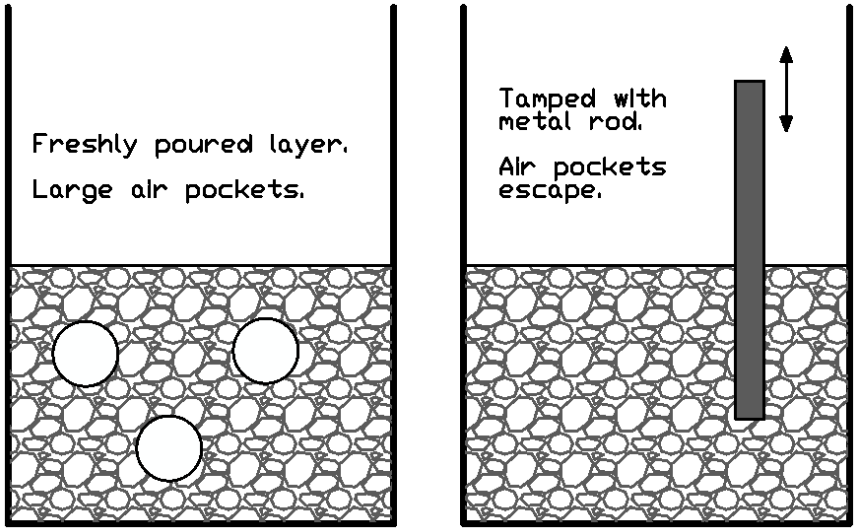

Figure 71. Diagram of tamping freshly concrete in generic mould

This was found to be a more scalable and versatile approach to dealing with excess air, producing good quality concrete in all geometries.

7.1.5 Age Strengthening

Another issue that is covered in the literature is the age strengthening behaviour of concrete (Un & Bardan, 2011). Some mixtures of concrete are shown to have a positive correlation between length of time curing and strength. Testing was undertaken to explore whether or not the concrete mixture in question was liable to age strengthening. A mixture that is prone to age strengthening does not lend itself to the work, as this would present an unwanted source of variation in material properties. A series of concrete batches were made and cured for different lengths of time before testing by means of splitting strength (this test method is explained in further detail in section 7.2). The results of the two specimen sizes tested are shown in Figure 72.

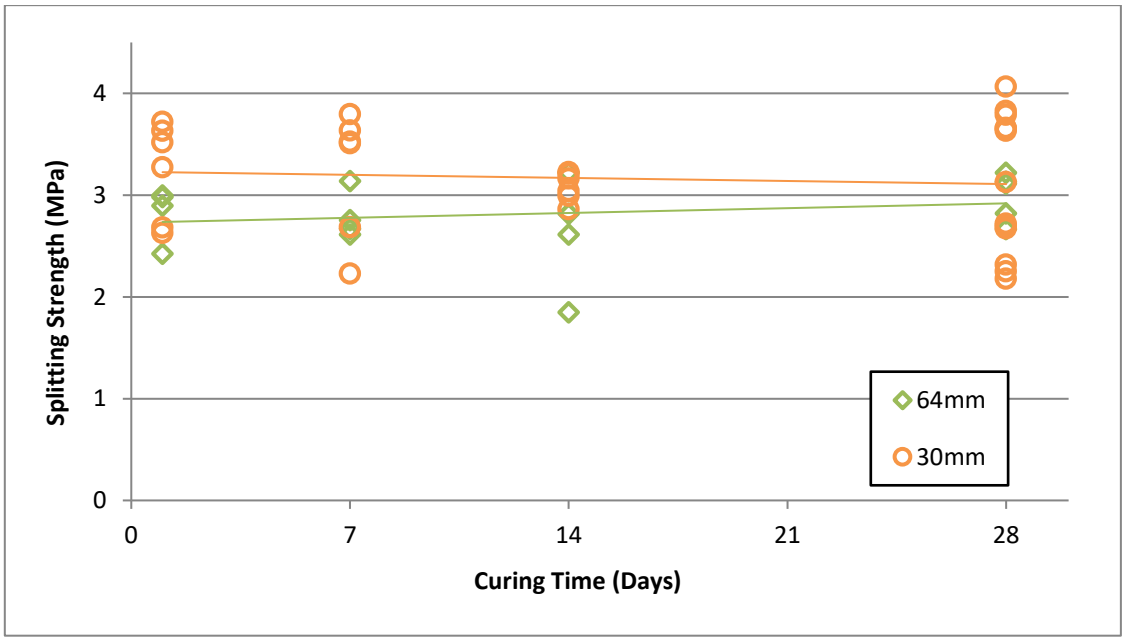

Figure 72. Splitting Strength against Curing Time

The data shows that there is not an appreciable age strengthening of the concrete mix in question. This is a good outcome for the project as it means that small variations in the curing time between batches will not jeopardise the data.

7.1.6 Poisson's Ratio

One material property that the project did not investigate experimentally was Poisson's ratio. This is because testing the Poisson's ratio presented technical challenges that could not be addressed in the time available. All the concrete testing undertaken was in accordance with BS12390 which dictates that the concrete must have as high a moisture content as possible at the time of testing, as discussed in 7.1.3 (Concrete Dehydration and Curing Procedure). The strain gauging approach that was available was not compatible with high moisture content. Figure 73 shows one such attempt at strain gauging a cubic specimen of concrete.

Figure 73. A strain gauged cube of concrete

As a result the project had to draw from the literature to find a constant value to work with where necessary. The typical value for Poisson's ratio found in the literature ranges from 0.1 to 0.2 with occasional outliers outside of that range. One such dataset can be found in the work of Allos & Martin (1981). A value of 0.15 was used in this work.

7.1.7 Summary of Preliminary Work

This chapter has detailed a series of experiments which ensured that the main body of experimentation would not be undermined by a period of uncertainty working with the material.

The topics that were considered were concrete mixture ratios, additives, mould prototyping, dehydration, curing, porosity and age strengthening.

The project has an improved output as a result of this period of preliminary work.

7.2 Splitting Strength

A large experimental campaign was carried out to see if a scale effect could be seen in the splitting strength of concrete. This test is of interest to the project as the specimens are relatively simple to prepare, requiring only cylindrical moulds and a simple tension/compression machine. Six sizes of specimen were tested, with over 270 samples being produced. A pronounced negative correlation between strength and size was observed.

7.2.1 Splitting Strength Theory

A standard test within the concrete industry is splitting strength (British Standards Institution, 2009d) whereby a cylinder of material is loaded diametrically until failure. This is shown in Figure 74.

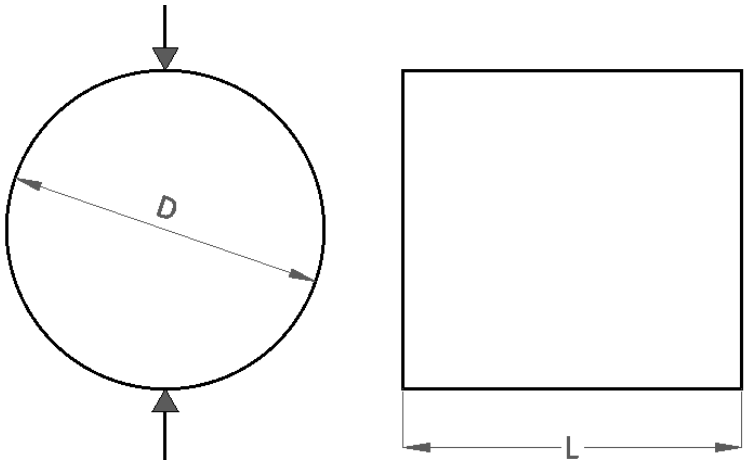

Figure 74. Splitting strength geometry and loading case

The splitting strength of the material is given in Equation 12. This is equal to the first principle stress.

$$\sigma_{split} = \frac{2P}{\pi DL} \quad (12)$$

Where P is the critical load (Newtons), D is the diameter of the cylinder (metres) and L is the length of the cylinder (metres). All cylinders that were tested followed a length to diameter ratio of 2:1, as is the standard.

7.2.2 Splitting Strength Preparation

As stated in 4.0 Methodology, six sizes of cylinder were decided upon. These were (in terms of diameter) 7, 14, 30, 42, 64 and 103mm. This is illustrated in Figure 75.

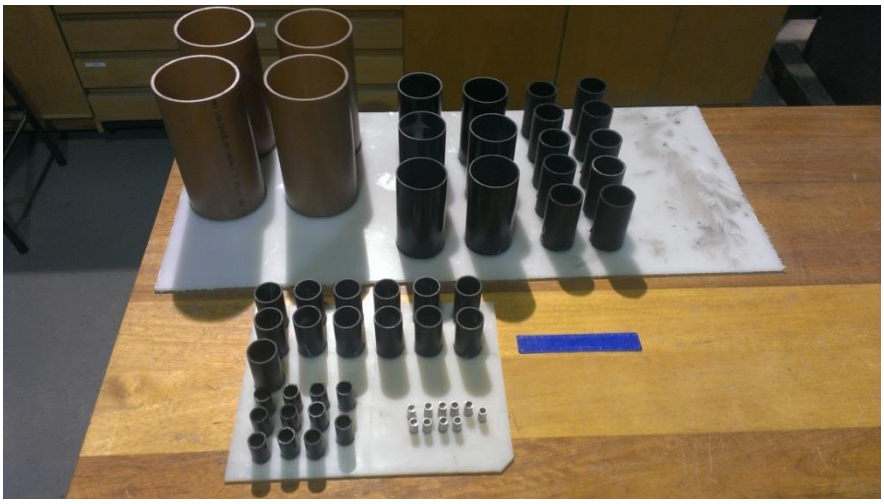

Figure 75. All cylinder sizes with 150mm ruler

One point to note in relation to Figure 75 is that the two smallest cylinder sizes were produced in different moulds after preliminary work with these small moulds showed them to be impractical. However, the photo does serve to demonstrate the range of sizes being studied. In terms of volume, the largest specimen is 3185 times larger than the smallest. By the standards of published works in size effect this is a significant breadth of scale to be studied (Kanos, et al., 2006).

An issue that needed to be addressed during the development of the moulding process was sealing the moulds so that they did not leak. After attempts with other approaches the most repeatable was found to be a process using “blue tack”. Blue tack would be rolled out into thin strands and then applied to the ends of the cylinders to form a gasket. This is shown in Figure 76 and Figure 77.

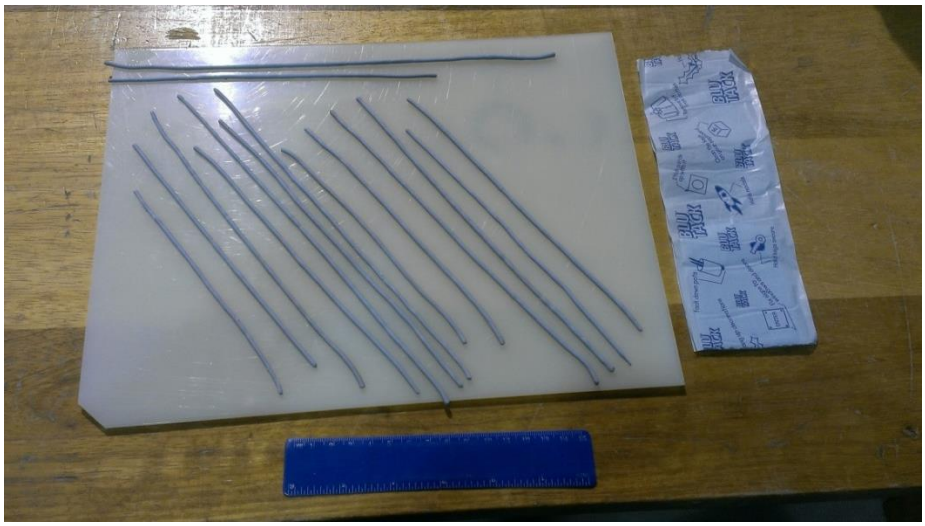

Figure 76. Blue tack, rolled, with 150mm ruler

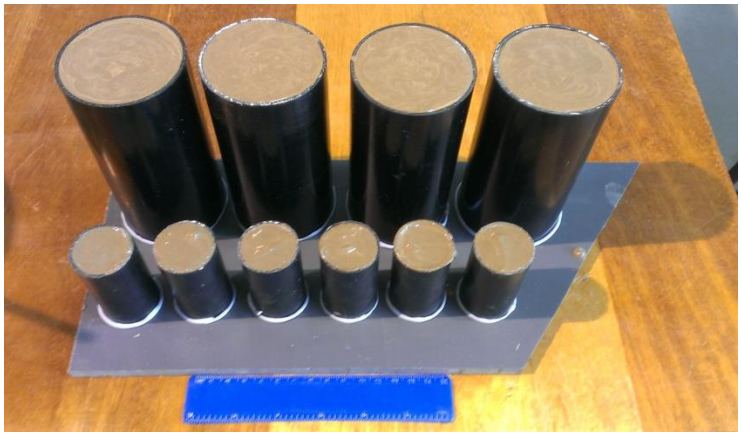

Figure 77. A small, early batch of concrete with blue tack visible at the base and a 150mm ruler

The system shown in Figure 76 and Figure 77 proved versatile and repeatable, although it was time consuming. It was also possible to reuse the blue tack. As previously stated, it was found to be impractical to mould the smallest specimens in this way. Instead the smallest specimens were cast in multiple cavity moulds, whereby the cavities are drilled into a large piece of plastic of the required thickness. The manufacture of the 14mm mould is shown in Figure 78 and the 7mm mould in Figure 79. The drawings for these moulds are given in Appendix B.

Figure 78. 14mm cylinder mould, manufacture

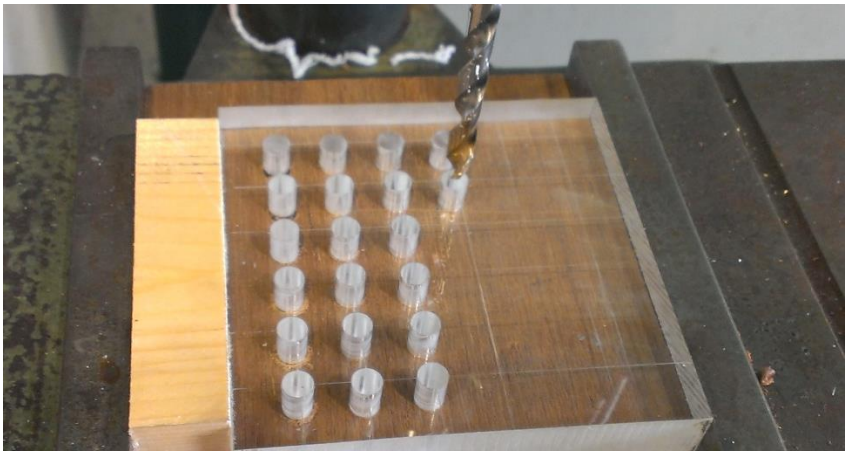

Figure 79. 7mm cylinder mould, manufacture

Figure 80 shows the completed 14mm mould. Figure 81 shows the mould with a cured batch of concrete before the specimens were pressed out.

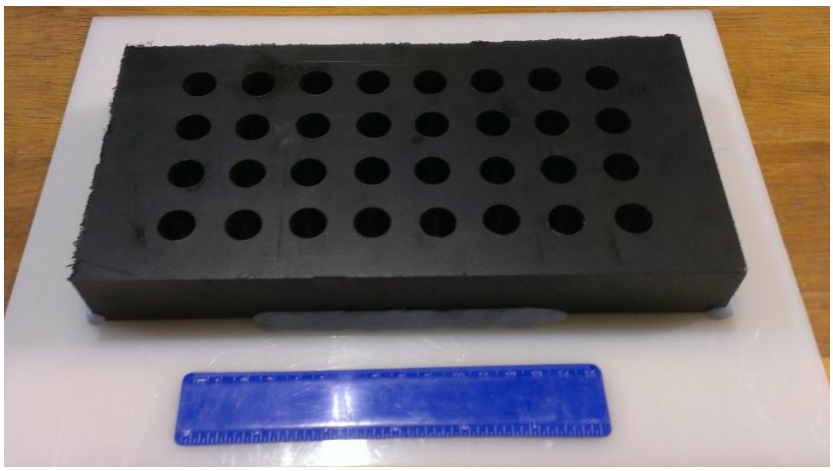

Figure 80. 14mm mould with 150mm ruler

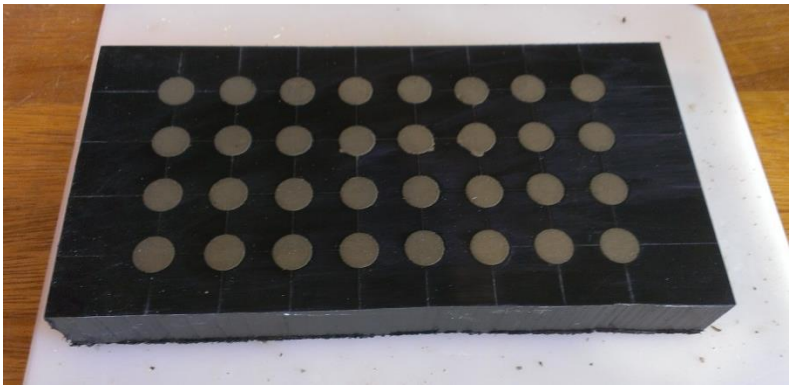

Figure 81. 14mm mould with cured concrete

Figure 82 shows the 7mm mould with cured concrete in, a single specimen removed and the steel drift that was used to press the specimens out.

Figure 82. 7mm mould with cured specimens, steel drift and approximately 150mm of ruler showing

All specimens were measured using a digital height gauge on a precision ground flat surface. The cylinders were measured four times across their diameter and the height measured twice to achieve a nominal size for each specimen.

Figure 83 shows the apparatus used to measure the cylinders and also the printed tables that would be filled in for every batch. Figure 84 shows an example of the smallest specimen size being measured.

Figure 83. Four 64mm cylinders, height gauge and printed excel table for recording dimensions

Figure 84. A 7mm cylinder being measured

7.2.3 Splitting Strength Experiments

After measuring the geometry of the specimens each batch would be loaded until failure in either a Testometric or Mayes testing machine under diametric compression. The loading speed was varied according to the British Standard (BS EN 12390-6, 2009d).

Figure 85 and Figure 86 show two different sizes of specimen before loading. The 103mm specimen in Figure 86 was tested in the more powerful Mayes machine. The smaller 30mm specimen makes use of the Testometric, which was used for the majority of testing; being that it was suitable for all but the very largest specimens. Figure 87 and Figure 88 show tested specimens, all with the crack path typical to this type of test. The load at failure for each specimen was tabulated and the results reproduced in section 7.2.4.

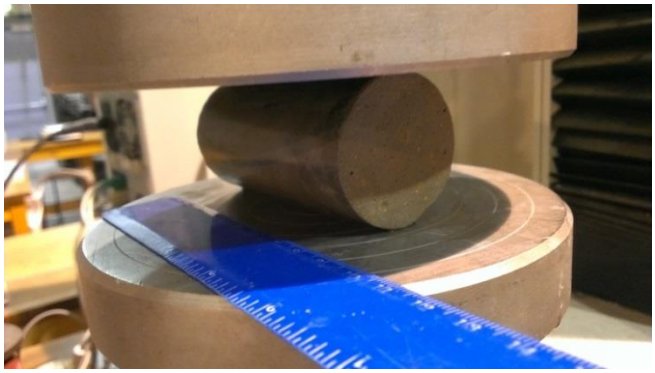

Figure 85. A 30mm specimen before loading, with a 150mm ruler

Figure 86. A 103mm specimen before loading, with tape measure

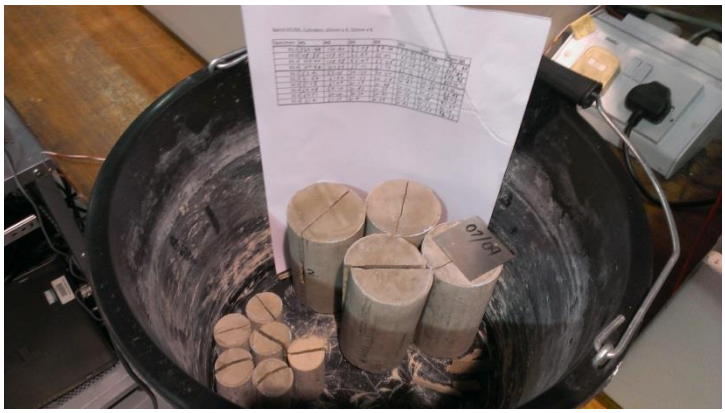

Figure 87. A small batch of 64 and 30mm specimens, having been tested

Figure 88. Assortment of tested specimens, with 300mm of tape measure

7.2.4 Splitting Strength Data

The raw data for the specimen dimensions and failure loads can be found in Appendix A. The data is summarised here in Table 6. The 103mm cylinders did not have enough samples for valid standard deviations so the table does not include values in those cells.

Nominal Diameter (mm)	Average Splitting Strength (MPa)	St.Dev. (MPa)	+1.5 St.Dev. (MPa)	-1.5 St.Dev. (MPa)
7	3.75	0.44	4.41	3.10
14	3.78	0.41	4.39	3.16
30	2.95	0.44	3.61	2.28
42	2.73	0.25	3.10	2.36
64	2.75	0.32	3.22	2.27
103	2.17	n/a	n/a	n/a

Table 6. Splitting strength summarised

Figure 89 summarises the results of the experimental campaign into size effect in splitting strength in concrete. There is a definite size effect; as the specimens increase in size they show a decrease in splitting strength, with the smallest specimens having a splitting strength of 3.74MPa and the largest specimens having a splitting strength of 2.17MPa. This trend is in agreement with the literature and can be attributed to larger specimens having a higher probability of containing a critical flaw.

An interesting point is that the negative correlation between size and strength does bear a similarity to that described in the literature by Bazant (1999). This is explored in Figure 90. In the work it is stated that as structures increase in size they go from obeying a constant stress criterion (possibly seen at 7 and 14mm here) to following a power law. Bazant states that the power law that the decrease in strength tends towards is -0.5 while in this data set it is -0.26. The lower value could be due to the range of sizes being within the transitional size range. However, it is difficult to subscribe to any particular scaling law given the scatter in the data.

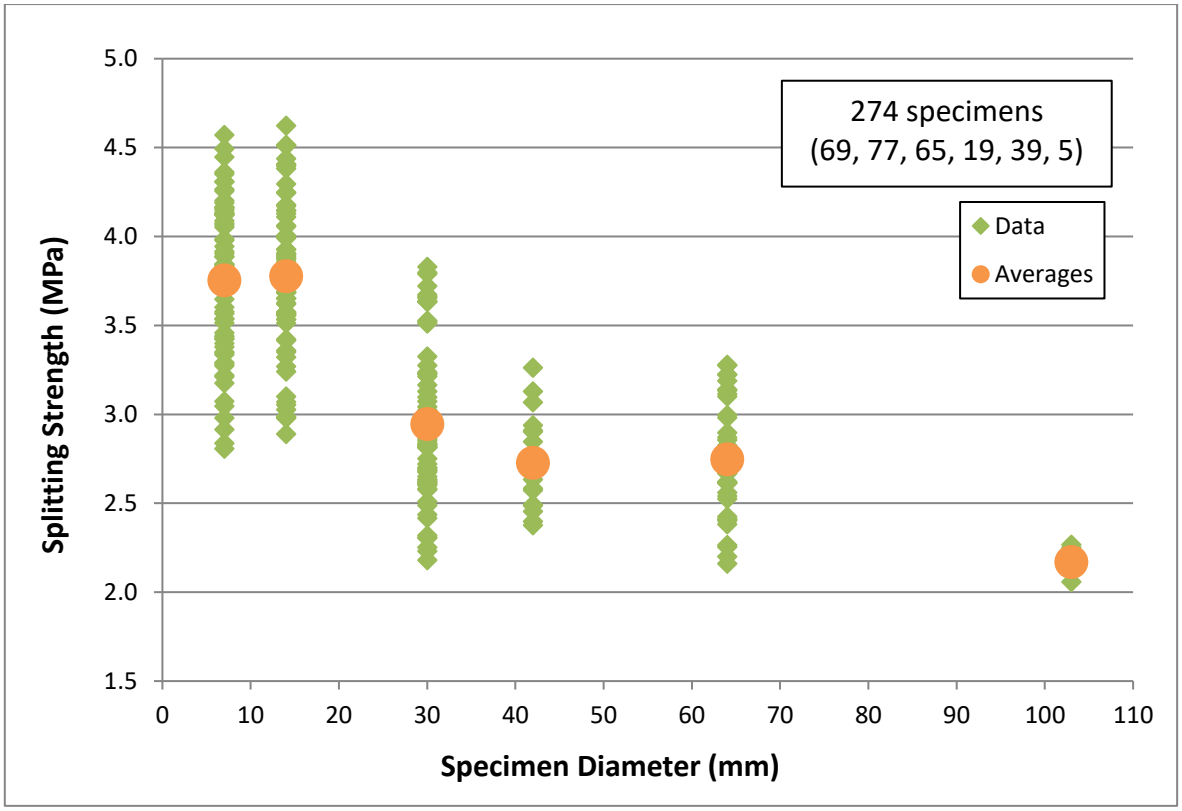

Figure 89. Splitting strength against specimen diameter

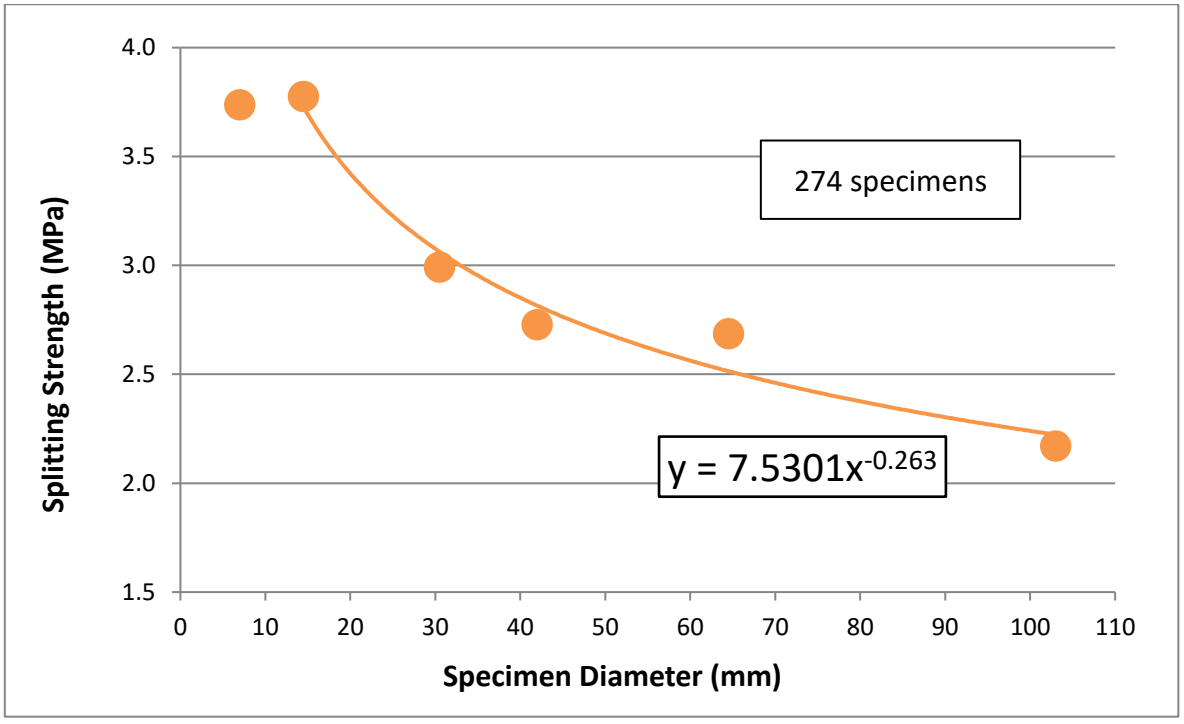

Figure 90. Relationship of averaged splitting strength against specimen diameter with power law

7.3 Compressive Strength

An experimental campaign looked to see if a size effect could be observed with relation to compressive strength. This study benefits from using the same cylindrical moulds as the splitting strength experiments. The only additional equipment was steel end caps with rubber inserts to ensure even loading, as minor misalignment of the specimen end faces can cause premature failure. 118 specimens were tested in compression.

7.3.1 Compressive Strength Theory

Cylinders are loaded in direct axial compression and the load at failure is used to calculate the compressive strength. A basic diagram of the test is shown in Figure 20.

Compressive strength is simple in its formulation, given in Equation 13.

$$\sigma = \frac{F}{A} \quad (13)$$

Where F is the load at failure (Newtons) and A is the cross sectional area of the cylinder being tested (metres).

7.3.2 Compressive Strength Preparation

The cylindrical moulds for the splitting strength tests were used again for the compressive tests. 14, 30 and 64mm cylinders were tested. An important aspect of testing brittle materials in compression is ensuring that any slight misalignment between the faces under compression is dealt with. Typically standards for testing concrete favour casting each end of a cylindrical specimen in a sulphur compound (British Standards Institution, 2009b). Other standards offer a more accessible option of using rubber pads in steel end caps (ASTM, 2000). This option will be used for these tests as the facilities are not available to work with molten sulphur or other similar processes. In total 118 specimens were tested.

7.3.3 Compressive Strength Experiments

Figure 91, Figure 92 and Figure 93 show the cylinders in their end caps before being loaded.

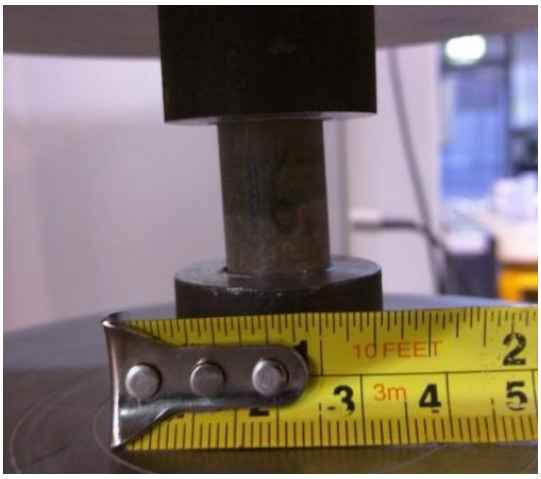

Figure 91. 14mm cylinder in compression with metal caps and rubber pads

Figure 92. 30mm cylinder in compression with metal caps and rubber pads

Figure 93. 64mm cylinder in compression with metal caps and rubber pads

7.3.4 Compressive Strength Data

The raw data for the specimen dimensions and failure loads can be found in Appendix A. The data is summarised here in Table 7. 118 specimens were tested. Due to the lack of size effect an overall average is given in Table 7.

Nominal Diameter (mm)	Average Compressive Strength (Mpa)	St.Dev. (MPa)	+1.5 St.Dev. (MPa)	-1.5 St.Dev. (MPa)
14	25.20	3.17	29.95	20.45
30	24.26	1.35	26.29	22.23
64	24.57	2.38	28.14	21.01
All	*24.92*	*2.82*	*29.15*	*20.70*

Table 7. Summarised compressive strength data

Figure 94 shows a summary of the results of the size effect study into concrete compression. There appears to be no size effect at the sizes tested. This is interesting as industry standards for concrete typically prefer using specimens which are 150mm in diameter, when this work would indicate there is little reason to go to the effort (and higher loading requirements) of working with larger specimens. One possibility is that working with larger aggregate is not suitable for smaller moulds, thus standards must state specimen sizes that are compatible with all possible aggregate mixes.

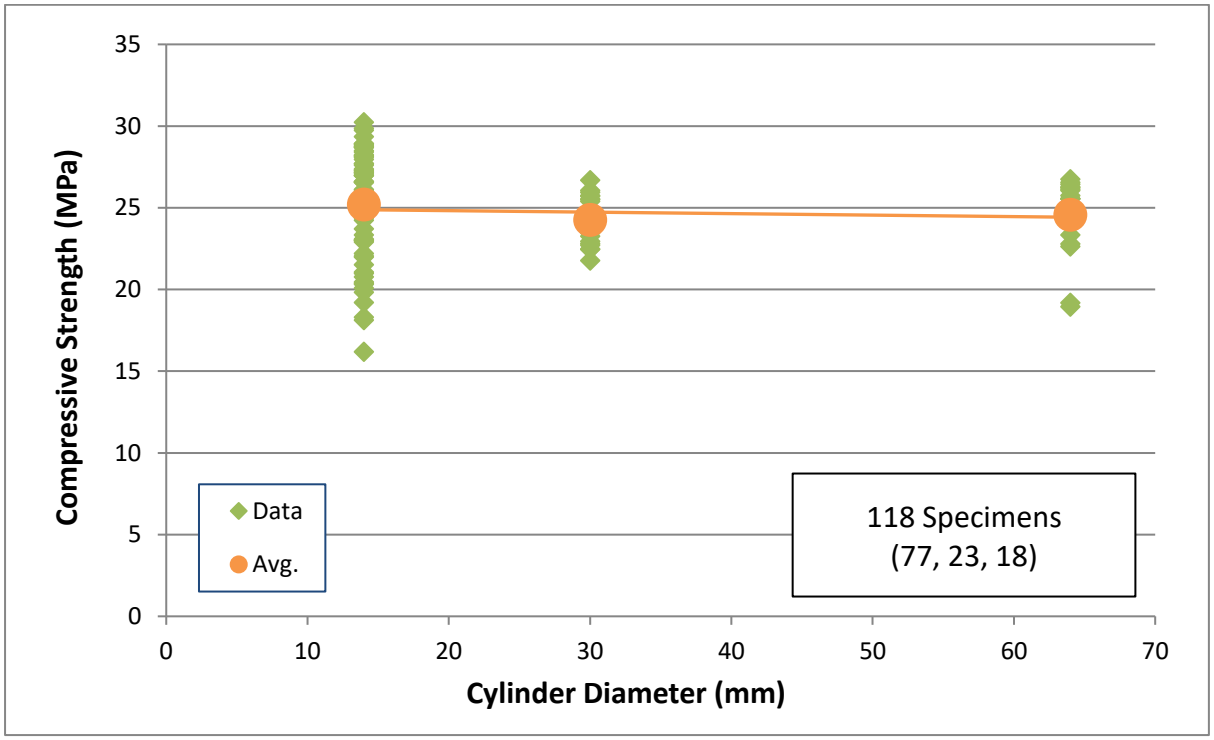

Figure 94. Compressive strength against Cylinder Diameter

A hypothesis for the lack of size effect in this data set is that the mechanism by which a compressive specimen fails is fundamentally different to a tensile or splitting specimen. In this instance flaws are being closed rather than opened. This is one possible reason that the literature does not present as unified a view of size effect in compression as it does in tension or splitting.

7.4 Flexural Strength (3PT)

The third experimental campaign was to investigate the effect of size on flexural strength in three point bending. Again, only conventional testing equipment was needed for these specimens and once the moulds had been produced the batch production of specimens was efficient. Three sizes of specimen were produced and a minor negative size effect was observed.

7.4.1 Flexural Strength Theory

Three point flexural testing is considered a standard test across a range of materials. It also presents the project with a different type of stress state to observe the effects of scale; a stress gradient rather than a uniform stress state. The loading case and geometry variables are given in Figure 25.

The flexural strength is given by Equation 14.

$$\sigma_{flex} = \frac{3FL}{2bd^2} \quad (14)$$

Where F is the critical load, L is the length of support span, b is the breadth of the beam and d is the depth of the beam. All specimens that were tested had a square cross section (b = d) and span to depth ratio was 4:1.

7.4.2 Flexural Strength Preparation

There were two aspects to the preparation for these tests; the moulds and the testing equipment. Both needed to offer the repeatability required for testing large numbers of specimens. The mould design was that of a disassemblable, plastic mould, the drawings are available in Appendix B and are shown in Figure 95. The specimen sizes were 8, 15 and 30mm depth cuboids.

A testing fixture was produced to ensure that the spans were consistent between tests carried out on different specimen batches. The design also meant that less time was spent setting up for each different test. The manufacture of the jig is shown in Figure 96.

Figure 95. Cuboid moulds

The grooves being milled in Figure 96 give good repeatable roller positions for the three sizes of specimen under investigation. The specimens were made and measured in a similar way to that shown in Figure 83, but the cuboids' breadth and depth were recorded rather than the diameter.

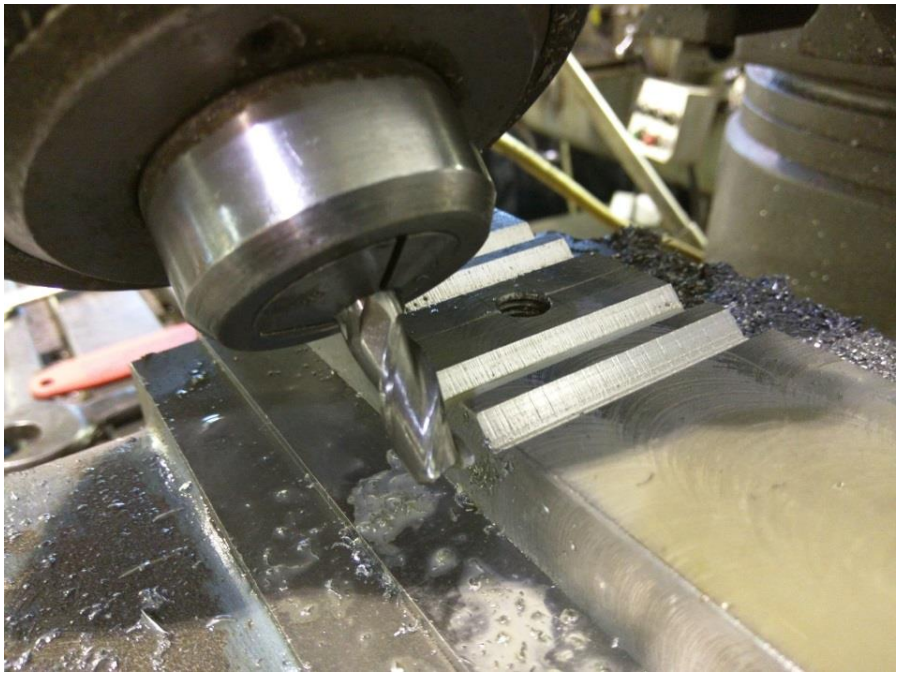

Figure 96. Three point bend test fixture being machined

A batch of cuboid specimens is shown in Figure 97.

Figure 97. A batch of cuboid specimens

7.4.3 Flexural Strength Experiments

Shown in Figure 98, Figure 99 and Figure 100 are the 8, 15 and 30mm cuboids before being tested. The complete test apparatus can be seen in the figures, with the rollers set for each span. The spans are 32, 60 and 120mm (4x depth in each case). All specimens were tested to failure and the peak load recorded.

Figure 98. An 8mm cuboid before testing, with 300mm of tape measure

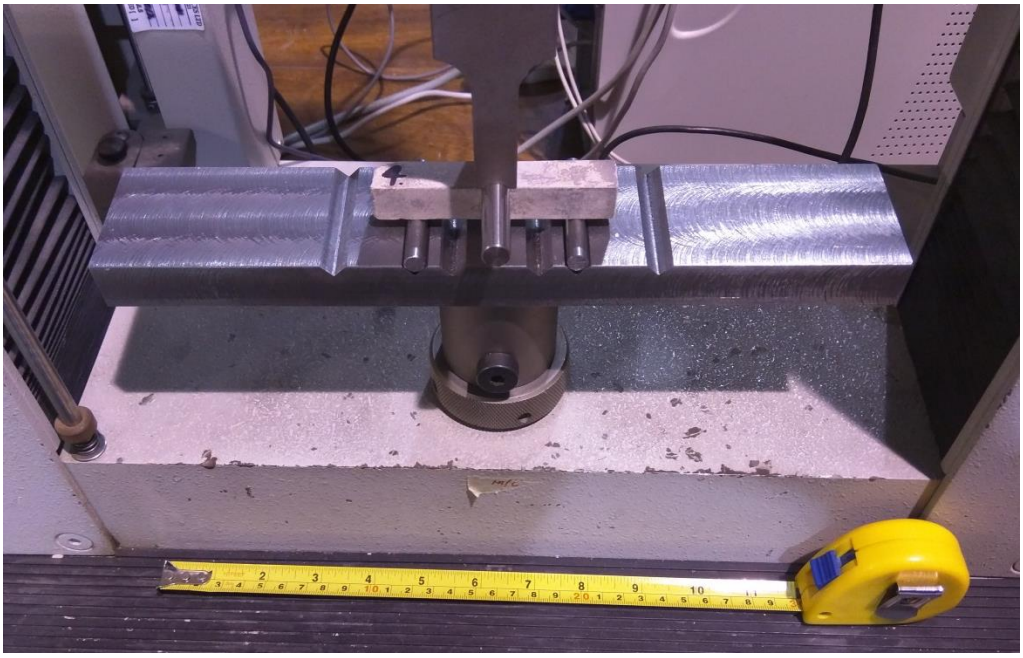

Figure 99. A 15mm cuboid before testing, with 300mm of tape measure

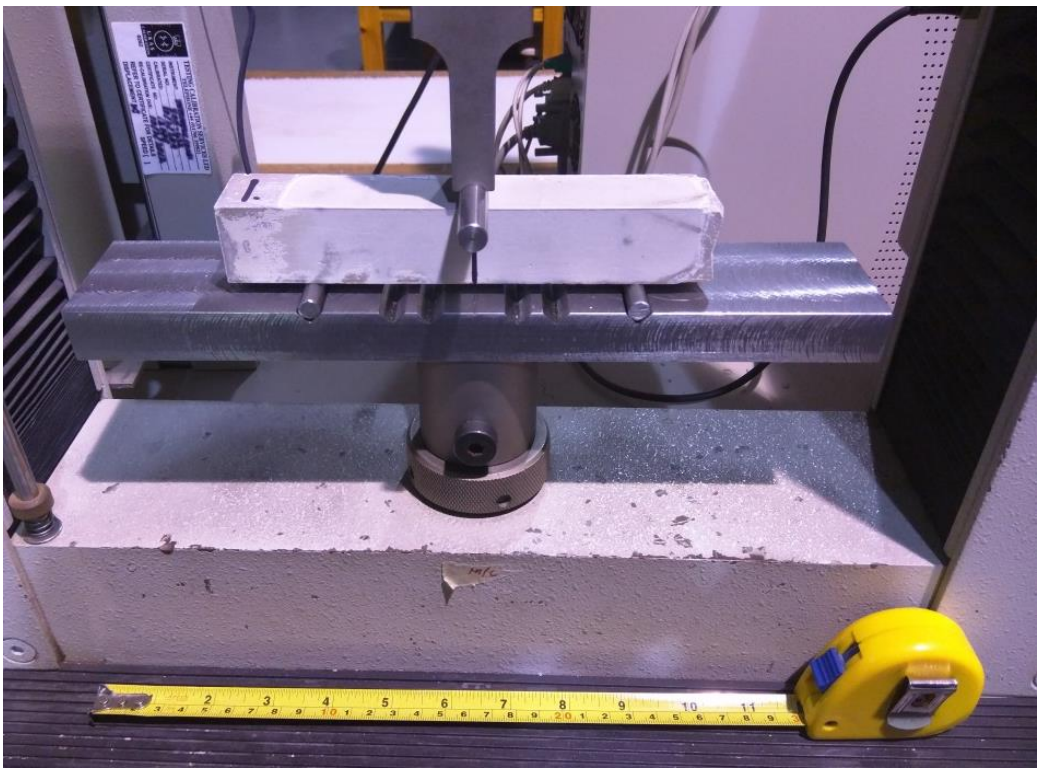

Figure 100. A 30mm cuboid before testing, with 300mm of tape measure

7.4.4 Flexural Strength Data

The results are summarised in Table 8 and Figure 101. A small and inconclusive size effect was observed, with a reduction from 8.16 to 7.57MPa average flexural strength being seen between the 8 and the 30mm specimens. More testing with larger specimens would be necessary to confirm this trend. Due to the amount of overlap between the data sets for the three specimen sizes an average of all of the specimens is shown. Any further reference to strength will simply refer to the overall data set rather than any individual size.

Nominal Depth (mm)	Average Flexural Strength (MPa)	St. Dev. (MPa)	+1.5 St. Dev (MPa)	-1.5 St. Dev. (MPa)
8	8.16	1.25	10.05	6.28
15	8.16	1.05	9.73	6.58
30	7.57	0.89	8.91	6.23
All	*7.96*	*1.11*	*9.63*	*6.30*

Table 8. Summarised flexural strength data

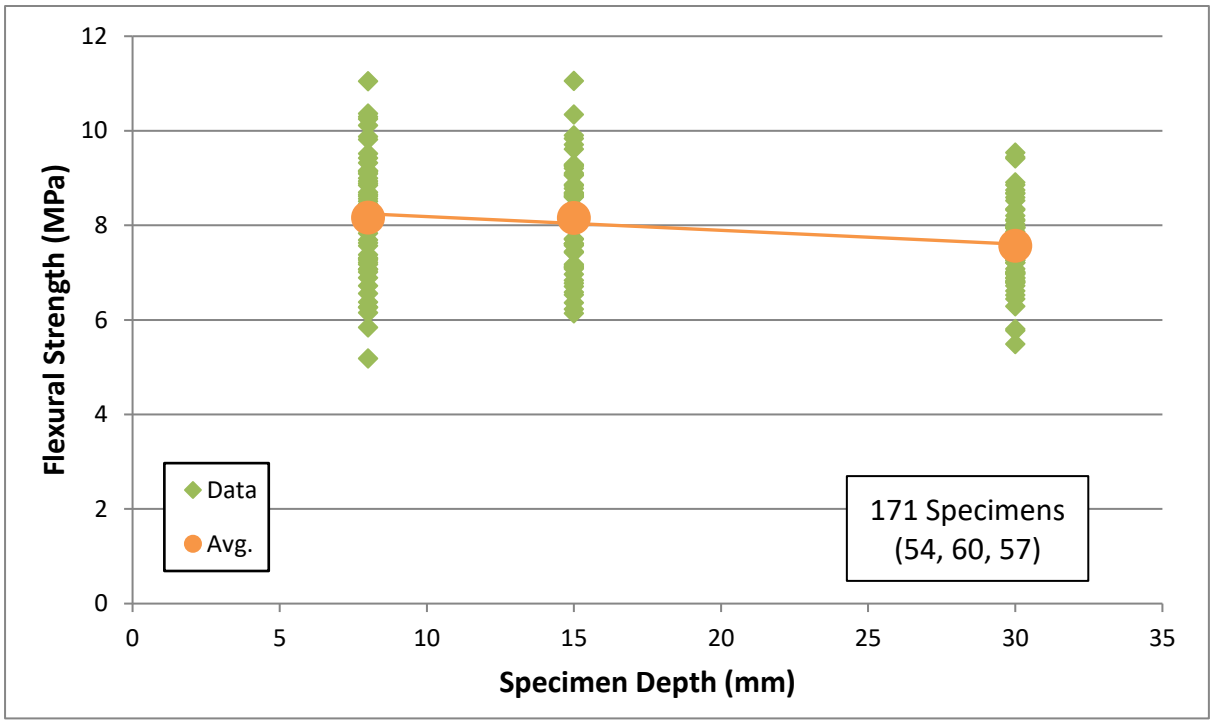

Figure 101. Flexural strength against specimen depth for 4:1 3PT testing with square cross section specimens

7.4.5 Stiffness

A value which is important in the FEA portion of this project is Young's modulus. Due to the difficulties mentioned earlier with strain gauging of high moisture concrete specimens indirect means are used instead. Equation 15, derived from beam theory, shows the expression used for calculating Young's modulus, E.

$$E = \frac{L^3 F}{4bd^3\delta} \qquad (15)$$

Here L, F, b and d are the same as in Equation 14. A lowercase delta, δ, is used to denote deflection; the units are Newtons per metre. This deflection value was taken from the linear portion of each trace. This is summarised in Figure 102. It is important to note that taking the deflection directly from the tension/compression machine to use in these calculations is only an acceptable approximation because the material in question has a low stiffness value. If the material in question were steel, for example, then the stiffness of the machine itself would need to be factored in to the approach. However, as the stiffness of the material (concrete) is low the approximation is judged to be acceptable.

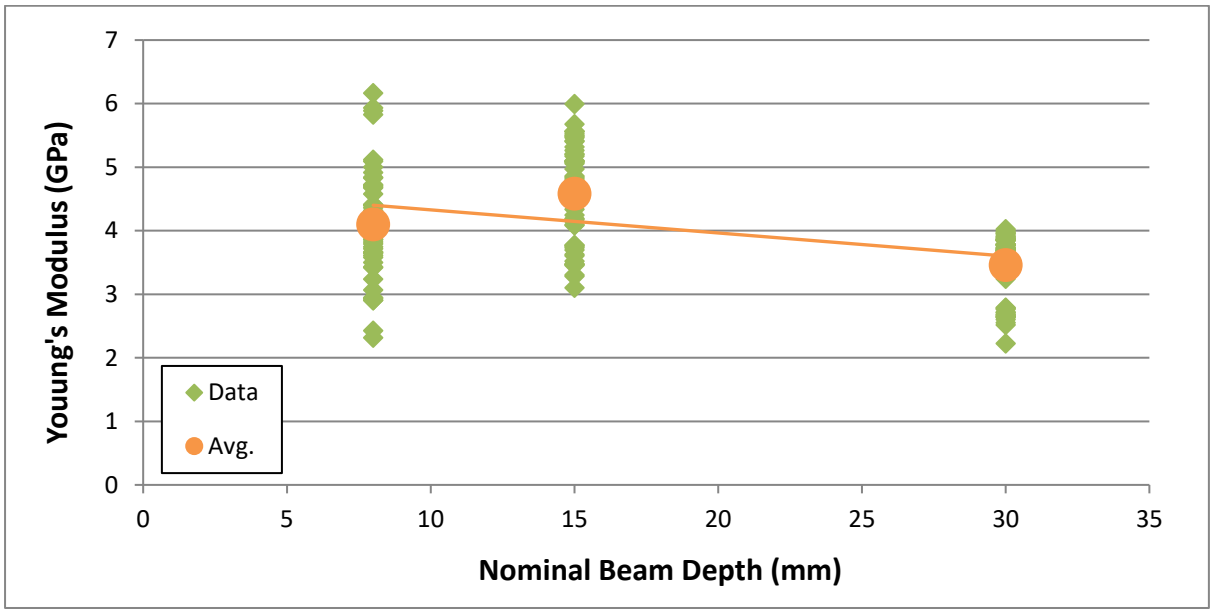

Figure 102. Young's Modulus against Beam Depth

Taken in isolation the data shows overlap between the 8mm and 15mm beam specimen stiffnesses and a considerably less stiff data set for the 30mm beam. However, it was observed that the 30mm beams experienced localised crushing at the point where they were loaded. It is thought that this is the reason for the apparent reduction in stiffness seen with the 30mm beams. This does highlight the limitations of using indirect methods for determining stiffness values. For this reason the 30mm beam data for Young's modulus has been ignored. In light of this the project will take an average value of 4.30GPa from the 8 and 15mm beams.

7.5 Fracture Toughness (SENB)

The fourth experimental campaign was to investigate the effect of scale on the fracture toughness of concrete. It is an important material property when dealing with brittle materials. This investigation benefitted from sharing the same specimen geometry and testing apparatus as the flexural study. The test being employed was single edge notched beam (SENB); here a sharp defect is introduced into the specimen so that a crack grows from a pre-existing stress concentration. The data shows a positive correlation between size and fracture toughness.

7.5.1 Fracture Toughness Theory

For the purposes of this work stress intensity factors were calculated by means of an ASTM standard (ASTM, 2002). One benefit of this standard is that it does not prescribe the specimen sizes in the same was as other standards discussed in the literature review. The formulae are reproduced here in Equation 16 and Equation 17.

$$K = \frac{YP}{BD^{0.5}} \quad (16)$$

$$Y = \frac{6\left(\frac{a}{D}\right)^{0.5}\left[1.99 - \frac{a}{D}\left(1 - \frac{a}{D}\right)\left(2.15 - \frac{3.93a}{D} + 2.7\left(\frac{a}{D}\right)^2\right)\right]}{\left(1 + \frac{2a}{D}\right)\left(1 - \frac{a}{D}\right)^{1.5}} \quad (17)$$

Where a is the initial crack length in metres, D is the specimen depth in metres, B is the specimen breadth in metres, Y is the dimensionless geometry parameter, P is the load in Newtons and K is the stress intensity factor in Pa.m^0.5.

7.5.2 Fracture Toughness Preparation

As stated, the specimens used were of the same overall geometry as the flexural test specimens, being produced in the same moulds. The difference between the specimens being the sharp notch introduced into these specimens. Cuboid specimens had a blunt notch cut on a mill with a cutting wheel attachment, the blunt notches were then sharpened with a razor blade and these were then photographed under a microscope and had the notch tip geometry recorded through the integrated computer software.

Figure 103. Mill with diamond cutting wheel, 30mm specimen and 300mm ruler

Shown in Figure 103 is the mill used for introducing the blunt notches into the specimens.
The cutting procedure went as follows:

1. The first specimen of each type would be mounted into the jaws of the vice.
2. The pre-marked midpoint of the specimen would then be positioned under the cutting disc.
3. The specimen would be brought up on the table's vertical axis until it was touching the disc.
4. The mill would be zeroed in the vertical axis.
5. The specimen would be brought forward, away from the disc.
6. The table would then be brought up to the required cut depth.
7. The cutting disc and extractor fans would now be turned on and the specimen would be run back, cutting the specimen and safely extracting the dust.

Each subsequent specimen of the same size would be cut in this way without the need for re-zeroing the mill. Each specimen was cut in this way.

Figure 104 shows a numbered batch of cuboids with the notches clearly visible, having undergone the aforementioned process.

Figure 104. A batch of 8, 15 and 30mm cuboids with notches, and 500mm of tape measure

Figure 105 shows the apparatus for sharpening each specimen; a microscope with computer imaging, a soft jawed vice, razor blades, a blade handle and an airline. Cutting paste was not required due to the softness of the material. Here each specimen was sharpened by hand and then the notch tip geometry was recorded. After other techniques for sharpening notches were attempted it was this approach that was found to be best.

Figure 105. Apparatus for sharpening notches

Figure 106 shows a typical sharpened notch that was produced by the means shown in Figure 105. All of the notches were photographed in this way and had the notch tip depth, the notch tip radius and notch tip opening angle recorded. Notches were machined and then sharpened to a= 0.42D with a standard deviation of 0.1mm (see Appendix A). In total 124 specimens were prepared in this way.

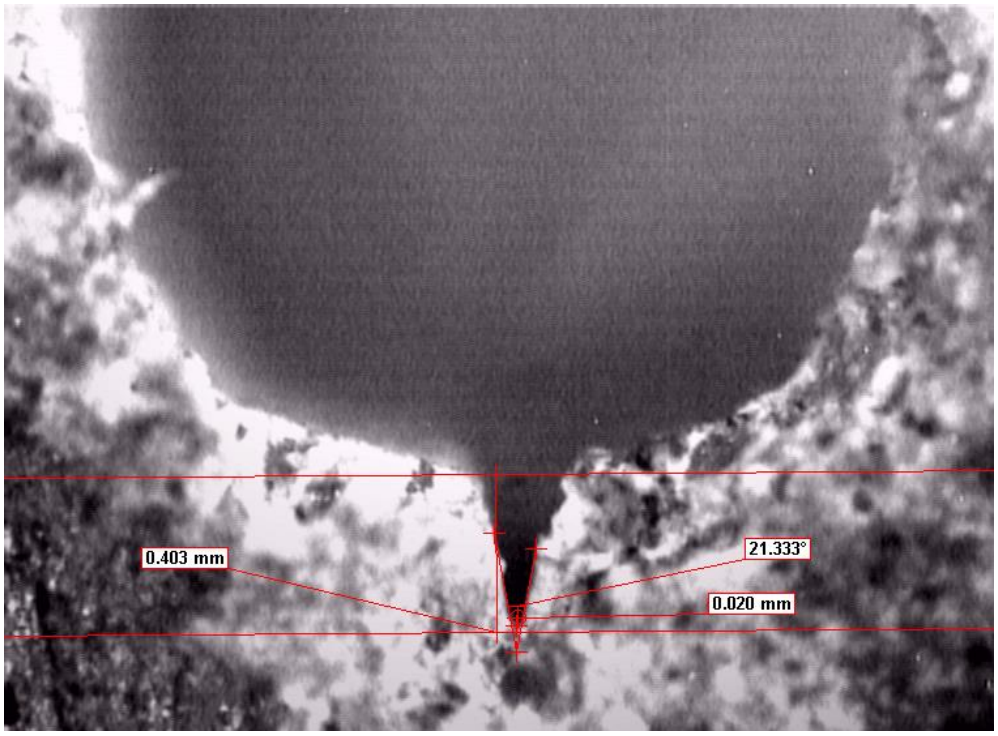

Figure 106. A sharpened notch in an SENB specimen

7.5.3 Fracture Toughness Experiments

Experiments were carried out with the same three point apparatus as the flexural testing. The loading case is shown in Figure 31. However, as discussed, the geometry of the specimens in this case has a square cross section (b=d).

A 30mm deep SENB specimen with the test apparatus is shown in Figure 107.

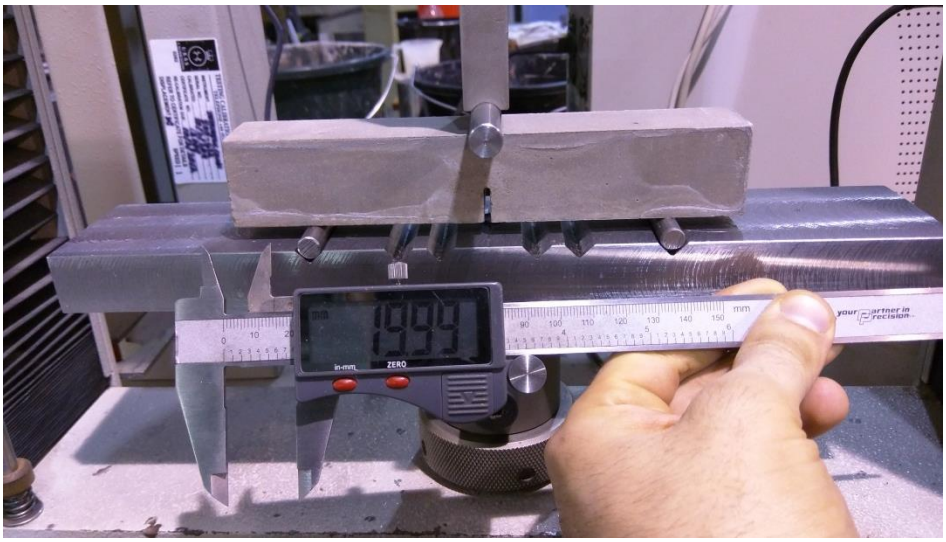

Figure 107. A 30mm SENB specimen before being tested

All specimens were tested to failure. The peak loads reached by each specimen (the point at which cracking reduced the load bearing capacity of the specimen) were then used with the equations outlined in the theory section to produce a fracture toughness value per specimen tested.

7.5.4 Fracture Toughness Data

Table 9 and Figure 109 summarise the fracture toughness values from the 124 specimens that were tested across the three specimen sizes.

Nominal Beam Depth (mm)	Avg. Fracture Toughness (Mpa.m^0.5)	St.Dev. (Mpa.m^0.5)	Proportional St.Dev. (%)	-1.5 St. Dev. (Mpa.m^0.5)	+1.5 St. Dev. (Mpa.m^0.5)
8	0.274	0.027	9.9	0.233	0.315
15	0.367	0.031	8.4	0.320	0.413
30	0.435	0.031	7.2	0.389	0.482
∞	*0.525*	*0.042*	*8*	*0.462*	*0.588*

Table 9. Summarised fracture toughness data

The scatter in the results is narrower than for three point bending. This is because there is one single, large defect that is responsible for failure rather than the random assortment of defects that exist in the concrete which will contribute to failure in plain flexural test. There is a clear size effect, with the average fracture toughness values being 0.279, 0.369 and 0.433 MPa.√m for the 8, 15 and 30mm size beams respectively. A rational function is used to fit the experimental data. This rational function is expanded upon in Figure 109, showing the way that the function converges on a fracture toughness value. Table 9 includes a line of data which is described as having an infinite beam depth, based on the fitted rational function. An average fracture toughness and standard deviation are given for the infinitely large beam based on the data set. This size effect has been observed in the literature amongst a range of geometries and materials (Akbardoost, et al., 2014).

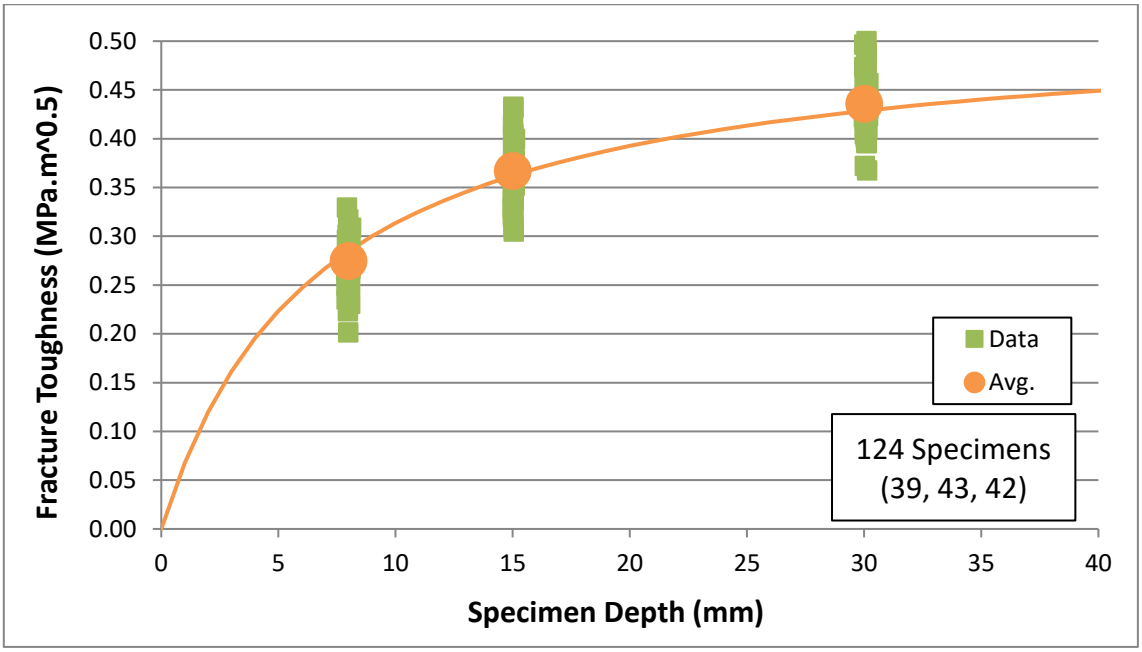

Figure 108. Fracture toughness against specimen depth for 3PT SENB specimens

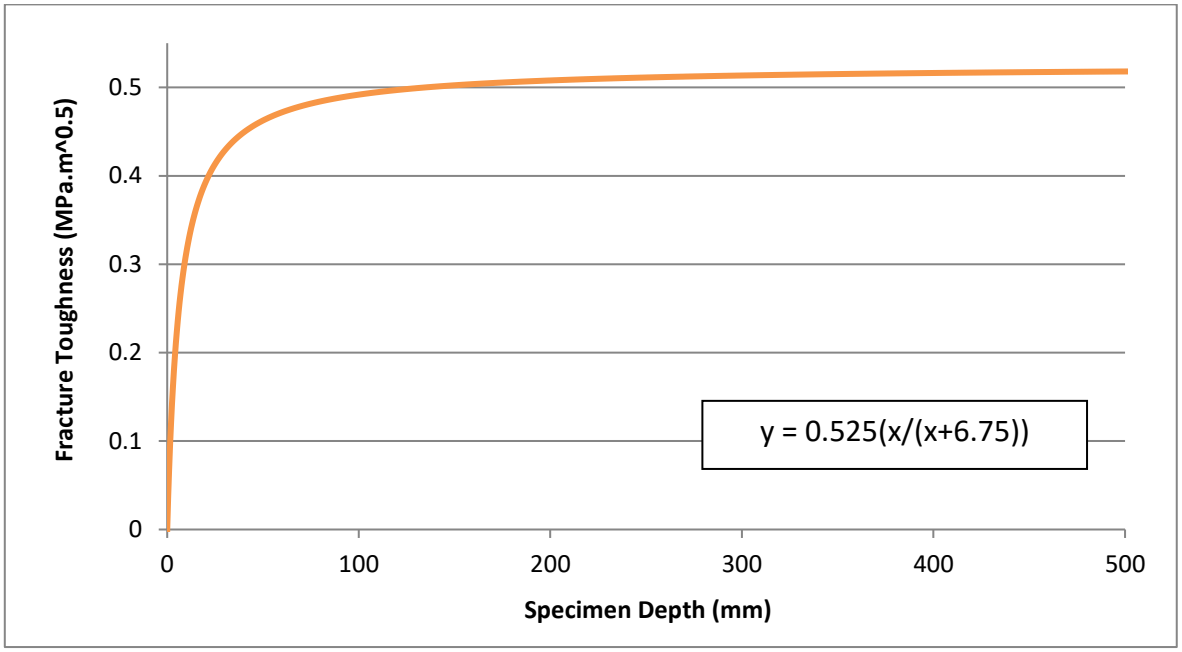

Figure 109. Fracture toughness extrapolation with rational function

7.6 Collated Data

This sub-chapter collates the average material properties at each size and normalises them by dividing each value by the peak value in that set. This is shown in Table 10 and Table 11. There are some “apples to oranges” comparisons in collating the data in this way. For example, the “characteristic size” here can mean the diameter of a cylindrical specimen or the depth of a cuboid in bending. With that in mind it is still considered a useful illustration of the divergent scaling behaviour of different stress states.

Characteristic Size (mm)	Average Splitting Strength (MPa)	Average Compressive Strength (MPa)	Average Flexural Strength (MPa)	Average Fracture Toughness (MPa.m^0.5)
(Approx.) 7	3.75		8.16	0.274
(Approx.) 15	3.78	25.20	8.16	0.367
30	2.95	24.26	7.57	0.435
42	2.73	-	-	-
64	2.75	24.57	-	-
103	2.17	-	-	-
Peak Values	3.78	25.20	8.16	0.435

Table 10. Average material properties at characteristic sizes

Characteristic Size (mm)	Normalised Splitting Strength	Normalised Compressive Strength	Normalised Flexural Strength	Normalised Fracture Toughness
(Approx.) 7	0.99	-	1.00	0.63
(Approx.) 15	1.00	1.00	1.00	0.84
30	0.78	0.96	0.93	1.00
42	0.72	-	-	-
64	0.73	0.98	-	-
103	0.57	-	-	-

Table 11. Normalised material properties at characteristic sizes

Figure 110 shows graphically the data from Table 11. This means that direct comparisons can be made between different geometries and stress states as specimen size increases.

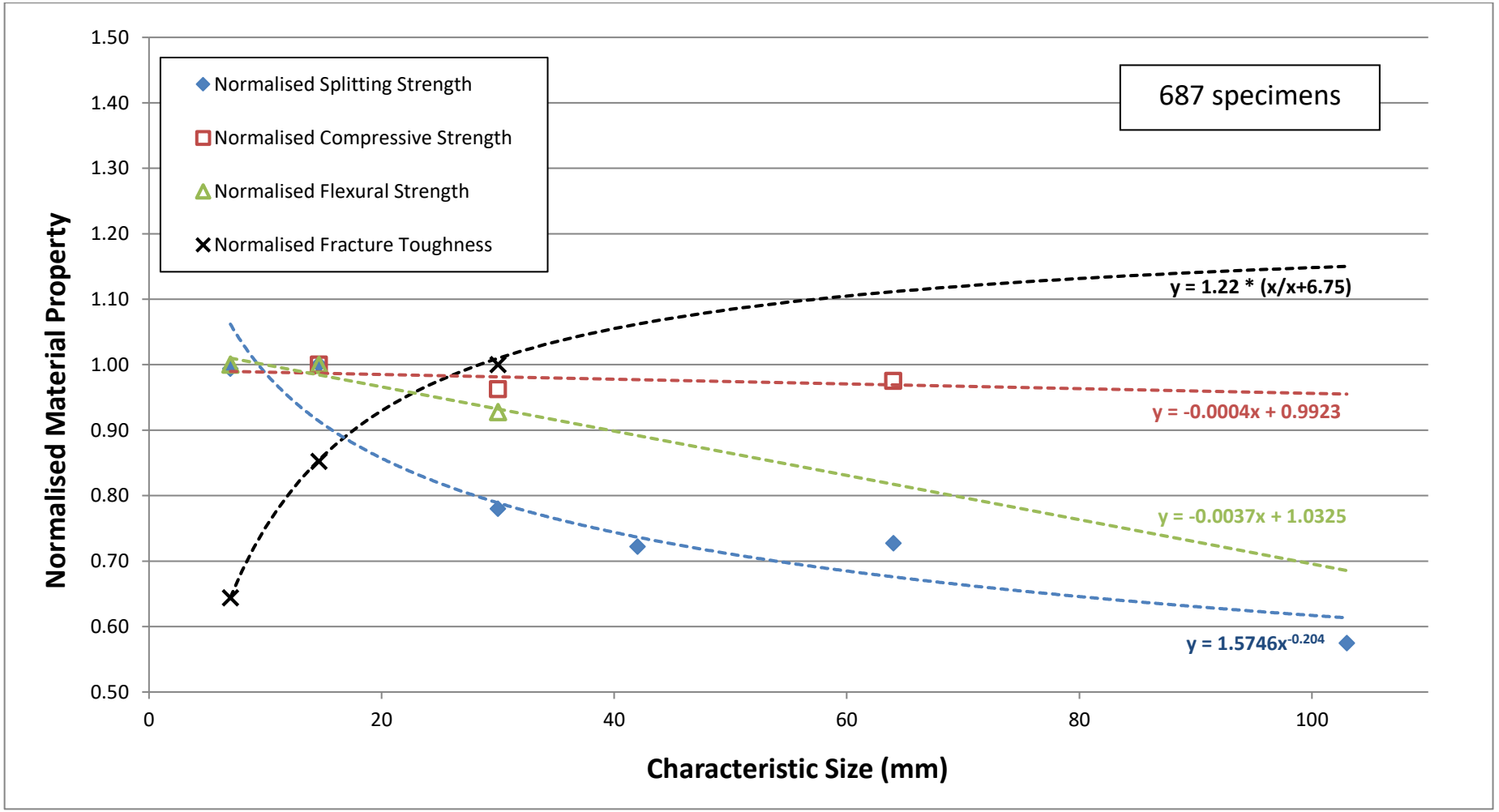

Figure 110. Collated size effect data, normalised

Compressive strength (in red) has shown effectively no size effect; any possible size effect is within experimental scatter

Flexural strength (in green) saw a 7% decrease in strength between the smallest and the largest specimen tested. However, no size effect was seen between the two smallest sizes. Further work with a larger specimen size would be necessary to see which trend continues as the amount of scatter in the data makes it difficult to come to a definitive conclusion.

Splitting strength (in blue) saw a very pronounced size effect which followed an initial constant stress criterion and then followed an inverse power law. This is similar to that shown by in the literature (Bazant, 1999). Bazant discusses a -0.5 power scaling law whereas the power law seen in this data is -0.26.

It is interesting to note the difference in response between the three point flexural strength and the splitting strength. It is possible that four point bend would have produced a size effect trend closer to the splitting strength. This is due to the larger stressed volume of the four point bend test. The increased stressed volume would increase the influence of flaws within the specimen.

Fracture toughness (in black) has been shown to increase with specimen size. A rational function was used to describe the behaviour. This behaviour is also shown in the literature (Bazant, et al., 1991).

7.6.1 Considerations

These competing physical phenomena are cause for thought when considering the design of monolithic structures with disparate stress states distributed throughout the geometry. For example, consider a hypothetical structure which has two types of features which are expected to exhibit different failure modes. This dataset would indicate that a “crack like” feature will become safer with increasing scale while a feature under a splitting load will become less safe with increasing scale. This is something that further work could investigate.

For fracture toughness in particular this is something that current standards do not reflect. For example, in BS EN ISO 23146 the recommended cross sectional dimensions for the SENB specimen are 3mm by 4mm (breadth by depth). This is approximately half the size of the smallest SENB specimen tested in this project. The standard makes no reference to specimen size influencing the outcome of the testing. The project determines this to be an oversight only made safe by the tendency for small test specimens to give an under estimate of the actual fracture toughness expected to be exhibited by a large structure.

8.0 Mixed Mode (I/II) Fracture

This chapter considers the scaling of complex stress states in contrast to the scaling of the less complex stress states in the previous chapter. The test specimen which will be the basis of this chapter is a disc with a square defect. The failure loads of the discs will be compared to FEA predictions from a mixed mode strain energy density approach. This will show the suitability of the approach for dealing with size effects in complex, mixed mode (I/II) stress states.

8.1 Specimen

This test differs from the types of tests that have been done up to this point. In earlier testing the output from the experiments can be expressed as simple material properties, such as compressive strength. In these tests it is the failure criterion that is being tested to see if a given criterion can predict failure loads from different loading angles and their corresponding mixes of Mode-I and Mode-II stress states. The test specimen is a disc with a square defect; in this testing the diagonal length of the defect, n, is 0.4 of the diameter, D, and the thickness of the disc, t, is 0.1 of the diameter.

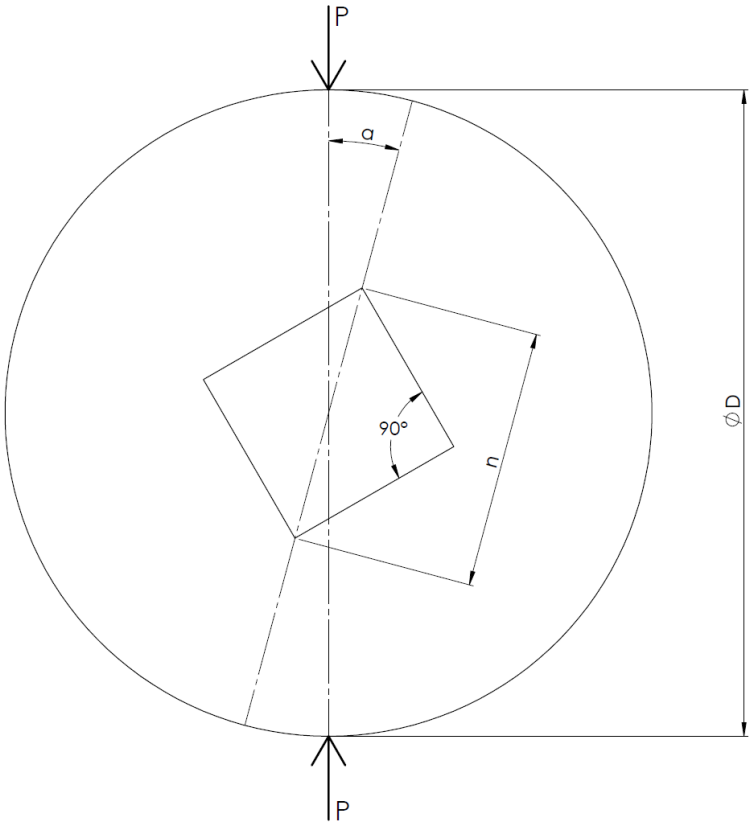

Figure 111. Specimen geometry

Here a loading angle of 0° corresponds to a dominant Mode-I (tensile) stress state. As the loading angle increases the influence of Mode-II (shear) increases and the stress state is said to be “Mixed Mode I/II”. Figure 112 and Figure 113 help to show, in general terms, the nature of the stress states that the discs undergo. At a zero degree angle the top and bottom corners are undergoing a predominantly tensile stress state while the other corners are undergoing a compressive stress state (which is inherently less critical, and therefore will not feature in detailed analysis). At non-zero loading angles the two sides of the disc can be approximated to be trying to slide past one another, this leads to shear at the top and bottom corners of the discs.

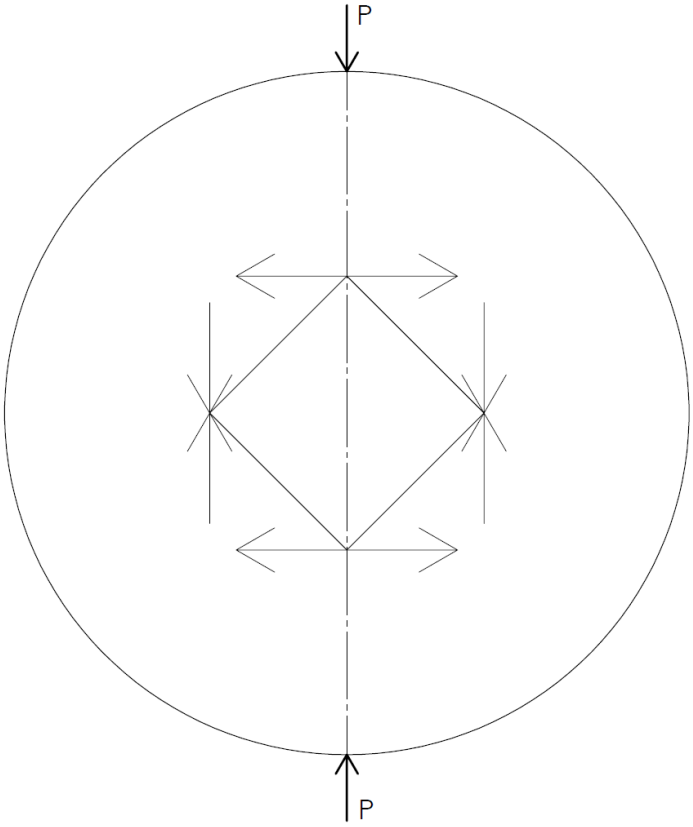

Figure 112. Tensile and compressive stress at defect corners at zero degree loading

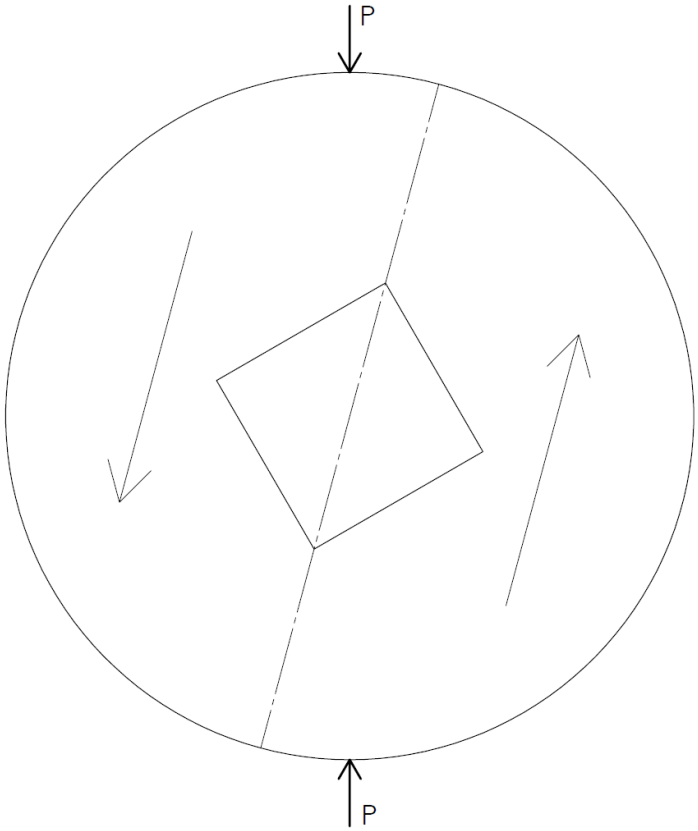

Figure 113. Simplified introduction of shear at non-zero loading angles

8.2 Modelling Background and Configuration

This subchapter expands in more detail the FEA approach outlined in Section 3.7.2 for predicting failure in brittle and quasi-brittle components with stress concentrations undergoing Mode I/II loading. The method relies on considering the average strain energy density within a control volume which is defined by the material properties.

The models in this chapter are fundamentally the same as those described in 5.0 Mixed Mode (I/II) Nodal Displacement Characterisation but with the inclusion of the control volume for the application of the failure criterion.

Figure 43 demonstrated the location of the control volume at the point of the stress concentration. In the case of the square defect disc the stress concentration is a sharp 90° re-entrant corner. Equation 9 demonstrated how to calculate the radius of the control volume. The control volume is the focus of the FEA study. As outlined in the literature (Berto & Lazzarin, 2014) the control volume is three dimensional and has a depth that is equal to this radius. The control volume radius can be considered a material constant.

Equation 10 showed the means by which the critical strain energy density, W_c, is calculated; being the integral of stress and strain and re-organised to remove the expression for strain and introduce Young's modulus instead. Equation 11 gives the critical load P_c based on the theoretical load P_{FEA} applied in the FEA study, where the critical strain energy density is W_C and the average theoretical strain energy density in the control volume at the given load is $W_{FEA\ avg}$.

The control volume had a radius and a depth equal to the expression given in Equation 9. This is shown, with a mesh, in Figure 114. The criterion predicts failure when the average strain energy density in the control volume is equal to the critical value given in Equation 10.

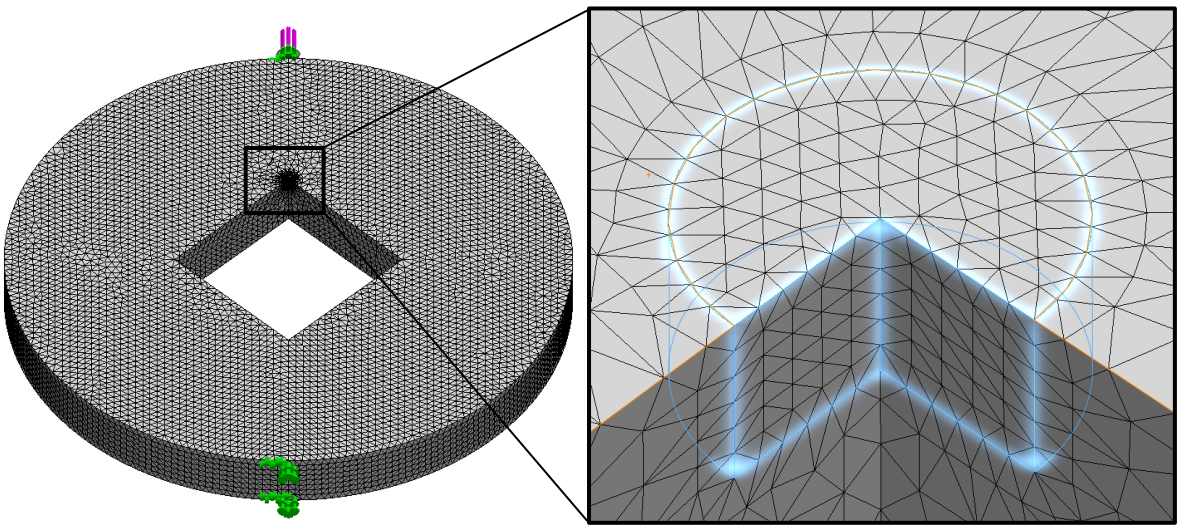

Figure 114. Control volume

Strain energy density data can be taken directly from the control volume. This function is native to Solidworks Simulation. It is detailed in Figure 115.

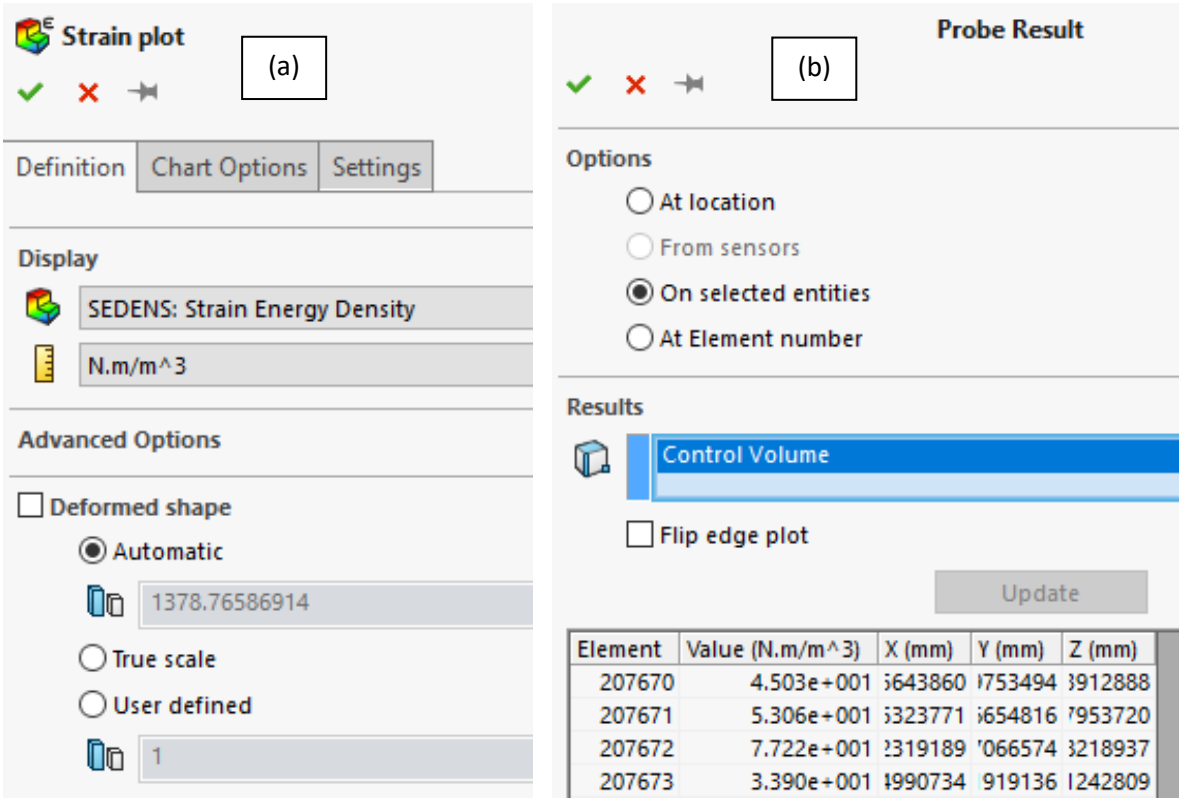

Figure 115. Solidworks FEA plot settings (a) and control volume probe (b)

8.3 Mesh Convergence

The strain energy density FEA technique which has been applied to complex stress states in the literature has shown promising insensitivity to mesh parameters (Lazzarin, et al., 2008). This subchapter investigates an arbitrary disc of 100mm diameter, 10mm thickness with a square defect with diagonal length 40mm. These ratios are used throughout. It has a strength of 8.95MPa, a stiffness of 3GPa, a fracture toughness of 0.48MPa.√m and a Poisson's ratio of 0.15. These material properties give a 1.00mm control volume radius using Equation 9. The disc was loaded at 15° with 100N load with a variety of different meshes densities. An example is shown in Figure 116.

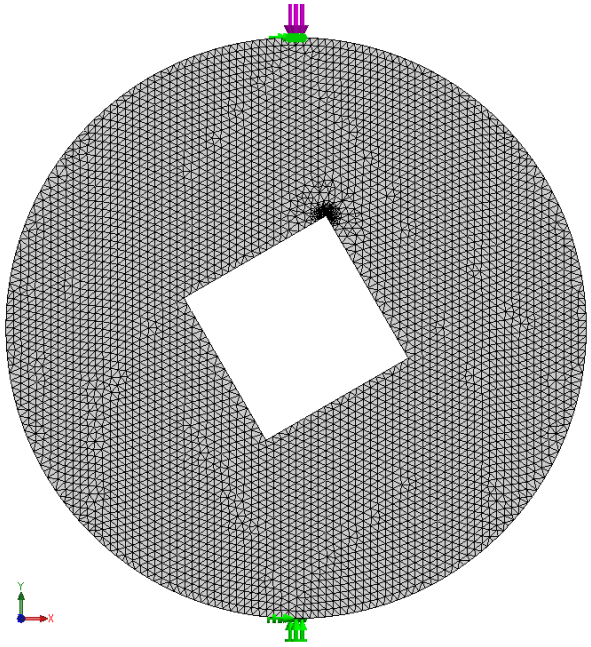

Figure 116. Disc with mesh

For simplicity the mesh was only controlled as two parameters; the control volume and the rest of the disc. The control volume had a comparatively fine mesh while the rest of the disc was coarser by a factor of ten. Two control volume meshes, the coarsest and the finest, are shown in Figure 117 to illustrate the difference in mesh refinement. The mesh convergence parameters and the predicted failure loads given by each mesh are shown in Table 12 and this is plotted in Figure 118.

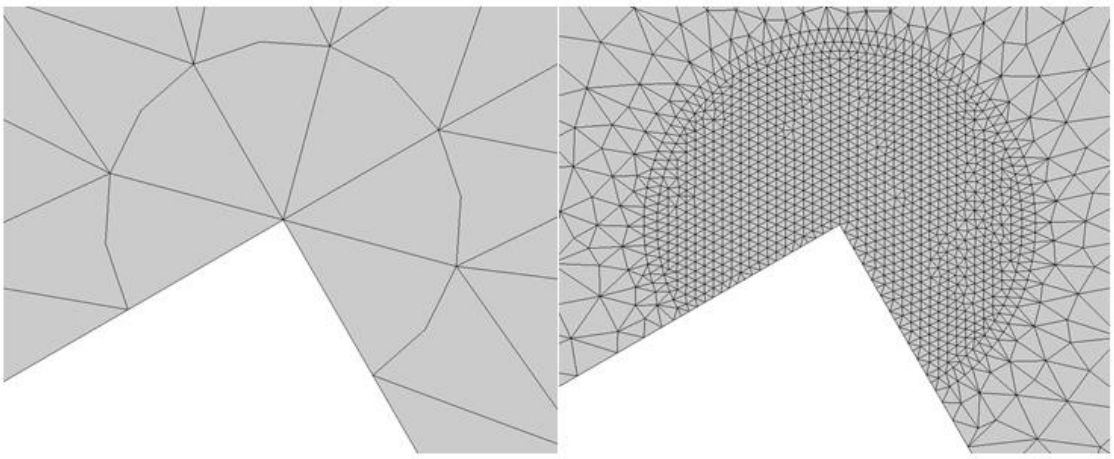

Figure 117. Mesh 1 and mesh 7 control volumes

Mesh No.	Control Volume Mesh (mm)	Global Mesh (mm)	Wth (J)	Pc (N)
1	1	10	109.6	1103.7
2	0.5	5	113.6	1084.1
3	0.33	3.33	107.8	1112.9
4	0.25	2.5	112.26	1090.5
5	0.125	1.25	114.89	1078.0
6	0.075	0.75	115.35	1075.8
7	0.05	0.5	114	1082.2

Table 12. Disc mesh convergence data

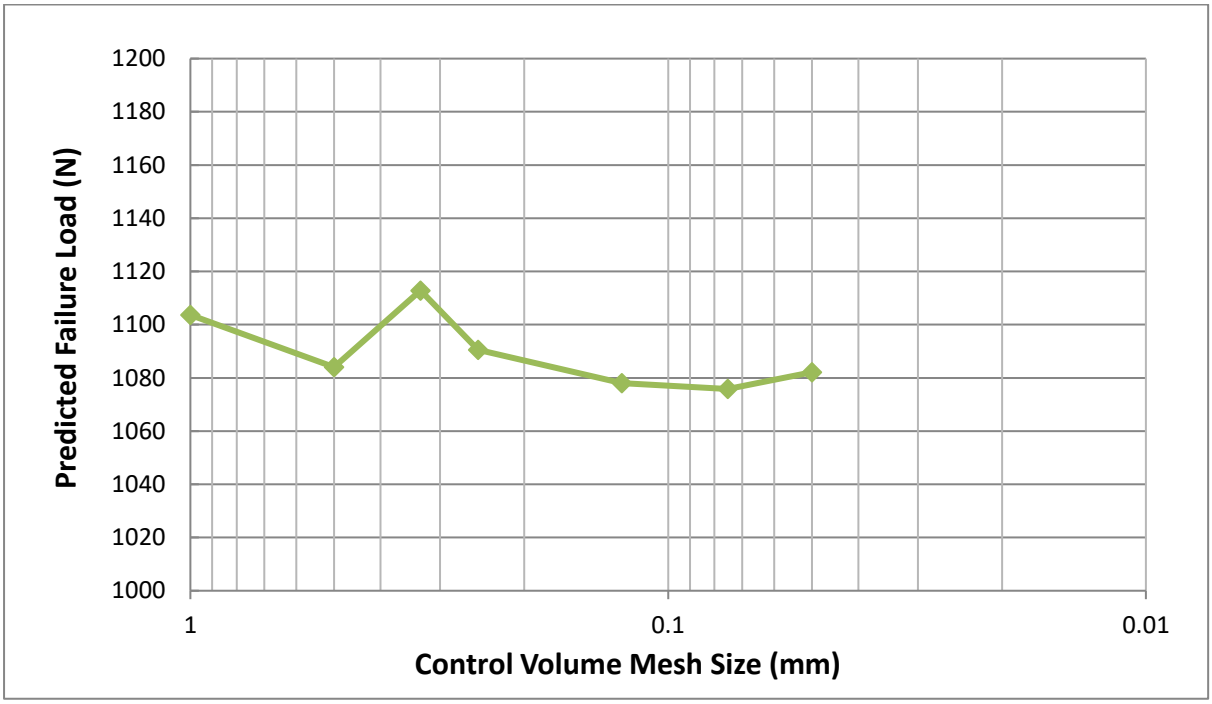

Figure 118. Mesh convergence of SED FEA study

The meshes described in Table 12 are a representative span of the investigated meshes; a coarser mesh (>1mm) would not fit within this control volume and a finer mesh (<0.05mm) proved computationally impractical to produce. All of the meshes gave failure predictions between 1115N and 1075N; the mesh can be considered for practical purposes converged by the fourth mesh at a solution of 1090.5N. At the fourth mesh size the entire FEA study took 30 seconds to run. Subsequent studies with finer meshes took considerably longer with no significant improvement.

Typically stress concentrations present a substantial challenge to FEA studies. Here no mesh is outside of ±2% of the converged solution. In accordance with the literature the control volume SED FEA approach has demonstrated mesh insensitivity.

8.4 Predictions

This subchapter will give a range of predicted failure loads for the three sizes of discs; 74, 155 and 290mm. The material properties that were used to drive the predictions are given in Table 13. An average, weak and strong set of material properties is given. The weak and strong represent ±1.5 standard deviations on the strength and fracture toughness values. Ideally this should cover approximately 86% of possible failures. However, if the average proves to be highly inaccurate then the weak and strong will not cover 86% of failures. Table 13 includes the control volume radius (and diameter), the critical strain energy density and the theoretical load that the studies were run at, in this case an arbitrary load of 100N for all studies.

	Average	Weak	Strong
Strength (MPa)	7.96	6.30	9.63
Fracture Toughness (MPa.m^0.5)	0.525	0.462	0.588
Poissons ratio	0.15	0.15	0.15
Modulus (GPa)	4.35	4.35	4.35
Rc (mm)	1.5127	1.8701	1.2965
Dc (mm)	3.0255	3.7403	2.5930
Wc (J)	7282.9	4562.1	10659.4
P_{FEA} (N)	100	100	100

Table 13. FEA input values

Figure 119 and Figure 120 show the whole 155mm disc and the stress state at the control volume, respectively.

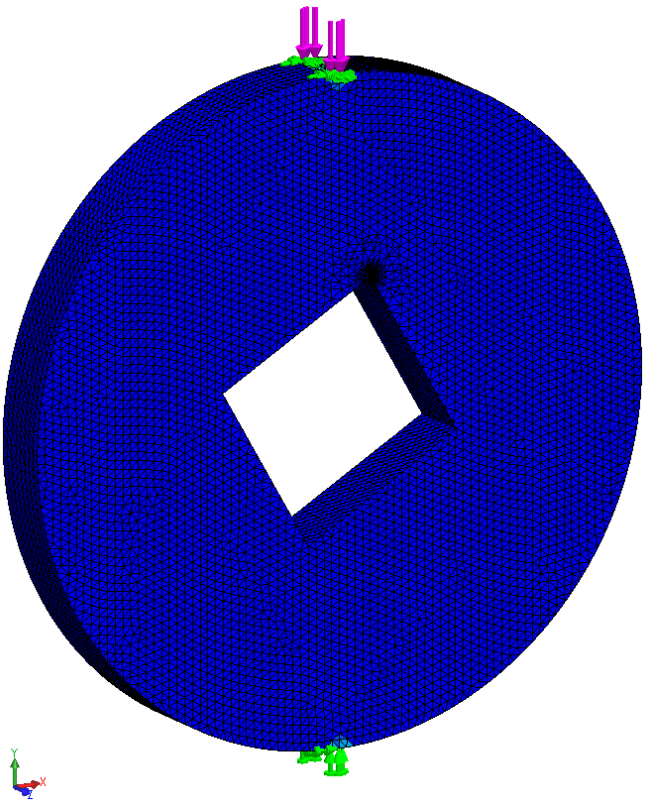

Figure 119. FEA study, whole 155mm disc view

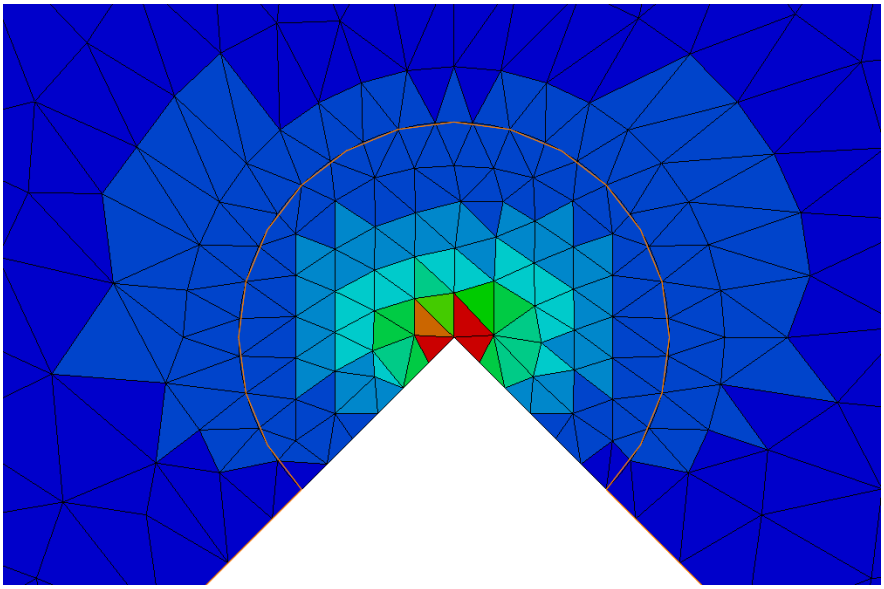

Figure 120. Stress state in control volume

Figure 121, Figure 122 and Figure 123 show the predicted failure loads for loading angles between 0 and 30°. These studies have been carried out on a constant material property basis, without accounting for size effect at the point of inputting material properties.

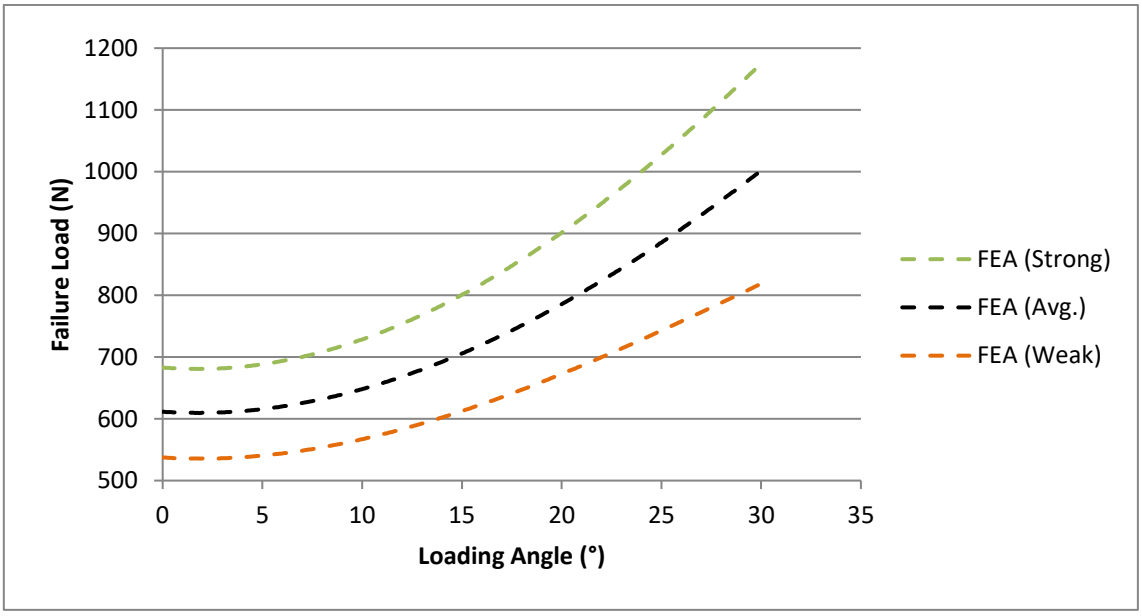

Figure 121. 74mm discs FEA predictions

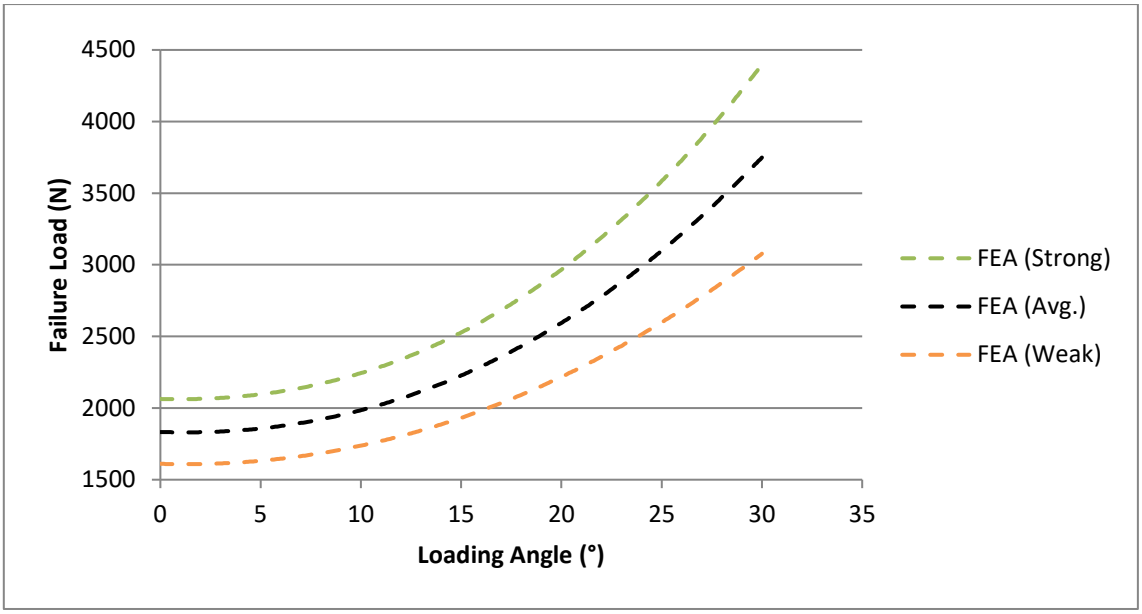

Figure 122. 155mm discs FEA predictions

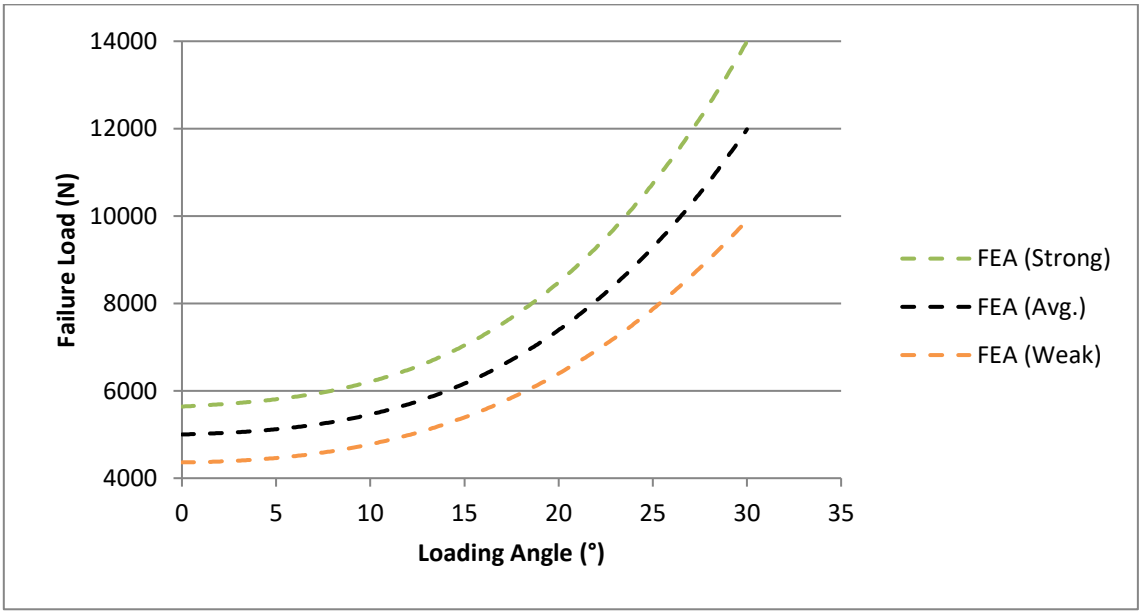

Figure 123. 290mm discs FEA predictions

8.5 Specimen Preparation

This subchapter shows the steps taken to produce the physical specimens that were tested. As previously mentioned, this work concentrates on discs which follow the ratios: diagonal length of the defect equal to 0.4 of the diameter and the thickness of the disc equal to 0.1 of the diameter. The diameters of discs that were produced were 74, 155 and 290mm.

The moulds consisted of a polymer outer wall, a polymer base attached to plywood and a square central defect. Figure 124 shows the parts which make up the outer wall of the concrete moulds. These were carefully cut from acrylic tubes on a horizontal band saw. Figure 124 also includes an image of a single, prototype 74mm disc mould.

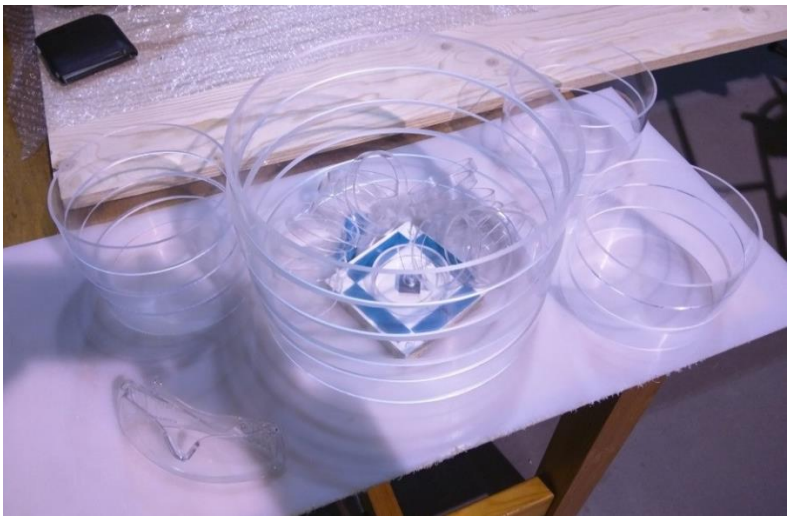

Figure 124. Mould parts made from acrylic tubes

The other parts of the moulds are shown in Figure 125; holes are being drilled before the square central defect parts are fitted. In Figure 125 the polymer base has already been attached to the plywood and the interstitial parts have been attached to the base with adhesive to provide the individual mould cells. The outline of the moulds is visible and the centre of each cell is marked using machinist's dividers to aid in drilling. After this threaded inserts were fixed in place.

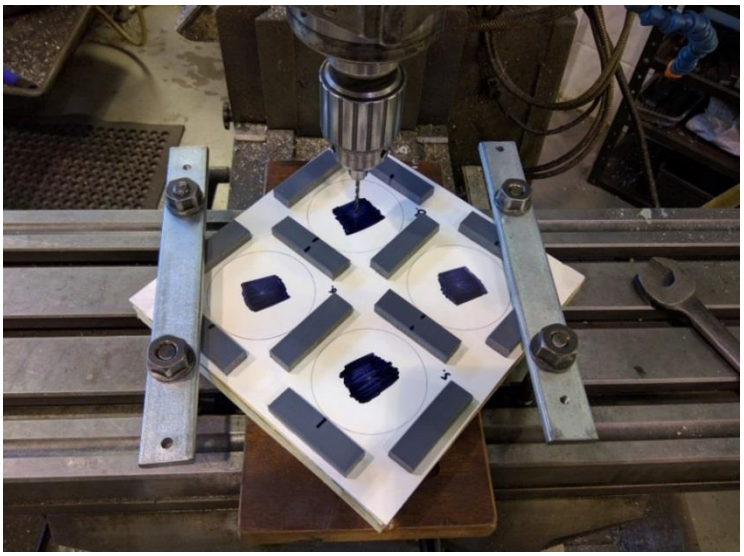

Figure 125. 74mm mould, 4 mould cells

Figure 126 and Figure 127 show completed moulds with the square defects in place (in PTFE). If PTFE is not used on the square defect pieces then it becomes highly probably that the concrete specimen will be compromised at the point of removing the square due to friction. Similar to the earlier concrete specimen production, efforts were made to seal the base of these moulds before pouring the concrete but it was found that very little leakage occurred even with no sealant used. This also made re-using the moulds easier as there was less peripheral work associated with setting them up and cleaning them after use. Concrete was poured and then the moulds covered over to ensure humidity as discussed in 7.1.3 Concrete Dehydration and Curing Procedure. Specimens were then removed from moulds after 24 hours and placed under water to cure.

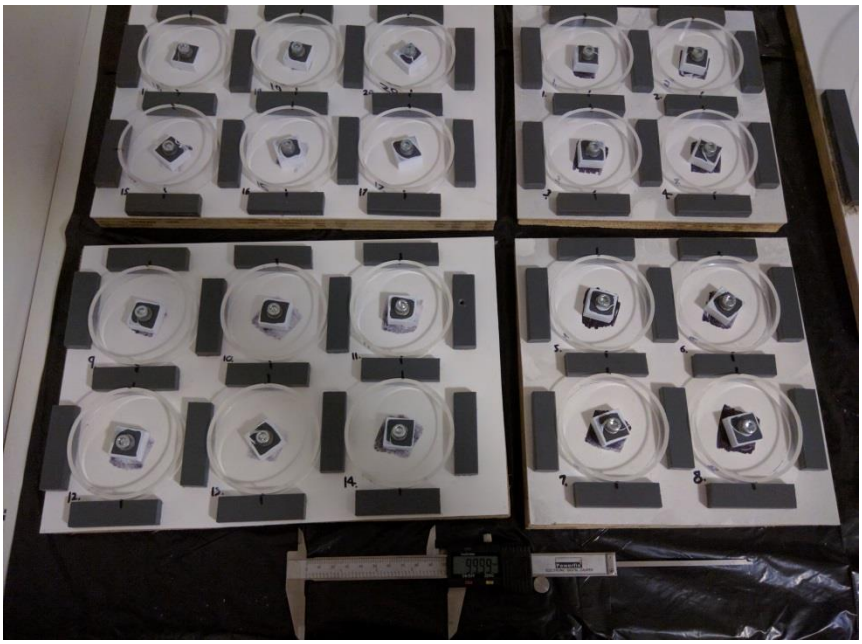

Figure 126. 74mm disc moulds, 20 cells

Figure 127. Two 290mm moulds

As with previous geometries, specimens were submerged in water until testing with the exception of time spent sanding, measuring and photographing, such as shown in Figure 128 and Figure 129. Specimens were numbered and marked with letters (a, b, c and d) at the corners of the square defects to aid in taking and recording disc measurements. The full dimensions of the disc specimens are shown in Appendix A.

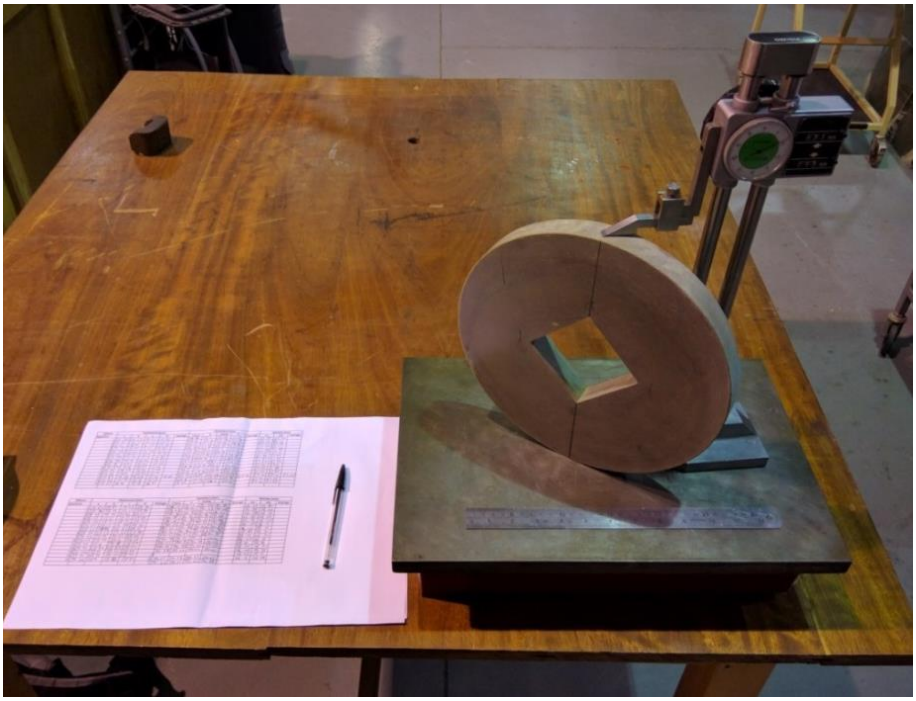

Figure 128. 290mm disc being measured

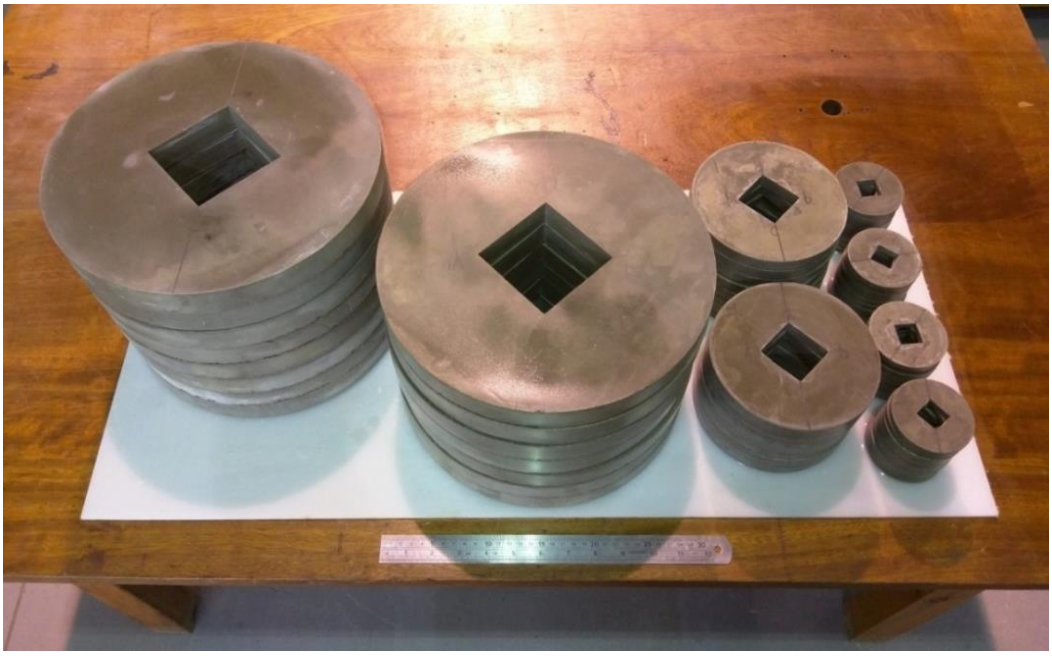

Figure 129. Square defect discs; 290, 155 and 74mm sizes

8.6 Experiments

The specimens were loaded diametrically until the onset of rapid fracture at three different loading angles. The tests were carried out with a Testometric tension-compression machine. Figure 130, Figure 131 and Figure 132 show 74, 155 and 290mm discs respectively that have been loaded to failure at a 15° loading angle.

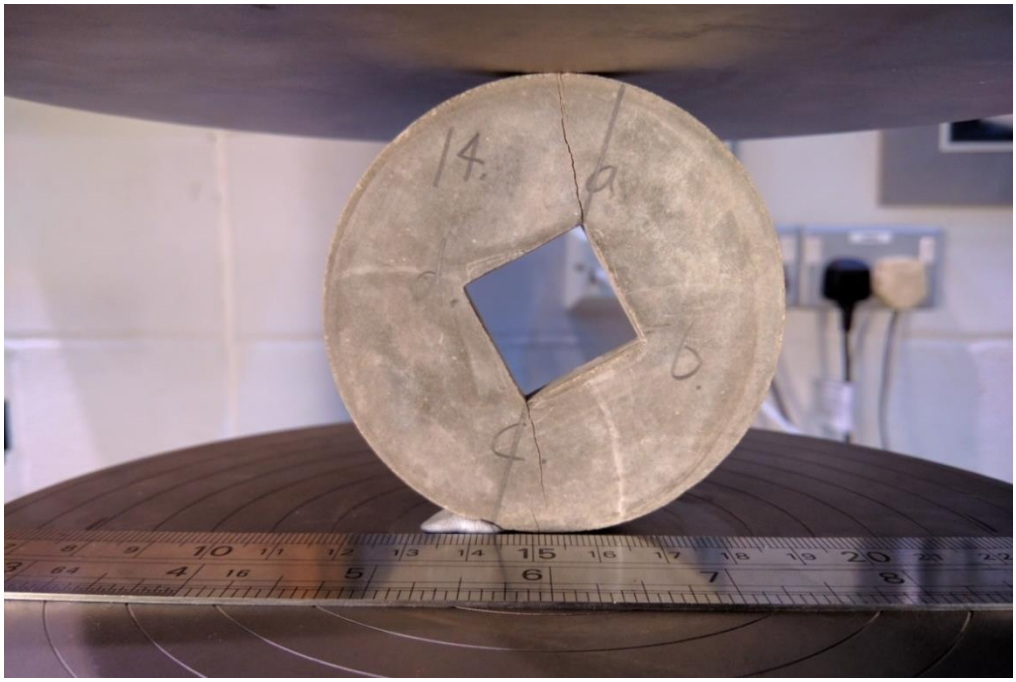

Figure 130. 74mm disc, 15° angle

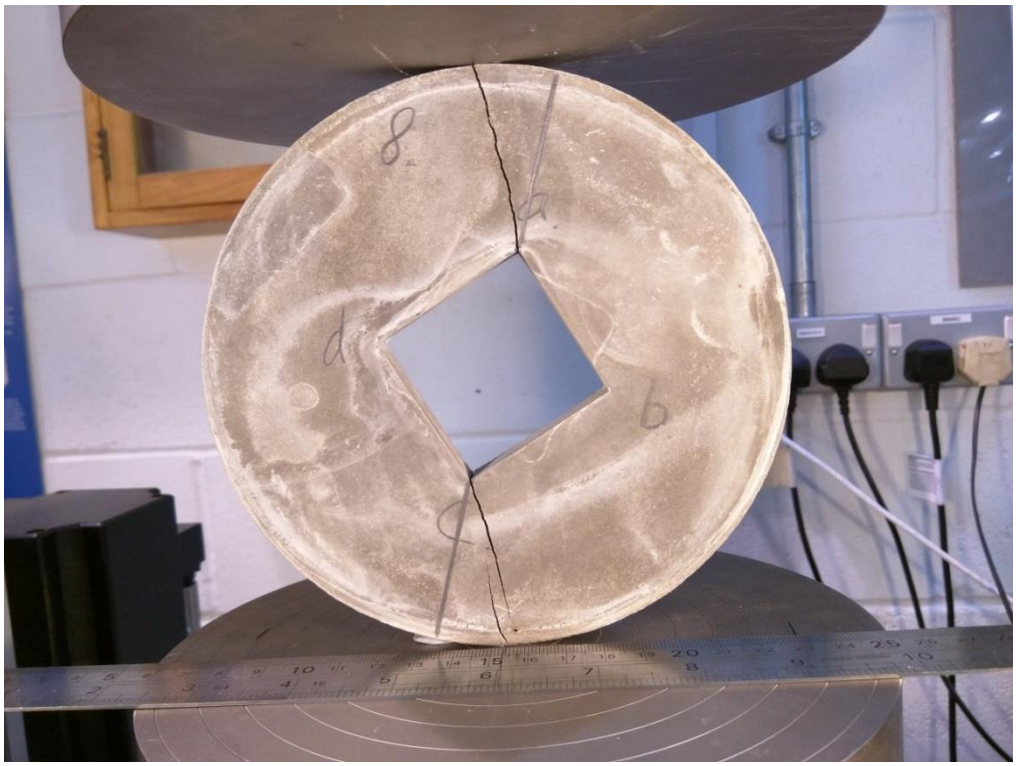

Figure 131. 155mm disc, 15° angle

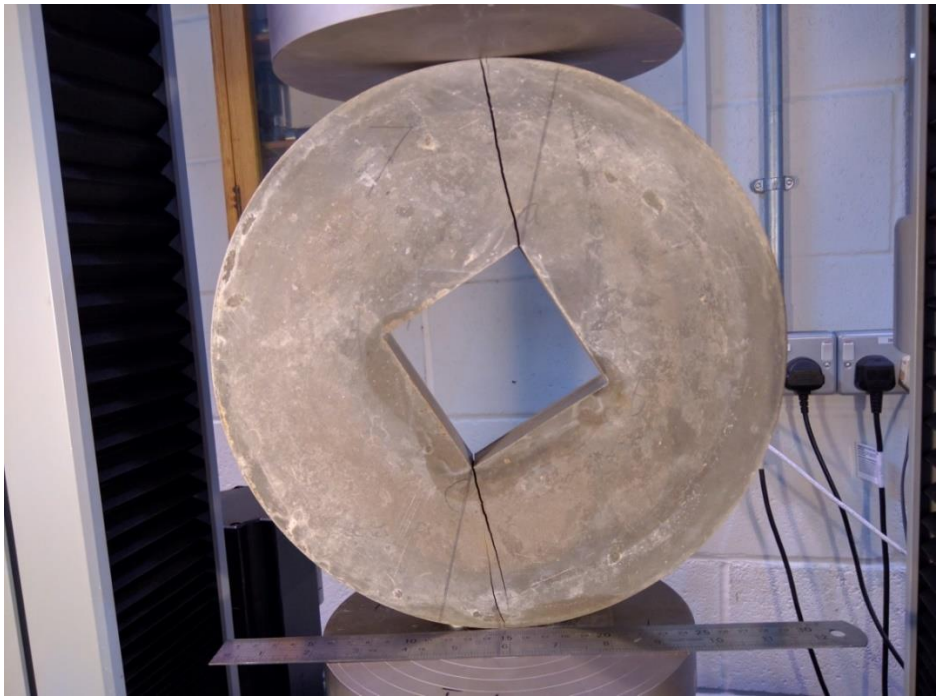

Figure 132. 290mm disc, 15° angle

The number of discs tested and at which angles is summarised in Table 14. The failure load data is summarised in Figure 133, Figure 134 and Figure 135.

	Disc Sizes (mm)		
Angle (°)	**74**	**155**	**290**
0	13	5	5
15	13	5	5
30	14	7	5

Table 14. Disc specimen testing regime

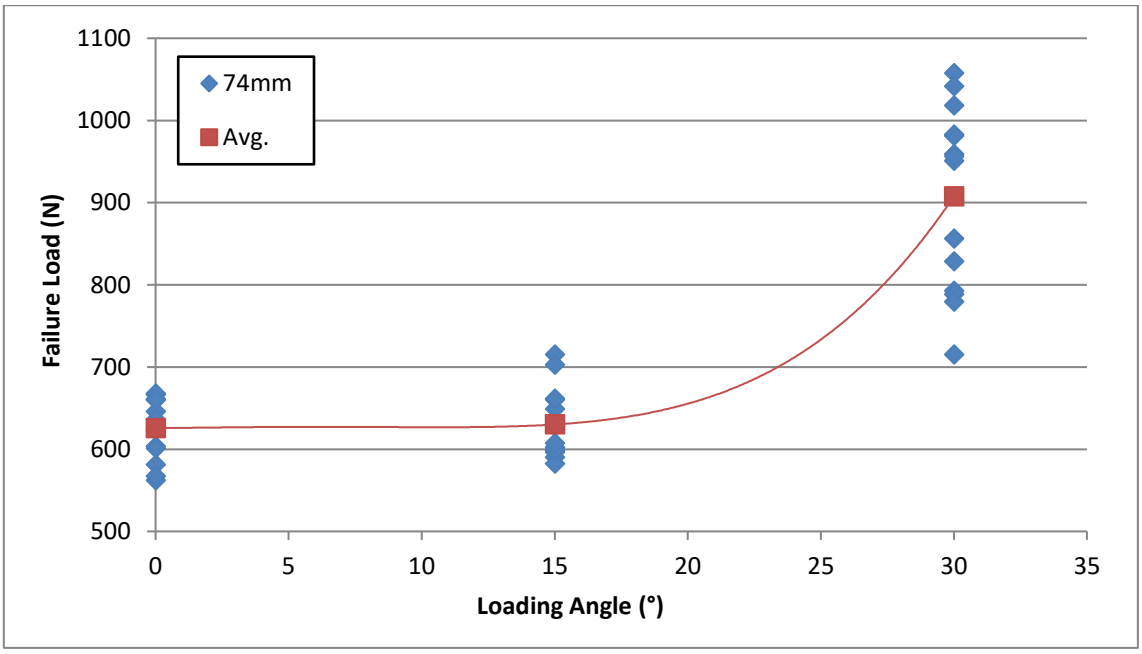

Figure 133. 74mm disc failure loads against loading angle

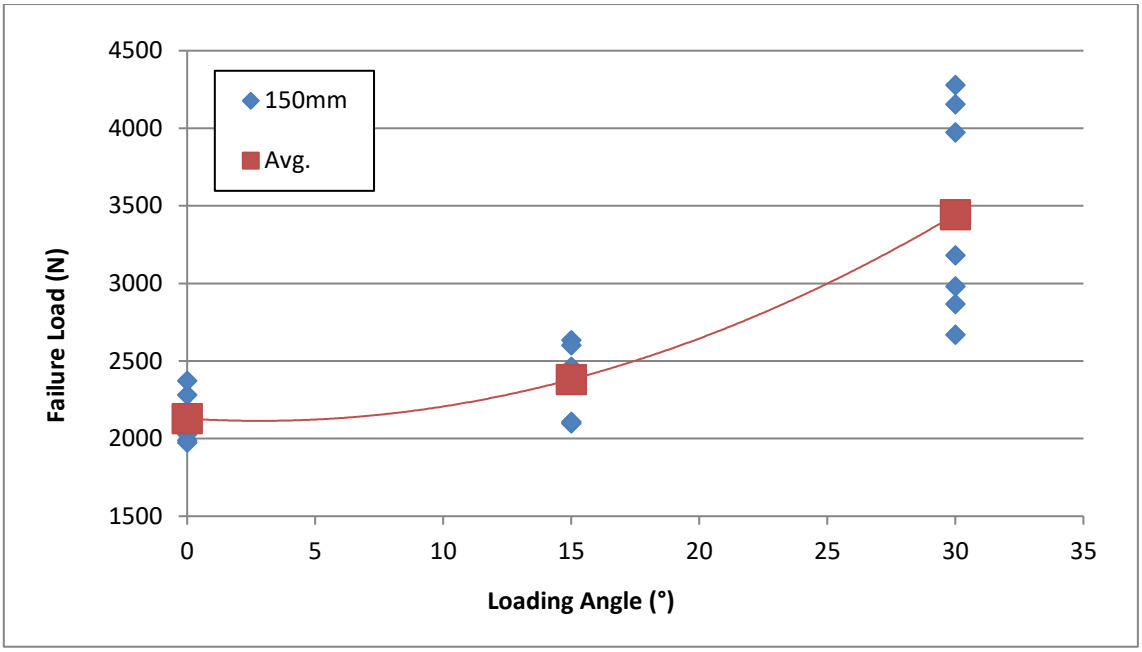

Figure 134. 155mm disc failure loads against loading angle

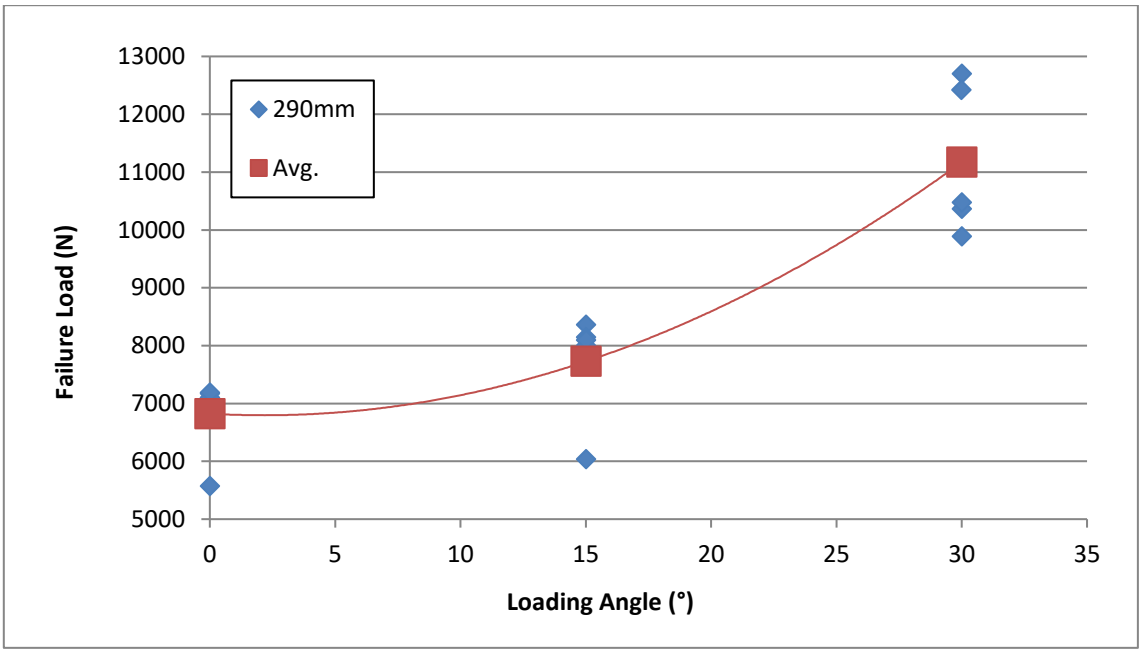

Figure 135. 290mm disc failure loads against loading angle

In accordance with the literature, failure load increases with loading angle. This is due to the mode mix of the stress state at the upper and lower corner of the defect is going from mode-I dominant stress state to a more mode-II dominant stress state. The tabulated data is in Appendix A with the disc dimensions. It is interesting to note that the 30° loading angle (Mode-II dominant) consistently gives the most scatter. It is possible that this is down to there being two, or more, distinct orientations of flaws which contributed to failure. It is possible that the 0° and 15° loading angles aren't susceptible flaws in a certain orientation while the 30° loading angle is susceptible to flaws in all orientations. This would produce distinct failure populations within the 30° dataset; e.g. more scatter than 0° and 15° loading angles.

8.7 Comparison

Figure 136, Figure 137 and Figure 138 show the predicted failure loads from the FEA in comparison to the experimental failure loads. The most striking aspect of this is that, from the perspective of the SED FEA, there is no discernible size effect at the 30° loading angle while there is a pronounced size effect at the 0° and 15° loading angles. The scaling effect seen at 0° and 15° is similar to the scaling effect seen in various geometries and materials when studying fracture toughness, as seen in the literature (Kataoka & Obara, 2015). The 74mm disc predictions have good agreement with the experimental disc failure loads across all loading angles.

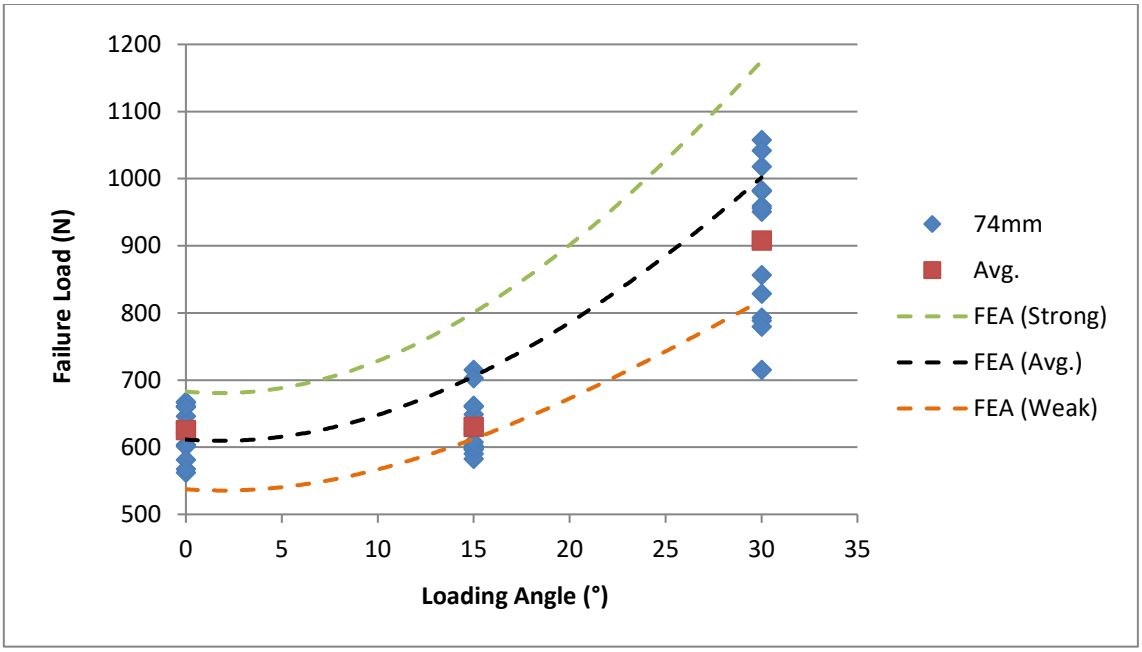

Figure 136. FEA and experimental data against loading angle for 74mm discs

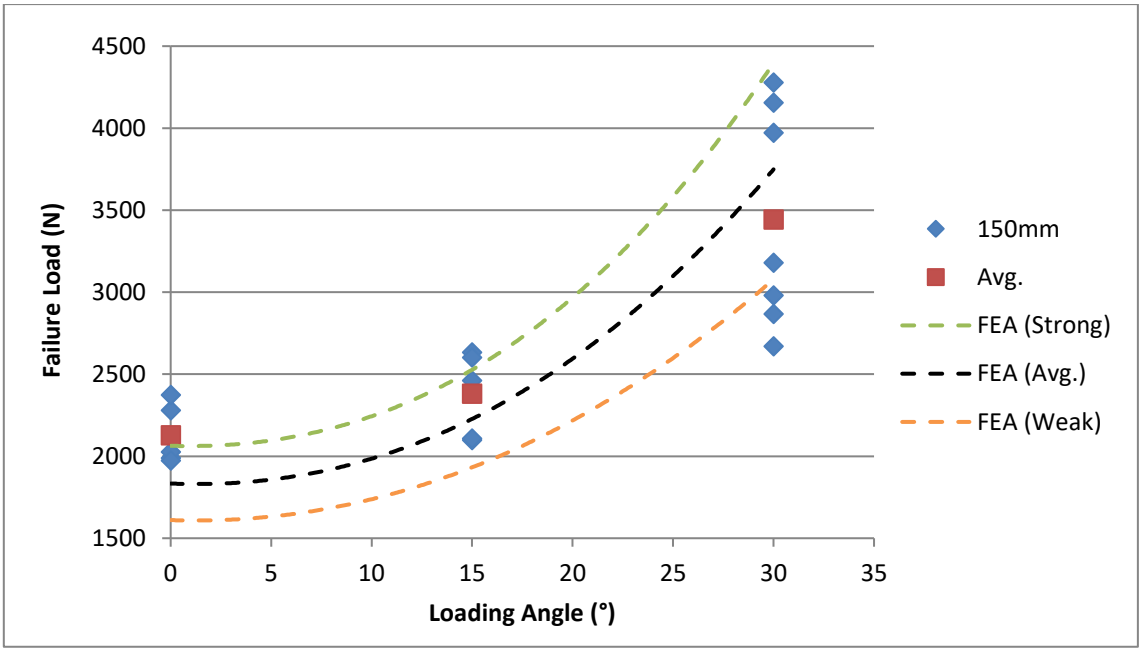

Figure 137. FEA and experimental data against loading angle for 155mm discs

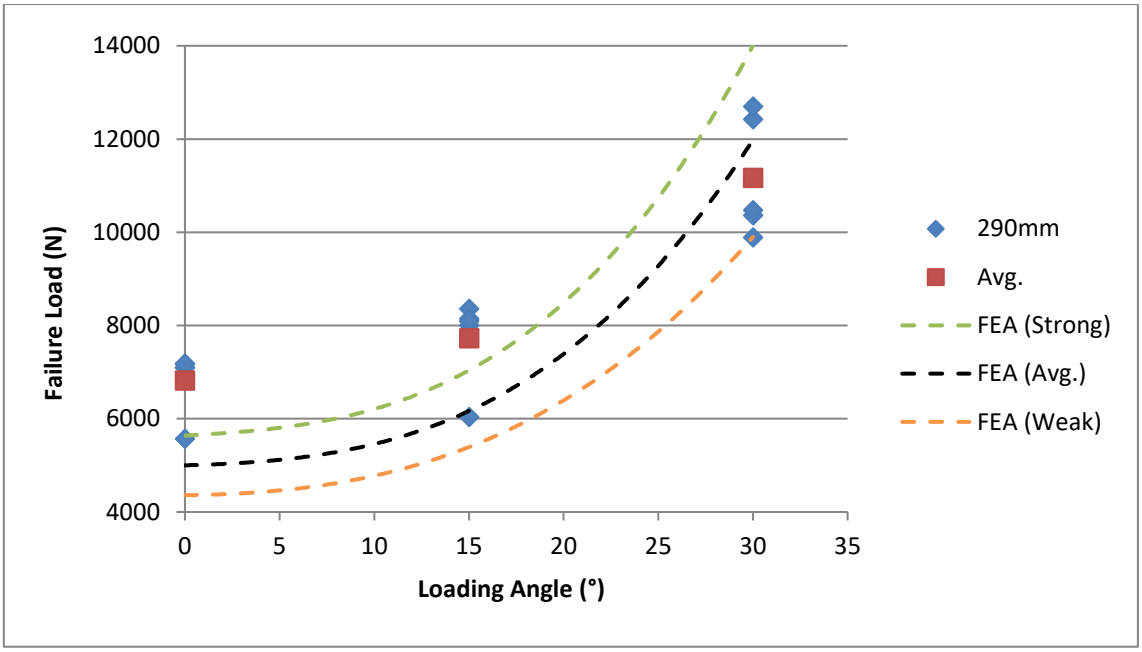

Figure 138. FEA and experimental data against loading angle for 290mm discs

The performance of the FEA is summarised in Table 15. As stated, the FEA error at the 30° loading angles remains quite constant; overestimating by between 6.8 and 9.2% across the three sizes. However, for the 0° angle the size effect is not accounted for by the FEA and the error goes from -2.6 to -36.3% when considering the 74mm and 290mm discs respectively.

	0°	15°	30°
74mm	-2.6%	10.0%	9.2%
155mm	-16.4%	-7.9%	7.9%
290mm	-36.3%	-25.4%	6.8%

Table 15. Prediction error based on average loads and average FEA

8.8 Summary

This chapter has explored theoretically and experimentally size effect in mixed mode I/II stress states. Predictions for failure loads of three sizes of square defect discs have been presented. The discs were loaded at three angles, these loading angles induced different stress states; from mode-I dominant to mode-II dominant. The predictions were made possible by a control volume driven strain energy density FEA criterion. 72 square defect discs were produced and tested. The criterion was found to have good agreement with the 74mm disc data and the 30° loading angle at all sizes. However, at the 0 and 15° loading angles (Mode-I dominant) size effect was observed in the 155 and 290mm discs that the criterion did not account for.

9.0 Discussion

The major findings of this body of work are two fold; control volume driven SED FEA is size insensitive in Mode-II dominant stress states and AGR brick re-entrant corners have a Mode-II dominant stress state after the brick has completely turned around. Secondarily, a direct nodal approach for observing mode I/II mix has been demonstrated and a substantial dataset in size effect across a range of stress states has been generated.

The main finding, the size insensitivity of the control volume approach under Mode-II, is an exciting demonstration of the potential of the approach. It is already considered a highly versatile technique, having been applied to an array of stress states and materials in the literature. It has consistently shown a mesh insensitive solution for predicting failure. This work has served to demonstrate a new facet to the versatility, size insensitivity in Mode-II dominant states. In this area the project has built on works, such as that of Ayatollahi et al (2011), where SED FEA and disc specimens were explored, by introducing the study of the effect of scale.

The context for investigation within the project has been possible application of SED FEA to AGR cores. It was demonstrated through a direct nodal analysis that late life graphite bricks experience Mode-II dominant stress states after going through a period of increasingly Mode-I dominated stress states. The nodal displacement study has been a valuable addition to the knowledge base of AGR brick ageing. Although the near parabolic turn around behaviour is well understood when considering plane laboratory specimens, the effect at the keyway roots is a comparatively new avenue of research. Emphasis is only now being placed on this area due to newly detected cracks. This work was made possible by building on the work of Tsang & Marsden (2007) and Brocklehurst & Kelly (1993).

The nodal displacement mixed mode ratio approach is an interesting development. It serves to make the study of mixed mode more accessible by means of a generalised approach, considering the Mode-I and Mode-II nodal displacements directly. The technique itself was based in large part on the FEA approaches for finding stress intensity factors described by Aliabadi & Rooke (1991). It was the work of Torabi & Taherkhani (2011) that made it possible to validate the approach, with good qualitative agreement observed.

The dataset presented on different strength parameters and fracture toughness gives a broad experimental overview of size effect in quasi-brittle materials. The work demonstrates the disparate scaling behaviours that are exhibited by different stress states. Similarities are seen when comparing with published data. For example, splitting strength scales similarly to that shown by Bazant (2005) and fracture toughness scales similarly to that shown by Kataoka & Obara (2015). Separate to giving input values and a frame of reference for further work within the project it has served to stimulate thought on complex structures.

10.0 Conclusion

This project has met its aim and fulfilled the incremental steps to reach this goal. In conclusion, this project has:

1. Demonstrated a generalised mixed mode ratio for analysing mode I/II mixes at 90° re-entrant corners. This was based on nodal displacements measured at the root of the corner. This had similarity to published work. Application of such a technique can inform an engineer as to whether or not a complex loading case is resulting in a locally mode I dominant, mode II dominant or mixed mode (I/II) stress state.
2. Applied this approach to the stress states found in AGR brick keyways. Showing that these keyways, once "turned around", go into a shear dominant stress state.
3. Shown that splitting/tensile strength correlates negatively with size through the testing of 274 cylindrical specimens across six sizes. This is in agreement with the literature.
4. Shown that fracture toughness correlates positively with increasing size through the testing of 124 cuboid specimens across three sizes. This is in agreement with the literature.
5. Investigated size effect in mode I/II re-entrant corners in brittle components by means of a control volume based SED FEA technique. The technique showed good agreement with experimental data at all sizes for the 30° loading angle (Mode-II dominant stress state).

In summation, the project has demonstrated that a control volume driven SED FEA approach has potential for predicting failure in late life AGR bricks due to insensitivity to scale in mode-II dominant stress states. Further work to expand upon this is suggested in the next chapter.

11.0 Limitations of Study

It is important to note several limitations within the research, both numerically and experimentally. Some of these limitations present avenues for further work while others are inherent to the current study of fracture.

Fundamentally all applications of LEFM approaches to quasi-brittle materials are an approximation. This work is no different in that regard. The underlying principles of LEFM were originally validated experimentally by means of research with glass fibres (Griffith, 1921). The assumptions inherent to LEFM become less valid if the material under consideration is not purely brittle.

The SED FEA applied here also approximated the corners of the square defects to being sharp. In reality they had a radii of ≈200μm. While it was impractical to run the studies as having a tangible radii due to computational restraints it should be noted that running such studies would lead to a small increase in predicted failure loads across all tests.

It is important to note that although applied in a 3D FEA environment, the underlying SED FEA solutions rely on 2D assumptions. In this case plane strain. This is inherent to the current study of mixed mode (I/II) fracture.

Experimentally the principal limitation was not producing enough 155mm and 290mm discs. This partially undermined the ability to assess the efficacy of the SED FEA approach.

12.0 Further Work

Following on from the previous section, there are several aspects of this project that present opportunities for further work.

The mixed mode ratio presented in this work represents an easily implemented, generalised approach for demonstrating a change in a stress state between mode I and mode II. It would, however, benefit from further work in three aspects; mesh convergence, singularities and quantitativity. The 3D approach was used as it gave better mesh performance than a 2D approach but it did not achieve a complete convergence. Further research in this area could yield a substantial improvement in versatility and repeatability of the process. Also, the range of mode mixes seen in the disc specimen geometry and the AGR keyways were not entirely congruent. Work needs to be undertaken to improve the ability of the approach to track mode mixes in a physically meaningful, quantitative and repeatable way, avoiding singularities of either Mode-I or Mode-II.

Reducing reliance on published strain data to power the AGR brick model would represent an improvement. Reproducing the work of existing researchers directly in ABAQUS would provide a better indication of the evolution of the mode mixes seen at the brick keyways.

A substantial step forward would be to test the criterion in an FEA package where an accurate code is in place to properly describe the strain energy accumulated in a given element of AGR graphite which is undergoing radiation induced strain. Comparing predictions with EDF's safety cases for the expected lifetime of the AGRs would be an interesting test. Also, an experimental campaign looking at creep in mixed-mode quasi-brittle specimens could offer a simple validation for the criterion's ability to model in a non-linear strain energy stress state.

A comparatively ordinary line of testing that this project was unable to explore is direct shear testing of quasi-brittle materials. It is an area which is under explored in the literature and the dataset presented here would benefit from the addition of direct shear testing at a range of specimen sizes.

A simple branch of further experimental would be investigating disc specimens at various other thicknesses. One such option to expand upon the work presented here would be to take the 155mm diameter discs (already tested at approximately 15mm thick) and test them at 7mm and 30mm thicknesses at the three loading angles experimented with here. There is little testing as exhaustive as this in the literature. It would be valuable to see how the control volume FEA copes with the geometries.

Beyond this, testing discs of IM1-24 graphite would be a natural progression. There have been graphite discs successfully modelled in the literature so there is good reason to think that an IM1-24 disc would also have good agreement with the aforementioned modelling technique. A more difficult prospect would be to test irradiated graphite specimens. Preferably specimens irradiated in a high temperature, high CO_2, high gamma ray flux environment to reproduce the type of graphite decay that is typical to the inside of an AGR core. This would offer valuable insight to the ability of the control volume SED FEA criterion to adequately predict AGR brick failures.

References

Akbardoost, J. et al., 2014. Size-dependent fracture behavior of Guiting limestone under mixed mode loading. *International Journal of Rock Mechanics & Mining Sciences,* 71(1), pp. 369-380.

Aliabadi, M. H. & Rooke, D. P., 1991. *Numerical Fracture Mechanics.* s.l.:Kluwer.

Allos, A. E. & Martin, L. H., 1981. Factors Affecting Poisson's Ratio for Concrete. *Building and Environment,* 16(1), pp. 1-9.

ASTM, 2000. *C1231 Standard Practice for Use of Unbonded Caps in Determination of Compressive Strength of Hardened Concrete Cylinders.* West Conshohocken: ASTM.

ASTM, 2001. *E1820 Standard Test Method for Measurement of Fracture Toughness.* West Conshohocken, PA: ASTM.

ASTM, 2002. *E1290 Standard Test Method for Crack-Tip Opening Displacement (CTOD) Fracture Toughness Measurement.* West Conshohocken: ASTM.

ASTM, 2009. *E399 Standard Test Method for Linear-Elastic Plane-Strain Fracture Toughness KIC of Metallic Materials.* West Conshohocken, PA: ASTM.

ASTM, 2014. *STP 1578. Graphite Testing for Nuclear Applications: The Significance of Test Specimen Volume and Geometry and the Statistical Significance of Test Specimen Population.* West Conshohocken, PA: ASTM.

Ayatollahi, M. R. & Akbardoost, J., 2012. Size effects on fracture toughness of quasi-brittle materials - A new approach. *Engineering Fracture Mechanics,* 92(1), pp. 89-100.

Ayatollahi, M. R., Berto, F. & Lazzarin, P., 2011. Mixed mode brittle fracture of sharp and blunt V-notches in polycrystalline graphite. *Carbon,* 49(1), pp. 2465-2474.

Bazant, Z. P., 1999. Size effect on structural strength: a review. *Archive of Applied Mechanics,* 69(1), pp. 703-725.

Bazant, Z. P., 2005. *Scaling of structural strength.* 2 ed. Oxford: Butterworth-Heinemann.

Bazant, Z. P., Gettu, R. & Kazemi, M. T., 1991. Identification of Nonlinear Fracture Properties From Size Effect Tests and Structural Analysis Based on Geometry-dependent R-curves. *International Journal of Rock Mechanics and Mining Sciences & Geomechanics Abstracts,* 28(1), pp. 43-51.

Bazant, Z. P. & Planas, J., 1998. *Fracture and size effect in concrete and other quasibrittle materials.* Boca Raton: CRC Press.

Bazant, Z. P. & Yavari, A., 2005. Is The Cause of Size Effect on Structural Strength Fractal or Energetic-Statistical?. *Engineering Fracture Mechanics,* 72(1), pp. 1-31.

Berenbaum, R. & Brodie, I., 1959. Measurement of the Tensile Strength of Brittle Materials. *British Journal of Applied Physics,* 10(1), pp. 281-287.

Berto, F. & Lazzarin, P., 2014. Recent developments in brittle and quasi-brittle failure assessment of engineering materials by means of local approaches. *Materials Science and Engineering R,* 75(1), pp. 1-48.

Berto, F., Lazzarin, P. & Ayatollahi, M. R., 2012b. Brittle Fracture of Sharp and Blunt V-notches in Isostatic Graphite Under Torsion Loading. *Carbon,* 50(1), pp. 1942-1952.

Berto, F., Lazzarin, P. & Ayatollahi, M. R., 2013. Brittle fracture of sharp and blunt V-notches in isostatic graphite under pure compression loading. *Carbon,* 63(1), pp. 101-116.

Berto, F., Lazzarin, P. & Marangon, C., 2012a. Brittle fracture of U-notched graphite plates under mixed mode loading. *Materials and Design,* 41(1), pp. 421-432.

British Standards Institution, 2003. *DD CEN/TS 14425-1 Advanced Technical Ceramics - Test Methods for Determination of Fracture Toughness of Monolithic Ceramics.* London: BSI Group.

British Standards Institution, 2005. *Fine Ceramics - Test Method for Fracture Toughness of Monolithic Ceramics at Room Temperature by Single Edge Precracked Beam (SEPB) Method.* London: BSI Group.

British Standards Institution, 2009a. *BS EN 12390-2 Testing hardened concrete. Part 2: Making and curing specimens for strength tests.* London: BSI Group.

British Standards Institution, 2009b. *BS EN 12390-3 Testing hardened concrete. Part 3: Compressive strength of test specimens.* London: BSI Group.

British Standards Institution, 2009c. *BS EN 12390-5 Testing Hardened Concrete. Part 5: Flexural Strength of Test Specimens.* London: BSI Group.

British Standards Institution, 2009d. *BS EN 12390-6 Testing hardened concrete. Part 6: Tensile splitting strength of test specimens.* London: BSI Group.

British Standards Institution, 2010. *BS EN 14425-3 Advanced Technical Ceramics - Test Methods for Determination of Fracture Toughness of Monolithic Ceramics. Part 3: Chevron Notched Beam (CNB) Method.* London: BSI Group.

British Standards Institution, 2012. *BS EN 12390-1 Testing hardened concrete. Part 1: Shape, dimensions and other requirements for specimens and moulds.* London: BSI Group.

British Standards Institution, 2016. *BS EN ISO 23146 Test methods for fracture toughness of monolithic ceramics.* London: BSI Group.

Brocklehurst, J. E., 1977. Fracture in polycrystalline graphite. *Chemistry and physics of carbon,* 13(1), pp. 145-279.

Brocklehurst, J. E. & Kelly, B. T., 1993. Analysis of the Dimensional Changes and Strutural Changes in Polycrystalline Graphite Under Fast Neutron Irradiation. *Carbon,* 31(1), pp. 155-178.

Chi, S., 2013. Specimen size effects on the compressive strength and Weibull modulus of nuclear graphite of different coke particle size: IG-110 and NBG-18. *Journal of Nuclear Materials,* 436(1), pp. 185-190.

Davidson, H. W. & Losty, H. H. W., 1958. Plasticity of Graphite. *Nature,* Volume 181, pp. 1057-1059.

Davies, M. W., 1996. *Graphite Core Design in UK Reactors (IAEA-TECDOC--901),* Vienna, Austria: IAEA.

Dugdale, D. S., 1960. Yielding of Steel Sheets Containing Slits. *Journal of the Mechanics and Physics of Solids,* 8(1), pp. 100-104.

Eason, E. D., Hall, G. & Marsden, B. J., 2007. Development of a Model of Dimensional Change in AGR Graphites Irradiated in Inert Environments. In: G. B. Neighbour, ed. *Management of Ageing Processes in Graphite Reactor Cores.* Cambridge: RSC Publishing, pp. 43-50.

Erdogan, F. & Sih, G. C., 1963. On the Crack Extension in Plates Under Plane Loading and Transverse Shear. *Journal of Basic Engineering,* 85(4), pp. 519-525.

Glasstone, S. & Sesonske, A., 2004. *Nuclear Reactor Engineering. Reactor Design Basics (Vol. 1).* 4th ed. Delhi: CBS Publishers.

Globmarble, 2014. *youtube.* [Online]
Available at: https://www.youtube.com/watch?v=9ySyaKb2_b0
[Accessed 19 11 2017].

Goeddel, W. V. & Siltanen, J. N., 1967. Materials for High Temperature Nuclear Reactors. *Annual Review of Nuclear Science,* 17(1), pp. 189-252.

Gomez, F. J., Elices, M., Berto, F. & Lazzarin, P., 2007. Local strain energy to assess the static failure of U-notches in plates under mixed mode loading. *International Journal of Fracture,* 145(1), pp. 29-45.

Griffith, A. A., 1921. The Phenomena of Rupture and Flow in Solids. *Philosophical Transation of the Royal Society of London,* 221(1), pp. 163-198.

Heys, G. B., 2007. UK Regulatory Strategy for Management of Graphite Aging in Gas-Cooled, Graphite Moderated Reactors. In: G. B. Neighbour, ed. *Management of Ageing Processes in Graphite Reactor Cores.* Cambridge: RSC Publishing, pp. 25-32.

Hull, D. & Bacon, D. J., 2011. *Introduction to Dislocations.* 5th ed. Oxford: Butterworth-Heinemann.

IAEA, 2000. *Irradiation Damage in Graphite due to Fast Neutrons in Fission and Fusion Systems, TECDOC-1154,* Vienna: IAEA.

Irwin, G. R., 1948. Fracture Dynamics. In: *Fracturing of Metals.* Cleveland: American Society for Metals, pp. 147-166.

Irwin, G. R., 1957. Analysis of stresses and strains near the end of a crack traversing a plate. *Journal of Applied Mechanics,* 24(1), pp. 361-364.

Irwin, G. R., 1958. Fracture. In: *Elasticity and Plasticity.* Berlin: Springer, pp. 551-590.

Jenkins, G. M., 1962. Fracture in Reactor Graphite. *Journal of Nuclear Materials,* 5(3), pp. 280-286.

Jishan, X. & Xixi, H., 1990. Size effect on the strength of a concrete member. *Engineering Fracture Mechanics,* 35(4/5), pp. 687-695.

Jones, C. J., 2007. Predicting the Stresses and Deformation of Irradiated Graphite Moderator Bricks. In: G. B. Neighbour, ed. *Management of Ageing Processes in Graphite Reactor Cores.* Cambridge: RSC Publishing, pp. 167-174.

Kadlecek, V., Modry, S. & Kadlecek, V., 2002. Size effect of test specimens on tensile splitting strength of concrete: general relation. *Materials and Structures,* 35(1), pp. 28-34.

Kanos, A., Giannakopoulos, A. E. & Perdikaris, P. C., 2006. Size effect on concrete splitting tensile strength and modulus of elasticity. In: M. S. Konsta-Gdoutos, ed. *Measuring, Monitoring and Modeling Concrete Properties.* Dordrecht: Springer, pp. 239-246.

Karihaloo, B. L. & Huang, X., 1991. Tensile Response of Quasi-Brittle Materials. *Pure and Applied Geophysics,* 137(4), pp. 461-487.

Karikaloo, B. L., Abdalla, H. M. & Xiao, Q. Z., 2003. Size effect in concrete beams. *Engineering Fracture Mechanics,* 70(1), pp. 979-993.

Kataoka, M. & Obara, Y., 2015. *Size Effect in Fracture Toughness of Sandstone.* Montreal, International Society for Rock Mechanics and Rock Engineering.

Kelly, B. T., 1978. Radiation Damage in Graphite and its Relevance to Reactor Design. *Progress in Nuclear Energy,* 2(4), pp. 219-269.

Kipling, G. D., Easton, A. & Neighbour, G. B., 2010. Biaxial Testing: Appropriate for Mechanical Characterisation?. In: G. B. Neighbour, ed. *Securing the Safe Performance of Graphite Reactor Cores.* Cambridge: RSC Publishing, pp. 152-160.

Kotousov, A., Lazzarin, P., Berto, F. & Harding, S., 2010. Effect of the thickness on elastic deformation and quasi-brittle fracture of plate components. *Engineering Fracture Mechanics,* 77(1), pp. 1665-1681.

Kubler, J., 1999. *VAMAS Report 37, Fracture Toughness of Ceramics Using the SEVNB Method, Round Robin,* Dubendorf, Switzerland: EMPA.

Kujawski, D. & Ellyin, F., 1986. On the Size of Plastic Zone Ahead of Crack Tip. *Engineering Fracture Mechanics,* 25(2), pp. 229-236.

Lazzarin, P. & Berto, F., 2005. Some expressions for the strain energy in a finite volume surrounding the root of blunt V-notches. *International Journal of Fracture,* 135(1), pp. 161-185.

Lazzarin, P., Berto, F., Gomez, F. J. & Zappalorto, M., 2008. Some advantages derived from the use of the strain energy density over a control volume in fatigue strength assessments of welded joints. *International Journal of Fatigue,* 30(1), pp. 1345-1357.

Lazzarin, P. & Zambardi, R., 2001. A finite-volume-energy based approach to predict the static and fatigue behaviour of components with sharp V-shaped notches. *International Journal of Fracture,* 112(1), pp. 275-298.

Lewis, D. & Oyler, S. M., 1976. An experimental test of weibull scaling theory. *Journal of the American ceramic society,* 59(1), pp. 507-510.

Liang, T., 2012. *Something About Nuclear Graphite.* Beijing, China, IAEA.

Liu, D., Heard, P. J., Nakhodchi, S. & Flewitt, P. E. J., 2014. Small-Scale Approaches to Evaluate the Mechanical Properties of Quasi-Brittle Reactor Core Graphite. In: A. Tzelepi & M. C. Carroll, eds. *Graphite Testing for Nuclear Applications, STP1578.* West Conshohocken: ASTM, pp. 84-104.

Livieri, P., 2008. Use of J-integral to predict static failures in sharp V-notches and rounded U-notches. *Engineering Fracture Mechanics,* 75(1), pp. 1779-1793.

Lund, J. R. & Byrne, J. P., 2001. Leonardo Da Vinci's tensile strength tests: Implications for the discovery of engineering mechanics. *Civil Engineering and Environmental Systems,* 15(1), pp. 243-250.

Matvienko, Y. G., 2012. Maximum average tangential stress criterion for prediction of the crack path. *International Journal of Fracture,* 176(1), pp. 113-118.

Metcalfe, M. P., Tzelepi, N. & Wilde, D., 2014. Effect of Test Specimen Size on Graphite Strength. In: A. Tzelepi & M. C. Carroll, eds. *Graphite Testing for Nuclear Applications, STP1578.* West Conshohocken: ASTM, pp. 1-30.

Minshall, P. C., Sadler, I. A. & Wickham, A. J., 1996. *Radiolytic graphite oxidation revisited (IAEA-TECDOC--901),* Vienna: IAEA.

Mir, A. E. & Nehme, S. G., 2015. Porosity of self-compacting concrete. *Procedia Engineering,* 123(1), pp. 145-152.

Mostafavi, M. & Marrow, T. J., 2011. In situ observation of crack nuclei in poly-granular graphite under ring-on-ring equi-biaxial and flexural loading. *Engineering Fracture Mechanics,* 78(1), pp. 1756-1770.

Otsuka, K. & Date, H., 2000. Fracture Process Zone in Concrete Tension Specimen. *Engineering Fracture Mechanics,* 65(1), pp. 111-131.

Ouchi, M., Hibino, M. & Okamura, H., 1997. Effect of Superplasticizer on Self-Compactability of Fresh Concrete. *Transportation Research Record,* 1574(1), pp. 37-40.

Persson, B., 1996. Hydration and strength of high performance concrete. *Advanced Cement Based Materials,* 3(3), pp. 107-123.

Poulose, P. K., Jones, D. L. & Liebowitz, H., 1983. A Comparison of the Geometry Dependence of Several Nonlinear Fracture Toughness Parameters. *Engineering Fracture Mechanics,* 17(2), pp. 133-151.

Powers, T. C., 1958. Structure of Physical Properties of Hardened Portland Cement Paste. *Journal of the American Ceramic Society,* 41(1), pp. 1-6.

Purdy, D. M., 2009. *Wikipedia.* [Online]
Available at: https://upload.wikimedia.org/wikipedia/commons/8/8d/Concretevibrator.jpg
[Accessed 21 11 2017].

Quinn, G. D., 2002. The Fracture Toughness Round Robin in VAMAS: What We Have Learned. In: J. J. Salem, G. D. Quinn & M. G. Jenkins, eds. *Fracture Resistance Testing of Monolithic and Composite Brittle Materials, ASTM STP 1409.* West Conshohocken, PA: ASTM, pp. 107-126.

Rice, J. R., 1968. A path independent integral and the approximate analysis of strain concentration by notches and cracks. *Journal of Applied Mechanics,* 35(2), pp. 379-386.

Richart, F. E., Brandtzaeg, A. & Brown, R. L., 1928. *A Study of the Failure of Concrete Under Combined Compressive Stresses,* Urbana-Champaign, Illinois: University of Illinois at Urbana Champaign, College of Engineering. Engineering Experiment Station..

Rigby, R. H. & Aliabadi, M. H., 1998. Decomposition of the Mixed Mode J-integral - Revisited. *International Journal of Solids and Structures,* Volume 35, pp. 2073-2099.

Saghafi, H., Ayatollahi, M. R. & Sistaninia, M., 2010. A modified MTS criterion (MMTS) for mixed-mode fracture toughness assessment of brittle materials. *Materials Science and Engineering A,* 527(1), pp. 5624-5630.

Sakai, M. & Nonoyama, R., 2005. Nonlinear Fracture of a Polycrystalline Graphite - Size effect Law and Irwin's Similarity. *Fracture Mechanics of Ceramics,* 14(1), pp. 337-351.

Shah, R. C., 1974. *Fracture Under Combined Modes in 4340 Steel. STP 560.* Philadelphia, ASTM.

Smith, D. J., Ayatollahi, M. R. & Pavier, M. J., 2001. The role of T-stress in brittle fracture for linear elastic materials under mixed-mode loading. *Fatigue & Fracture of Engineering Materials & Structures,* 24(1), pp. 137-150.

Srinivasan, M., 2014. The Use of Small Graphite Specimen Test Data for Large Core Components for HTGR. In: A. Tzelepi & M. C. Carroll, eds. *Graphite Testing for Nuclear Applications. STP1578.* West Conshohocken: ASTM, pp. 30-64.

Steer, A., 2007. AGR Core Design, Operation and Safety Functions. In: G. B. Neighbour, ed. *Management of Ageing Processes in Graphite Reactor Cores.* Cambridge: RSC Publishing, pp. 11-18.

Tokyay, M. & Ozdemir, M., 1997. Specimen shape and size effect on the compressive strength of higher strength concrete. *Cemend and concrete research,* 27(8), pp. 1281-1289.

Torabi, A. & Taherkhani, M., 2011. Extensive data of notch shape factors for V-notched Brazilian disc specimen under mixed mode loading. *Materials Science and Engineering A,* 528(1), p. 8599– 8609.

Tsang, D. K. L. & Marsden, B. J., 2006. The Developent of a Stress Analysis Code for Nuclear Graphite Components in Gas Cooled Reactors. *Journal of Nuclear Materials,* 350(1), pp. 208-220.

Tsang, D. & Marsden, B. J., 2007. Effects of dimensional change strain in nuclear graphite component stress analysis. *Nuclear Engineering and Design,* 237(1), pp. 897-904.

Un, H. & Bardan, B., 2011. The effect of curing temperature and relative humidity on the strength development of Portland cement mortar. *Scientific Research and Essays,* 6(12), pp. 2504-2511.

van Vliet, M. R. A. & van Mier, J. G. M., 2000. Experimental investigation of size effect in concrete and sandstone under uniaxial tension. *Engineering Fracture Mechanics,* 65(3), pp. 165-188.

Williams, M. L., 1957. On the Stress Distribution at the Base of a Stationary Crack. *Journal of Applied Mechanics,* 24(1), pp. 109-114.

Wittmann, F. H., Mihashi, H. & Nomura, N., 1990. Size Effect on Fracture Energy of Concrete. *Engineering Fracture Mechanics,* 35(1), pp. 107-115.

Yi, S. T., Yang, E. I. & Choi, J. C., 2006. Effect of specimen sizes, specimen shapes, and placement directions on compressive strength of concrete. *Nuclear engineering and design,* 236(1), pp. 115-127.

Yoon, J. H., Byun, T. S., Strizak, J. P. & Snead, L. L., 2011. Characterization of tensile strength and fracture toughness of nuclear graphite NBG-18 using subsize specimens. *Journal of Nuclear Materials,* 412(1), pp. 315-320.

Yosibash, Z., Bussiba, A. & Gilad, I., 2004. Failure criteria for brittle elastic materials. *International Journal of Fracture,* 125(1), pp. 307-333.

Appendix A

This appendix shows the raw batch information.

Splitting strength

This table shows the nominal size (diameter), specimen number, two height measurements (H1, H2), four diameter measurements (D1, D2, D3, D4), average height, average diameter, load at failure and splitting strength of 274 cylindrical specimens. Note: the two smallest cylindrical specimen sizes came from drilled moulds, rather than tubes, as a result their diameters are taken to be exactly 7 and 14.6mm respectively due to such small variation being present at the time of production.

Table A 1. Cylindrical specimen dimensions, failure loads and splitting strengths

Nominal Size	Specimen	H1 (mm)	H2 (mm)	D1 (mm)	D2 (mm)	D3 (mm)	D4 (mm)	Avg H (mm)	Avg D (mm)	Load at failure (N)	Splitting Strength (MPa)
7	1	13.97	13.97	7	7	7	7	13.97	7	655	4.26
7	2	14.11	14.1	7	7	7	7	14.105	7	533	3.44
7	3	14.13	14.13	7	7	7	7	14.13	7	525	3.38
7	4	14.03	14.03	7	7	7	7	14.03	7	593	3.84
7	5	14.02	14.01	7	7	7	7	14.015	7	641	4.16
7	6	14.09	14.1	7	7	7	7	14.095	7	593	3.83
7	7	14.03	14.05	7	7	7	7	14.04	7	507	3.28
7	8	14.07	14.07	7	7	7	7	14.07	7	516	3.34
7	9	14.01	14.04	7	7	7	7	14.025	7	625	4.05
7	10	14.05	14.01	7	7	7	7	14.03	7	542	3.51
7	11	14.01	14.01	7	7	7	7	14.01	7	672	4.36
7	12	13.93	13.95	7	7	7	7	13.94	7	611	3.99
7	13	14.11	14.08	7	7	7	7	14.095	7	630	4.06
7	14	14.06	14.06	7	7	7	7	14.06	7	615	3.98

7	15	14.1	14.1	7	7	7	7	14.1	7	573	3.70
7	16	14.06	14.06	7	7	7	7	14.06	7	547	3.54
7	17	14.04	14.03	7	7	7	7	14.035	7	563	3.65
7	18	14.01	14.03	7	7	7	7	14.02	7	545	3.54
7	19	13.93	13.93	7	7	7	7	13.93	7	595	3.88
7	20	14.1	14.1	7	7	7	7	14.1	7	553	3.57
7	21	14.1	14.1	7	7	7	7	14.1	7	533.4	3.44
7	22	14.07	14.07	7	7	7	7	14.07	7	553.4	3.58
7	23	13.9	13.9	7	7	7	7	13.9	7	664.9	4.35
7	24	14.08	14.08	7	7	7	7	14.08	7	593.7	3.83
7	25	13.93	13.93	7	7	7	7	13.93	7	470.6	3.07
7	26	14.08	14.08	7	7	7	7	14.08	7	518.6	3.35
7	27	14.04	14.04	7	7	7	7	14.04	7	608.8	3.94
7	28	14.02	14.02	7	7	7	7	14.02	7	504.6	3.27
7	29	13.97	13.97	7	7	7	7	13.97	7	526	3.42
7	30	14.03	14.03	7	7	7	7	14.03	7	490	3.18
7	31	13.98	13.98	7	7	7	7	13.98	7	522.6	3.40
7	32	14.02	14.02	7	7	7	7	14.02	7	432.6	2.81
7	33	13.95	13.95	7	7	7	7	13.95	7	530.4	3.46
7	34	14.04	14.04	7	7	7	7	14.04	7	528.7	3.42
7	35	14.04	14.04	7	7	7	7	14.04	7	470.3	3.05
7	36	13.92	13.92	7	7	7	7	13.92	7	456.1	2.98
7	37	14.03	14.03	7	7	7	7	14.03	7	584.7	3.79
7	38	14.02	14.02	7	7	7	7	14.02	7	449.4	2.92
7	39	13.26	13.26	7	7	7	7	13.26	7	469.4	3.22
7	40	13.98	13.98	7	7	7	7	13.98	7	634.4	4.13
7	41	14.01	14.01	7	7	7	7	14.01	7	506.9	3.29
7	42	13.91	13.91	7	7	7	7	13.91	7	637.2	4.17
7	43	14.15	14.15	7	7	7	7	14.15	7	706.1	4.49

7	44	14.1	14.1	7	7	7	7	14.1	7	666.5	4.26
7	45	13.66	13.66	7	7	7	7	13.66	7	653.5	4.31
7	46	14.18	14.18	7	7	7	7	14.18	7	719.7	4.57
7	47	14.1	14.1	7	7	7	7	14.1	7	640.2	4.09
7	48	14.12	14.12	7	7	7	7	14.12	7	602.7	3.84
7	49	14.13	14.13	7	7	7	7	14.13	7	639.3	4.07
7	50	14.13	14.13	7	7	7	7	14.13	7	657.5	4.19
7	51	14.17	14.17	7	7	7	7	14.17	7	505.4	3.21
7	52	14.1	14.1	7	7	7	7	14.1	7	674.7	4.31
7	53	14.15	14.15	7	7	7	7	14.15	7	591.9	3.77
7	54	14.14	14.14	7	7	7	7	14.14	7	614.9	3.92
7	55	14.17	14.17	7	7	7	7	14.17	7	649.7	4.13
7	56	12.68	12.68	7	7	7	7	12.68	7	626.1	4.45
7	57	14.07	14.07	7	7	7	7	14.07	7	562.9	3.60
7	58	13.95	13.95	7	7	7	7	13.95	7	518.5	3.35
7	59	13.98	13.98	7	7	7	7	13.98	7	573.7	3.70
7	60	14.17	14.17	7	7	7	7	14.17	7	661.1	4.20
7	61	14.14	14.14	7	7	7	7	14.14	7	445.4	2.84
7	62	14.14	14.14	7	7	7	7	14.14	7	647.1	4.12
7	63	14.14	14.14	7	7	7	7	14.14	7	647.1	4.12
7	64	14.04	14.04	7	7	7	7	14.04	7	644.9	4.14
7	65	14.22	14.22	7	7	7	7	14.22	7	616.7	3.91
7	66	14.18	14.18	7	7	7	7	14.18	7	594.9	3.78
7	67	14.07	14.07	7	7	7	7	14.07	7	648.3	4.15
7	68	14.06	14.06	7	7	7	7	14.06	7	649.8	4.16
7	69	14.05	14.05	7	7	7	7	14.05	7	606.8	3.89
14	1	29.47	29.49	14.6	14.6	14.6	14.6	29.48	14.6	2491	3.68

14	2	29.64	29.66	14.6	14.6	14.6	14.6	29.65	14.6	2795	4.11
14	3	28.79	28.76	14.6	14.6	14.6	14.6	28.775	14.6	2592	3.93
14	4	29.45	29.46	14.6	14.6	14.6	14.6	29.455	14.6	2560	3.79
14	5	29.72	29.71	14.6	14.6	14.6	14.6	29.715	14.6	2586	3.79
14	6	29.83	29.83	14.6	14.6	14.6	14.6	29.83	14.6	2480	3.63
14	7	29.27	29.25	14.6	14.6	14.6	14.6	29.26	14.6	2473	3.69
14	8	28.8	28.83	14.6	14.6	14.6	14.6	28.815	14.6	2350	3.56
14	9	28.34	28.34	14.6	14.6	14.6	14.6	28.34	14.6	2353	3.62
14	10	29.54	29.56	14.6	14.6	14.6	14.6	29.55	14.6	2614	3.86
14	11	29.52	29.51	14.6	14.6	14.6	14.6	29.515	14.6	2794	4.13
14	12	28.82	28.79	14.6	14.6	14.6	14.6	28.805	14.6	2412	3.65
14	13	28.91	28.89	14.6	14.6	14.6	14.6	28.9	14.6	2570	3.88
14	14	28.81	28.84	14.6	14.6	14.6	14.6	28.825	14.6	2336	3.53
14	15	28.74	28.76	14.6	14.6	14.6	14.6	28.75	14.6	2356	3.57
14	16	29.74	29.74	14.6	14.6	14.6	14.6	29.74	14.6	2438	3.57
14	17	29.5	29.52	14.6	14.6	14.6	14.6	29.51	14.6	2212	3.27
14	18	29.11	29.13	14.6	14.6	14.6	14.6	29.12	14.6	2768	4.14
14	19	29.31	29.28	14.6	14.6	14.6	14.6	29.295	14.6	2725	4.06
14	20	29.44	29.45	14.6	14.6	14.6	14.6	29.445	14.6	2537	3.76
14	21	29.29	29.25	14.6	14.6	14.6	14.6	29.27	14.6	2617	3.90
14	22	29.64	29.64	14.6	14.6	14.6	14.6	29.64	14.6	2277	3.35
14	23	29.04	29.04	14.6	14.6	14.6	14.6	29.04	14.6	2778	4.17
14	24	29.63	29.66	14.6	14.6	14.6	14.6	29.645	14.6	2548	3.75
14	25	28.29	28.29	14.6	14.6	14.6	14.6	28.29	14.6	2315	3.57
14	26	28.81	28.81	14.6	14.6	14.6	14.6	28.81	14.6	2581.6	3.91
14	27	28.95	28.95	14.6	14.6	14.6	14.6	28.95	14.6	2009.3	3.03
14	28	28.97	28.97	14.6	14.6	14.6	14.6	28.97	14.6	2661.4	4.01
14	29	29.25	29.25	14.6	14.6	14.6	14.6	29.25	14.6	2954	4.40
14	30	28.63	28.63	14.6	14.6	14.6	14.6	28.63	14.6	2723	4.15

14	31	29.08	29.08	14.6	14.6	14.6	14.6	29.08	14.6	1986.7	2.98
14	32	29.14	29.14	14.6	14.6	14.6	14.6	29.14	14.6	3014.4	4.51
14	33	29.1	29.1	14.6	14.6	14.6	14.6	29.1	14.6	3152.9	4.72
14	34	29.11	29.11	14.6	14.6	14.6	14.6	29.11	14.6	3234.5	4.84
14	35	28.77	28.77	14.6	14.6	14.6	14.6	28.77	14.6	2443.1	3.70
14	36	29.23	29.23	14.6	14.6	14.6	14.6	29.23	14.6	3024.1	4.51
14	37	29.16	29.16	14.6	14.6	14.6	14.6	29.16	14.6	2552.8	3.82
14	38	29.15	29.15	14.6	14.6	14.6	14.6	29.15	14.6	1991.7	2.98
14	39	29.15	29.15	14.6	14.6	14.6	14.6	29.15	14.6	2625.1	3.93
14	40	29.22	29.22	14.6	14.6	14.6	14.6	29.22	14.6	2605.1	3.89
14	41	28.87	28.87	14.6	14.6	14.6	14.6	28.87	14.6	2441	3.69
14	42	29.21	29.21	14.6	14.6	14.6	14.6	29.21	14.6	2001.8	2.99
14	43	29.02	29.02	14.6	14.6	14.6	14.6	29.02	14.6	2277.1	3.42
14	44	28.99	28.99	14.6	14.6	14.6	14.6	28.99	14.6	2950.3	4.44
14	45	29.18	29.18	14.6	14.6	14.6	14.6	29.18	14.6	2671.3	3.99
14	46	29.09	29.09	14.6	14.6	14.6	14.6	29.09	14.6	2162	3.24
14	47	29.33	29.33	14.6	14.6	14.6	14.6	29.33	14.6	2622	3.90
14	48	29.25	29.25	14.6	14.6	14.6	14.6	29.25	14.6	2956.4	4.41
14	49	29.28	29.28	14.6	14.6	14.6	14.6	29.28	14.6	2951.5	4.40
14	50	29.26	29.26	14.6	14.6	14.6	14.6	29.26	14.6	2080.7	3.10
14	51	29.34	29.34	14.6	14.6	14.6	14.6	29.34	14.6	2377.8	3.53
14	52	29.23	29.23	14.6	14.6	14.6	14.6	29.23	14.6	3026.6	4.51
14	53	29.26	29.26	14.6	14.6	14.6	14.6	29.26	14.6	2228.8	3.32
14	54	29.26	29.26	14.6	14.6	14.6	14.6	29.26	14.6	2583.9	3.84
14	55	29.14	29.14	14.6	14.6	14.6	14.6	29.14	14.6	2491.1	3.72
14	56	29.12	29.12	14.6	14.6	14.6	14.6	29.12	14.6	2843.3	4.25
14	57	29.2	29.2	14.6	14.6	14.6	14.6	29.2	14.6	3101.8	4.62
14	58	29.24	29.24	14.6	14.6	14.6	14.6	29.24	14.6	2359.7	3.51
14	59	29.17	29.17	14.6	14.6	14.6	14.6	29.17	14.6	2448.9	3.65

14	60	26.26	26.26	14.6	14.6	14.6	14.6	26.26	14.6	2149.6	3.56
14	61	29.21	29.21	14.6	14.6	14.6	14.6	29.21	14.6	2599.6	3.87
14	62	29.09	29.09	14.6	14.6	14.6	14.6	29.09	14.6	2464.9	3.69
14	63	29.15	29.15	14.6	14.6	14.6	14.6	29.15	14.6	1844.5	2.75
14	64	29.21	29.21	14.6	14.6	14.6	14.6	29.21	14.6	2682.7	4.00
14	65	29.16	29.16	14.6	14.6	14.6	14.6	29.16	14.6	2571.2	3.84
14	66	28.93	28.93	14.6	14.6	14.6	14.6	28.93	14.6	2913.4	4.38
14	67	29.11	29.11	14.6	14.6	14.6	14.6	29.11	14.6	2043	3.05
14	68	28.97	28.97	14.6	14.6	14.6	14.6	28.97	14.6	2043.3	3.07
14	69	29.18	29.18	14.6	14.6	14.6	14.6	29.18	14.6	2846.4	4.24
14	70	29.19	29.19	14.6	14.6	14.6	14.6	29.19	14.6	2514.9	3.75
14	71	29.19	29.19	14.6	14.6	14.6	14.6	29.19	14.6	1938.2	2.89
14	72	28.42	28.42	14.6	14.6	14.6	14.6	28.42	14.6	1713.3	2.62
14	73	29.1	29.1	14.6	14.6	14.6	14.6	29.1	14.6	2283.4	3.41
14	74	29.03	29.03	14.6	14.6	14.6	14.6	29.03	14.6	2865.8	4.30
14	75	29.11	29.11	14.6	14.6	14.6	14.6	29.11	14.6	2795.8	4.18
14	76	29.28	29.28	14.6	14.6	14.6	14.6	29.28	14.6	2575.2	3.83
14	77	29.12	29.12	14.6	14.6	14.6	14.6	29.12	14.6	2247.7	3.36
14	78	28.9	28.9	14.6	14.6	14.6	14.6	28.9	14.6	2465.4	3.71
14	79	28.89	28.89	14.6	14.6	14.6	14.6	28.89	14.6	2502.6	3.77
14	80	29.05	29.05	14.6	14.6	14.6	14.6	29.05	14.6	2376.4	3.56
14	81	29.09	29.09	14.6	14.6	14.6	14.6	29.09	14.6	2715.4	4.06
30	1	62.36	62.35	30.51	30.36	30.58	30.33	62.355	30.445	9332	3.13
30	2	62.05	62.05	30.43	30.56	30.45	30.61	62.05	30.5125	6700	2.25
30	3	62.55	62.53	30.36	30.4	30.44	30.45	62.54	30.4125	6929	2.32
30	4	61.87	61.85	30.34	30.54	30.38	30.59	61.86	30.4625	8050	2.72
30	5	61.49	61.42	30.47	30.47	30.31	30.49	61.455	30.435	7926	2.70

30	6	60.11	60.13	30.44	30.31	30.42	30.36	60.12	30.3825	8596	3.00
30	7	60.15	60.16	30.44	30.39	30.35	30.31	60.155	30.3725	9220	3.21
30	8	58.55	58.53	30.42	30.34	30.38	30.32	58.54	30.365	9011	3.23
30	9	60.88	60.94	30.38	30.35	30.42	30.35	60.91	30.375	9197	3.16
30	10	59.66	59.68	30.28	30.49	30.26	30.49	59.67	30.38	8152	2.86
30	11	58.89	58.89	30.42	30.61	30.48	30.45	58.89	30.49	8582	3.04
30	12	62.41	62.36	30.32	30.55	30.27	30.45	62.385	30.3975	6645	2.23
30	13	61.64	61.6	30.37	30.58	30.42	30.49	61.62	30.465	10399	3.53
30	14	61.08	61.04	30.29	30.48	30.3	30.5	61.06	30.3925	11067	3.80
30	15	60.08	60.1	30.43	30.32	30.35	30.46	60.09	30.39	10070	3.51
30	16	60.51	60.52	30.3	30.41	30.27	30.53	60.515	30.3775	7754	2.69
30	17	61.41	61.36	30.41	30.29	30.42	30.27	61.385	30.3475	10643	3.64
30	18	60.53	60.48	30.51	30.32	30.46	30.22	60.505	30.3775	7749	2.68
30	19	60.56	60.54	30.26	30.31	30.25	30.28	60.55	30.275	10716	3.72
30	20	60.92	60.94	30.28	30.25	30.25	30.34	60.93	30.28	10205	3.52
30	21	60.65	60.68	30.32	30.28	30.28	30.42	60.665	30.325	7603	2.63
30	22	60.93	60.96	30.19	30.35	30.18	30.38	60.945	30.275	10527	3.63
30	23	60.74	60.74	30.33	30.23	30.29	30.2	60.74	30.2625	9453	3.27
30	24	60.71	60.67	30.36	30.41	30.37	30.32	60.69	30.365	7742	2.67
30	25	60.23	60.24	30.25	30.47	30.27	30.35	60.235	30.335	6258	2.18
30	26	59.76	59.75	30.47	30.36	30.49	30.21	59.755	30.3825	10808	3.79
30	27	60.88	60.9	30.15	30.28	30.32	30.31	60.89	30.265	11775	4.07
30	28	59.1	59.13	30.47	30.21	30.45	30.47	59.115	30.4	10808	3.83
30	29	59.33	59.41	30.54	30.25	30.36	30.22	59.37	30.3425	10361	3.66
30	30	60.81	60.98	30.32	30.32	30.35	30.33	60.895	30.33	10605	3.66
30	31	60.92	60.94	30.3	30.33	30.36	30.46	60.93	30.3625	10559	3.63
30	32	60.95	60.97	30.26	30.28	30.45	30.39	60.96	30.345	7651	2.63
30	33	59.53	59.5	30.4	30.29	30.33	30.24	59.515	30.315	6901	2.44
30	34	60.75	60.75	30.34	30.31	30.29	30.43	60.75	30.3425	7580	2.62

30	35	57.73	57.74	30.21	29.97	30.71	30.37	57.735	30.315	7739	2.81
30	36	60.54	60.6	30.16	30.52	30.21	30.51	60.57	30.35	7942	2.75
30	37	59.25	59.23	30.36	30.67	30.25	30.48	59.24	30.44	7371	2.60
30	38	60.95	60.94	30.15	30.23	30.14	30.27	60.945	30.1975	7542	2.61
30	39	60.22	60.2	30.13	30.55	30.1	30.45	60.21	30.3075	7516	2.62
30	40	60.85	60.79	30.41	30.27	30.4	30.25	60.82	30.3325	6677	2.30
30	41	58.9	58.84	30.25	30.44	30.22	30.44	58.87	30.3375	7888	2.81
30	42	62.31	62.34	30.38	30.38	30.39	30.28	62.325	30.3575	8468	2.85
30	43	60.33	60.36	30.38	30.59	30.4	30.52	60.345	30.4725	7186	2.49
30	44	60.83	60.79	30.47	30.38	30.36	30.31	60.81	30.38	8582	2.96
30	45	60.46	60.42	30.59	30.39	30.57	30.28	60.44	30.4575	8649	2.99
30	46	59.99	60.01	30.59	30.41	30.57	30.49	60	30.515	7424	2.58
30	47	61.02	60.98	30.45	30.41	30.49	30.32	61	30.4175	8250	2.83
30	48	60.97	61	30.57	30.27	30.47	30.29	60.985	30.4	7717	2.65
30	49	61.37	61.36	30.43	30.46	30.31	30.55	61.365	30.4375	6770	2.31
30	50	60.68	60.64	30.23	30.46	30.24	30.5	60.66	30.3575	8201	2.84
30	51	60.99	60.93	30.51	30.46	30.5	30.41	60.96	30.47	7049	2.42
30	52	61	61.03	30.44	30.53	30.42	30.46	61.015	30.4625	8236	2.82
30	53	60.26	60.24	30.42	30.55	30.33	30.56	60.25	30.465	7781	2.70
30	54	61.23	61.19	30.51	30.35	30.44	30.32	61.21	30.405	9461	3.24
30	55	61.01	61	30.43	30.48	30.4	30.48	61.005	30.4475	8964	3.07
30	56	60.78	60.7	30.44	30.53	30.47	30.52	60.74	30.49	8231	2.83
30	57	61.43	61.46	30.39	30.41	30.41	30.42	61.445	30.4075	8704	2.97
30	58	60.52	60.53	30.42	30.56	30.41	30.56	60.525	30.4875	8761	3.02
30	59	61.11	61.11	30.71	30.2	30.63	30.26	61.11	30.45	9717	3.32
30	60	60.47	60.51	30.57	30.49	30.55	30.5	60.49	30.5275	9357	3.23
30	61	61.11	61.13	30.49	30.66	30.44	30.65	61.12	30.56	8259	2.81
30	62	61.01	61.05	30.27	30.69	30.38	30.58	61.03	30.48	7621	2.61
30	63	61.1	61.12	30.39	30.48	30.4	30.51	61.11	30.445	10733	3.67

30	64	60.99	60.99	30.49	30.54	30.51	30.52	60.99	30.515	7531	2.58
30	65	60.69	60.68	30.23	30.45	30.37	30.6	60.685	30.4125	8976	3.10
30	66	61.18	61.24	30.51	30.34	30.56	30.44	61.21	30.4625	7351	2.51
42	1	84.08	84.09	41.87	42.19	41.9	42.23	84.085	42.0475	14347	2.58
42	2	85.07	85.07	41.65	42.27	41.74	42.38	85.07	42.01	14789	2.63
42	3	83.91	83.92	42.09	42.2	41.93	42.02	83.915	42.06	13782	2.49
42	4	84.85	84.89	42.16	41.75	42.09	41.92	84.87	41.98	13730	2.45
42	5	85.12	85.11	42.2	41.68	42.2	41.72	85.115	41.95	15067	2.69
42	6	83.1	83.1	41.89	42.08	42.03	42.18	83.1	42.045	13674	2.49
42	7	83.76	83.75	42.25	41.75	42.24	41.73	83.755	41.9925	15115	2.74
42	8	85.09	85.12	42.12	42	42.07	42.12	85.105	42.0775	14475	2.57
42	9	84.67	84.67	42.31	41.9	42.31	42	84.67	42.13	13317	2.38
42	10	85.42	85.41	42.12	41.96	42.29	41.86	85.415	42.0575	13534	2.40
42	11	81.86	81.85	42.01	42.36	42.01	42.36	81.855	42.185	14548	2.68
42	12	81.88	81.84	42	42.33	41.94	42.36	81.86	42.1575	16630	3.07
42	13	80.91	80.91	42.06	42.21	41.97	42.04	80.91	42.07	15556	2.91
42	14	81.92	81.95	42.11	42.03	42.16	42.14	81.935	42.11	17678	3.26
42	15	81.33	81.15	42.33	42.04	42.32	41.96	81.24	42.1625	15311	2.85
42	16	80.85	80.95	41.91	42.36	41.98	42.34	80.9	42.1475	14275	2.67
42	17	80.94	80.86	42.12	42.01	41.91	41.99	80.9	42.0075	16705	3.13
42	18	84.17	84.1	42.4	42.04	42.31	41.99	84.135	42.185	16176	2.90
42	19	81.85	81.84	42.03	42.04	42.07	42.05	81.845	42.0475	15880	2.94
64	1	128.9	128.89	63.66	65.12	63.71	65.2	128.895	64.4225	36791	2.82
64	2	127.17	127.1	65.02	63.62	65.02	63.94	127.135	64.4	23786	1.85

64	3	128.48	128.52	63.56	65.05	63.93	65.31	128.5	64.4625	36653	2.82
64	4	128.15	128.17	63.93	64.53	64.22	64.93	128.16	64.4025	33906	2.62
64	5	127.87	127.82	65.28	63.75	64.96	63.62	127.845	64.4025	41708	3.22
64	6	130.44	130.4	63.78	64.94	63.85	64.94	130.42	64.3775	36328	2.75
64	7	128.86	128.87	63.62	65.07	63.73	65.07	128.865	64.3725	34783	2.67
64	8	129	128.98	65.07	63.26	65.04	63.33	128.99	64.175	34003	2.62
64	9	129.64	129.64	65.01	63.74	65.13	63.57	129.64	64.3625	41157	3.14
64	10	128.9	128.89	63.66	65.12	63.71	65.2	128.895	64.4225	38879	2.98
64	11	129.59	129.57	63.75	65.09	63.78	64.44	129.58	64.265	37893	2.90
64	12	129.85	129.85	64.47	64.29	64.42	64.51	129.85	64.4225	31863	2.42
64	13	129.81	129.78	64.57	64.54	64.58	64.19	129.795	64.47	39386	3.00
64	14	128.59	128.54	65.05	63.75	65.15	63.92	128.565	64.4675	34728	2.67
64	15	129.38	129.32	64.26	64.79	64.74	64.51	129.35	64.575	42277	3.22
64	16	129.37	129.36	65.04	64.32	64.94	63.78	129.365	64.52	41095	3.13
64	17	128.85	128.98	65.25	63.29	65.26	63.79	128.915	64.3975	40622	3.12
64	18	129.83	129.82	65.09	63.59	65.07	63.74	129.825	64.3725	35577	2.71
64	19	127.57	127.58	63.47	65.09	63.46	65.12	127.575	64.285	32717	2.54
64	20	129.17	129.12	64.71	64.36	64.32	64.28	129.145	64.4175	28745	2.20
64	21	129.76	129.75	63.36	65.13	63.82	65.15	129.755	64.365	31625	2.41
64	22	127.13	127.11	64.65	64.56	64.57	64.59	127.12	64.5925	27874	2.16
64	23	129.54	129.5	63.6	65.01	63.48	65.2	129.52	64.3225	33509	2.56
64	24	129.2	129.24	63.44	65.09	63.56	65.2	129.22	64.3225	29422	2.25
64	25	127.8	127.82	63.91	65.03	63.85	64.79	127.81	64.395	32624	2.52
64	26	128.74	128.77	64.33	64.71	63.77	64.86	128.755	64.4175	34154	2.62
64	27	128.52	128.52	63.86	64.97	63.98	64.79	128.52	64.4	30960	2.38
64	28	128.53	128.54	65.03	64.03	64.78	63.6	128.535	64.36	29430	2.26
64	29	127.73	127.71	64.55	63.99	65.29	64.31	127.72	64.535	36563	2.82
64	30	128.04	128.08	64.44	64.9	63.94	64.88	128.06	64.54	31173	2.40
64	31	129.3	129.07	65.15	63.89	65.31	64.09	129.185	64.61	31575	2.41

64	32	128.58	128.64	65.26	63.61	65.29	63.89	128.61	64.5125	34038	2.61
64	33	127.31	127.27	65.16	63.79	65.11	63.34	127.29	64.35	36744	2.86
64	34	125.76	125.71	65.09	63.39	65.21	64.17	125.735	64.465	35716	2.81
64	35	130.06	130.06	65.15	64.02	64.9	63.77	130.06	64.46	37801	2.87
64	36	126.12	126.14	65.11	63.88	65.16	63.39	126.13	64.385	35448	2.78
64	37	128.99	128.99	63.79	65.03	63.52	65.33	128.99	64.4175	41609	3.19
64	38	129	128.99	65.28	63.59	65.36	63.81	128.995	64.51	42808	3.27
64	39	128.2	128.22	64.8	64.53	64.54	64.46	128.21	64.5825	42631	3.28
64	40	128.15	128.13	63.49	65.35	63.62	65.21	128.14	64.4175	40190	3.10
103	1	205.61	205.57	103.14	103.69	103.22	103.53	205.59	103.395	68730	2.06
103	2	205.64	205.65	103.55	103.18	103.5	103.01	205.645	103.31	75630	2.27
103	3	205.32	205.43	103.05	103.53	103.35	103.32	205.375	103.3125	71780	2.15
103	4	205.71	205.75	103.35	103.4	103.67	103.25	205.73	103.4175	70880	2.12
103	5	205.13	205.27	103.32	103.62	103.13	103.66	205.2	103.4325	75000	2.25

Compression

As the cylindrical specimens used in splitting strength had a small range of variation the compressive specimens are only listed as having the average dimensions of the equivalent splitting strength specimens. This table shows the nominal sizes of the cylinders (height and diameter), load at failure (N) and the compressive strength of 118 cylindrical specimens.

Table A 2. Cylindrical specimen dimensions, failure loads and compressive strengths

Nominal	Specimen	D (mm)	H (mm)	Load at Failure (N)	Compressive Strength (N/mm^2)
14	1	14.6	29.1	4024.5	24.37
14	2	14.6	29.1	4304.8	26.07
14	3	14.6	29.1	4260.6	25.80
14	4	14.6	29.1	4219	25.55
14	5	14.6	29.1	4482.4	27.15
14	6	14.6	29.1	3810.8	23.08
14	7	14.6	29.1	4751.1	28.77
14	8	14.6	29.1	4618	27.97
14	9	14.6	29.1	4737.4	28.69
14	10	14.6	29.1	4508.3	27.30
14	11	14.6	29.1	4775.5	28.92
14	12	14.6	29.1	4571.8	27.69
14	13	14.6	29.1	4169.2	25.25
14	14	14.6	29.1	4457.1	26.99
14	15	14.6	29.1	4910.1	29.74
14	16	14.6	29.1	4454.8	26.98
14	17	14.6	29.1	4391.6	26.60
14	18	14.6	29.1	4703.1	28.48

14	19	14.6	29.1	4654.1	28.18
14	20	14.6	29.1	4386	26.56
14	21	14.6	29.1	4123.8	24.97
14	1	14.6	29.1	4106.5	24.87
14	2	14.6	29.1	4148.1	25.12
14	3	14.6	29.1	4742.3	28.72
14	4	14.6	29.1	4847.4	29.36
14	5	14.6	29.1	4477.4	27.11
14	6	14.6	29.1	4575.8	27.71
14	7	14.6	29.1	4102.4	24.84
14	8	14.6	29.1	4743.8	28.73
14	9	14.6	29.1	4503	27.27
14	10	14.6	29.1	4238.3	25.67
14	11	14.6	29.1	4491.7	27.20
14	12	14.6	29.1	4558	27.60
14	13	14.6	29.1	4070.2	24.65
14	14	14.6	29.1	4394.5	26.61
14	15	14.6	29.1	4222.7	25.57
14	16	14.6	29.1	4311.5	26.11
14	17	14.6	29.1	4639.6	28.10
14	18	14.6	29.1	4235.2	25.65
14	19	14.6	29.1	4774.3	28.91
14	20	14.6	29.1	4518.7	27.37
14	21	14.6	29.1	4645.9	28.14
14	22	14.6	29.1	4990.7	30.22
14	23	14.6	29.1	4690.3	28.40
14	24	14.6	29.1	4764.2	28.85
14	25	14.6	29.1	4931.2	29.86
14	26	14.6	29.1	4450.1	26.95

14	27	14.6	29.1	4662	28.23
14	1	14.6	29.1	3793.3	22.97
14	2	14.6	29.1	4090.2	24.77
14	3	14.6	29.1	3170.1	19.20
14	4	14.6	29.1	4382.6	26.54
14	5	14.6	29.1	3316.5	20.08
14	6	14.6	29.1	4141.2	25.08
14	7	14.6	29.1	3801.2	23.02
14	8	14.6	29.1	2993.9	18.13
14	9	14.6	29.1	3915.6	23.71
14	10	14.6	29.1	3464.4	20.98
14	11	14.6	29.1	3780.8	22.90
14	12	14.6	29.1	4196.6	25.41
14	13	14.6	29.1	3477.5	21.06
14	14	14.6	29.1	3366	20.38
14	15	14.6	29.1	3666.4	22.20
14	16	14.6	29.1	3853	23.33
14	17	14.6	29.1	4029.7	24.40
14	18	14.6	29.1	3801.5	23.02
14	19	14.6	29.1	3021.6	18.30
14	20	14.6	29.1	3275.5	19.84
14	21	14.6	29.1	3629.1	21.98
14	22	14.6	29.1	3640.5	22.05
14	23	14.6	29.1	3356.1	20.32
14	24	14.6	29.1	4001.2	24.23
14	25	14.6	29.1	3378.5	20.46
14	26	14.6	29.1	4109.5	24.89
14	27	14.6	29.1	2672.6	16.19
14	28	14.6	29.1	3430.3	20.77

14	29	14.6	29.1	3554	21.52
30	1	30.4	60.7	16766	22.95
30	2	30.4	60.7	18810	25.75
30	3	30.4	60.7	18633	25.50
30	4	30.4	60.7	17837	24.41
30	5	30.4	60.7	17869	24.46
30	6	30.4	60.7	17773	24.33
30	7	30.4	60.7	19031	26.05
30	1	30.4	60.7	19491	26.68
30	2	30.4	60.7	18548	25.39
30	3	30.4	60.7	18786	25.71
30	4	30.4	60.7	18955	25.94
30	5	30.4	60.7	18091	24.76
30	6	30.4	60.7	17558	24.03
30	7	30.4	60.7	18649	25.53
30	8	30.4	60.7	16661	22.80
30	1	30.4	60.7	16586	22.70
30	2	30.4	60.7	16990	23.25
30	3	30.4	60.7	16420	22.47
30	4	30.4	60.7	17139	23.46
30	5	30.4	60.7	16411	22.46
30	6	30.4	60.7	15907	21.77
30	7	30.4	60.7	17535	24.00
30	8	30.4	60.7	17191	23.53
64	1	64.4	128.7	84510	26.27
64	2	64.4	128.7	83810	26.05
64	3	64.4	128.7	84410	26.24
64	4	64.4	128.7	82160	25.54
64	5	64.4	128.7	77270	24.02

64	6	64.4	128.7	86050	26.75
64	1	64.4	128.7	85030	26.43
64	2	64.4	128.7	85370	26.54
64	3	64.4	128.7	82200	25.55
64	4	64.4	128.7	84090	26.14
64	5	64.4	128.7	82810	25.74
64	6	64.4	128.7	82190	25.55
64	1	64.4	128.7	72810	22.63
64	2	64.4	128.7	73290	22.78
64	3	64.4	128.7	75040	23.33
64	4	64.4	128.7	61680	19.17
64	5	64.4	128.7	60950	18.95
64	6	64.4	128.7	79350	24.67

3PT Bend

This table shows the nominal size (depth), specimen number, actual depth (D), width (W), support span (L), load at failure and flexural strength of 170 three point bend specimens.

Table A 3. Cuboid specimen dimensions, failure loads and flexural strengths

Nominal Size	Specimen	D (mm)	W (mm)	Span, L (mm)	Load at failure (N)	Flexural Strength (MPa)
8	1	8.03	8.12	32	92.8	8.51
8	2	8.02	7.89	32	92	8.70
8	3	8.06	8.11	32	99.8	9.09
8	4	7.98	8.15	32	106.8	9.88
8	5	8.01	8.06	32	98.6	9.15
8	6	7.99	8.03	32	91.44	8.56
8	7	8.01	8.05	32	93.1	8.65
8	8	8.01	8.06	32	95.8	8.89
8	9	7.94	8.09	32	71.4	6.72
8	10	8.05	8.06	32	106.8	9.81
8	11	8.05	7.88	32	85.3	8.02
8	12	7.97	8.13	32	90.2	8.38
8	13	8.05	7.93	32	88.2	8.24
8	14	8.05	7.93	32	75.7	7.07
8	15	8.08	8.11	32	101	9.16
8	16	7.95	8.06	32	95.5	9.00
8	17	8.09	8.11	32	122.2	11.05
8	18	8	8.1	32	102.8	9.52
8	19	7.95	8.09	32	66.8	6.27
8	20	7.92	8.11	32	109.1	10.29
8	21	7.99	8.1	32	100.4	9.32

8	22	8.07	8.09	32	113.8	10.37
8	23	7.97	8.09	32	67.1	6.27
8	24	7.91	8.11	32	106.9	10.11
8	25	8.02	8.12	32	111.5	10.25
8	26	8.05	8.09	32	97.6	8.94
8	27	8.06	8.1	32	103.3	9.42
8	28	7.96	8.11	32	97.8	9.14
8	29	7.93	8.04	32	93.2	8.85
8	30	7.88	8.04	32	78.7	7.57
8	31	7.9	8.06	32	87.4	8.34
8	32	7.92	8.07	32	87.1	8.26
8	33	7.99	8.08	32	75.4	7.02
8	34	8	8.05	32	85	7.92
8	35	8.09	8.13	32	95.5	8.62
8	36	7.93	8.06	32	82.7	7.83
8	37	7.94	8.02	32	72.6	6.89
8	38	8.01	8.04	32	90.8	8.45
8	39	7.91	8.01	32	74.9	7.17
8	40	8.04	8.04	32	91.4	8.44
8	41	8.02	8.03	32	78.7	7.31
8	42	7.92	8.09	32	76.9	7.27
8	43	7.92	8.1	32	78.1	7.38
8	44	7.91	8.04	32	64.5	6.15
8	45	8.06	8.16	32	64.5	5.84
8	46	8.03	8.06	32	83.3	7.69
8	47	7.99	8.08	32	70.5	6.56
8	48	7.96	8.05	32	55.1	5.19
8	49	7.97	8.05	32	87.2	8.19
8	50	7.9	8.14	32	74.9	7.08

8	51	7.99	8.04	32	68.2	6.38
8	52	7.99	8.04	32	85.3	7.98
8	53	8	8.1	32	82.4	7.63
8	54	8.06	8.06	32	78.7	7.21
8	55	7.9	8.05	32	82.7	7.90
8	56	7.9	8.04	32	76.3	7.30
15	1	15.06	15.25	60	348.6	9.07
15	2	15.08	15.31	60	342.9	8.86
15	3	15.04	15.35	60	321	8.32
15	4	15.04	15.28	60	356.8	9.29
15	5	15.13	15.35	60	403.9	10.34
15	6	15.06	15.29	60	374.2	9.71
15	7	15.05	15.36	60	318.2	8.23
15	8	15.05	15.37	60	358.5	9.27
15	10	15.05	15.32	60	426.2	11.05
15	11	15.04	15.33	60	338.2	8.78
15	12	15.02	15.36	60	334.7	8.69
15	13	15.1	15.27	60	262.1	6.78
15	14	15.03	15.18	60	366.4	9.62
15	15	15.04	15.33	60	354.8	9.21
15	16	15.1	15.35	60	312.7	8.04
15	17	15.04	15.21	60	274.4	7.18
15	18	15.06	15.3	60	319.1	8.28
15	19	15.05	15.28	60	356	9.26
15	20	15.05	15.28	60	310.1	8.06
15	21	15.05	15.3	60	321.1	8.34
15	22	15.05	15.39	60	298.4	7.70
15	23	15.04	15.27	60	330.1	8.60

15	24	15.01	15.34	60	380.3	9.90
15	25	15.05	15.35	60	275.8	7.14
15	26	15.05	15.28	60	350.1	9.10
15	27	15.05	15.3	60	348.7	9.06
15	28	15.05	15.32	60	310.7	8.06
15	29	15.04	15.32	60	378.8	9.84
15	30	15.03	15.25	60	329.8	8.62
15	31	15.04	15.31	60	292.9	7.61
15	32	15.03	15.34	60	293.2	7.61
15	33	15.04	15.25	60	285.4	7.45
15	34	15.07	15.27	60	274	7.11
15	35	15.02	15.23	60	331.3	8.68
15	36	15.02	15.3	60	290.6	7.58
15	37	15.01	15.36	60	306.6	7.97
15	38	15.07	15.33	60	334.7	8.65
15	39	15.02	15.28	60	314.7	8.22
15	40	15.05	15.36	60	333.3	8.62
15	41	15.01	15.33	60	339.3	8.84
15	42	15.06	15.21	60	273.1	7.13
15	43	15.02	15.23	60	251.4	6.59
15	44	15.06	15.27	60	313.5	8.15
15	45	15.06	15.34	60	324.2	8.39
15	46	15.02	15.37	60	323.4	8.39
15	47	15.04	15.29	60	292.4	7.61
15	48	15.06	15.38	60	270	6.97
15	49	15.04	15.4	60	274	7.08
15	50	15.04	15.25	60	310	8.09
15	51	15.09	15.31	60	287.7	7.43
15	52	15.01	15.34	60	235.8	6.14

15	53	15.08	15.33	60	253.1	6.53
15	54	15.07	15.34	60	298.7	7.72
15	55	15.09	15.24	60	315.9	8.19
15	56	15.08	15.35	60	260.1	6.71
15	57	15.08	15.33	60	241.3	6.23
15	58	15.08	15.36	60	247	6.36
15	59	15.04	15.25	60	262.1	6.84
15	60	15.07	15.4	60	308.6	7.94
30	1	30.12	30.31	120	1066.7	6.98
30	2	30.07	30.44	120	1254.5	8.20
30	3	30.13	30.3	120	1191.8	7.80
30	4	30.05	30.4	120	1435.9	9.42
30	5	30.07	30.35	120	1174.7	7.71
30	6	30.15	30.32	120	1195.9	7.81
30	7	30.08	30.34	120	1216.2	7.97
30	8	30.14	30.35	120	1104.1	7.21
30	9	30.1	30.28	120	1066.9	7.00
30	10	30.15	30.35	120	1341	8.75
30	11	30.02	30.26	120	1203.1	7.94
30	12	30.02	30.39	120	1032.4	6.79
30	13	30.08	30.48	120	1178.4	7.69
30	14	30.16	30.34	120	1192.3	7.78
30	15	30.08	30.33	120	1125.9	7.38
30	16	30	30.39	120	1209.2	7.96
30	17	30.16	30.35	120	1330.6	8.68
30	18	30.13	30.27	120	1301.6	8.53
30	19	30.12	30.3	120	1240.6	8.12
30	20	30.14	30.27	120	1236.4	8.09

30	21	30.06	30.24	120	1167.4	7.69
30	22	30.07	30.37	120	1310.9	8.59
30	23	29.98	30.45	120	1160.8	7.63
30	24	30.01	30.34	120	1352.1	8.91
30	25	30.03	30.24	120	1316.1	8.69
30	26	30.04	30.55	120	1228.7	8.02
30	27	30.05	30.3	120	1436	9.45
30	28	30.06	30.28	120	1450.2	9.54
30	29	30.11	30.51	120	1222.6	7.96
30	30	30.14	30.32	120	1069.9	6.99
30	31	30.02	30.35	120	991.2	6.52
30	32	30.1	30.4	120	1045.1	6.83
30	33	30.04	30.26	120	978.1	6.45
30	34	30.11	30.44	120	1030.9	6.72
30	35	30	30.46	120	1078.3	7.08
30	36	30.04	30.42	120	1200.2	7.87
30	37	30.02	30.44	120	958.9	6.29
30	38	30.13	30.25	120	1131.6	7.42
30	39	30.07	30.31	120	1120.9	7.36
30	40	30.02	30.37	120	1096.5	7.21
30	41	30.13	30.34	120	1111	7.26
30	42	30.06	30.26	120	1004.8	6.61
30	43	30.12	30.24	120	1272.2	8.35
30	44	30.05	30.27	120	881.7	5.81
30	45	30.09	30.44	120	1136.6	7.42
30	46	30.05	30.48	120	1188	7.77
30	47	30.07	30.39	120	1039.1	6.81
30	48	30.08	30.38	120	1063.5	6.96
30	49	30.1	30.27	120	1049.7	6.89

30	50	30.12	30.25	120	836.7	5.49
30	51	30.11	30.47	120	1077.7	7.02
30	52	30.12	30.28	120	1108.4	7.26
30	53	30.1	30.32	120	1050.3	6.88
30	54	30.05	30.54	120	1275.4	8.32
30	55	30.13	30.29	120	882.5	5.78
30	56	30.14	30.37	120	1042.9	6.80
30	57	30.03	30.41	120	1349.4	8.86

3PT SENB

This table shows the nominal size (depth), specimen number, measured depth (D), breadth (B), support span (L), load at failure and fracture toughness of 124 SENB specimens.

Table A 4. Cuboid specimen dimensions, failure loads and fracture toughness (K_c)

Nominal Size (mm)	Specimen	D (mm)	B (mm)	L (mm)	Sharp Notch Radius (µm)	Sharp Notch Angle (°)	Sharp Notch Depth (mm)	Load at failure (N)	Fracture Toughness (Mpa.m$^{0.5}$)
8	1	8	8.05	32	27	32.7	0.387	20.9	0.242
8	2	7.98	8.03	32	23	43.8	0.407	17.2	0.202
8	3	7.92	7.98	32	24	38.1	0.436	20.9	0.250
8	4	7.98	8.04	32	31	36.8	0.350	23.6	0.271
8	5	7.96	8	32	27	35.4	0.353	19.3	0.223
8	6	8.1	8.11	32	50	38.3	0.451	26.4	0.309
8	7	8.05	8.1	32	20	37.8	0.343	20.4	0.231
8	8	7.9	8.06	32	34	41.1	0.376	21.4	0.248
8	9	7.97	8.08	32	35	48.7	0.462	26.7	0.317
8	10	8.03	8.11	32	27	35.0	0.358	25	0.284
8	11	8.07	8.07	32	37	33.9	0.450	24.7	0.291
8	12	7.93	8.1	32	27	45.7	0.397	24.7	0.287
8	13	7.99	8.08	32	17	24.0	0.449	24.7	0.292
8	14	8	8.09	32	24	36.0	0.351	23.8	0.271
8	15	8.02	8.07	32	22	28.4	0.361	24.4	0.279
8	16	7.99	8.07	32	30	39.8	0.356	27	0.309
8	17	7.92	8.09	32	20	25.8	0.438	27.9	0.329
8	18	8.04	8.04	32	27	30.1	0.403	26.4	0.307
8	19	8.01	8.06	32	20	21.9	0.411	22	0.257
8	20	8.04	8.09	32	21	38.6	0.361	24.4	0.278

8	21	7.93	8.07	32	34	39.0	0.381	25	0.290
8	22	8	8.08	32	31	34.9	0.419	26.2	0.306
8	23	8.07	8.08	32	32	24.7	0.383	23.2	0.266
8	24	7.98	8.05	32	27	20.6	0.442	24.7	0.292
8	25	7.95	8.04	32	30	33.5	0.400	25.8	0.302
8	26	7.9	8.1	32	34	31.8	0.370	22.7	0.262
8	27	7.92	8.13	32	36	38.9	0.407	25.5	0.296
8	28	7.9	8.03	32	27	34.1	0.387	20.1	0.235
8	29	7.89	8.04	32	14	36.2	0.200	24.2	0.265
8	30	8.02	8.06	32	20	35.3	0.380	26.1	0.301
8	31	7.98	8.01	32	14	39.1	0.179	27	0.293
8	32	8.02	8.05	32	12	37.8	0.219	24.6	0.269
8	33	8	8.05	32	10	34.2	0.294	24.9	0.279
8	34	7.94	8.03	32	9	53.6	0.165	25	0.270
8	35	7.96	8.03	32	14	40.4	0.211	25.2	0.276
8	36	8.05	8.06	32	15	36.6	0.225	23	0.251
8	37	8.03	8.04	32	15	43.7	0.224	24.2	0.265
8	38	7.99	8.05	32	15	36.2	0.302	23.3	0.262
8	39	8.02	8.06	32	20	30.7	0.229	22.1	0.242
15	1	15.02	15.26	60	44	83.5	0.376	75.8	0.338
15	2	15.03	15.36	60	24	23.8	0.350	77.2	0.340
15	3	15.04	15.31	60	20	21.3	0.403	68.2	0.305
15	4	15.01	15.31	60	31	34.9	0.350	86.8	0.384
15	5	15	15.3	60	31	41.6	0.377	73.7	0.328
15	6	15.06	15.37	60	40	31.5	0.457	78.7	0.354
15	7	15.02	15.17	60	28	35.3	0.427	81.6	0.370
15	8	15	15.31	60	30	33.8	0.426	76.1	0.342

15	9	15.04	15.35	60	30	35.7	0.444	81.6	0.366
15	10	15.01	15.22	60	28	29.2	0.387	71.8	0.322
15	11	15.01	15.27	60	30	34.4	0.414	81.6	0.367
15	12	15.09	15.28	60	33	46.2	0.457	88.5	0.400
15	13	15.02	15.31	60	40	38.4	0.391	69.7	0.311
15	14	15.01	15.28	60	20	29.4	0.388	71.5	0.319
15	15	15.01	15.36	60	31	25.7	0.348	91.5	0.404
15	16	15.08	15.32	60	24	33.4	0.403	84.5	0.377
15	17	15.06	15.31	60	30	30.2	0.483	83.6	0.379
15	18	15.04	15.28	60	17	43.6	0.396	87.6	0.392
15	19	15.08	15.29	60	41	42.3	0.442	78.1	0.351
15	20	15.04	15.24	60	27	37.0	0.440	83.3	0.376
15	21	15.02	15.17	60	24	53.0	0.377	96.1	0.431
15	22	15.01	15.32	60	33	24.9	0.502	90.9	0.414
15	23	15.02	15.35	60	66	59.7	0.370	89.4	0.396
15	24	15.05	15.4	60	30	27.8	0.495	82.7	0.374
15	25	15.03	15.24	60	33	47.8	0.369	97	0.433
15	26	15.03	15.27	60	24	33.6	0.563	87.6	0.405
15	27	15.06	15.33	60	30	38.6	0.400	88.5	0.394
15	28	15.03	15.3	60	38	34.8	0.433	83	0.373
15	29	15.01	15.33	60	50	19.0	0.421	83.6	0.375
15	30	15.01	15.26	60	15	47.9	0.184	74.4	0.320
15	31	15.04	15.3	60	24	51.9	0.383	75.5	0.336
15	32	15.02	15.34	60	12	34.3	0.262	92.3	0.401
15	33	15.03	15.33	60	13	38.0	0.254	85.7	0.372
15	34	15.05	15.22	60	21	64.4	0.300	80.5	0.355
15	35	15.03	15.18	60	13	54.4	0.181	79.3	0.343
15	36	15.01	15.38	60	13	33.3	0.236	79.6	0.343

15	37	15.02	15.23	60	12	43.4	0.267	88.9	0.389
15	38	15.02	15.33	60	13	48.8	0.185	85.7	0.367
15	39	15.05	15.31	60	15	41.7	0.197	88.3	0.379
15	40	15.01	15.25	60	11	43.4	0.249	75.6	0.330
15	41	15	15.29	60	12	30.7	0.300	83.7	0.368
15	42	15.03	15.28	60	18	36.1	0.219	84.5	0.366
15	43	15.03	15.28	60	15	35.3	0.255	84.8	0.369
30	1	30.12	30.27	120	32	41.7	0.408	230	0.367
30	2	30.09	30.25	120	30	41.4	0.466	295.6	0.475
30	3	30.11	30.17	120	41	32.5	0.551	278.8	0.453
30	4	30.1	30.3	120	24	72.6	0.369	294.7	0.469
30	5	30.11	30.41	120	37	46.8	0.378	307.7	0.488
30	6	30.1	30.27	120	47	37.4	0.436	312.1	0.500
30	7	30.18	30.41	120	43	38.6	0.506	285.1	0.457
30	8	30.03	30.37	120	31	27.4	0.423	262.2	0.419
30	9	30.12	30.35	120	32	54.0	0.427	275.2	0.439
30	10	30.13	30.49	120	41	35.7	0.446	284	0.452
30	11	30	30.3	120	40	46.1	0.423	310.1	0.496
30	12	30.01	30.3	120	37	44.4	0.400	277	0.442
30	13	30.02	30.22	120	27	39.0	0.433	287.1	0.461
30	14	30.02	30.41	120	24	25.4	0.363	288	0.457
30	15	30.18	30.31	120	76	59.8	0.402	270.8	0.431
30	16	30.06	30.24	120	47	60.7	0.387	275.8	0.440
30	17	30.08	30.47	120	32	30.7	0.435	297.6	0.474
30	18	30.14	30.27	120	33	33.4	0.472	272.9	0.438
30	19	30.02	30.39	120	37	34.3	0.463	255	0.408
30	20	30.08	30.28	120	37.4	40	0.485	302.5	0.487

30	21	30.16	30.32	120	27	29.3	0.405	265.6	0.423
30	22	30.07	30.36	120	32	61.7	0.400	283.4	0.451
30	23	30.11	30.23	120	44	53.7	0.397	257.2	0.411
30	24	30.03	30.3	120	42	45.6	0.370	268	0.427
30	25	30.03	30.41	120	60	55.4	0.360	234.8	0.372
30	26	30.1	30.38	120	40	40.3	0.369	260.4	0.413
30	27	30.14	30.44	120	24	47.7	0.470	257.5	0.411
30	28	29.98	30.34	120	47	48.5	0.607	259.3	0.422
30	29	30.08	30.33	120	24	25.4	0.363	249.1	0.396
30	30	30.07	30.14	120	37	43.2	0.443	248.8	0.401
30	31	30.11	30.44	120	47	49.3	0.697	242.1	0.395
30	32	30.03	30.39	120	37	74.8	0.297	278.4	0.439
30	33	30.12	30.2	120	50	50.2	0.570	264.8	0.430
30	34	30	30.39	120	44	55.3	0.588	292	0.473
30	35	30.05	30.55	120	47	39.6	0.821	253.1	0.417
30	36	30.11	30.44	120	33	47.3	0.771	244.2	0.402
30	37	30.07	30.29	120	51	53.2	0.347	265.6	0.422
30	38	30.04	30.35	120	33	54.5	0.393	262.1	0.417
30	39	30.1	30.3	120	38	38.9	0.694	277.2	0.455
30	40	30.03	30.18	120	30	34.9	0.483	250.2	0.404
30	41	30.05	30.42	120	17	26.2	0.231	273.2	0.427
30	42	30.04	30.26	120	31	38.7	0.460	266.2	0.428

Table A 5. SENB specimen notch averages and standard deviations

	Sharp Notch Radius (µm)	Sharp Notch Angle (°)	Sharp Notch Depth (mm)
Average	29.6	39.7	0.391
Standard Dev.	11.9	11.1	0.111

Discs

The disc dimensions can be seen here. They include thicknesses measured in four places (a, b, c, d) and diameters measured in four places as well as the length of the squares, corner to corner (notches).

Table A 6. Disc dimensions, 74mm discs

74mm	Thicknesses (mm)					Diameters (mm)					Notches (mm)		
Specimen	**a**	**b**	**c**	**d**	**Average**	**1 (a,c)**	**2**	**3 (d,b)**	**4**	**Average**	**a,c**	**d,b**	**Average**
74-1	7.43	7.43	7.45	7.44	*7.44*	74.35	74.39	74.46	74.37	*74.39*	29.89	29.97	*29.93*
74-2	7.43	7.46	7.48	7.49	*7.47*	74.42	74.22	74.23	74.27	*74.29*	30.13	29.83	*29.98*
74-3	7.45	7.44	7.46	7.44	*7.45*	74.29	74.33	74.38	74.26	*74.32*	30.02	30.07	*30.05*
74-4	7.48	7.50	7.45	7.45	*7.47*	74.18	74.70	74.29	74.08	*74.31*	30.07	30.25	*30.16*
74-5	7.42	7.49	7.48	7.38	*7.44*	74.22	74.26	74.35	74.45	*74.32*	29.96	29.93	*29.95*
74-6	7.47	7.42	7.45	7.44	*7.45*	74.18	74.35	74.19	74.09	*74.20*	29.84	30.31	*30.08*
74-7	7.46	7.49	7.45	7.45	*7.46*	74.44	74.10	74.29	74.56	*74.35*	30.09	30.07	*30.08*
74-8	7.41	7.42	7.42	7.39	*7.41*	74.22	74.43	74.23	74.22	*74.28*	30.23	29.99	*30.11*
74-9	7.46	7.40	7.45	7.52	*7.46*	74.40	74.18	74.42	74.55	*74.39*	29.84	30.17	*30.01*
74-10	7.52	7.47	7.48	7.53	*7.50*	74.31	74.41	74.16	74.22	*74.28*	30.00	30.27	*30.14*
74-11	7.38	7.44	7.42	7.40	*7.41*	74.11	74.22	74.19	74.33	*74.21*	30.24	29.99	*30.12*
74-12	7.40	7.40	7.43	7.45	*7.42*	74.23	74.27	74.63	74.45	*74.40*	30.19	30.00	*30.10*
74-13	7.47	7.49	7.50	7.50	*7.49*	74.50	74.54	74.20	74.24	*74.37*	29.86	30.20	*30.03*
74-14	7.46	7.51	7.50	7.41	*7.47*	74.38	74.36	74.19	74.11	*74.26*	29.91	30.21	*30.06*
74-15	7.38	7.36	7.41	7.47	*7.41*	74.30	74.45	74.27	74.26	*74.32*	30.00	30.14	*30.07*
74-16	7.41	7.51	7.47	7.41	*7.45*	74.29	74.15	74.37	74.38	*74.30*	29.97	30.21	*30.09*
74-17	7.38	7.35	7.40	7.43	*7.39*	74.25	74.31	74.07	74.25	*74.22*	29.91	30.35	*30.13*
74-18	7.40	7.42	7.40	7.37	*7.40*	74.28	74.15	74.13	74.34	*74.23*	29.93	30.28	*30.11*
74-19	7.46	7.47	7.44	7.43	*7.45*	74.31	74.40	74.29	74.28	*74.32*	30.06	30.18	*30.12*
74-20	7.47	7.49	7.47	7.50	*7.48*	74.22	74.21	74.18	74.19	*74.20*	29.98	29.99	*29.99*
74-21	7.38	7.45	7.43	7.41	*7.42*	74.09	74.21	74.49	74.30	*74.27*	30.11	30.12	*30.12*
74-22	7.47	7.43	7.46	7.45	*7.45*	74.36	74.35	74.16	74.22	*74.27*	30.04	29.94	*29.99*

74-23	7.46	7.37	7.44	7.50	*7.44*	74.30	74.34	74.40	74.18	*74.31*	30.28	29.82	*30.05*
74-24	7.50	7.51	7.49	7.50	*7.50*	74.24	74.30	74.33	74.36	*74.31*	30.08	30.06	*30.07*
74-25	7.36	7.38	7.37	7.38	*7.37*	74.32	74.43	74.46	74.25	*74.37*	29.98	30.31	*30.15*
74-26	7.47	7.49	7.47	7.45	*7.47*	74.30	74.11	74.30	74.28	*74.25*	30.03	30.02	*30.03*
74-27	7.49	7.50	7.48	7.48	*7.49*	74.18	74.34	74.28	74.29	*74.27*	30.17	29.91	*30.04*
74-28	7.51	7.50	7.52	7.53	*7.52*	74.40	74.21	74.52	74.65	*74.45*	29.76	30.25	*30.01*
74-29	7.42	7.40	7.41	7.38	*7.40*	74.31	74.21	74.29	74.29	*74.28*	29.99	30.32	*30.16*
74-30	7.43	7.50	7.48	7.43	*7.46*	74.41	74.35	74.26	74.42	*74.36*	30.10	30.18	*30.14*
74-31	7.52	7.54	7.50	7.48	*7.51*	74.34	74.19	74.21	74.34	*74.27*	29.85	30.13	*29.99*
74-32	7.52	7.47	7.49	7.53	*7.50*	74.30	74.16	74.45	74.53	*74.36*	29.98	30.05	*30.02*
74-33	7.47	7.52	7.47	7.50	*7.49*	74.28	74.34	74.44	74.36	*74.36*	30.17	29.91	*30.04*
74-34	7.43	7.42	7.41	7.44	*7.43*	74.15	74.50	74.61	74.29	*74.39*	29.94	30.10	*30.02*
74-35	7.28	7.24	7.31	7.30	*7.28*	74.27	74.31	74.17	74.25	*74.25*	29.89	30.19	*30.04*
74-36	7.42	7.43	7.41	7.38	*7.41*	74.14	74.29	74.40	74.24	*74.27*	30.15	30.00	*30.08*
74-37	7.55	7.47	7.51	7.54	*7.52*	74.16	74.18	74.27	74.34	*74.24*	30.16	29.74	*29.95*
74-38	7.44	7.48	7.42	7.45	*7.45*	74.13	74.19	74.63	74.34	*74.32*	30.22	29.92	*30.07*
74-39	7.45	7.46	7.46	7.51	*7.47*	74.32	74.45	74.37	74.33	*74.37*	29.99	30.01	*30.00*
74-40	7.47	7.50	7.51	7.51	*7.50*	74.15	74.14	74.40	74.29	*74.25*	30.07	30.01	*30.04*
				Average	***7.45***				Average	***74.30***		Average	***30.06***
				st. dev.	0.045435				st. dev.	0.059416		st. dev.	0.059447
				% st dev	0.61%				% st dev	0.08%		% st dev	0.20%

Table A 7. Disc dimensions, 155mm discs

155mm	Thicknesses (mm)					Diameters (mm)					Notches (mm)		
Specimen	**a**	**b**	**c**	**d**	**Average**	**1 (a,c)**	**2**	**3 (d,b)**	**4**	**Average**	**a,c**	**d,b**	**Average**
155-1	15.45	15.56	15.35	15.36	*15.43*	154.64	154.11	155.09	155.26	*154.78*	61.99	62.00	*62.00*
155-2	15.23	15.32	15.30	15.01	*15.22*	154.09	154.10	155.74	155.18	*154.78*	62.00	62.01	*62.01*
155-3	15.02	14.92	15.26	15.18	*15.10*	154.05	155.04	155.44	154.46	*154.75*	62.06	62.08	*62.07*
155-4	15.33	15.43	15.51	15.63	*15.48*	154.64	155.80	154.45	153.93	*154.71*	62.05	62.03	*62.04*
155-5	15.29	15.07	15.18	15.32	*15.22*	154.39	154.23	155.11	155.21	*154.74*	62.04	61.96	*62.00*
155-6	15.25	15.05	15.10	15.03	*15.11*	155.29	154.40	154.19	155.18	*154.77*	62.00	62.00	*62.00*
155-7	15.00	15.08	15.15	14.80	*15.01*	154.40	155.49	155.48	154.34	*154.93*	62.14	61.99	*62.07*
155-8	14.90	14.16	14.93	14.95	*14.74*	153.85	154.74	155.68	154.53	*154.70*	61.99	61.95	*61.97*
155-9	15.39	15.65	15.30	15.28	*15.41*	153.97	155.27	155.55	154.07	*154.72*	61.97	61.94	*61.96*
155-10	15.27	15.16	15.57	15.30	*15.33*	154.74	154.40	154.55	155.59	*154.82*	62.29	62.11	*62.20*
155-11	15.33	15.59	15.31	15.56	*15.45*	154.51	155.50	154.84	154.34	*154.80*	62.08	61.84	*61.96*
155-12	15.30	14.81	15.00	15.13	*15.06*	154.46	154.98	154.90	154.59	*154.73*	61.90	61.66	*61.78*
155-13	15.62	15.38	15.54	15.70	*15.56*	153.72	154.86	155.54	154.69	*154.70*	62.13	62.00	*62.07*
155-14	15.38	15.35	15.31	15.18	*15.31*	154.76	155.16	154.65	154.34	*154.73*	62.02	62.08	*62.05*
155-15	15.25	14.76	15.18	14.91	*15.03*	154.52	155.09	154.15	154.05	*154.45*	62.10	61.88	*61.99*
155-16	15.29	15.08	15.30	15.51	*15.30*	154.62	155.82	154.43	154.01	*154.72*	61.98	62.05	*62.02*
155-17	15.13	15.20	15.27	14.95	*15.14*	154.71	154.44	154.55	155.57	*154.82*	61.94	61.99	*61.97*
				Average	**15.23**				Average	**154.74**		Average	**62.01**
				st. dev.	0.216105				st. dev.	0.095183		st. dev.	0.085293
				% st dev	1.42%				% st dev	0.06%		% st dev	0.14%

Table A 8. Disc dimensions, 290mm discs

290mm	Thicknesses (mm)					Diameters (mm)					Notches (mm)		
Specimen	**a**	**b**	**c**	**d**	**Average**	**1 (a,c)**	**2**	**3 (d,b)**	**4**	**Average**	**a,c**	**d,b**	**Average**
290-1	28.60	28.82	28.56	28.40	*28.60*	291.07	291.07	290.48	290.99	*290.90*	116.09	116.40	*116.25*
290-2	28.99	28.99	29.07	28.89	*28.99*	291.08	291.47	290.57	290.56	*290.92*	115.88	116.00	*115.94*
290-3	29.36	29.35	29.40	29.02	*29.28*	290.94	290.87	290.73	291.00	*290.89*	116.34	116.10	*116.22*
290-4	29.07	29.35	29.33	29.86	*29.40*	290.86	290.95	290.90	291.04	*290.94*	115.95	116.37	*116.16*
290-5	29.09	28.90	28.93	29.30	*29.06*	291.18	290.80	290.61	291.49	*291.02*	115.93	116.06	*116.00*
290-6	29.25	28.65	29.44	29.39	*29.18*	290.56	290.84	291.37	290.80	*290.89*	116.32	116.11	*116.22*
290-7	28.06	27.96	28.63	29.01	*28.42*	291.06	290.88	291.00	290.87	*290.95*	116.01	116.05	*116.03*
290-8	29.30	29.58	29.03	28.88	*29.20*	290.75	290.90	291.16	290.95	*290.94*	115.86	116.32	*116.09*
290-9	29.20	28.66	29.51	28.66	*29.01*	291.20	290.67	290.88	290.95	*290.93*	116.01	116.05	*116.03*
290-10	29.07	28.94	29.12	29.05	*29.05*	290.95	290.97	291.12	291.00	*291.01*	116.07	116.35	*116.21*
290-11	29.29	28.18	28.18	28.54	*28.55*	291.27	290.82	290.34	291.02	*290.86*	116.18	115.91	*116.05*
290-12	29.01	28.90	28.87	28.73	*28.88*	290.92	290.88	291.05	291.07	*290.98*	116.06	116.30	*116.18*
290-13	29.04	28.99	29.00	28.98	*29.00*	290.69	291.38	291.02	291.01	*291.03*	116.06	116.36	*116.21*
290-14	29.01	28.99	29.00	28.73	*28.93*	290.65	290.58	290.97	291.03	*290.81*	116.38	116.13	*116.26*
290-15	29.09	28.91	28.91	28.92	*28.96*	290.60	291.02	291.30	290.89	*290.95*	116.11	116.09	*116.10*
				Average	**28.99**				Average	**290.93**		Average	**116.13**
				st. dev.	0.262571				st. dev.	0.0582		st. dev.	0.09811
				% st dev	0.91%				% st dev	0.02%		% st dev	0.08%

The perfect disc would have a thickness/diameter ratio of 0.1 and a notch/diameter ratio of 0.4. The average ratios are shown in Table A 9.

Table A 9.True disc dimension ratios

Ratios	**t/d**	**n/d**
74	0.1003	0.4045
155	0.0984	0.4007
290	0.0997	0.3992

Appendix B

Drawings for parts, such as moulds and other apparatus, are on the following pages.

PART NUMBER	DESCRIPTION	QTY.
CUBOID-8-01	Interstitial Piece, 8mm	16
CUBOID-8-02	Front Plate, 8mm	1
CUBOID-8-03	Back Plate, 8mm	1
CUBOID-8-04	Lower Piece, 8mm	1
M6x35		39

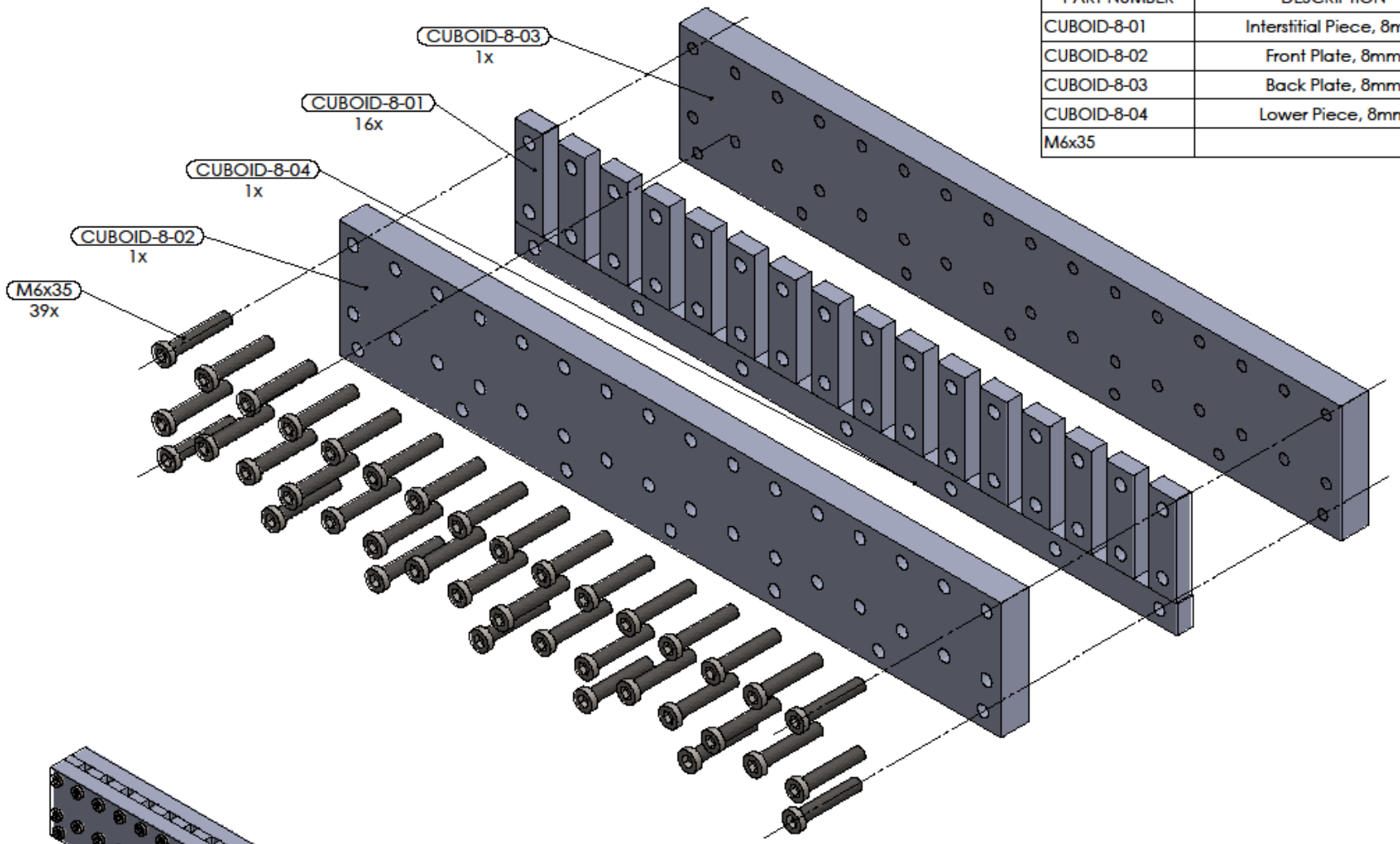

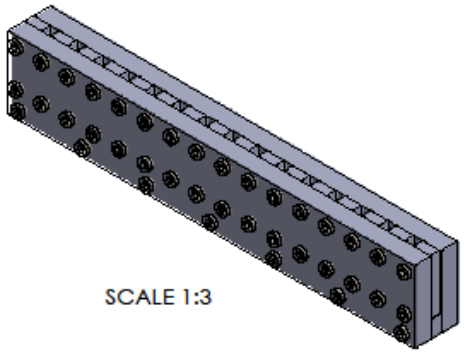

SCALE 1:3

UNLESS OTHERWISE SPECIFIED:
DIMENSIONS ARE IN MILLIMETERS
SURFACE FINISH: 3.2 µm Ra
TOLERANCES:
LINEAR: ± 0.1
ANGULAR: ± 0.5

FINISH: CLEAN

DEBUR AND BREAK SHARP EDGES

DO NOT SCALE DRAWING | REVISION 1A

	NAME	SIGNATURE	DATE
DRAWN	G.JOWASOWSKI		
CHK'D	G.JOWASOWSKI		
APPV'D	G.JOWASOWSKI		
MFG	WORKSHOP		
Q.A	G.JOWASOWSKI		

MATERIAL: PVC, GREY

TITLE: Cuboid Mould, 8mm

DWG NO. CUBOID-8-00 | A3

SCALE:2:3 | SHEET 1 OF 1

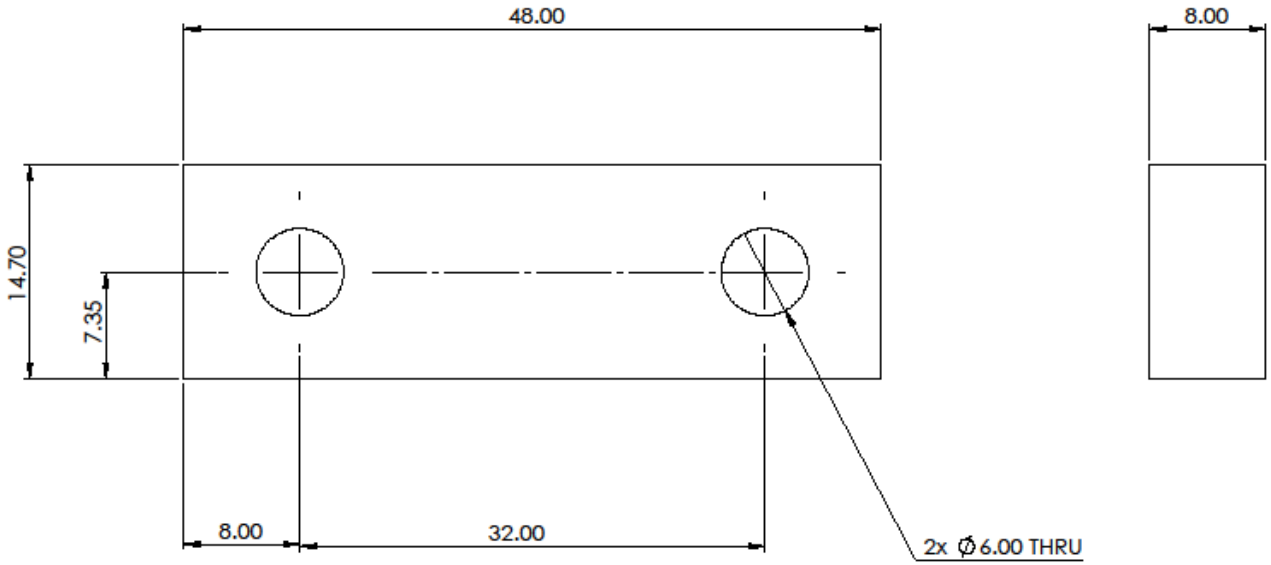

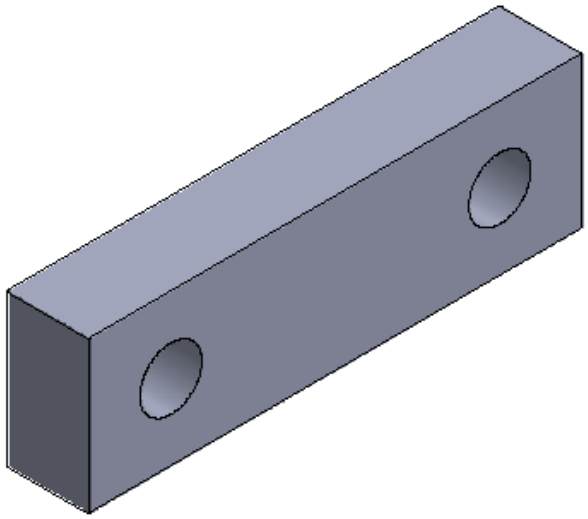

UNLESS OTHERWISE SPECIFIED: DIMENSIONS ARE IN MILLIMETERS SURFACE FINISH: 3.2 µm Ra TOLERANCES: LINEAR: ± 0.1 ANGULAR: ± 0.5	FINISH: CLEAN				DEBUR AND BREAK SHARP EDGES	DO NOT SCALE DRAWING / REVISION 1A
	NAME	SIGNATURE	DATE			TITLE: Interstitial Part, 8mm
DRAWN	G.JOWASOWSKI					
CHK'D	G.JOWASOWSKI					
APPV'D	G.JOWASOWSKI					
MFG	WORKSHOP					
Q.A	G.JOWASOWSKI			MATERIAL: PVC, GREY		DWG NO. CUBOID-8-01 / A3
						SCALE:3:1 / SHEET 1 OF 1

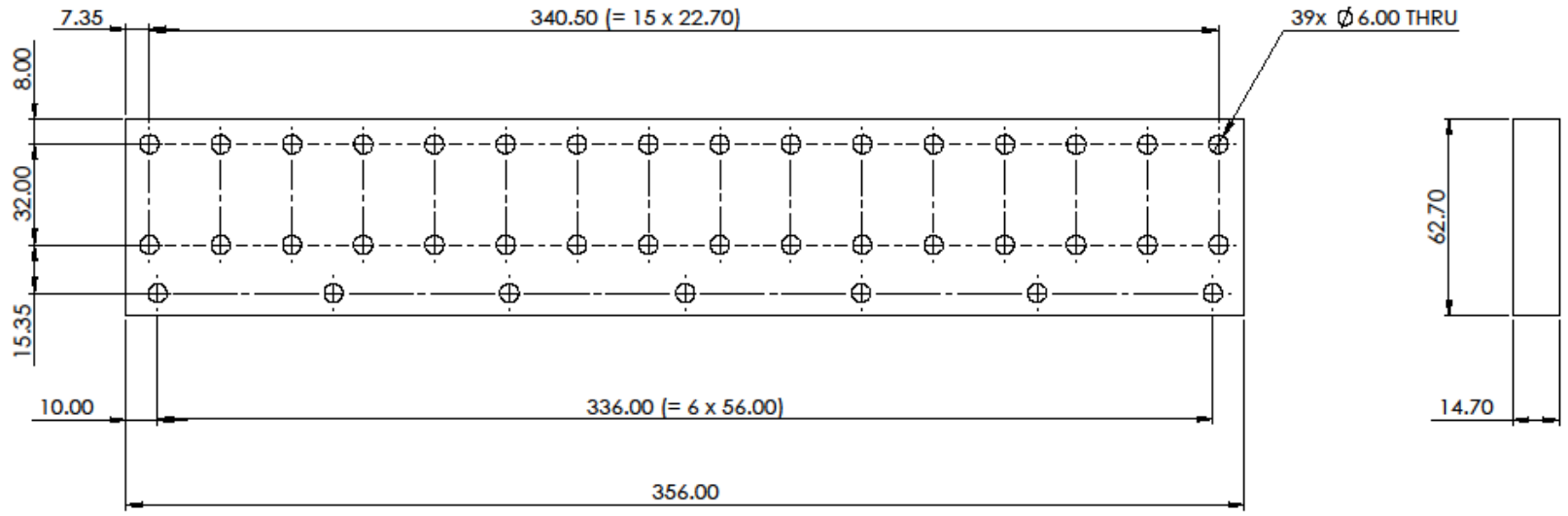

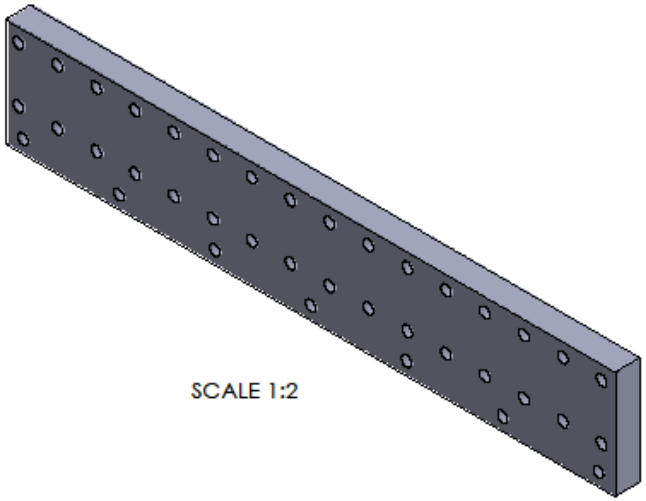

SCALE 1:2

UNLESS OTHERWISE SPECIFIED: DIMENSIONS ARE IN MILLIMETERS SURFACE FINISH: 3.2 µm Ra TOLERANCES: LINEAR: ± 0.1 ANGULAR: ± 0.5	FINISH: CLEAN			DEBUR AND BREAK SHARP EDGES	DO NOT SCALE DRAWING	REVISION 1A
	NAME	SIGNATURE	DATE		TITLE: Front Plate, 8mm	
DRAWN	G.JOWASOWSKI					
CHK'D	G.JOWASOWSKI					
APPV'D	G.JOWASOWSKI					
MFG	WORKSHOP					
Q.A	G.JOWASOWSKI			MATERIAL: PVC, GREY	DWG NO. CUBOID-8-02	A3
					SCALE:2:3	SHEET 1 OF 1

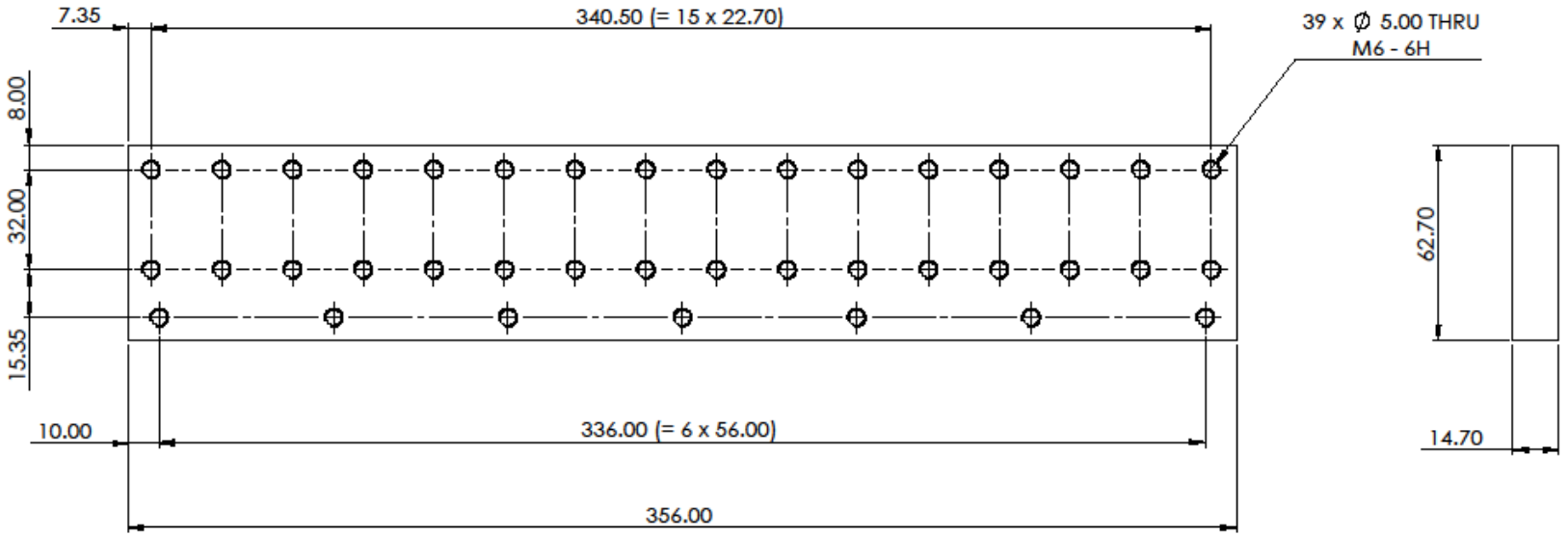

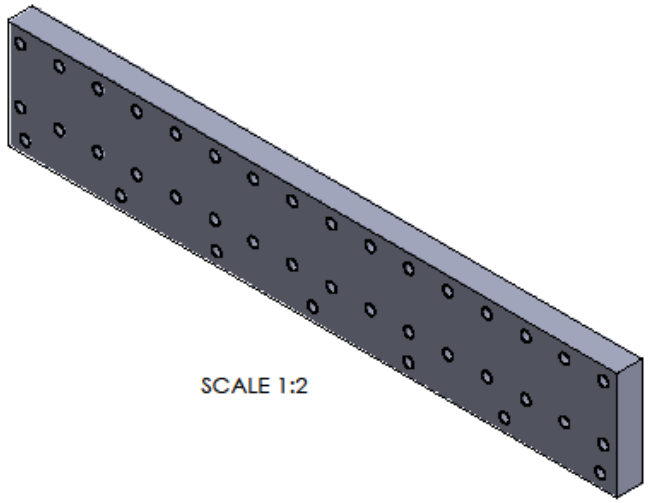

SCALE 1:2

UNLESS OTHERWISE SPECIFIED: DIMENSIONS ARE IN MILLIMETERS SURFACE FINISH: 3.2 µm Ra TOLERANCES: LINEAR: ± 0.1 ANGULAR: ± 0.5	FINISH: CLEAN				DEBUR AND BREAK SHARP EDGES	DO NOT SCALE DRAWING / REVISION 1A
	NAME	SIGNATURE	DATE			TITLE: Back Plate, 8mm
DRAWN	G.JOWASOWSKI					
CHK'D	G.JOWASOWSKI					
APPV'D	G.JOWASOWSKI					
MFG	WORKSHOP					
Q.A	G.JOWASOWSKI			MATERIAL: PVC, GREY		DWG NO. CUBOID-8-03 / A3
						SCALE:2:3 / SHEET 1 OF 1

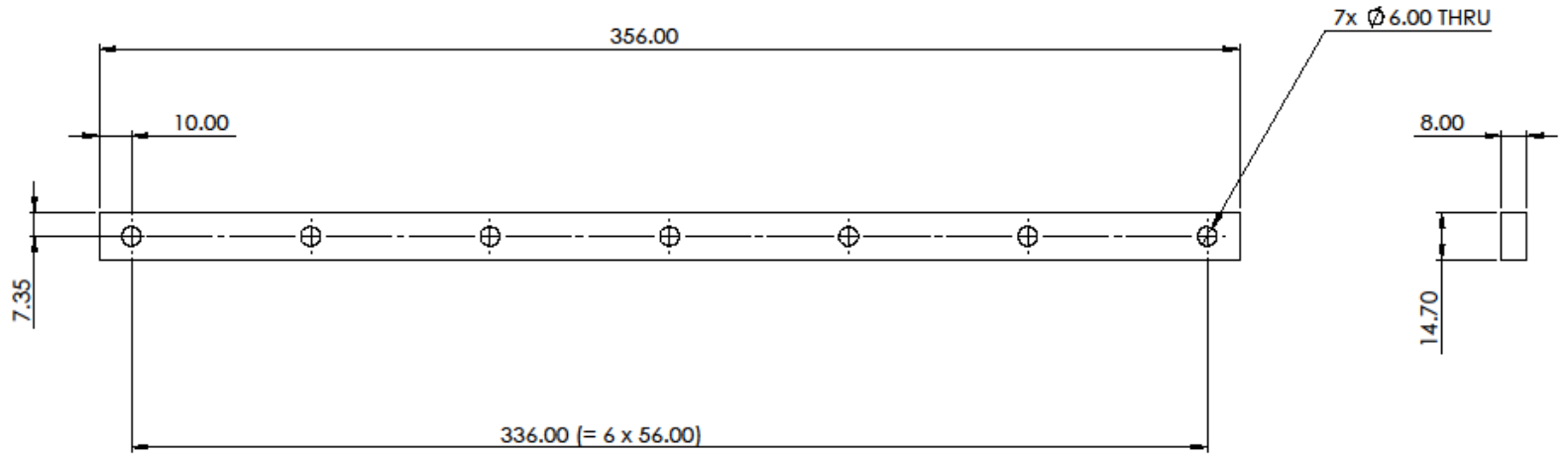

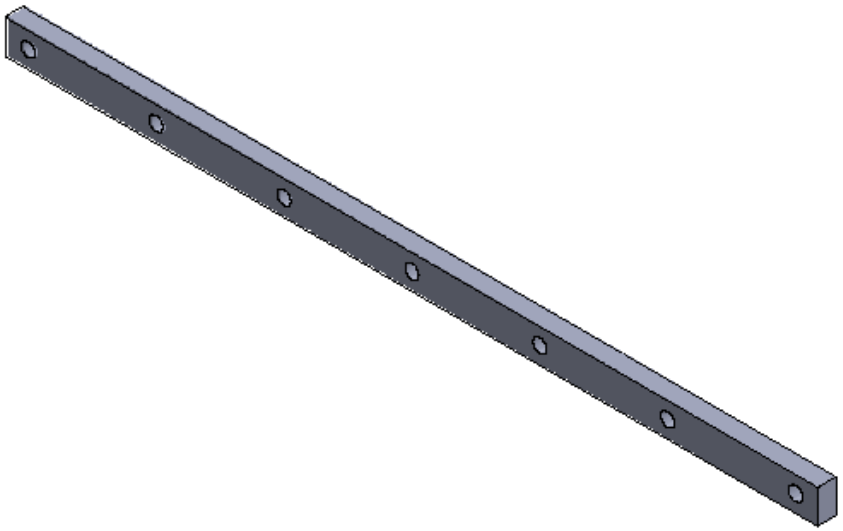

UNLESS OTHERWISE SPECIFIED: DIMENSIONS ARE IN MILLIMETERS SURFACE FINISH: 3.2 µm Ra TOLERANCES: LINEAR: ± 0.1 ANGULAR: ± 0.5	FINISH: CLEAN			DEBUR AND BREAK SHARP EDGES	DO NOT SCALE DRAWING	REVISION 1A
	NAME	SIGNATURE	DATE		TITLE: Lower Piece, 8mm	
DRAWN	G.JOWASOWSKI					
CHK'D	G.JOWASOWSKI					
APPV'D	G.JOWASOWSKI					
MFG	WORKSHOP					
Q.A	G.JOWASOWSKI			MATERIAL: PVC, GREY	DWG NO. CUBOID-8-04	A3
					SCALE:2:3	SHEET 1 OF 1

PART NUMBER	DESCRIPTION	QTY.
CUBOID-15-01	Interstitial Piece, 15mm	16
CUBOID-15-02	Front Plate, 15mm	1
CUBOID-15-03	Back Plate, 15mm	1
CUBOID-15-04	Lower Piece, 15mm	1
M6x45		39

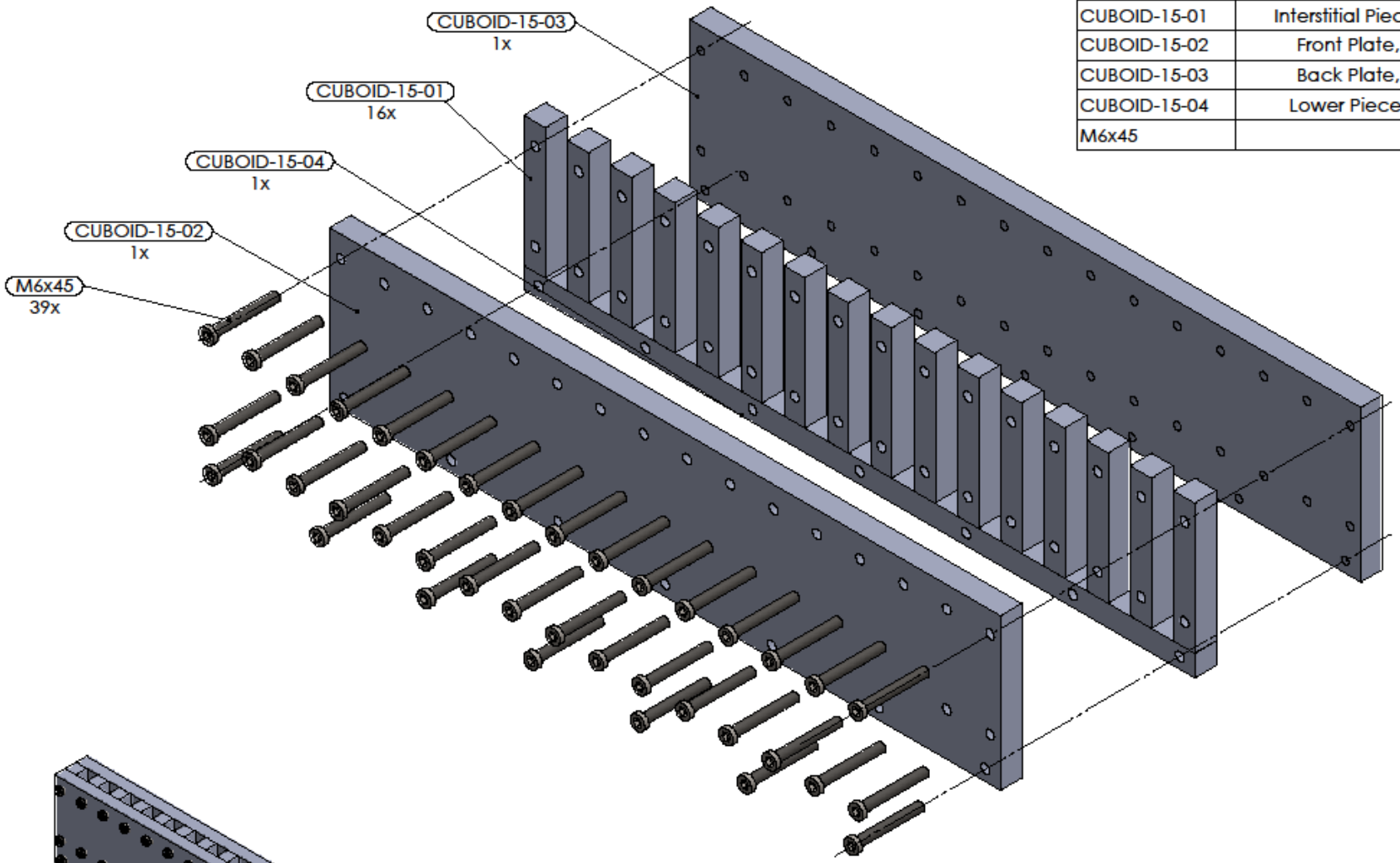

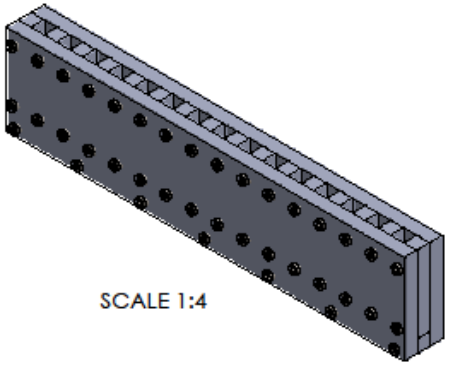

SCALE 1:4

UNLESS OTHERWISE SPECIFIED:
DIMENSIONS ARE IN MILLIMETERS
SURFACE FINISH: 3.2 µm Ra
TOLERANCES:
LINEAR: ± 0.1
ANGULAR: ± 0.5

FINISH: CLEAN

DEBUR AND BREAK SHARP EDGES

DO NOT SCALE DRAWING | REVISION 1A

	NAME	SIGNATURE	DATE
DRAWN	G.JOWASOWSKI		
CHK'D	G.JOWASOWSKI		
APPV'D	G.JOWASOWSKI		
MFG	WORKSHOP		
Q.A	G.JOWASOWSKI		

MATERIAL: PVC, GREY

TITLE: Cuboid Mould, 15mm

DWG NO. CUBOID-15-00 | A3

SCALE:1:2 | SHEET 1 OF 1

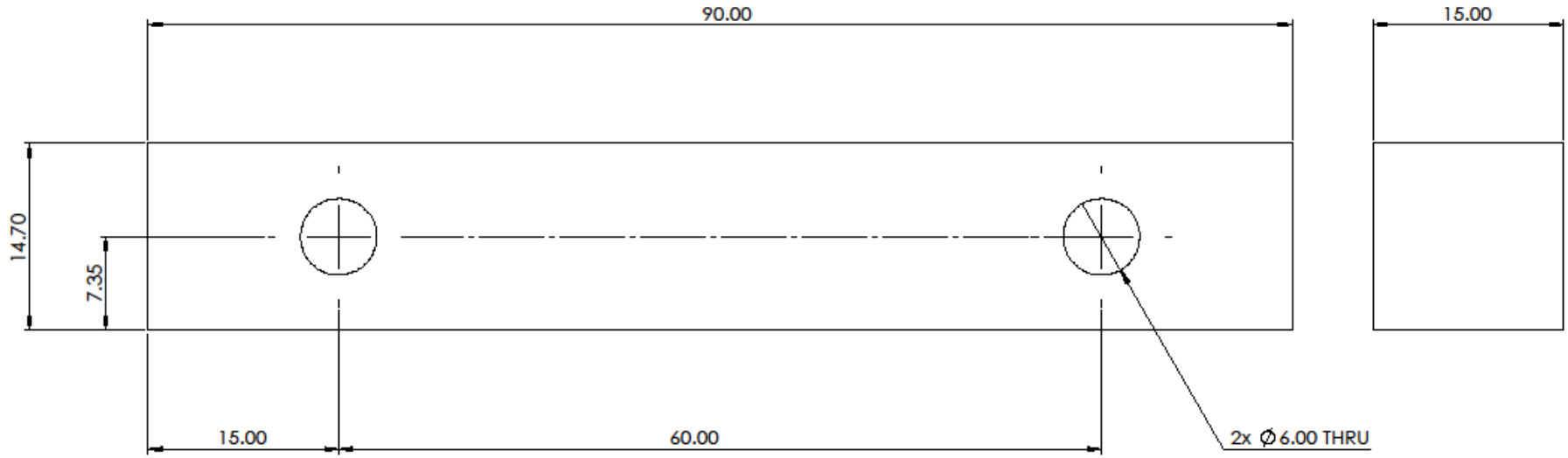

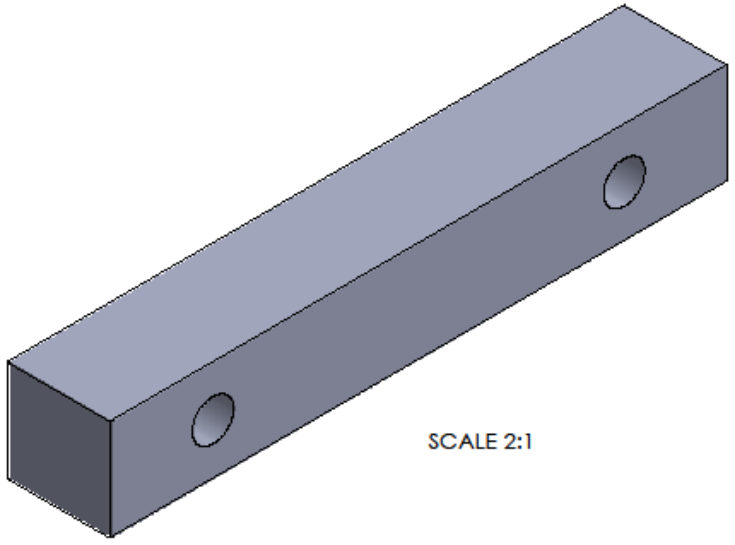

SCALE 2:1

UNLESS OTHERWISE SPECIFIED: DIMENSIONS ARE IN MILLIMETERS SURFACE FINISH: 3.2 µm Ra TOLERANCES: LINEAR: ± 0.1 ANGULAR: ± 0.5		FINISH: CLEAN		DEBUR AND BREAK SHARP EDGES	DO NOT SCALE DRAWING	REVISION 1A
	NAME	SIGNATURE	DATE		TITLE: Interstitial Part, 15mm	
DRAWN	G.JOWASOWSKI					
CHK'D	G.JOWASOWSKI					
APPV'D	G.JOWASOWSKI					
MFG	WORKSHOP					
Q.A	G.JOWASOWSKI			MATERIAL: PVC, GREY	DWG NO. CUBOID-15-01	A3
					SCALE:3:1	SHEET 1 OF 1

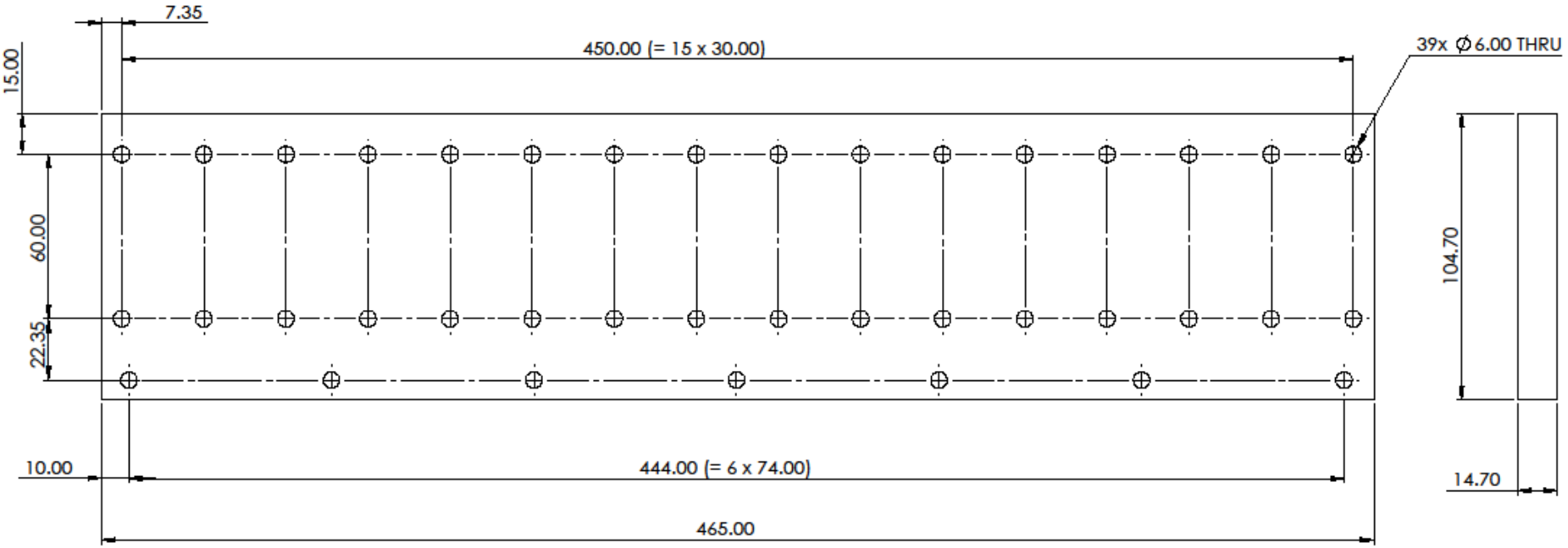

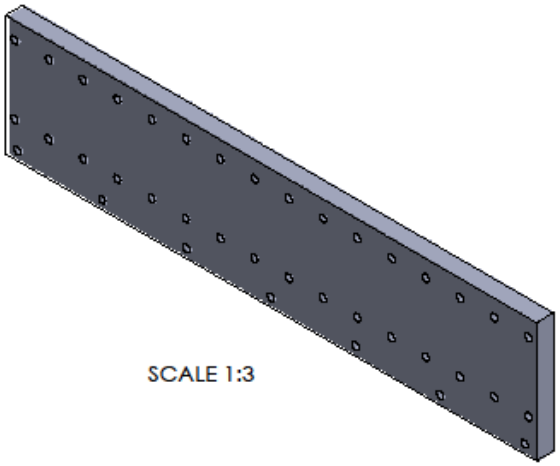

SCALE 1:3

UNLESS OTHERWISE SPECIFIED: DIMENSIONS ARE IN MILLIMETERS SURFACE FINISH: 3.2 µm Ra TOLERANCES: LINEAR: ± 0.1 ANGULAR: ± 0.5		FINISH: CLEAN		DEBUR AND BREAK SHARP EDGES	DO NOT SCALE DRAWING	REVISION 1A
	NAME	SIGNATURE	DATE		TITLE: Front Plate, 15mm	
DRAWN	G.JOWASOWSKI					
CHK'D	G.JOWASOWSKI					
APPV'D	G.JOWASOWSKI					
MFG	WORKSHOP					
Q.A	G.JOWASOWSKI			MATERIAL: PVC, GREY	DWG NO. CUBOID-15-02	A3
					SCALE:2:3	SHEET 1 OF 1

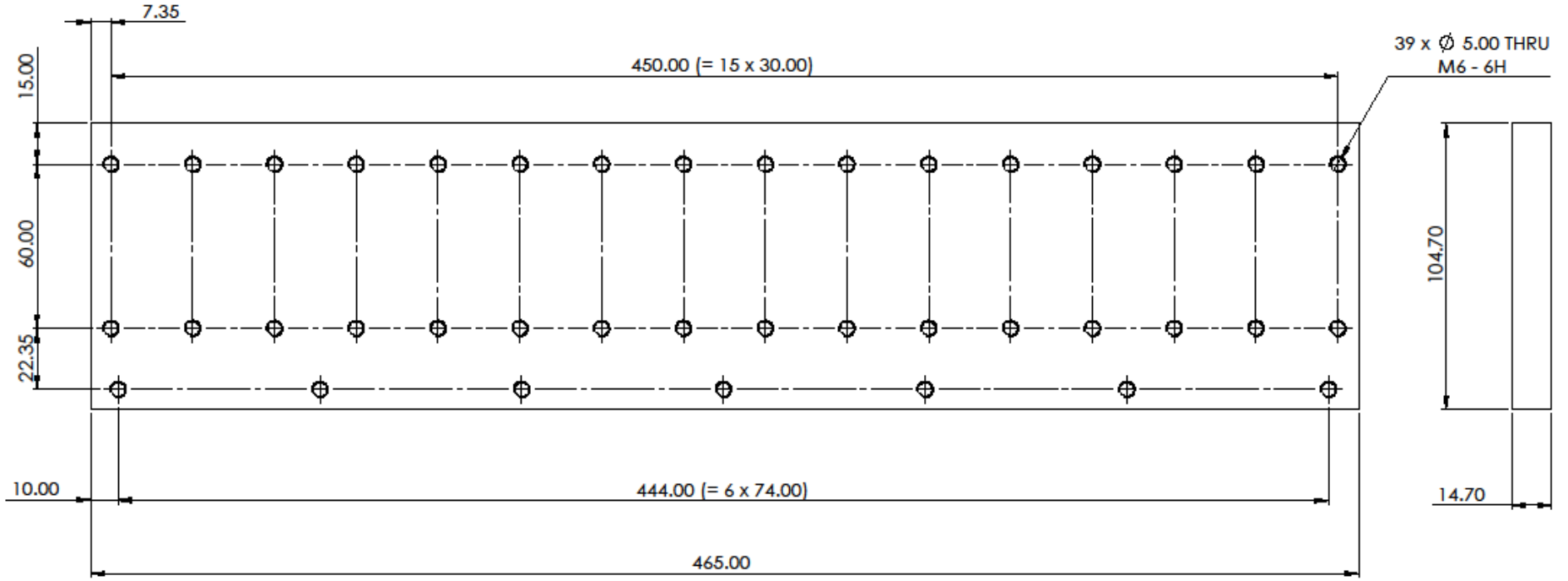

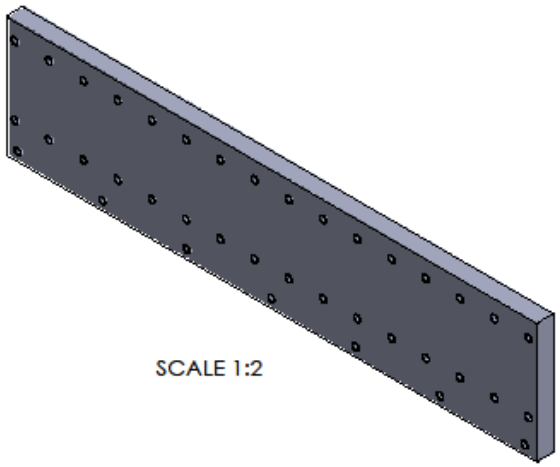

SCALE 1:2

UNLESS OTHERWISE SPECIFIED: DIMENSIONS ARE IN MILLIMETERS SURFACE FINISH: 3.2 µm Ra TOLERANCES: LINEAR: ± 0.1 ANGULAR: ± 0.5		FINISH: CLEAN		DEBUR AND BREAK SHARP EDGES		DO NOT SCALE DRAWING / REVISION 1A
	NAME	SIGNATURE	DATE			TITLE: Back Plate, 15mm
DRAWN	G.JOWASOWSKI					
CHK'D	G.JOWASOWSKI					
APPV'D	G.JOWASOWSKI					
MFG	WORKSHOP					
Q.A	G.JOWASOWSKI			MATERIAL: PVC, GREY		DWG NO. CUBOID-15-03 / A3
						SCALE:2:3 / SHEET 1 OF 1

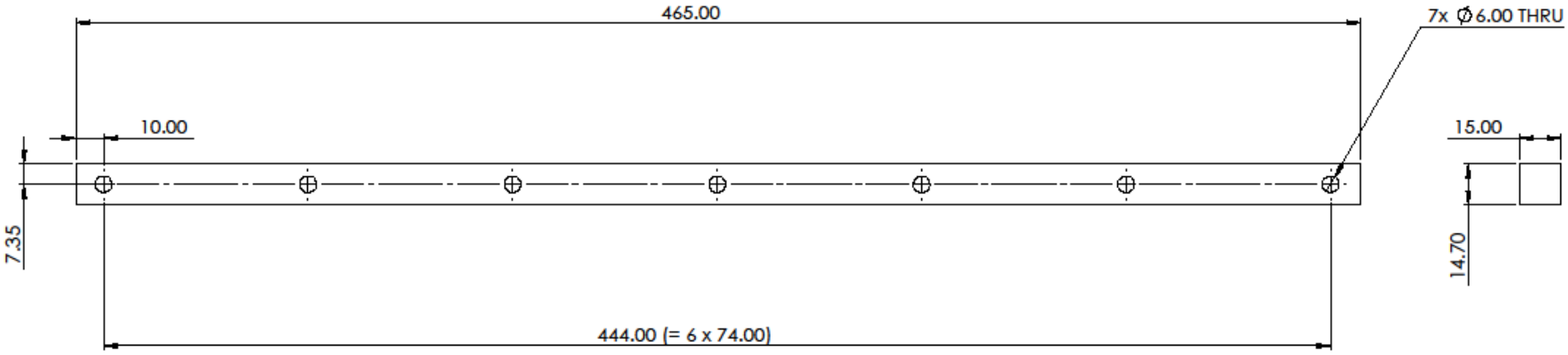

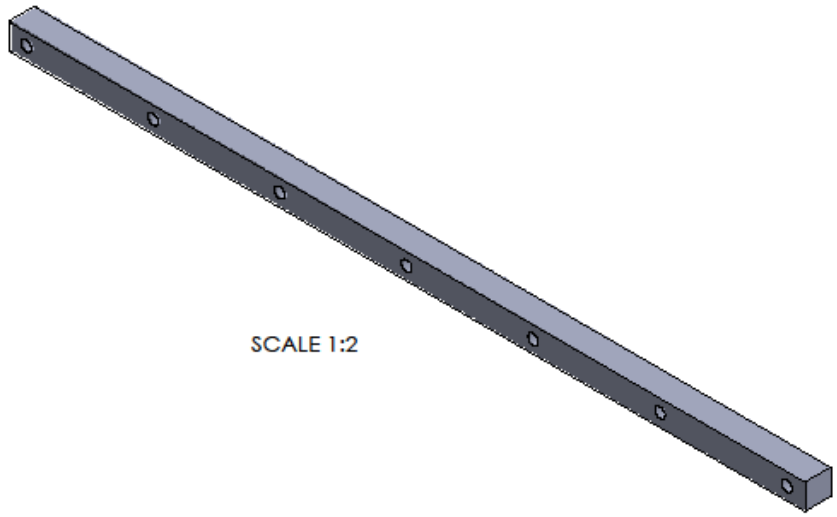

SCALE 1:2

UNLESS OTHERWISE SPECIFIED: DIMENSIONS ARE IN MILLIMETERS SURFACE FINISH: 3.2 µm Ra TOLERANCES: LINEAR: ± 0.1 ANGULAR: ± 0.5		FINISH: CLEAN		DEBUR AND BREAK SHARP EDGES		DO NOT SCALE DRAWING / REVISION 1A
	NAME	SIGNATURE	DATE			TITLE: Lower Piece, 15mm
DRAWN	G.JOWASOWSKI					
CHK'D	G.JOWASOWSKI					
APPV'D	G.JOWASOWSKI					
MFG	WORKSHOP					
Q.A	G.JOWASOWSKI			MATERIAL: PVC, GREY		DWG NO. CUBOID-15-04 / A3
						SCALE:2:3 / SHEET 1 OF 1

PART NUMBER	DESCRIPTION	QTY.
CUBOID-30-01	Interstitial Piece, 30mm	16
CUBOID-30-02	Front Plate, 30mm	1
CUBOID-30-03	Back Plate, 30mm	1
CUBOID-30-04	Lower Piece, 30mm	1
M6x60		55

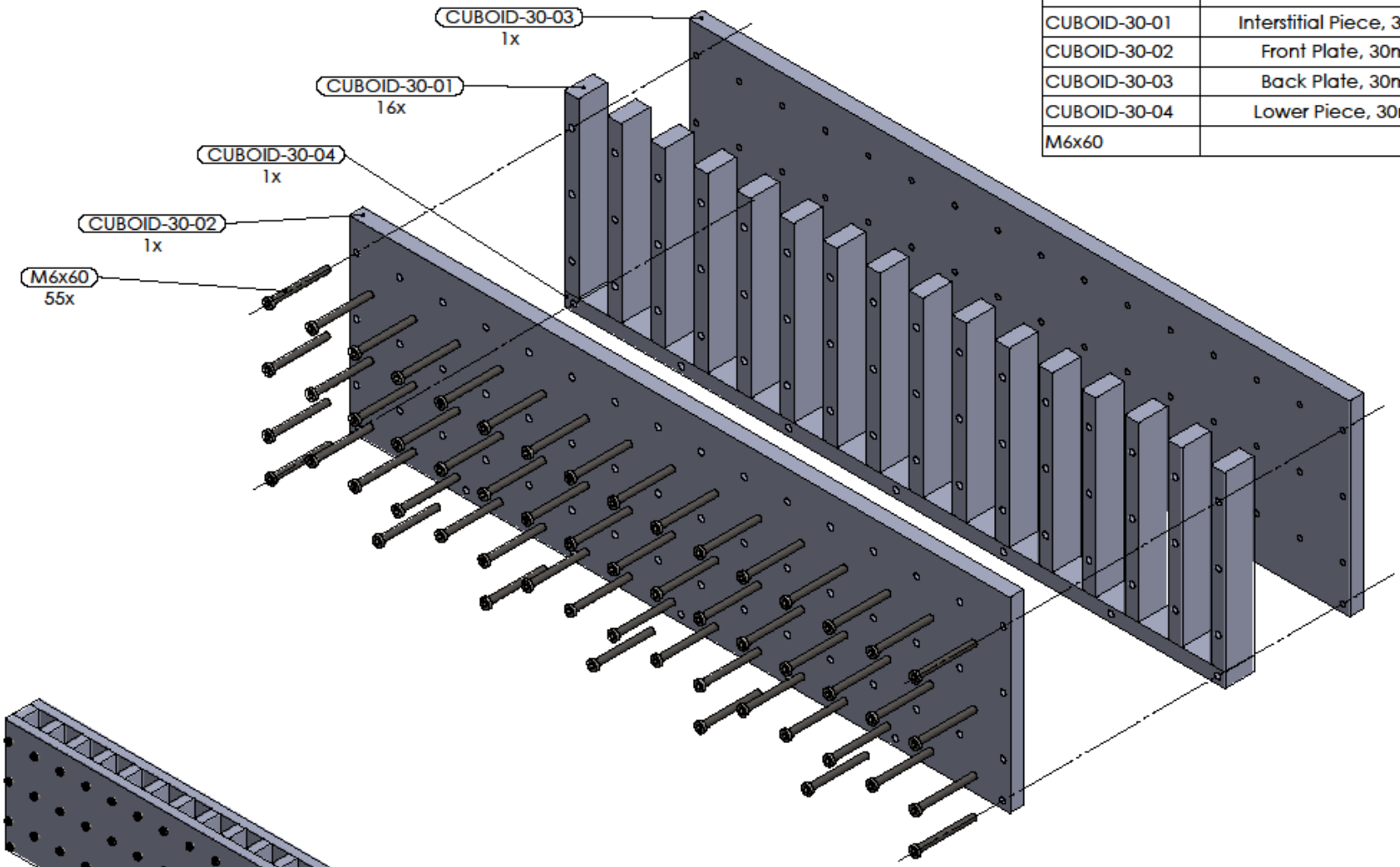

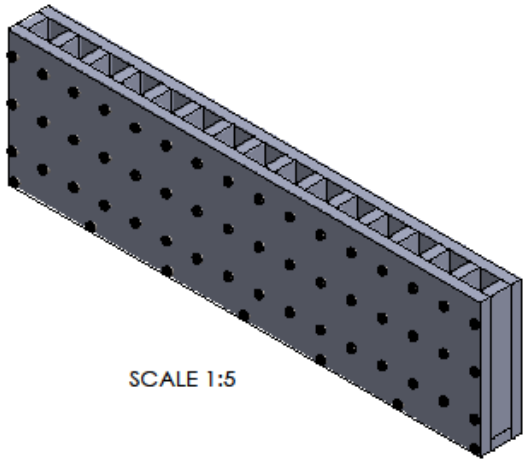

SCALE 1:5

UNLESS OTHERWISE SPECIFIED: DIMENSIONS ARE IN MILLIMETERS SURFACE FINISH: 3.2 µm Ra TOLERANCES: LINEAR: ± 0.1 ANGULAR: ± 0.5	FINISH: CLEAN	DEBUR AND BREAK SHARP EDGES	DO NOT SCALE DRAWING	REVISION 1A

	NAME	SIGNATURE	DATE
DRAWN	G.JOWASOWSKI		
CHK'D	G.JOWASOWSKI		
APPV'D	G.JOWASOWSKI		
MFG	WORKSHOP		
Q.A	G.JOWASOWSKI		

MATERIAL: PVC, GREY

TITLE: Cuboid Mould, 15mm

DWG NO. CUBOID-30-00 A3

SCALE:1:3 SHEET 1 OF 1

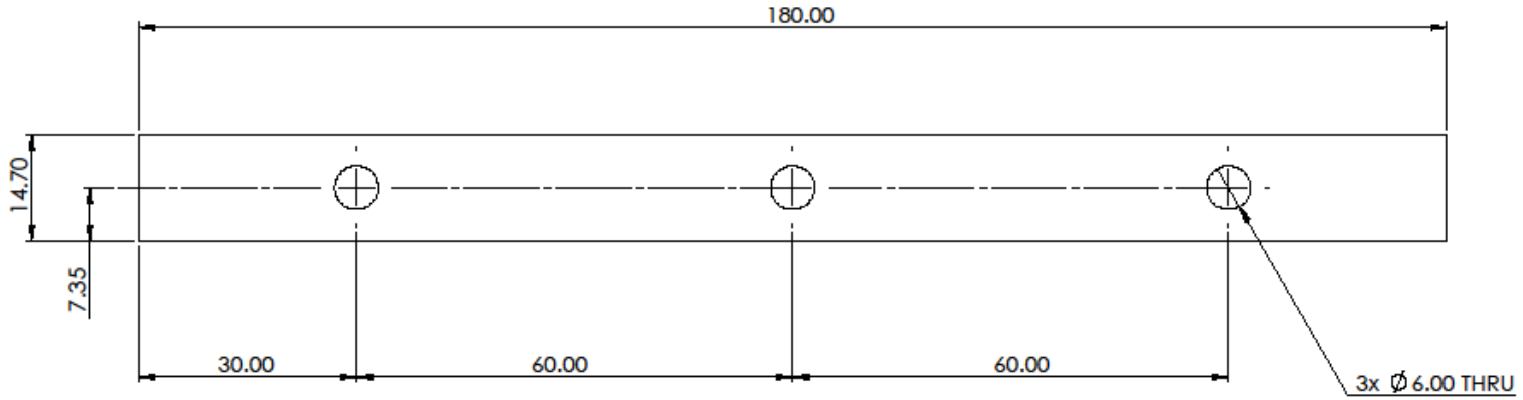

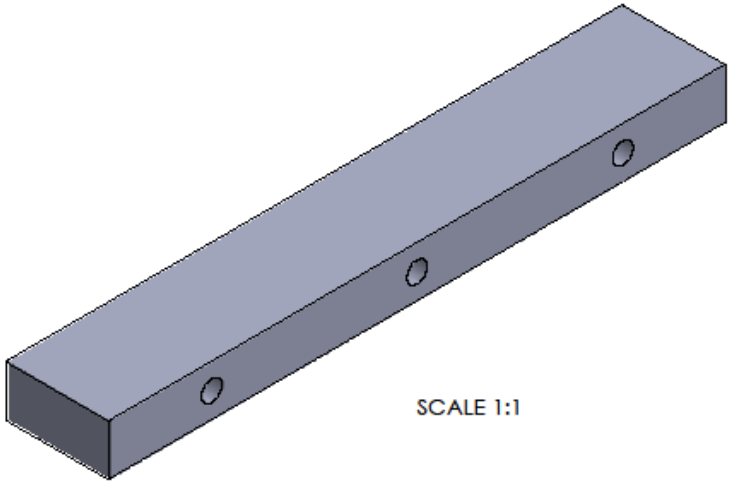

SCALE 1:1

UNLESS OTHERWISE SPECIFIED: DIMENSIONS ARE IN MILLIMETERS SURFACE FINISH: 3.2 µm Ra TOLERANCES: LINEAR: ± 0.1 ANGULAR: ± 0.5	FINISH: CLEAN				DEBUR AND BREAK SHARP EDGES	DO NOT SCALE DRAWING / REVISION 1A
	NAME	SIGNATURE	DATE			TITLE: Interstitial Part, 30mm
DRAWN	G.JOWASOWSKI					
CHK'D	G.JOWASOWSKI					
APPV'D	G.JOWASOWSKI					
MFG	WORKSHOP					
Q.A	G.JOWASOWSKI			MATERIAL: PVC, GREY		DWG NO. CUBOID-30-01 / A3
						SCALE:2:1 / SHEET 1 OF 1

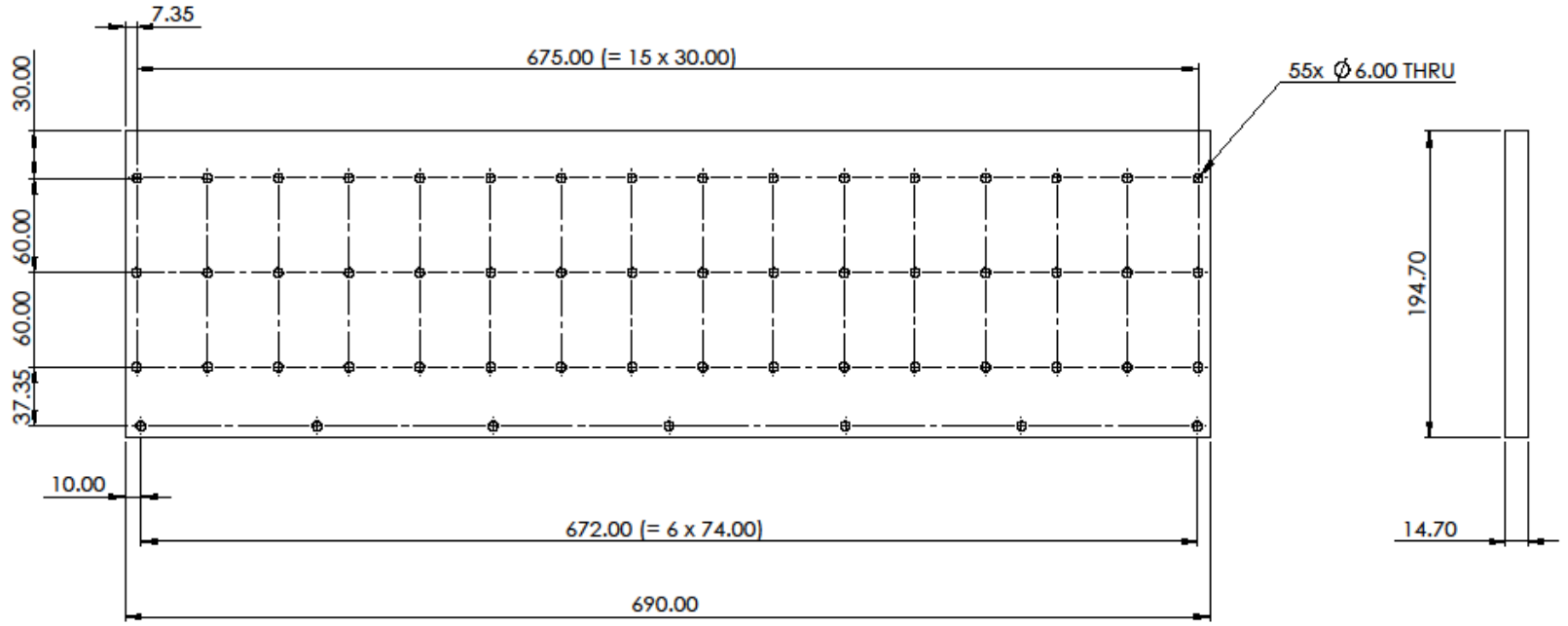

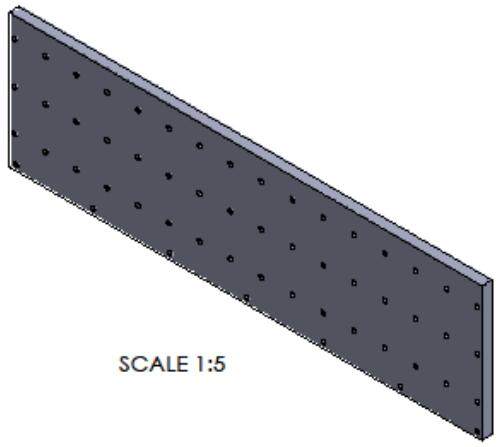

SCALE 1:5

UNLESS OTHERWISE SPECIFIED: DIMENSIONS ARE IN MILLIMETERS SURFACE FINISH: 3.2 µm Ra TOLERANCES: LINEAR: ± 0.1 ANGULAR: ± 0.5		FINISH: CLEAN		DEBUR AND BREAK SHARP EDGES		DO NOT SCALE DRAWING / REVISION 1A
	NAME	SIGNATURE	DATE			TITLE: Front Plate, 30mm
DRAWN	G.JOWASOWSKI					
CHK'D	G.JOWASOWSKI					
APPV'D	G.JOWASOWSKI					
MFG	WORKSHOP					
Q.A	G.JOWASOWSKI			MATERIAL: PVC, GREY		DWG NO. CUBOID-30-02 / A3
						SCALE:1:3 / SHEET 1 OF 1

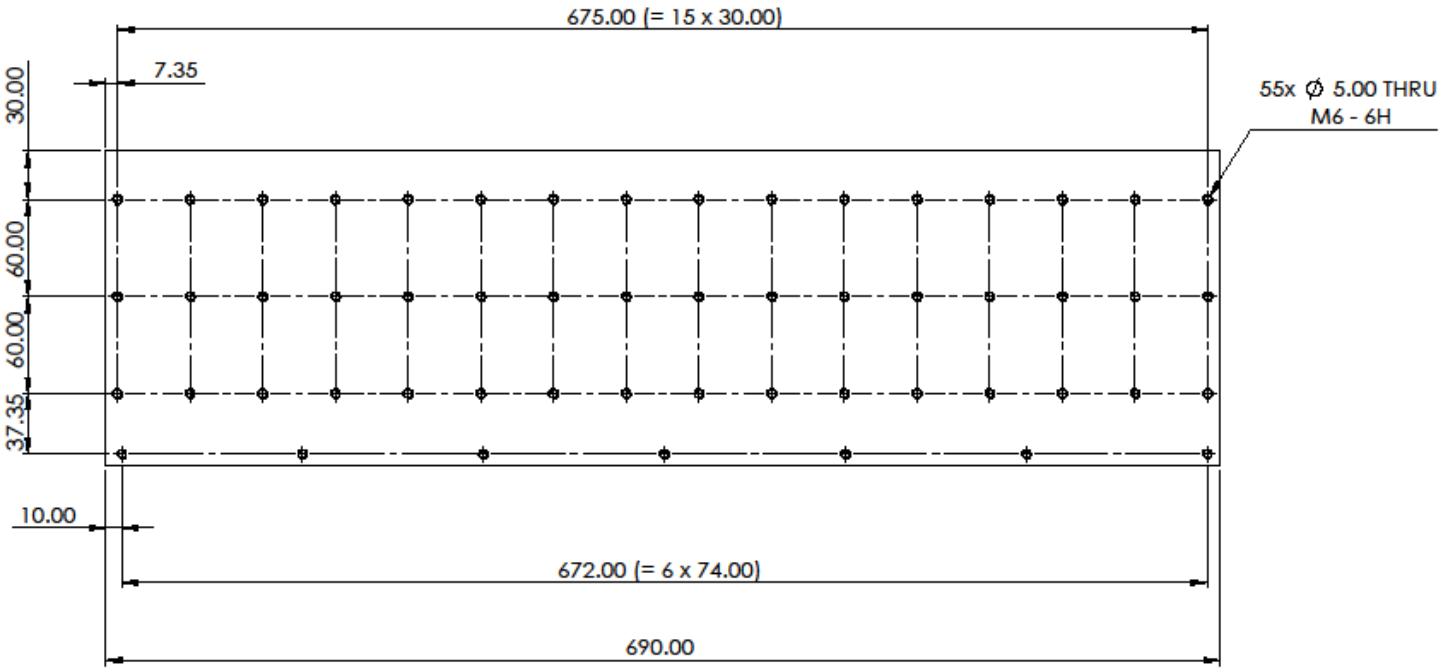

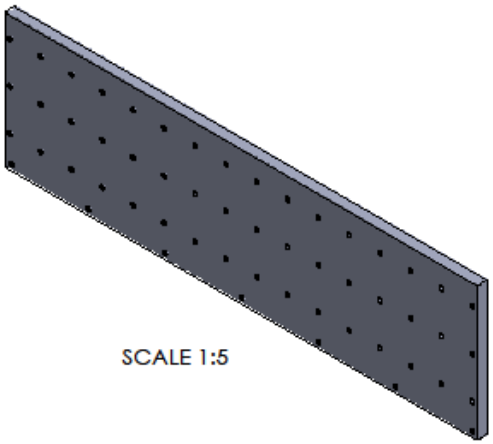

SCALE 1:5

UNLESS OTHERWISE SPECIFIED: DIMENSIONS ARE IN MILLIMETERS SURFACE FINISH: 3.2 µm Ra TOLERANCES: LINEAR: ± 0.1 ANGULAR: ± 0.5	FINISH: CLEAN				DEBUR AND BREAK SHARP EDGES	DO NOT SCALE DRAWING / REVISION 1A
	NAME	SIGNATURE	DATE			TITLE: Back Plate, 30mm
DRAWN	G.JOWASOWSKI					
CHK'D	G.JOWASOWSKI					
APPV'D	G.JOWASOWSKI					
MFG	WORKSHOP					
Q.A	G.JOWASOWSKI			MATERIAL: PVC, GREY		DWG NO. CUBOID-30-03 / A3
						SCALE:1:3 / SHEET 1 OF 1

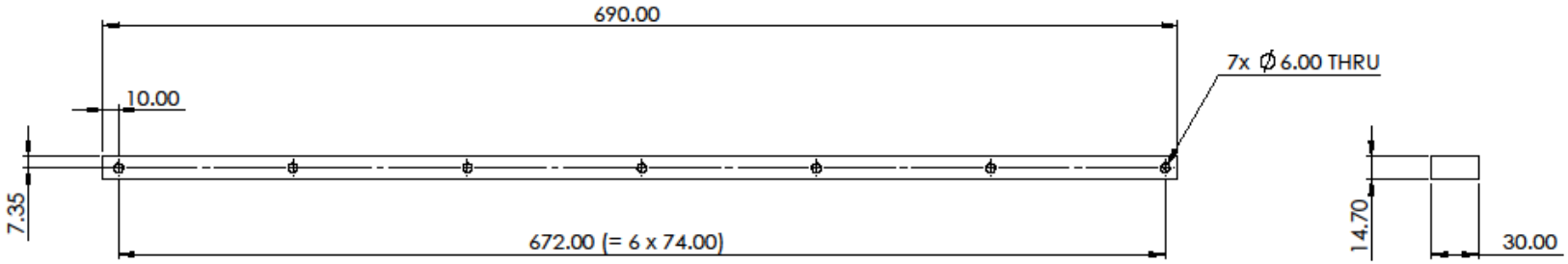

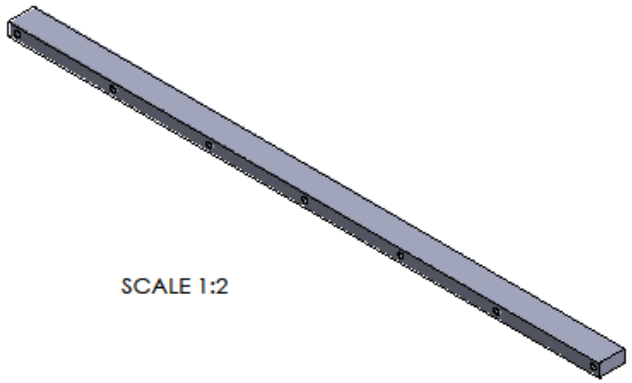

SCALE 1:2

UNLESS OTHERWISE SPECIFIED: DIMENSIONS ARE IN MILLIMETERS SURFACE FINISH: 3.2 µm Ra TOLERANCES: LINEAR: ± 0.1 ANGULAR: ± 0.5	FINISH: CLEAN			DEBUR AND BREAK SHARP EDGES	DO NOT SCALE DRAWING	REVISION 1A
	NAME	SIGNATURE	DATE		TITLE: Lower Piece, 30mm	
DRAWN	G.JOWASOWSKI					
CHK'D	G.JOWASOWSKI					
APPV'D	G.JOWASOWSKI					
MFG	WORKSHOP					
Q.A	G.JOWASOWSKI			MATERIAL: PVC, GREY	DWG NO. CUBOID-30-04	A3
					SCALE:1:3	SHEET 1 OF 1

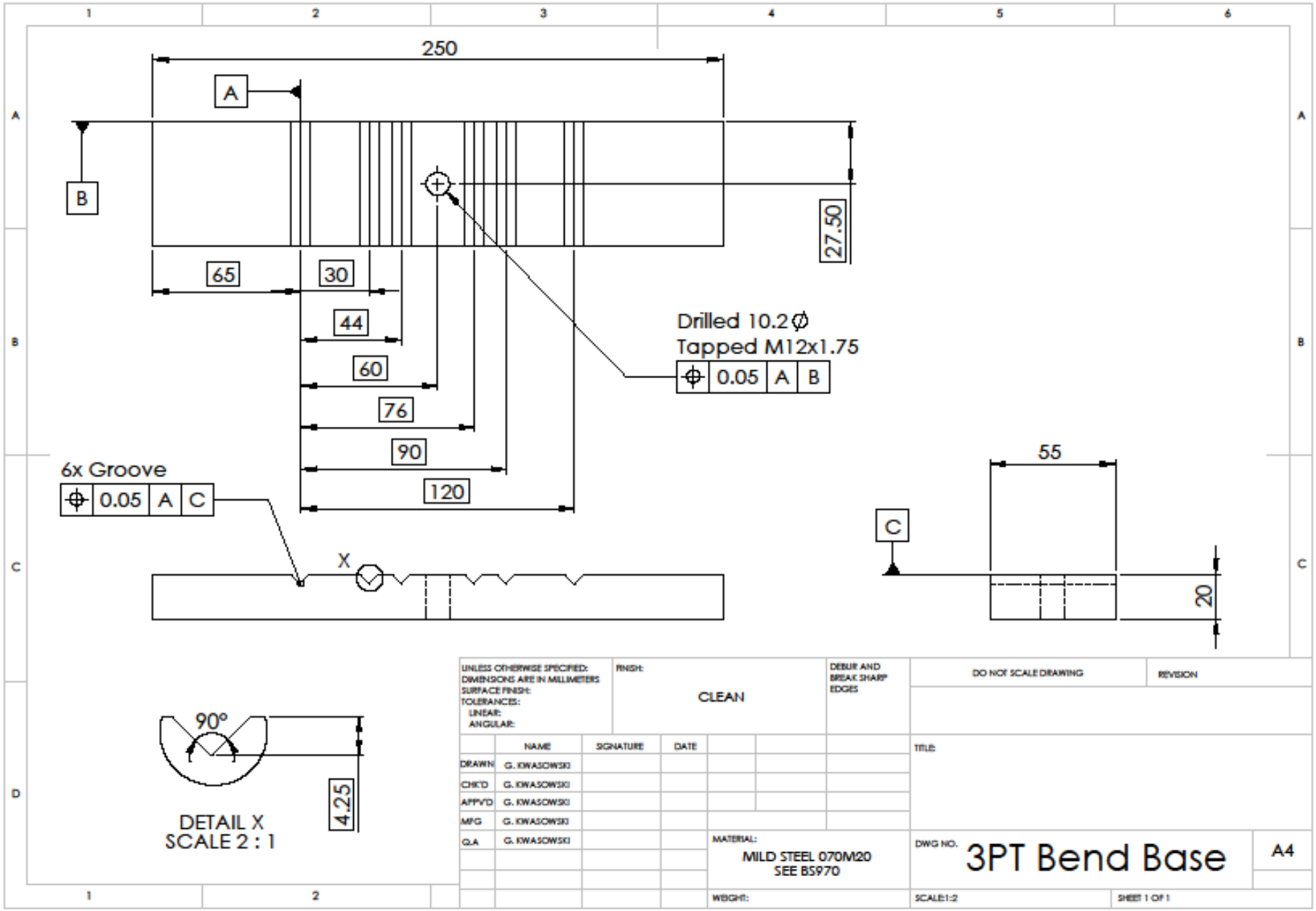
250
A
B
27.50
65
30
44
60
76
90
120
Drilled 10.2Ø
Tapped M12x1.75
0.05 A B
6x Groove
0.05 A C
X
55
C
20
90°
4.25
DETAIL X
SCALE 2 : 1
UNLESS OTHERWISE SPECIFIED:
DIMENSIONS ARE IN MILLIMETERS
SURFACE FINISH:
TOLERANCES:
LINEAR:
ANGULAR:
FINISH:
CLEAN
DEBUR AND BREAK SHARP EDGES
DO NOT SCALE DRAWING
REVISION
NAME
SIGNATURE
DATE
DRAWN G. KWASOWSKI
CHK'D G. KWASOWSKI
APP'D G. KWASOWSKI
MFG G. KWASOWSKI
Q.A G. KWASOWSKI
TITLE:
MATERIAL:
MILD STEEL 070M20
SEE BS970
DWG NO.
3PT Bend Base
A4
WEIGHT:
SCALE:1:2
SHEET 1 OF 1

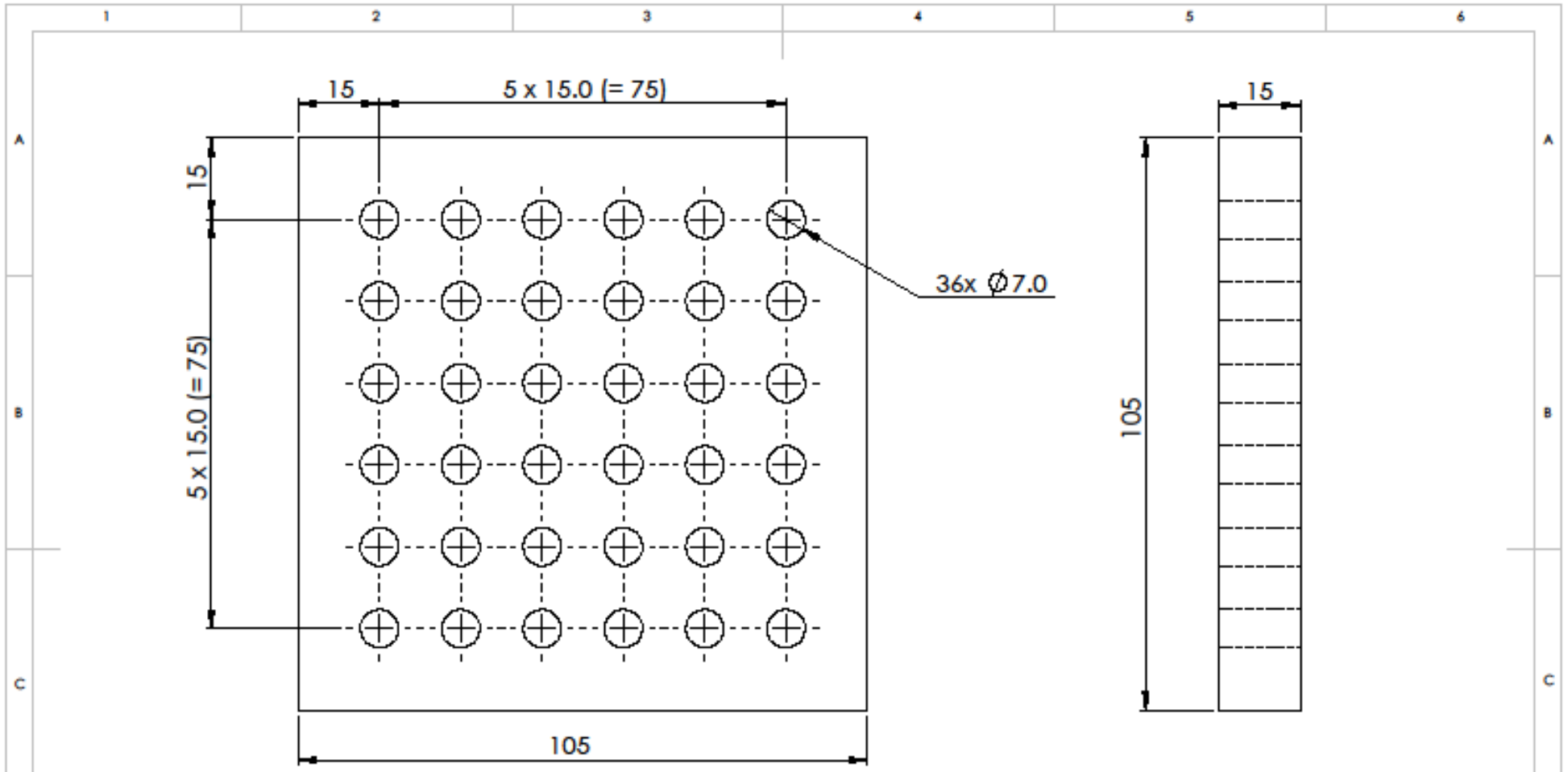

UNLESS OTHERWISE SPECIFIED: DIMENSIONS ARE IN MILLIMETERS SURFACE FINISH: TOLERANCES: LINEAR: ANGULAR:	FINISH: CLEAN		DEBUR AND BREAK SHARP EDGES	DO NOT SCALE DRAWING	REVISION	
	NAME	SIGNATURE	DATE	TITLE: Block Mould for 7mm cylinder specimens		
DRAWN	G. KWASOWSKI					
CHK'D	G. KWASOWSKI					
APPV'D	G. KWASOWSKI					
MFG	G. KWASOWSKI					
Q.A	G. KWASOWSKI					
				MATERIAL: PVC	DWG NO. MouldBlock7	A4
				WEIGHT:	SCALE: 1:1	SHEET 1 OF 1

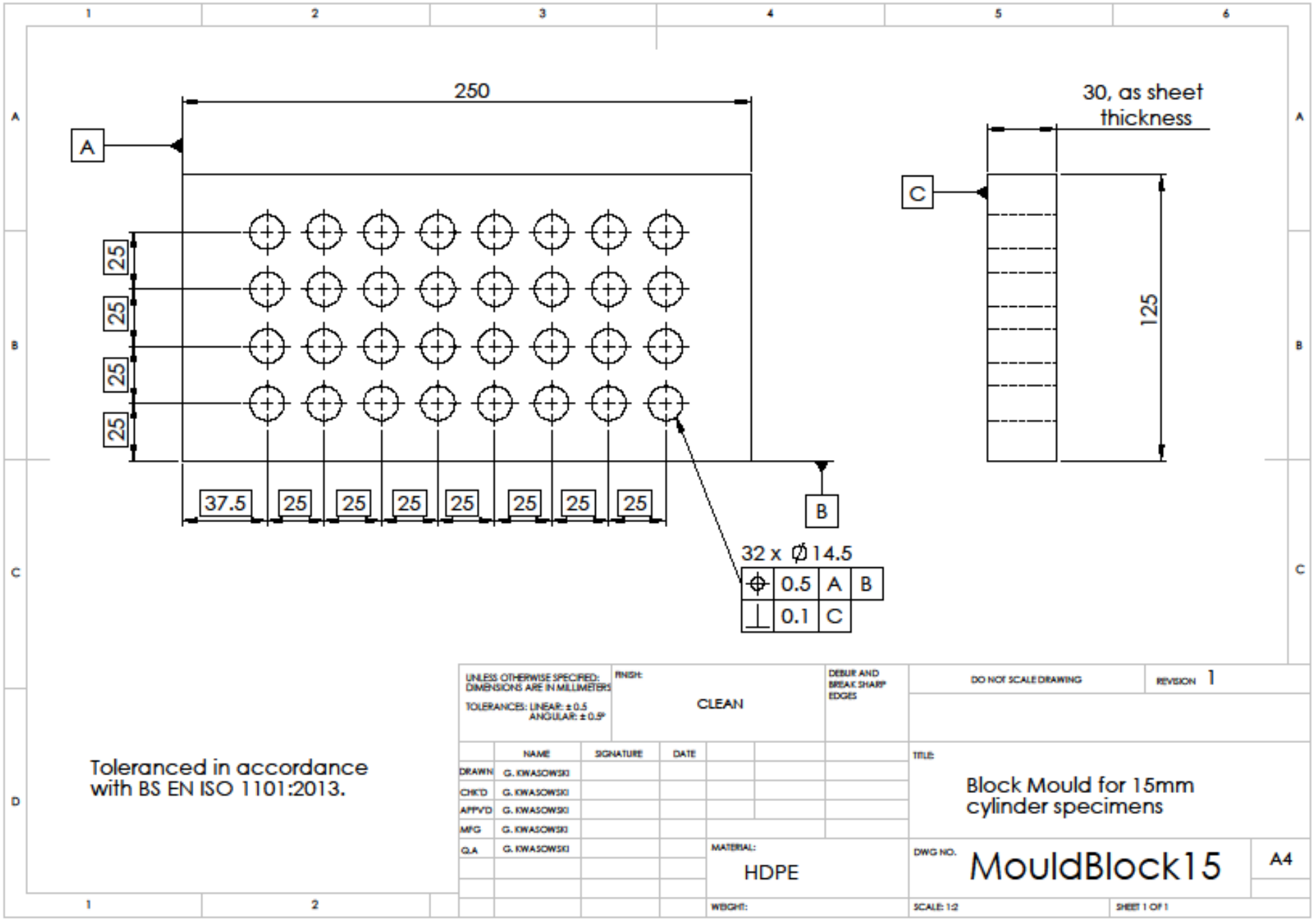
250
30, as sheet thickness
A
B
C
25
25
25
25
125
37.5
25
25
25
25
25
25
25
32 x Ø14.5
0.5 A B
0.1 C
Toleranced in accordance with BS EN ISO 1101:2013.
UNLESS OTHERWISE SPECIFIED: DIMENSIONS ARE IN MILLIMETERS
TOLERANCES: LINEAR: ± 0.5 ANGULAR: ± 0.5°
FINISH: CLEAN
DEBUR AND BREAK SHARP EDGES
DO NOT SCALE DRAWING
REVISION 1
NAME SIGNATURE DATE
DRAWN G. KWASOWSKI
CHK'D G. KWASOWSKI
APPV'D G. KWASOWSKI
MFG G. KWASOWSKI
Q.A G. KWASOWSKI
MATERIAL: HDPE
WEIGHT:
TITLE: Block Mould for 15mm cylinder specimens
DWG NO. MouldBlock15
A4
SCALE: 1:2
SHEET 1 OF 1

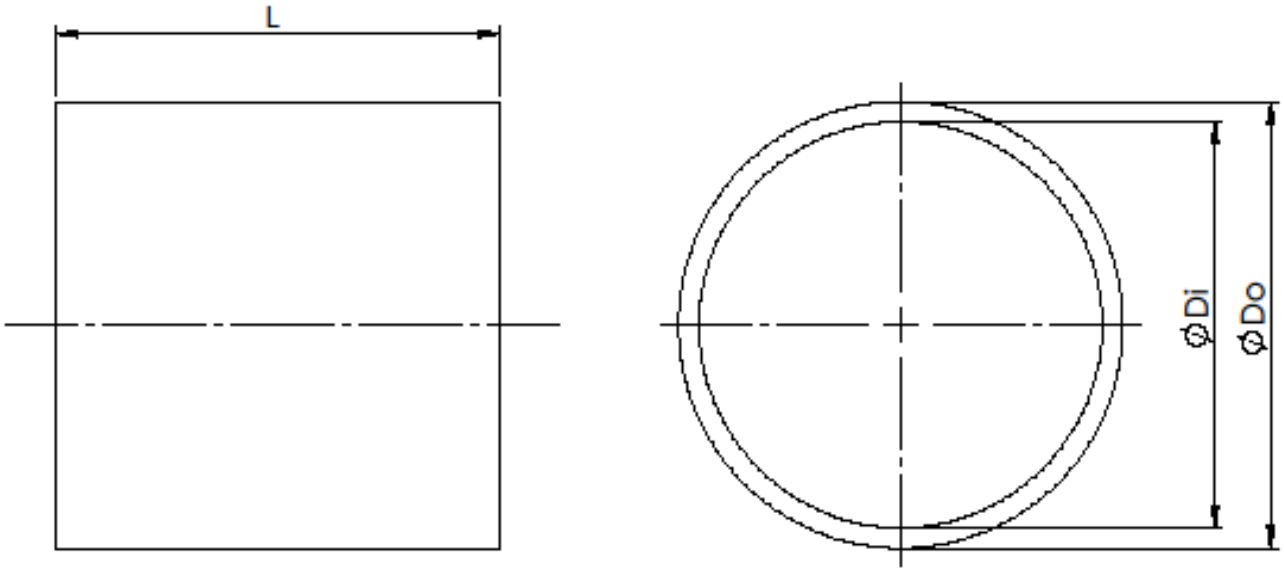

Inner Diameter (mm)	Outer Diameter (mm)	Length (mm)
30	>36	>60
42	>48	>84
64	>72	>128
103	>113	>206

UNLESS OTHERWISE SPECIFIED:
DIMENSIONS ARE IN MILLIMETERS
TOLERANCES: LINEAR: ± 0.5
ANGULAR: ± 0.5°

FINISH: CLEAN

DEBUR AND BREAK SHARP EDGES

DO NOT SCALE DRAWING

REVISION

	NAME	SIGNATURE	DATE
DRAWN	G. KWASOWSKI		
CHK'D	G. KWASOWSKI		
APPV'D	G. KWASOWSKI		
MFG	G. KWASOWSKI		
Q.A	G. KWASOWSKI		

MATERIAL: ABS (or similar)

WEIGHT:

TITLE: Tube moulds, various sizes

DWG NO. TUBES

A4

SCALE: 1:1

SHEET 1 OF 1

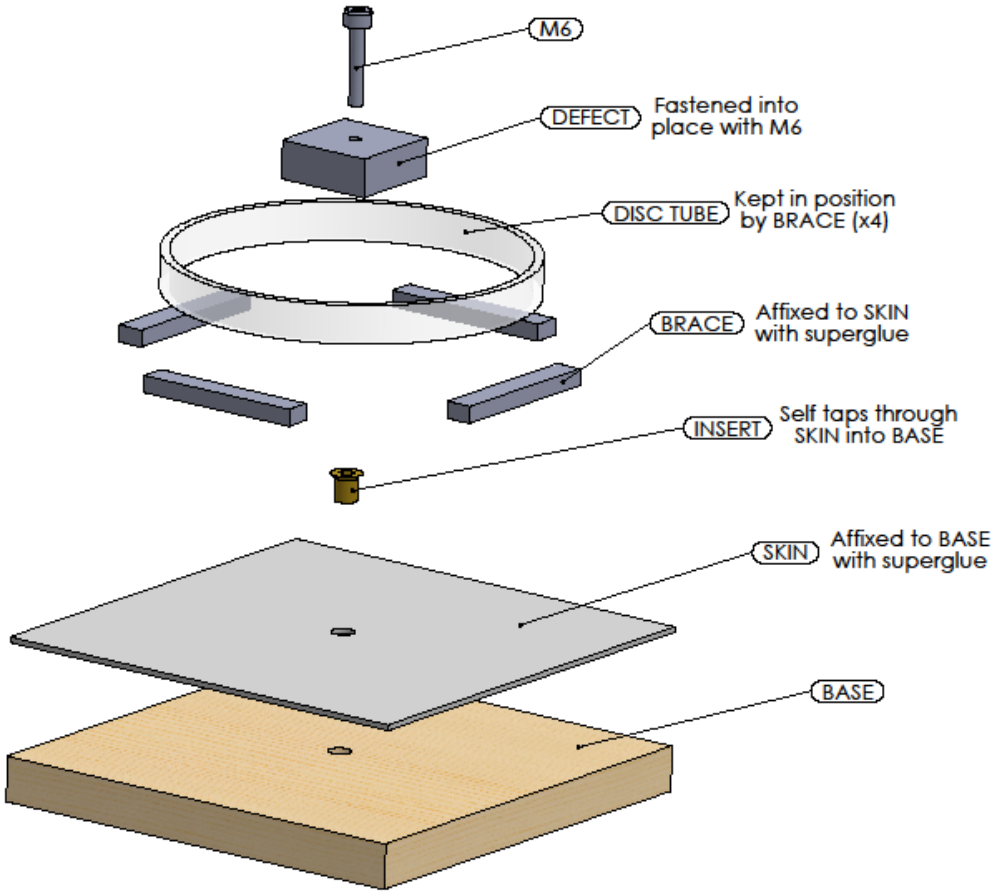

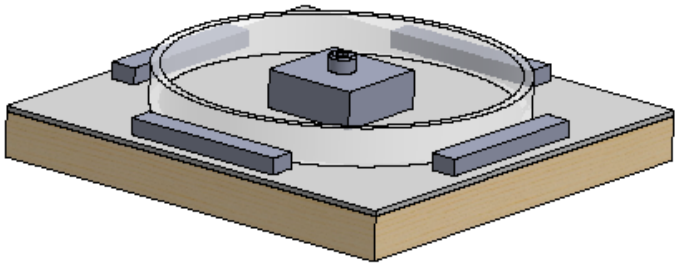

Multiple specimen moulds can be built up by placing mould cells adjacent to each other, as shown below with a 2x2 mould. This technique is photographed in the report for the 155 and 74mm discs.

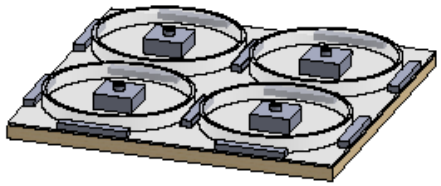

SCALE 1:5

PART NUMBER	DESCRIPTION	QTY
BASE	Plywood, approx. 15mm thick, cut to size	1
SKIN	PE, approx. 3mm thick, cut to size	1
INSERT	M6 thread insert	1
BRACE	Cuboid PVC pieces, approx. 60x12x7mm	4
DISC TUBE	Acrylic, see drawing	1
DEFECT	PMMA, see drawing	1
M6	M6 cap headed screw	1

UNLESS OTHERWISE SPECIFIED: DIMENSIONS ARE IN MILLIMETERS SURFACE FINISH: TOLERANCES: LINEAR: ANGULAR:		FINISH:			DEBUR AND BREAK SHARP EDGES	DO NOT SCALE DRAWING
	NAME	SIGNATURE	DATE			TITLE: Disc speciemn mould
DRAWN	G.KWASOWSKI					
CHK'D	G.KWASOWSKI					
APPV'D	G.KWASOWSKI					
MFG	G.KWASOWSKI					
Q.A	G.KWASOWSKI			MATERIAL: SEE BOM		DWG NO. DISC MOULD ASSEM
						A3
				WEIGHT:		SCALE:1:2 SHEET 1 OF 1

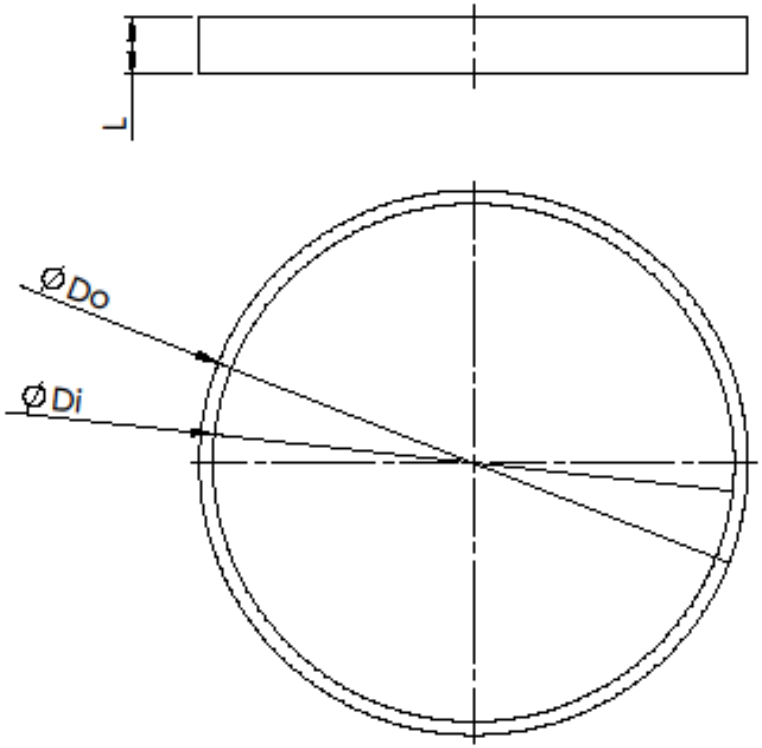

Inner Diameter (mm)	Outer Diameter (mm)	Length (mm)
74	>80	>80
155	>165	>16.5
290	>300	>30

UNLESS OTHERWISE SPECIFIED:
DIMENSIONS ARE IN MILLIMETERS
TOLERANCES: LINEAR: ± 0.5
ANGULAR: ± 0.5°

FINISH: CLEAN

DEBUR AND BREAK SHARP EDGES

DO NOT SCALE DRAWING

REVISION

	NAME	SIGNATURE	DATE
DRAWN	G. KWASOWSKI		
CHK'D	G. KWASOWSKI		
APPV'D	G. KWASOWSKI		
MFG	G. KWASOWSKI		
Q.A	G. KWASOWSKI		

TITLE: Disc specimen tubes, various sizes

MATERIAL: PVC

DWG NO. DISC TUBES

A4

WEIGHT:

SCALE: 1:1

SHEET 1 OF 1

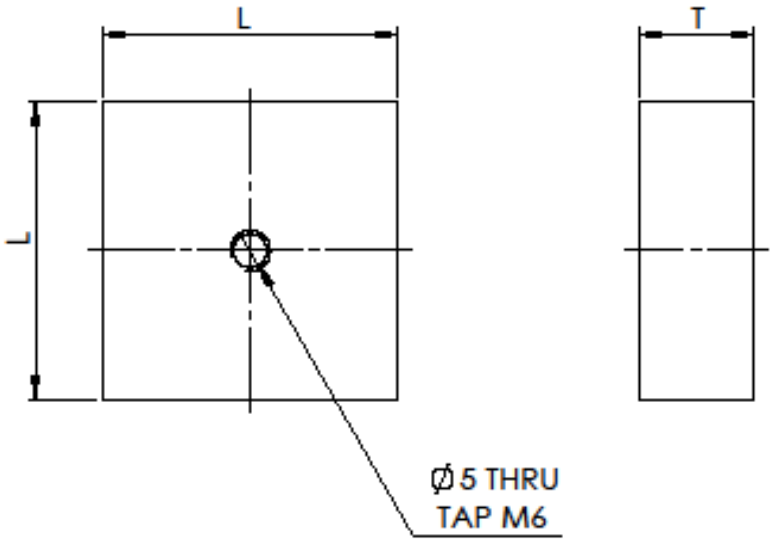

Length (mm)	Thickness (mm)
20.83	>8
43.74	>16.5
81.92	>30

UNLESS OTHERWISE SPECIFIED:
DIMENSIONS ARE IN MILLIMETERS
TOLERANCES: LINEAR: ± 0.5
ANGULAR: ± 0.5°

FINISH: CLEAN

DEBUR AND BREAK SHARP EDGES

DO NOT SCALE DRAWING | REVISION

	NAME	SIGNATURE	DATE
DRAWN	G. KWASOWSKI		
CHK'D	G. KWASOWSKI		
APPV'D	G. KWASOWSKI		
MFG	G. KWASOWSKI		
Q.A	G. KWASOWSKI		

MATERIAL: PVC

WEIGHT:

TITLE: Disc specimen defect, various sizes

DWG NO. DISC DEFECT

A4

SCALE: 1:1 | SHEET 1 OF 1